Lehrstuhl für Statik
Ingenieurfakultät Bau Geo Umwelt
Technische Universität München

Master's Thesis
in Computational Mechanics (Master of Science (M.Sc.))

Implementation and Assessment of Partitioned Schemes (Co–Simulation) for Closed–Loop Structural Control in Computational Fluid–Structure Interaction

Honours Project
in Bavarian Graduate School of Computational Engineering
(Master of Science with Honours (M.Sc. (hons)))

Analysis of Gauß–Seidel Fixed–Point Formulations for an Iteratively Coupled Model Problem with Reference to Fluid–Structure–Control Interaction

Author Christopher Lerch, B.Eng. M.Sc. (hons) (TUM)

Advisor Prof. Dr.-Ing. Kai-Uwe Bletzinger

Supervisors Dr.-Ing. Roland Wüchner
Dipl.-Ing. (FH) Andreas Winterstein (geb. Mini), M.Sc.

München
March 16, 2016

Revision November 3, 2018 9:58am

Ich versichere, dass ich die vorliegende Arbeit mit ihren beiden Bestandteilen Master's Thesis und Honours Project selbstständig verfasst und nur die angegebenen Quellen und Hilfsmittel verwendet habe.

München, 16. März 2016 Christopher Lerch

Nothing in life is to be feared, it is only to be understood. Now is the time to understand more, so that we may fear less.

—Marie Skłodowska Curie
(1867–1934)

Abstract

Master's Thesis

The present work deals with active vibration control on lightweight structures subject to periodic excitations in fluid-structure interactions. For this purpose partitioned schemes for co-simulation of computational fluid-structure-control interaction are developed and implemented. They are subsequently investigated in numerical experiments. In addition, different closed-loop control laws are derived and employed.

Thus, this work essentially covers two aspects: First, convergence and stability properties as well as numerical effort of the proposed schemes are analyzed. This is supported by investigations on a model problem within the Honours Project. Second, the effectiveness of the previously established closed-loop control laws is assessed.

Honours Project

A simple coupled model problem is developed and iteratively solved using fixed-point formulations for different Gauß-Seidel communication patterns. Convergence and stability properties of the resulting solution algorithms are analytically assessed. The results allow predictions on corresponding partitioned schemes (co-simulation) for computational fluid-structure-control interaction. The Honours Project mainly covers Chapter 3 Model Problem (pp. 32–51) as well as parts of Chapter 9 Fluid–Structure–Control Interaction (pp. 118–160) of this work.

Zusammenfassung

Master's Thesis

Die vorliegende Arbeit befasst sich mit der aktiven Schwingungsdämpfung an leichten Strukturen unter periodischer Anregung innerhalb von Fluid-Struktur Interaktionen. Zu diesem Zweck werden partitionierte Ansätze zur Co-Simulation von numerischer Fluid-Struktur-Regler Interaktion erarbeitet und umgesetzt. Anschließend werden sie in numerischen Experimenten näher untersucht. Ergänzend werden verschiedene Regelgesetze abgeleitet und angewendet.

Diese Arbeit betrachtet daher im Wesentlichen zwei Aspekte: Zum einen werden Konvergenz- und Stabilitätsverhalten sowie numerischer Aufwand der vorgeschlagenen Ansätze analysiert. Dies wird von Untersuchungen an einem Modellproblem im Rahmens des Honours Projects unterstützt. Zum anderen wird die Leistungsfähigkeit der vorher erarbeiteten Regelgesetze beurteilt.

Honours Project

Ein einfaches gekoppeltes Modellproblem wird erarbeitet und unter Verwenung von Fixpunktformulierungen für verschiedene Gauß-Seidel Kommunikationsschemata iterativ gelöst. Konvergenz- und Stabilitätsverhalten dieser Lösungsalgorithmen werden mittels einer analytischen Untersuchung beurteilt. Die Ergebnisse lassen Vorhersagen bei entsprechenden partitionierten Ansätzen (Co-Simulation) für numerische Fluid-Structur-Regler Interaktion zu. Das Honours Project umfasst im Wesentlichen Kapitel 3 Model Problem (S. 32–51) sowie Teile von Kapitel 9 Fluid–Structure–Control Interaction (S. 118–160) dieser Arbeit.

Acknowledgement

I would like to gratefully thank

all members of the Chair of Structural Analysis, in particular

Prof. Bletzinger
Roland Wüchner
Andreas Mini

Stefan Sicklinger

my family, in particular

Stefanie
Christine with Eberhard
Heinrich with Elli
Michaela
Maria with Siegfried

and my friends

for all given opportunities and provided support.

Contents

The important thing is not to stop questioning. Curiosity has its own reason for existence. [...] Never lose a holy curiosity.

—ALBERT EINSTEIN (1879–1955)

1 Introduction

The present work deals with numerical experiments on fluid-structure-control interaction, i.e. multi-physics involving fluid dynamics, structural mechanics and closed-loop control of structures. Purpose of this introductory chapter is to classify this work within the wide range of numerical simulation strategies. Please note, that relevant categorizations are *emphasized*.

In his introductory Sections 1.2 and 1.3 (pp. 2–4) Küttler (2009) briefly, but critically, discusses the aspects of *numerical experiments* and mathematical modelling. Numerical experiments are "the recalculation of the differential equations"[1], i.e. the process of solving the differential equations, which are results of mathematical modeling. Mathematical models "are themselves scientific theories, thus speculatively stated assumptions"[2] with a certain, mostly well-known, associated range of validity. Reliable statements can therefore be derived within the common physical domain.

Consequently, numerical experiments only allow observations on mathematical models whereas physical experiments reveal reality. It becomes evident that the solution of such simulations can only be as valuable as the underlying mathematical models. "Substantial surprises can not occur that way."[3]

On the contrary, the recombination of such classical mathematical models outside their common domains thus far, i.e. the application in a non-

[1] original Ger. "das Nachrechnen der Differentialgleichungen" (Küttler 2009, Section 1.2, p. 2)

[2] original Ger. "sind für sich wissenschaftliche Theorien, also spekulativ aufgestellte Vermutungen" (Küttler 2009, Section 1.2, p. 2)

[3] "Wirkliche Überraschungen können so nicht auftreten." (Küttler 2009, Section 1.2, p. 3)

classical manner demands more attention (Küttler 2009, Section 1.2, p. 2). This exceptional treatment beyond common borders may, however, lead to new helpful insights and a foundation for further numerical or physical experiments and applications. Additionally, the use of numerical experiments convinces with advantages like low effort, low costs and easy access to all quantities within the simulated spatial and temporal domains.

Multi-physics or *multi-physical problems* are the simulation of interactions, i.e. the coupling of two or more physical fields within one problem. This, for instance, can be fluid-structure-signal interactions on wind turbines (Sicklinger, Lerch, Wüchner, and Bletzinger 2015; Sicklinger 2014), fluid-structure-fluid interactions (Uekermann, Gatzhammer, and Mehl 2014), fluid-structure-electromagnetism interactions on hearts (Lafortune, Arís, Vázquez, and Houzeaux 2012) or fluid-structure-accoustic interactions (Link, Kaltenbacher, Breuer, and Döllinger 2009).

Field-coupling covers volume- and surface-coupling. Volume-coupling identifies interactions that take place in subdomains of the same dimension as the actual computational domain whereas *surface-coupling* characterizes interactions that are restricted to lower-dimensional subdomains such as common surfaces of two fields (interfaces). *Signal-coupling* refers to the interactions that are restricted to signals, quantities without affiliation to a spatial domain.

Fluid-structure interaction (FSI) is surface-coupling of a fluid and a structural field. Any change in the fluid domain triggers a response of the structural domain and vice versa. It depicts one of the classical multi-physical problems that arise in mechanics. In this context, the term fluid-structure interaction exclusively refers to the free and unforced dynamics between fluid and solid. Exterior modification of the behavior of any involved field, fluid or structure, results in an influenced or forced interaction behavior.

This work exclusively focuses on manipulating the dynamics of the structural field by a closed-loop controller. The objective is to get the desired over-all behavior "minimum or at best zero displacement" within a fluid-structure interaction. This multi-physical problem is referred to as *fluid-structure-control interaction (FSCI)*. Thus, it involves three domains, fluid dynamics, structural mechanics and closed-loop control of structures. The interactions are identified as surface-coupling of fluid and structure and signal-coupling of structure and closed-loop controller.

In literature, various numerical approaches for solving multi-physical problems can be found. Basically, they all can be boiled down to a blend of two basic approaches, the monolithic approach and the partitioned approach.

A monolithic approach is modeling all N physics of a multi-physical problem at once by formulating one large equation system

$$\left.\mathcal{F}_i\left(\boldsymbol{X}^{n+1}\right) = \mathbf{0} \quad (i = 1, \dots, N)\ \right\} \mathcal{F}\left(\boldsymbol{X}^{n+1}\right) = \mathbf{0}. \tag{1.1}$$

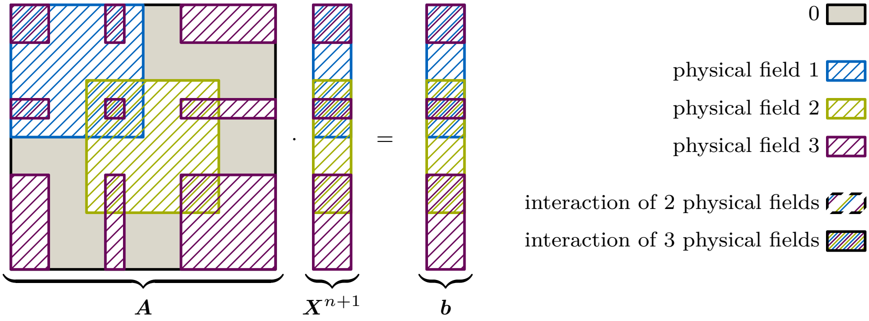

Figure 1.1 SCHEMATIC REPRESENTATION OF A MONOLITH SOLVER FOR THREE PHYSICAL FIELDS ($N = 3$).

This leads to a single monolithic solver $\mathcal{F}$ which determines all degrees of freedom or states $\boldsymbol{X}^{n+1}$ simultaneously, e.g. via a Newton-Raphson procedure each time step.

In a *partitioned approach*, by contrast, the multi-physical system is split up into N single-physics subsystems $\mathcal{F}_i$ $(i = 1, \ldots, N)$ exchanging input data $\boldsymbol{U}_i^{n+1}$ and output data $\boldsymbol{Y}_i^{n+1}$ via interfaces. This procedure is referred to as partitioning. Each resultant subsystem i is formulated and solved separately with own internal states $\boldsymbol{X}_i^{n+1}$:

$$\left.\begin{aligned}\mathcal{F}_i\left(\boldsymbol{X}_i^{n+1}, \boldsymbol{U}_i^{n+1}\right) = \boldsymbol{0}\\ \boldsymbol{Y}_i^{n+1} = \mathcal{G}_i\left(\boldsymbol{X}_i^{n+1}\right)\end{aligned}\right\} \boldsymbol{Y}_i^{n+1} = \mathcal{G}_i^{\left[\boldsymbol{X}_i^{n+1}\right]}\left(\boldsymbol{U}_i^{n+1}\right). \tag{1.2}$$

Herein operator $\mathcal{G}_i$ depicts the mapping of states onto output quantities and operator $\mathcal{G}_i^{[\,]}$ the input-output relation in a black box manner emphasizing internal states. That way the interaction, i.e. coupling is formulated in terms of $N!$ interface constraints $\mathcal{I}_{ij}$ between subsystems i and j

$$\mathcal{I}_{ij}\left(\boldsymbol{U}_i^{n+1}, \boldsymbol{Y}_i^{n+1}, \boldsymbol{U}_j^{n+1}, \boldsymbol{Y}_j^{n+1}\right) = \boldsymbol{0} \quad (i, j = 1, \ldots, N \quad i < j) \tag{1.3a}$$

i.e. one global interface constraint $\mathcal{I}$ between all subsystems

$$\mathcal{I}\left(\boldsymbol{U}_i^{n+1}, \boldsymbol{Y}_i^{n+1},\ i = 1, \ldots, N\right) = \boldsymbol{0} \tag{1.3b}$$

simplifying the replacement of solvers and reuse of existing, well established software tools. However, this modularity may lead to stability and accuracy issues demanding for special treatment. Partitioned coupling is sometimes also referred to as *co-simulation* or *N-code coupling*.

Partitioned coupling can either be realized as *iterative/strong/implicit coupling* or as loose/weak/staggered coupling. The difference lies in fulfillment of the interface constraints (1.3). Iterative coupling strictly satisfies all interface constraints demanding an interface iteration loop with desired convergence tolerance. Whereas, loose coupling misses any interface iteration

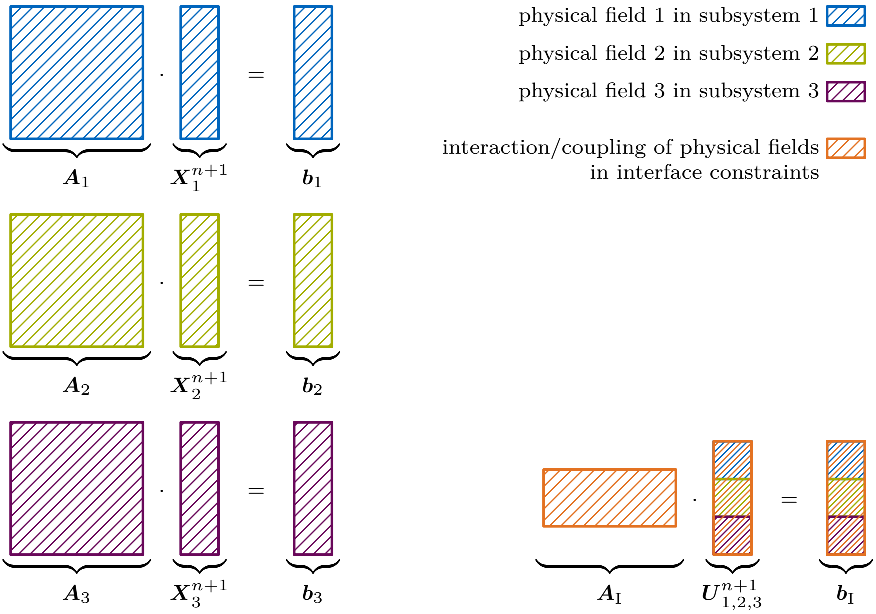

Figure 1.2 Schematic representation of a partitioned solution procedure for three physical fields ($N = 3$).

allowing partial violation of interface constraints. Therefore, in general, only iterative coupling matches the monolithic solution (1.1) paying, however, the price of a usually higher numerical effort. Reviewing fluid-structure interaction, iterative coupling guarantees kinematic compatibility and equilibrium of forces at the interface while loose coupling normally just satisfies kinematic compatibility.

The characterization of partitioned coupling states the exchange of data between the individual subsystems as an essential property. This temporal data exchange can be realized with two fundamental communication patterns: the serial *Gauß-Seidel (GS)* pattern and the parallel Jacobi (JC) pattern. The Gauß-Seidel pattern is similar to a chain. The output of one chain link, subsystem, always provides the input of the next one. These dependencies result in serial execution of the subsystems. The Jacobi pattern, on the other hand, runs all subsystems independently in parallel. In- and outputs do not necessarily have to be connectable. For further details it is referenced to Sicklinger (2014, Sections 3.3, 3.4, 4.6, pp. 57–65, 80–87) among others.

This work developes iterative coupling strategies using Gauß-Seidel communication patterns and *fixed-point iterations with dynamic relaxation* for solving the interface constraints. Details will be introduced in Chapter 3 Model Problem (pp. 32 ff.) together with Chapters 7 Fluid–Structure

Interaction (pp. 79 ff.) and 9 Fluid–Structure–Control Interaction (pp. 118 ff.). In literature this approach is also referred to as *Dirichlet-Neuman coupling/iterative strategy with relaxation* or *block Gauß-Seidel procedure*. *Aitken acceleration* is used for dynamically updating the relaxation factor. It is presented in Küttler and Wall (2008) and Küttler (2009). Similar concepts have already been mentioned in Uekermann, Gatzhammer, and Mehl (2014) without further investigation.

Differing coupling strategies would also be feasible, e.g. an iterative coupling strategy using a Jacobi communication pattern and the Interface Jacobian-based Co-Simulation Algorithm (IJCSA) (Sicklinger, Belsky, Engelmann, Elmqvist, Olsson, Wüchner, and Bletzinger 2014; Sicklinger 2014) for solving the interface constraints. Software limitations lead to postponement of that concept, since full Jacobian information at the interface (non-black-box) are demanded but not yet provided by the fluid solver. This fact is also mentioned in Uekermann, Gatzhammer, and Mehl (2014).

It should also be noted that a directly related topic to solving interface constraints is the realization of data transfer between non-matching spatial discretizations at the interfaces, also referred to as mapping. For an overview see for instance Wang (2016) or Wang, Sicklinger, Wüchner, and Bletzinger (2016).

One last important topic worth mentioning in connection to fluid-structure (-control) interaction is the added-mass effect. Added-mass is fluid mass accelerated by the deforming structure. Its amount has a tremendous effect on the dynamical behavior of the structure in the interaction. The arising strong non-linear effects themselves are decisive for the stability properties of the coupling algorithm. The added-mass effect depends on the ratio of fluid and solid density $\frac{\rho_\mathrm{F}}{\rho_\mathrm{S}}$ as well as geometrical conditions. Further discussions on added-mass can be found in Causin, Gerbeau, and Nobile (2005) and Brummelen (2009).

The remainder of this work is organized as follows: In Part I Theoretical Considerations (pp. 8 ff.) Chapter 2 Fundamentals (pp. 8 ff.) addresses some frequently required fundamentals on the mathematics/algorithmics of numerical initial value problems, i.e. numerical time integration and the phenomenologics of vortex shedding on cylinders in crossflow. Chapter 3 Model Problem (pp. 32 ff.) presents the above-mentioned coupling schemes for solving fluid-structure-control interaction problems. They are analyzed on an analytical basis using a one-dimensional model problem. In Part II Numerical Experiments (pp. 53 ff.) Chapter 4 The Experiment (pp. 53 ff.) introduces the multi-dimensional numerical experiment on fluid-structure-control interaction. Chapters 5 The Fluid (CFD) Subsystem (pp. 57 ff.), 6 The Structural (CSM) Subsystem (pp. 68 ff.) and 8 The Controller (CLC) Subsystem (pp. 94 ff.) cover details on the respective subsystems. The structure is realized in two levels, the controller in three. Chapter 7 Fluid–Structure Interaction (pp. 79 ff.) investigates the fluid-structure interaction

(FSI) sub-problem. Chapter 9 Fluid–Structure–Control Interaction (pp. 118 ff.) revisits the established coupling schemes and finally applies them to the multi-dimensional fluid-structure-control interaction (FSCI) problem. Numerical aspects as well as the applied control algorithms are analyzed. Part III Conclusion and Outlook (pp. 162 ff.) concludes the work of this thesis and motivates future investigations. Part III Appendices (pp. 165 ff.) covers additional material.

Part I

Theoretical Considerations

2 Fundamentals

This chapter contains a pure collection of frequently required fundamentals gathered in the beginning of this theses. Therefore, it makes no claim to completeness. The content covers certain aspects on the mathematics and algorithmics of numerical initial value problems, i.e. numerical time integration, and on the phenomenology of vortex shedding of circular and square cylinders in crossflow.

2.1 Numerical Initial Value Problems in Ordinary Differential Equations

Initial value problems (IVP's) arising in linear dynamics are most generally described by vectorial, first order, linear, ordinary differential equations (ODE's)

$$\dot{\boldsymbol{\phi}} = \boldsymbol{A}\boldsymbol{\phi} + \boldsymbol{B}\boldsymbol{\psi} \tag{2.1a}$$

with appropriate initial conditions (IC's)

$$\boldsymbol{\phi}(t_0) = \boldsymbol{\phi}_0. \tag{2.1b}$$

The initial velocity is calculated to

$$\dot{\boldsymbol{\phi}}(t_0) = \dot{\boldsymbol{\phi}}_0 = \boldsymbol{A}\boldsymbol{\phi}_0 + \boldsymbol{B}\boldsymbol{\psi}(t_0) \tag{2.2}$$

inserting the IC's (2.1b) into the ODE (2.1a).

By default, accuracy, stability and other properties of a numerical time integration scheme for first order IVP's are derived from application to the scalar, one-dimensional, autonomous $\psi \equiv 0$ and therefore simplest possible problem of form (2.1)

$$\dot{\phi} = a\phi \tag{2.3a}$$

$$\begin{aligned} \phi(t_0) &= \phi_0 \\ \dot{\phi}(t_0) &= \dot{\phi}_0 = a\phi_0. \end{aligned} \tag{2.3b}$$

It possesses one single eigenvalue $\lambda = a$.

Certain IVP's stemming for instance from linear structural dynamics are more commonly described by second order linear ODE's

$$\boldsymbol{M}\ddot{\boldsymbol{\phi}} + \boldsymbol{C}\dot{\boldsymbol{\phi}} + \boldsymbol{K}\boldsymbol{\phi} = \boldsymbol{\psi} \tag{2.4a}$$

with appropriate pairs of IC's

$$\begin{aligned} \boldsymbol{\phi}(t_0) &= \boldsymbol{\phi}_0 \\ \dot{\boldsymbol{\phi}}(t_0) &= \dot{\boldsymbol{\phi}}_0. \end{aligned} \tag{2.4b}$$

In this case the initial acceleration is accordingly calculated to

$$\ddot{\boldsymbol{\phi}}_0 = \boldsymbol{M}^{-1}\left(\boldsymbol{\psi}\left(t_0\right) - \boldsymbol{C}\dot{\boldsymbol{\phi}}_0 - \boldsymbol{K}\boldsymbol{\phi}_0\right) \tag{2.5}$$

applying the ODE (2.4a) on the IC's (2.4b).

Accuracy, stability and other properties of a particular numerical time integration scheme for second order IVP's are analogously derived from applying the scheme to the simplest possible problem of type (2.4)

$$m\ddot{\phi} + k\phi = 0 \tag{2.6a}$$

$$\begin{aligned} \phi(t_0) &= \phi_0 \\ \dot{\phi}(t_0) &= \dot{\phi}_0 \end{aligned} \tag{2.6b}$$

$$\ddot{\phi}(t_0) = \ddot{\phi}_0 = \frac{k}{m}\phi_0, \tag{2.6c}$$

describing an autonomous $\psi \equiv 0$, undamped $c = 0$, single degree of freedom system (SDoF) with the conjugate complex pair of eigenvalues $\lambda_{1/2} = \pm\sqrt{\frac{k}{m}}$.

Second order IVP's (2.4) can also be formulated in the more general form of first order IVP's (2.1)

$$\begin{bmatrix} \dot{\boldsymbol{\phi}} \\ \ddot{\boldsymbol{\phi}} \end{bmatrix} = \begin{bmatrix} \mathbf{0} & \mathbf{I} \\ -\boldsymbol{M}^{-1}\boldsymbol{K} & -\boldsymbol{M}^{-1}\boldsymbol{C} \end{bmatrix} \begin{bmatrix} \boldsymbol{\phi} \\ \dot{\boldsymbol{\phi}} \end{bmatrix} + \begin{bmatrix} \mathbf{0} \\ \boldsymbol{M}^{-1} \end{bmatrix} \boldsymbol{\psi} \tag{2.7a}$$

$$\begin{bmatrix} \boldsymbol{\phi}\left(t_0\right) \\ \dot{\boldsymbol{\phi}}\left(t_0\right) \end{bmatrix} = \begin{bmatrix} \boldsymbol{\phi}_0 \\ \dot{\boldsymbol{\phi}}_0 \end{bmatrix} \tag{2.7b}$$

$$\begin{bmatrix} \dot{\boldsymbol{\phi}}\left(t_0\right) \\ \ddot{\boldsymbol{\phi}}\left(t_0\right) \end{bmatrix} = \begin{bmatrix} \dot{\boldsymbol{\phi}}_0 \\ \ddot{\boldsymbol{\phi}}_0 \end{bmatrix} = \begin{bmatrix} \dot{\boldsymbol{\phi}}_0 \\ \boldsymbol{M}^{-1}\left(\boldsymbol{\psi}\left(t_0\right) - \boldsymbol{C}\dot{\boldsymbol{\phi}}_0 - \boldsymbol{K}\boldsymbol{\phi}_0\right) \end{bmatrix}. \tag{2.7c}$$

This way, the simplest possible problem (2.6) reads

$$\begin{bmatrix}\dot\phi\\ \ddot\phi\end{bmatrix} = \begin{bmatrix}0 & 1\\ -\frac{k}{m} & -\frac{c}{m}\end{bmatrix}\begin{bmatrix}\phi\\ \dot\phi\end{bmatrix} \tag{2.8a}$$

$$\begin{bmatrix}\phi(t_0)\\ \dot\phi(t_0)\end{bmatrix} = \begin{bmatrix}\phi_0\\ \dot\phi_0\end{bmatrix} \tag{2.8b}$$

$$\begin{bmatrix}\dot\phi(t_0)\\ \ddot\phi(t_0)\end{bmatrix} = \begin{bmatrix}\dot\phi_0\\ \ddot\phi_0\end{bmatrix} = \begin{bmatrix}\dot\phi_0\\ \frac{k}{m}\phi_0\end{bmatrix}. \tag{2.8c}$$

Vice versa, first order IVP's (2.1) can also be treated as pseudo second order IVP's (2.4)

$$\mathbf{I}\ddot{\mathbf{\Phi}} + (-\boldsymbol{A})\,\dot{\mathbf{\Phi}} + \mathbf{0}\mathbf{\Phi} = \boldsymbol{B}\boldsymbol{\psi} \tag{2.9a}$$

$$\begin{aligned}\mathbf{\Phi}(t_0) &= \mathbf{\Phi}_0\\ \dot{\mathbf{\Phi}}(t_0) &= \dot{\mathbf{\Phi}}_0 = \boldsymbol{\phi}_0\end{aligned} \tag{2.9b}$$

$$\ddot{\mathbf{\Phi}}(t_0) = \boldsymbol{A}\dot{\mathbf{\Phi}}_0 + \boldsymbol{B}\boldsymbol{\psi}(t_0) = \boldsymbol{A}\boldsymbol{\phi}_0 + \boldsymbol{B}\boldsymbol{\psi}(t_0) \tag{2.9c}$$

defining $\mathbf{\Phi}(t) := \mathbf{\Phi}_0 + \int_{t_0}^{t} \boldsymbol{\phi}(\tau)\,\mathrm{d}\tau$, i.e. $\dot{\mathbf{\Phi}}(t) := \boldsymbol{\phi}(t)$ and choosing for example $\mathbf{\Phi}_0 = \mathbf{0}$ without any loss of generality.

2.1.1 Backward Differentiation Formulae

This subsection is based on Gear (1971, 2007), Süli and Mayers (2003), and Iserles (2009).

The backward differentiation formulae (BDF's), also referred to as stiffly stable methods by Gear (1971), are one-level multi-step time integration methods for stiff first order IVP's. For details on stiff equations, the interested reader is referred to the literature, e.g. Gear (1971).

In the following some definitions of stability are given. Those are needed for distinction of the BDF's among themselves and other methods. The corresponding stability regions in the $\delta t\lambda$-plain are illustrated in Figure 2.1.

Definition 2.1 (A-STABILITY (GEAR 1971, DEFINITION 11.1, P. 212)[1])

> "A method is said to be A-stable if all numerical approximations tend to zero as $n \longrightarrow \infty$ when it is applied to the differential equation $\dot\phi = \lambda\phi$ with a fixed positive δt and a (complex) constant λ with a negative real part."

Definition 2.2 ($A(\alpha)$-STABILITY (GEAR 1971, DEFINITION 11.2, P. 213)[1])

> "A method is $A(\alpha)$-stable, $\alpha \in \left]0, \frac{\pi}{2}\right[$, if all numerical approximations to $\dot\phi = \lambda\phi$ converge to 0 as $n \longrightarrow \infty$ with δt fixed for all $|\arg(-\lambda)| < \alpha$, $|\lambda| \neq 0$."

Definition 2.3 (Stiff Stability (Gear 1971, Definition 11.3, p. 213)[1])

"A method is stiffly stable if in the region R_1 ($\mathrm{Re}(\delta t\lambda) \leq \sigma^-$) it is absolutely stable, and in R_2 ($\sigma^- < \mathrm{Re}(\delta t\lambda) < \sigma^+, |\mathrm{Im}(\delta t\lambda)| < \omega^\pm$) it is accurate."

For details on absolute stability, the interested reader is once again referred to the literature, e.g. Gear (1971).

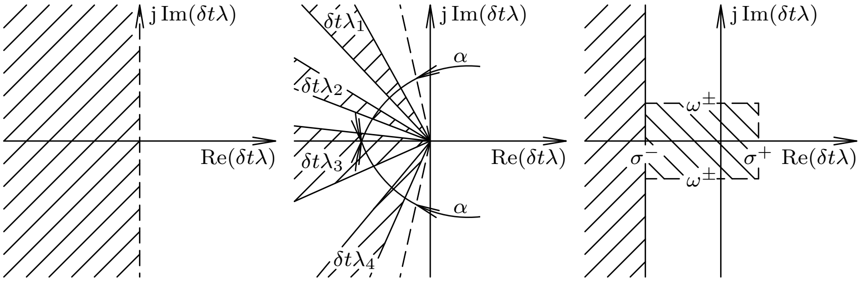

(a) A-stability. **(b)** $A(\alpha)$-stability. **(c)** Stiff stability.

Figure 2.1 A-stability, $A(\alpha)$-stability and stiff stability regions (Gear 1971, Figure 11.4, p. 213, 1971, Figure 11.5, p. 214).

The backward differentiation formula of order N ($N = 1, \ldots, 6$) is defined as

$$\boldsymbol{\phi}^{n+1} = \sum_{l=0}^{N-1} \left(\alpha_{n-l}\boldsymbol{\phi}^{n-l}\right) + \delta t\beta_{n+1}\dot{\boldsymbol{\phi}}^{n+1} \tag{2.10}$$

along with the coefficients α_{n-l} ($l = 0, \ldots, N-1$) and β_{n+1} according to Table 2.1. Therein also the stability properties are listed. The BDF1 is most commonly known as backward or implicit Euler method.

Definition (2.10) can be rewritten as

$$\dot{\boldsymbol{\phi}}^{n+1} = \widehat{\alpha}_{n+1}\boldsymbol{\phi}^{n+1} + \sum_{l=0}^{N-1} \left(\widehat{\alpha}_{n-l}\boldsymbol{\phi}^{n-l}\right) \tag{2.11a}$$

$$\widehat{\alpha}_{n+1} = \frac{1}{\delta t\beta_{n+1}} \tag{2.11b}$$

$$\widehat{\alpha}_{n-l} = -\frac{\alpha_{n-l}}{\delta t\beta_{n+1}} \quad (l = 0, \ldots, N-1) \tag{2.11c}$$

and its first temporal derivative

$$\dot{\boldsymbol{\phi}}^{n+1} = \sum_{l=0}^{N-1} \left(\alpha_{n-l}\dot{\boldsymbol{\phi}}^{n-l}\right) + \delta t\beta_{n+1}\ddot{\boldsymbol{\phi}}^{n+1} \tag{2.12}$$

[1] Notation adapted.

Table 2.1 COEFFICIENTS IN THE BACKWARD DIFFERENTIATION FORMULAE (GEAR 1971, P. 217, TABLE 11.1, 2007, TABLE "BDF COEFFICIENTS"; SÜLI AND MAYERS 2003, EQUATION 12.36, P. 331, EQUATIONS 12.50FF, P. 349; ISERLES 2009, EQUATIONS (1.15, 215, 2.16)).

N	α_n	α_{n-1}	α_{n-2}	α_{n-3}	α_{n-4}	α_{n-5}	β_{n+1}	*stability*
1	1	—	—	—	—	—	1	A
2	$\frac{4}{3}$	$-\frac{1}{3}$	—	—	—	—	$\frac{2}{3}$	A
3	$\frac{18}{11}$	$-\frac{9}{11}$	$\frac{2}{11}$	—	—	—	$\frac{6}{11}$	$A(\alpha)$/stiff
4	$\frac{48}{25}$	$-\frac{36}{25}$	$\frac{16}{25}$	$-\frac{3}{25}$	—	—	$\frac{12}{25}$	$A(\alpha)$/stiff
5	$\frac{300}{137}$	$-\frac{300}{137}$	$\frac{200}{137}$	$-\frac{75}{137}$	$\frac{12}{137}$	—	$\frac{60}{137}$	$A(\alpha)$/stiff
6	$\frac{360}{147}$	$-\frac{450}{147}$	$\frac{400}{147}$	$-\frac{225}{147}$	$\frac{72}{147}$	$-\frac{10}{147}$	$\frac{60}{147}$	$A(\alpha)$/stiff
7	—	—	—	—	—	—	—	none
$\vdots$	$\vdots$	$\vdots$	$\vdots$	$\vdots$	$\vdots$	$\vdots$	$\vdots$	$\vdots$

accordingly

$$\begin{aligned}\ddot{\boldsymbol{\phi}}^{n+1} &= \widehat{\alpha}_{n+1}\dot{\boldsymbol{\phi}}^{n+1} + \sum_{l=0}^{N-1}\left(\widehat{\alpha}_{n-l}\dot{\boldsymbol{\phi}}^{n-l}\right) \\ &= \widehat{\alpha}_{n+1}^2\boldsymbol{\phi}^{n+1} + \sum_{l=0}^{N-1}\left(\widehat{\alpha}_{n+1}\widehat{\alpha}_{n-l}\boldsymbol{\phi}^{n-l} + \widehat{\alpha}_{n-l}\dot{\boldsymbol{\phi}}^{n-l}\right).\end{aligned} \tag{2.13}$$

Thus, the forward integration of a first order IVP (2.1) is obtained as

$$\begin{aligned}&\begin{bmatrix}\mathbf{I} & -\delta t\beta_{n+1}\mathbf{I} \\ -\boldsymbol{A} & \mathbf{I}\end{bmatrix}\begin{bmatrix}\boldsymbol{\phi}^{n+1} \\ \dot{\boldsymbol{\phi}}^{n+1}\end{bmatrix} \\ &\quad= \sum_{l=0}^{N-1}\left(\begin{bmatrix}\alpha_{n-l}\mathbf{I} & \mathbf{0} \\ \mathbf{0} & \mathbf{0}\end{bmatrix}\begin{bmatrix}\boldsymbol{\phi}^{n} \\ \dot{\boldsymbol{\phi}}^{n}\end{bmatrix}\right) + \begin{bmatrix}\mathbf{0} \\ \boldsymbol{B}\end{bmatrix}\boldsymbol{\psi}\left(t^{n+1-\alpha_f}\right)\end{aligned} \tag{2.14a}$$

$$\begin{bmatrix}\boldsymbol{\phi}^{-l} \\ \dot{\boldsymbol{\phi}}^{-l}\end{bmatrix} = \begin{bmatrix}\boldsymbol{\phi}_{-l} \\ \dot{\boldsymbol{\phi}}_{-l}\end{bmatrix} \quad (l = 0, \ldots, N-1) \tag{2.14b}$$

combining Equations (2.10) and (2.1a) or equivalent as

$$\left(\mathbf{I} - \beta_{n+1}\delta t\boldsymbol{A}\right)\boldsymbol{\phi}^{n+1} = \sum_{l=0}^{N-1}\left(\alpha_{n-l}\boldsymbol{\phi}^{n-l}\right) + \beta_{n+1}\delta t\boldsymbol{B}\boldsymbol{\psi}^{n+1} \tag{2.14c}$$

$$\dot{\boldsymbol{\phi}}^{n+1} = \widehat{\alpha}_{n+1}\boldsymbol{\phi}^{n+1} + \sum_{l=0}^{N-1}\left(\widehat{\alpha}_{n-l}\boldsymbol{\phi}^{n-l}\right) \tag{2.14d}$$

$$\boldsymbol{\phi}^{-l} = \boldsymbol{\phi}_{-l} \quad (l = 0, \ldots, N-1) \tag{2.14e}$$

inserting Equation (2.11) in Equation (2.1a). It remains the problem of determining $\boldsymbol{\phi}_{-l}$ (and $\dot{\boldsymbol{\phi}}_{-l}$) for $l = 1, \ldots, N-1$ out of $\boldsymbol{\phi}_0$ and $\dot{\boldsymbol{\phi}}_0$.

With this, also the forward integration of the simplest first order problem (2.3)

$$(1 - \beta_{n+1}\delta ta)\,\phi^{n+1} = \sum_{l=0}^{N-1} \left(\alpha_{n-l}\phi^{n-l}\right) \tag{2.15a}$$

$$\dot{\phi}^{n+1} = \widehat{\alpha}_{n+1}\phi^{n+1} + \sum_{l=0}^{N-1} \left(\widehat{\alpha}_{n-l}\phi^{n-l}\right) \tag{2.15b}$$

$$\phi^{-l} = \phi_{-l} \quad (l = 0, \ldots, N-1) \tag{2.15c}$$

is given. As previously mentioned, this formulation is now used to determine the stability properties of the BDF's.

Equation (2.15a), i.e. the BDFN ($N = 1, \ldots, 6$) has the characteristic equation

$$p(\lambda) = (1 - \beta_{n+1}\delta ta)\,\lambda^N - \sum_{l=0}^{N-1} \left(\alpha_{n-l}\lambda^{N-1-l}\right), \tag{2.16}$$

i.e. the eigenvalues

$$\{\lambda_l,\ l = 1, \ldots, N\} = \left\{\lambda \in \mathbb{C} \middle| p(\lambda) = 0\right\} \tag{2.17}$$

and as a consequence the spectral radius

$$\rho(\delta ta) = \max_{\delta ta} \{|\lambda_l|,\ l = 1, \ldots, N\}. \tag{2.18}$$

Absolute stability of the BDFN is ensured, if and only if for its spectral radius

$$\rho(\delta ta) \leq 1 \tag{2.19}$$

holds.

Analytical evaluation of the statements (2.16) to (2.19) proves difficult, in particular for the cases $N = 2, \ldots, 6$. Therefore, the resulting contour lines of the spectral radii and regions of absolute stability are illustrated in Figure 2.2 for BDF1 through BDF6.

Furthermore, the forward integration of a second order IVP (2.4) is

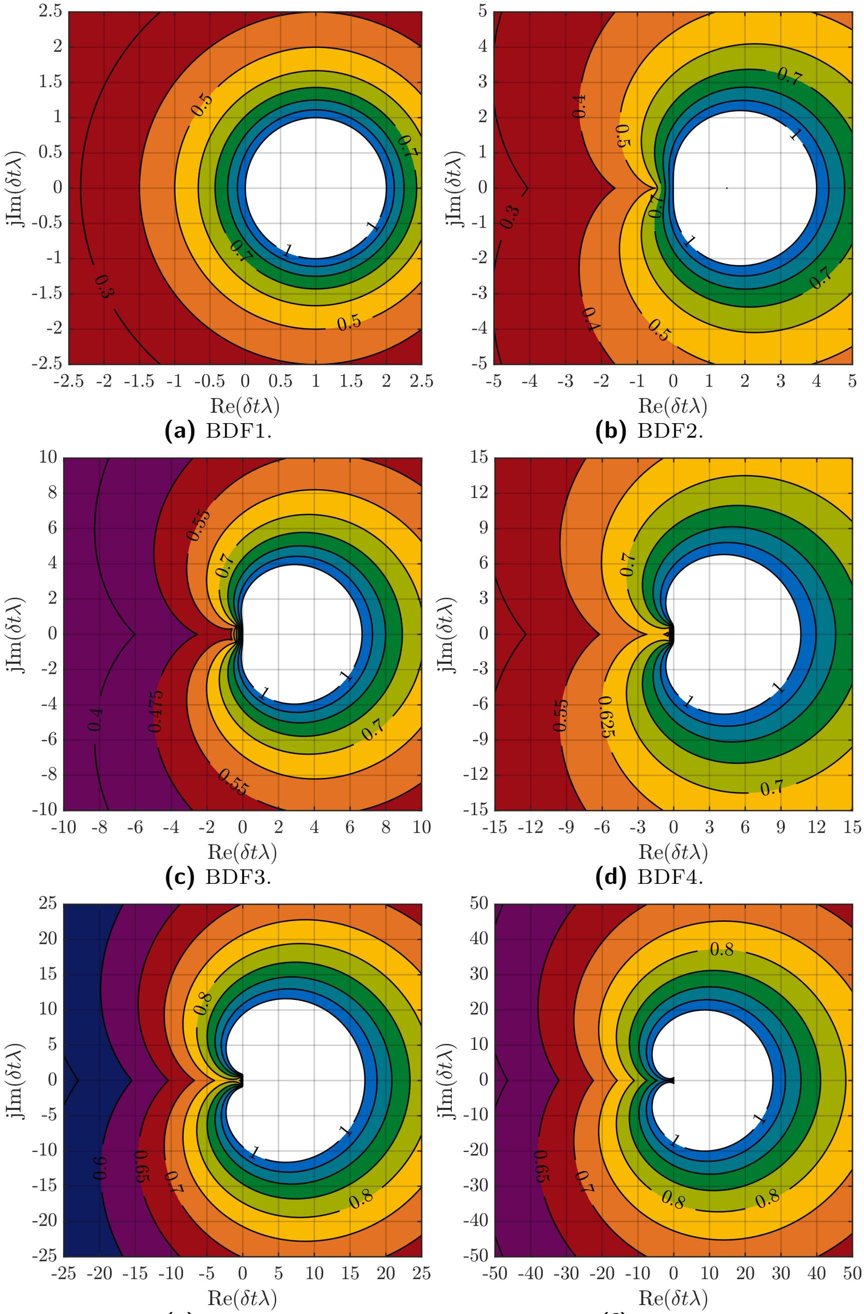

(a) BDF1. **(b)** BDF2.

(c) BDF3. **(d)** BDF4.

(e) BDF5. **(f)** BDF6.

Figure 2.2 Regions of absolute stability with contour lines of spectral radii for backward differentiation formulae (in accordance with Gear (1971, Figures 11.6/11.7, pp. 215/216) and Süli and Mayers (2003, Figure 12.5, pp. 350–351)).

obtained as

$$
\begin{bmatrix} \mathbf{I} & -\delta t \beta_{n+1} \mathbf{I} & \mathbf{0} \\ \mathbf{0} & \mathbf{I} & -\delta t \beta_{n+1} \mathbf{I} \\ \boldsymbol{K} & \boldsymbol{C} & \boldsymbol{M} \end{bmatrix} \begin{bmatrix} \boldsymbol{\phi}^{n+1} \\ \dot{\boldsymbol{\phi}}^{n+1} \\ \ddot{\boldsymbol{\phi}}^{n+1} \end{bmatrix}
= \sum_{l=0}^{N-1} \left(\begin{bmatrix} \alpha_{n-l} \mathbf{I} & \mathbf{0} & \mathbf{0} \\ \mathbf{0} & \alpha_{n-l} \mathbf{I} & \mathbf{0} \\ \mathbf{0} & \mathbf{0} & \mathbf{0} \end{bmatrix} \begin{bmatrix} \boldsymbol{\phi}^{n-l} \\ \dot{\boldsymbol{\phi}}^{n-l} \\ \ddot{\boldsymbol{\phi}}^{n-l} \end{bmatrix} \right) + \begin{bmatrix} \mathbf{0} \\ \mathbf{0} \\ \mathbf{I} \end{bmatrix} \boldsymbol{\psi}^{n+1} \tag{2.20a}
$$

$$
\begin{bmatrix} \boldsymbol{\phi}^{-l} \\ \dot{\boldsymbol{\phi}}^{-l} \\ \ddot{\boldsymbol{\phi}}^{-l} \end{bmatrix} = \begin{bmatrix} \boldsymbol{\phi}_{-l} \\ \dot{\boldsymbol{\phi}}_{-l} \\ \ddot{\boldsymbol{\phi}}_{-l} \end{bmatrix} \quad (l = 0, \ldots, N-1) \tag{2.20b}
$$

combining Equations (2.10), (2.12) and (2.4a) or equivalent as

$$
\left(\widehat{\alpha}_{n+1}^2 \boldsymbol{M} + \widehat{\alpha}_{n+1} \boldsymbol{C} + \boldsymbol{K} \right) \boldsymbol{\phi}^{n+1}
= - \sum_{l=0}^{N-1} \left(\widehat{\alpha}_{n-l} \left(\left(\widehat{\alpha}_{n+1} \boldsymbol{M} + \boldsymbol{C} \right) \boldsymbol{\phi}^{n-l} + \boldsymbol{M} \dot{\boldsymbol{\phi}}^{n-l} \right) \right) + \boldsymbol{\psi}^{n+1} \tag{2.20c}
$$

$$
\dot{\boldsymbol{\phi}}^{n+1} = \widehat{\alpha}_{n+1} \boldsymbol{\phi}^{n+1} + \sum_{l=0}^{N-1} \left(\widehat{\alpha}_{n-l} \boldsymbol{\phi}^{n-l} \right) \tag{2.20d}
$$

$$
\ddot{\boldsymbol{\phi}}^{n+1} = \widehat{\alpha}_{n+1} \dot{\boldsymbol{\phi}}^{n+1} + \sum_{l=0}^{N-1} \left(\widehat{\alpha}_{n-l} \dot{\boldsymbol{\phi}}^{n-l} \right) \tag{2.20e}
$$

$$
\begin{aligned} \boldsymbol{\phi}^{-l} &= \boldsymbol{\phi}_{-l} \\ \dot{\boldsymbol{\phi}}^{-l} &= \dot{\boldsymbol{\phi}}_{-l} \end{aligned} \quad (l = 0, \ldots, N-1) \tag{2.20f}
$$

inserting Equations (2.11) and (2.13) in Equation (2.4a). It remains the problem of determining $\boldsymbol{\phi}_{-l}$, $\dot{\boldsymbol{\phi}}_{-l}$ (and $\ddot{\boldsymbol{\phi}}_{-l}$) for $l = 1, \ldots, N-1$ out of $\boldsymbol{\phi}_0$, $\dot{\boldsymbol{\phi}}_0$ and $\ddot{\boldsymbol{\phi}}_0$.

2.1.2 The Class of Generalized–α Methods

The following subsection is based on Newmark (1959), Gear (1971), Hilber, Hughes, and Taylor (1977), Wood, Bossak, and Zienkiewicz (1980), Chung and Hulbert (1993), Jansen, Whiting, and Hulbert (2000), Shearer and Cesnik (2006), Brüls and Arnold (2008), and Jay and Negrut (2009). It holds information on the class of generalized–α methods which includes the generalized–α method itself as well as the Wood–Bossak–Zienkiewicz–α (WBZ–α) method, the Hilber–Hughes–Taylor–α (HHT–α) method and the Newmark–β method. All methods belong to the class of one-step, three-level numerically dissipative time integration schemes for second order IVP's. The last three and further methods originate from the generalized–α method by choosing certain sets of parameters.

Generalized–α Method

As the most general form the generalized–α method for second order IVP's (2.4) is defined as

$$\boldsymbol{\phi}^{n+1} = \boldsymbol{\phi}^{n} + \delta t \dot{\boldsymbol{\phi}}^{n} + \delta t^2 \left(\left(\frac{1}{2} - \beta \right) \ddot{\boldsymbol{\phi}}^{n} + \beta \ddot{\boldsymbol{\phi}}^{n+1} \right) \tag{2.21a}$$

$$\dot{\boldsymbol{\phi}}^{n+1} = \dot{\boldsymbol{\phi}}^{n} + \delta t \left((1-\gamma) \ddot{\boldsymbol{\phi}}^{n} + \gamma \ddot{\boldsymbol{\phi}}^{n+1} \right) \tag{2.21b}$$

$$\boldsymbol{M} \ddot{\boldsymbol{\phi}}^{n+1-\alpha_m} + \boldsymbol{C} \dot{\boldsymbol{\phi}}^{n+1-\alpha_f} + \boldsymbol{K} \boldsymbol{\phi}^{n+1-\alpha_f} = \boldsymbol{\psi} \left(t^{n+1-\alpha_f} \right) \tag{2.21c}$$

$$\begin{aligned} \boldsymbol{\phi}^{0} &= \boldsymbol{\phi}_0 \\ \dot{\boldsymbol{\phi}}^{0} &= \dot{\boldsymbol{\phi}}_0 \\ \ddot{\boldsymbol{\phi}}^{0} &= \ddot{\boldsymbol{\phi}}_0 \end{aligned} \tag{2.21d}$$

along with

$$\ddot{\boldsymbol{\phi}}^{n+1-\alpha_m} = (1-\alpha_m) \ddot{\boldsymbol{\phi}}^{n+1} + \alpha_f \ddot{\boldsymbol{\phi}}^{n} \tag{2.21e}$$

$$\dot{\boldsymbol{\phi}}^{n+1-\alpha_f} = (1-\alpha_f) \dot{\boldsymbol{\phi}}^{n+1} + \alpha_f \dot{\boldsymbol{\phi}}^{n} \tag{2.21f}$$

$$\boldsymbol{\phi}^{n+1-\alpha_f} = (1-\alpha_f) \boldsymbol{\phi}^{n+1} + \alpha_f \boldsymbol{\phi}^{n} \tag{2.21g}$$

$$t^{n+1-\alpha_f} = (1-\alpha_f) t^{n+1} + \alpha_f t^{n}. \tag{2.21h}$$

In more compact matrix notation this reads

$$\begin{aligned} &\begin{bmatrix} \mathbf{I} & \mathbf{0} & -\delta t^2 \beta \mathbf{I} \\ \mathbf{0} & \mathbf{I} & -\delta t \gamma \mathbf{I} \\ (1-\alpha_f)\boldsymbol{K} & (1-\alpha_f)\boldsymbol{C} & (1-\alpha_m)\boldsymbol{M} \end{bmatrix} \begin{bmatrix} \boldsymbol{\phi}^{n+1} \\ \dot{\boldsymbol{\phi}}^{n+1} \\ \ddot{\boldsymbol{\phi}}^{n+1} \end{bmatrix} \\ &= \begin{bmatrix} \mathbf{I} & \delta t \mathbf{I} & \delta t^2 \left(\frac{1}{2} - \beta\right) \mathbf{I} \\ \mathbf{0} & \mathbf{I} & \delta t (1-\gamma) \mathbf{I} \\ -\alpha_f \boldsymbol{K} & -\alpha_f \boldsymbol{C} & -\alpha_m \boldsymbol{M} \end{bmatrix} \begin{bmatrix} \boldsymbol{\phi}^{n} \\ \dot{\boldsymbol{\phi}}^{n} \\ \ddot{\boldsymbol{\phi}}^{n} \end{bmatrix} + \begin{bmatrix} \mathbf{0} \\ \mathbf{0} \\ \mathbf{I} \end{bmatrix} \boldsymbol{\psi} \left(t^{n+1-\alpha_f} \right) \end{aligned} \tag{2.22a}$$

$$\begin{bmatrix} \boldsymbol{\phi}^{0} \\ \dot{\boldsymbol{\phi}}^{0} \\ \ddot{\boldsymbol{\phi}}^{0} \end{bmatrix} = \begin{bmatrix} \boldsymbol{\phi}_0 \\ \dot{\boldsymbol{\phi}}_0 \\ \ddot{\boldsymbol{\phi}}_0 \end{bmatrix} \tag{2.22b}$$

i.e.

$$\boldsymbol{\Phi}^{n+1} = \boldsymbol{A}_{\mathrm{d}}\boldsymbol{\Phi}^{n} + \boldsymbol{B}_{\mathrm{d}}\boldsymbol{\psi}\left(t^{n+1-\alpha_f}\right) \tag{2.22c}$$

$$\boldsymbol{\Phi}^{0} = \boldsymbol{\Phi}_0 \tag{2.22d}$$

where $\boldsymbol{\Phi}^n = \left[\boldsymbol{\phi}^n, \dot{\boldsymbol{\phi}}^n, \ddot{\boldsymbol{\phi}}^n\right]^{\mathrm{T}}$, $\boldsymbol{\Phi}_0 = \left[\boldsymbol{\phi}_0, \dot{\boldsymbol{\phi}}_0, \ddot{\boldsymbol{\phi}}_0\right]^{\mathrm{T}}$ and $\boldsymbol{A}_{\mathrm{d}}$ is called the discrete amplification matrix.

Eigenvalue analysis of the discrete amplification matrix $\boldsymbol{A}_{\mathrm{d}}$ for the simplest second order problem (2.6) leads to certain requirements on the choice of parameters α_m, α_f, β and γ. Thus, in the best case, the generalized–α method is unconditionally stable, second-order accurate and possesses an optimal combination of strictly controllable, maximum high-frequency dissipation and minimal low-frequency dissipation for

$$\alpha_m = \frac{2\rho_\infty - 1}{\rho_\infty + 1} \tag{2.23a}$$

$$\wedge \qquad \alpha_f = \frac{\rho_\infty}{\rho_\infty + 1} \tag{2.23b}$$

$$\wedge \qquad \beta = \frac{1}{4}\left(1 - \alpha_m + \alpha_f\right)^2 \tag{2.23c}$$

$$\wedge \qquad \gamma = \frac{1}{2} - \alpha_m + \alpha_f \tag{2.23d}$$

where $\rho_\infty \in [0, 1]$ is the user-specified spectral radius in the high-frequency limit, i.e. the user-specified high-frequency dissipation. If $\rho_\infty = 0$ is chosen then frequencies above $\frac{\delta t}{T}$ will be dissipated within one time step. This is called asymptotic annihilation (Shearer and Cesnik 2006, p. 3).

If just unconditional stability, second-order accuracy and maximum high-frequency dissipation are demanded, it is sufficient to fulfill

$$\alpha_m \leq \alpha_f \leq \frac{1}{2} \tag{2.24a}$$

$$\wedge \qquad \beta \geq \frac{1}{4} + \frac{1}{2}\left(\alpha_f - \alpha_m\right) \tag{2.24b}$$

$$\wedge \qquad \gamma = \frac{1}{2} - \alpha_m + \alpha_f. \tag{2.24c}$$

The generalized–α method can then be described in terms of the two remaining parameters α_m and α_f. This is illustrated in Figure 2.3 where straight line

$$\alpha_f = \frac{1}{3}\left(1 + \alpha_m\right) \tag{2.25}$$

states the condition for parameter sets corresponding to the best case (2.23) with additional minimum low-frequency dissipation.

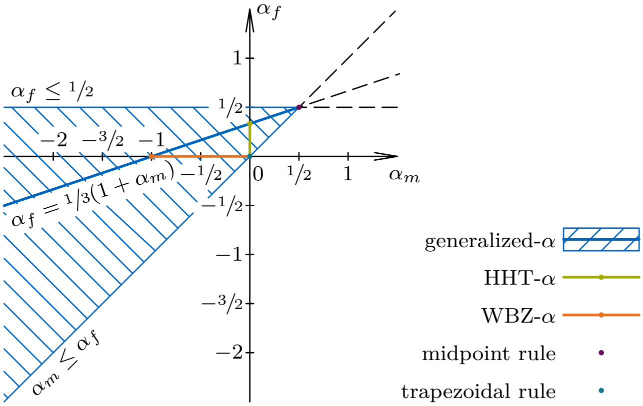

Figure 2.3 Generalized–α method in the α_f-α_m-plane, provided Equation (2.24) holds (Chung and Hulbert 1993, Figure 1, p. 373).

Wood–Bossak–Zienkiewicz–α Method

The Wood–Bossak–Zienkiewicz–α (WBZ–α) method emerges from the generalized–α method by fixing the parameter $\alpha_f = 0$. For second order IVP's (2.4) it is defined as

$$\boldsymbol{\phi}^{n+1} = \boldsymbol{\phi}^{n} + \delta t \dot{\boldsymbol{\phi}}^{n} + \delta t^2 \left(\left(\frac{1}{2} - \beta \right) \ddot{\boldsymbol{\phi}}^{n} + \beta \ddot{\boldsymbol{\phi}}^{n+1} \right) \tag{2.26a}$$

$$\dot{\boldsymbol{\phi}}^{n+1} = \dot{\boldsymbol{\phi}}^{n} + \delta t \left((1-\gamma) \ddot{\boldsymbol{\phi}}^{n} + \gamma \ddot{\boldsymbol{\phi}}^{n+1} \right) \tag{2.26b}$$

$$\boldsymbol{M} \ddot{\boldsymbol{\phi}}^{n+1-\alpha_m} + \boldsymbol{C} \dot{\boldsymbol{\phi}}^{n+1} + \boldsymbol{K} \boldsymbol{\phi}^{n+1} = \boldsymbol{\psi}^{n+1} \tag{2.26c}$$

$$\begin{aligned} \boldsymbol{\phi}^{0} &= \boldsymbol{\phi}_0 \\ \dot{\boldsymbol{\phi}}^{0} &= \dot{\boldsymbol{\phi}}_0 \\ \ddot{\boldsymbol{\phi}}^{0} &= \ddot{\boldsymbol{\phi}}_0 \end{aligned} \tag{2.26d}$$

along with

$$\ddot{\boldsymbol{\phi}}^{n+1-\alpha_m} = (1-\alpha_m) \ddot{\boldsymbol{\phi}}^{n+1} + \alpha_f \ddot{\boldsymbol{\phi}}^{n} \tag{2.26e}$$

In more compact matrix notation this reads

$$\begin{bmatrix} \mathbf{I} & \mathbf{0} & -\delta t^2\beta\mathbf{I} \\ \mathbf{0} & \mathbf{I} & -\delta t\gamma\mathbf{I} \\ \boldsymbol{K} & \boldsymbol{C} & (1-\alpha_m)\boldsymbol{M} \end{bmatrix} \begin{bmatrix} \boldsymbol{\phi}^{n+1} \\ \dot{\boldsymbol{\phi}}^{n+1} \\ \ddot{\boldsymbol{\phi}}^{n+1} \end{bmatrix}$$
$$= \begin{bmatrix} \mathbf{I} & \delta t\mathbf{I} & \delta t^2\left(\frac{1}{2}-\beta\right)\mathbf{I} \\ \mathbf{0} & \mathbf{I} & \delta t(1-\gamma)\mathbf{I} \\ \mathbf{0} & \mathbf{0} & -\alpha_m\boldsymbol{M} \end{bmatrix} \begin{bmatrix} \boldsymbol{\phi}^{n} \\ \dot{\boldsymbol{\phi}}^{n} \\ \ddot{\boldsymbol{\phi}}^{n} \end{bmatrix} + \begin{bmatrix} \mathbf{0} \\ \mathbf{0} \\ \mathbf{I} \end{bmatrix} \boldsymbol{\psi}^{n+1} \tag{2.27a}$$

$$\begin{bmatrix} \boldsymbol{\phi}^{0} \\ \dot{\boldsymbol{\phi}}^{0} \\ \ddot{\boldsymbol{\phi}}^{0} \end{bmatrix} = \begin{bmatrix} \boldsymbol{\phi}_{0} \\ \dot{\boldsymbol{\phi}}_{0} \\ \ddot{\boldsymbol{\phi}}_{0} \end{bmatrix} \tag{2.27b}$$

i.e.

$$\boldsymbol{\Phi}^{n+1} = \boldsymbol{A}_{\mathrm{d}}\boldsymbol{\Phi}^{n} + \boldsymbol{B}_{\mathrm{d}}\boldsymbol{\psi}^{n+1} \tag{2.27c}$$

$$\boldsymbol{\Phi}^{0} = \boldsymbol{\Phi}_{0} \tag{2.27d}$$

where $\boldsymbol{\Phi}^n = \left[\boldsymbol{\phi}^n, \dot{\boldsymbol{\phi}}^n, \ddot{\boldsymbol{\phi}}^n\right]^{\mathrm{T}}$, $\boldsymbol{\Phi}_0 = \left[\boldsymbol{\phi}_0, \dot{\boldsymbol{\phi}}_0, \ddot{\boldsymbol{\phi}}_0\right]^{\mathrm{T}}$ and $\boldsymbol{A}_{\mathrm{d}}$ is called the discrete amplification matrix.

As before, eigenvalue analysis of the discrete amplification matrix $\boldsymbol{A}_{\mathrm{d}}$ for the simplest second order problem (2.6) leads to certain requirements on the choice of parameters α_m, β and γ. Thus, in the best case, the WBZ–α method is unconditionally stable, second-order accurate and possesses strictly controllable, maximum high-frequency dissipation for

$$\alpha_m = \frac{\rho_\infty - 1}{\rho_\infty + 1} \tag{2.28a}$$

$$\wedge \qquad \beta = \frac{1}{4}(1-\alpha_m)^2 \tag{2.28b}$$

$$\wedge \qquad \gamma = \frac{1}{2} - \alpha_m \tag{2.28c}$$

where $\rho_\infty \in [0,1]$ is again the user-specified spectral radius in the high-frequency limit, i.e. the user-specified high-frequency dissipation.

Recalling that $\alpha_f = 0$ and observing that Equation (2.28a) together with $\rho_\infty \in [0,1]$ can also be formulated as

$$-1 \leq \alpha_m \leq 0, \tag{2.29}$$

the WBZ–α method can also be described in terms of the remaining parameter α_m. This is also illustrated in Figure 2.3 with point

$$\alpha_m = -1 \tag{2.30a}$$

corresponding, however, to a fixed

$$\rho_\infty = 0 \tag{2.30b}$$

stating the parameter choice for minimum low-frequency dissipation.

Hilber–Hughes–Taylor–α Method

Similar to the WBZ–α method, the Hilber–Hughes–Taylor–α (HHT–α) method emerges from the generalized–α method by fixing the parameter $\alpha_m = 0$. For second order IVP's (2.4) it is defined as

$$\boldsymbol{\phi}^{n+1} = \boldsymbol{\phi}^n + \delta t \dot{\boldsymbol{\phi}}^n + \delta t^2 \left(\left(\frac{1}{2} - \beta \right) \ddot{\boldsymbol{\phi}}^n + \beta \ddot{\boldsymbol{\phi}}^{n+1} \right) \tag{2.31a}$$

$$\dot{\boldsymbol{\phi}}^{n+1} = \dot{\boldsymbol{\phi}}^n + \delta t \left((1-\gamma) \ddot{\boldsymbol{\phi}}^n + \gamma \ddot{\boldsymbol{\phi}}^{n+1} \right) \tag{2.31b}$$

$$\boldsymbol{M} \ddot{\boldsymbol{\phi}}^{n+1} + \boldsymbol{C} \dot{\boldsymbol{\phi}}^{n+1-\alpha_f} + \boldsymbol{K} \boldsymbol{\phi}^{n+1-\alpha_f} = \boldsymbol{\psi}\left(t^{n+1-\alpha_f}\right) \tag{2.31c}$$

$$\begin{aligned} \boldsymbol{\phi}^0 &= \boldsymbol{\phi}_0 \\ \dot{\boldsymbol{\phi}}^0 &= \dot{\boldsymbol{\phi}}_0 \\ \ddot{\boldsymbol{\phi}}^0 &= \ddot{\boldsymbol{\phi}}_0 \end{aligned} \tag{2.31d}$$

along with

$$\dot{\boldsymbol{\phi}}^{n+1-\alpha_f} = (1-\alpha_f)\, \dot{\boldsymbol{\phi}}^{n+1} + \alpha_f \dot{\boldsymbol{\phi}}^n \tag{2.31e}$$

$$\boldsymbol{\phi}^{n+1-\alpha_f} = (1-\alpha_f)\, \boldsymbol{\phi}^{n+1} + \alpha_f \boldsymbol{\phi}^n \tag{2.31f}$$

$$t^{n+1-\alpha_f} = (1-\alpha_f)\, t^{n+1} + \alpha_f t^n \tag{2.31g}$$

In more compact matrix notation this reads

$$\begin{aligned} &\begin{bmatrix} \mathbf{I} & \mathbf{0} & -\delta t^2 \beta \mathbf{I} \\ \mathbf{0} & \mathbf{I} & -\delta t \gamma \mathbf{I} \\ (1-\alpha_f)\boldsymbol{K} & (1-\alpha_f)\boldsymbol{C} & \boldsymbol{M} \end{bmatrix} \begin{bmatrix} \boldsymbol{\phi}^{n+1} \\ \dot{\boldsymbol{\phi}}^{n+1} \\ \ddot{\boldsymbol{\phi}}^{n+1} \end{bmatrix} \\ &\quad = \begin{bmatrix} \mathbf{I} & \delta t \mathbf{I} & \delta t^2 \left(\frac{1}{2} - \beta\right) \mathbf{I} \\ \mathbf{0} & \mathbf{I} & \delta t (1-\gamma) \mathbf{I} \\ -\alpha_f \boldsymbol{K} & -\alpha_f \boldsymbol{C} & \mathbf{0} \end{bmatrix} \begin{bmatrix} \boldsymbol{\phi}^{n} \\ \dot{\boldsymbol{\phi}}^{n} \\ \ddot{\boldsymbol{\phi}}^{n} \end{bmatrix} + \begin{bmatrix} \mathbf{0} \\ \mathbf{0} \\ \mathbf{I} \end{bmatrix} \boldsymbol{\psi}\left(t^{n+1-\alpha_f}\right) \end{aligned} \tag{2.32a}$$

$$\begin{bmatrix} \boldsymbol{\phi}^0 \\ \dot{\boldsymbol{\phi}}^0 \\ \ddot{\boldsymbol{\phi}}^0 \end{bmatrix} = \begin{bmatrix} \boldsymbol{\phi}_0 \\ \dot{\boldsymbol{\phi}}_0 \\ \ddot{\boldsymbol{\phi}}_0 \end{bmatrix} \tag{2.32b}$$

i.e.

$$\boldsymbol{\Phi}^{n+1} = \boldsymbol{A}_{\mathrm{d}}\boldsymbol{\Phi}^{n} + \boldsymbol{B}_{\mathrm{d}}\boldsymbol{\psi}\left(t^{n+1-\alpha_f}\right) \tag{2.32c}$$

$$\boldsymbol{\Phi}^{0} = \boldsymbol{\Phi}_{0} \tag{2.32d}$$

where $\boldsymbol{\Phi}^n = \left[\boldsymbol{\phi}^n, \dot{\boldsymbol{\phi}}^n, \ddot{\boldsymbol{\phi}}^n\right]^{\mathrm{T}}$, $\boldsymbol{\Phi}_0 = \left[\boldsymbol{\phi}_0, \dot{\boldsymbol{\phi}}_0, \ddot{\boldsymbol{\phi}}_0\right]^{\mathrm{T}}$ and $\boldsymbol{A}_{\mathrm{d}}$ is called the discrete amplification matrix.

As before, eigenvalue analysis of the discrete amplification matrix $\boldsymbol{A}_{\mathrm{d}}$ for the simplest second order problem (2.6) leads to certain requirements on the choice of parameters α_f, β and γ. Thus, in the best case, the HHT–α method is unconditionally stable, second-order accurate and possesses strictly controllable, maximum high-frequency dissipation for

$$\alpha_f = \frac{1-\rho_\infty}{1+\rho_\infty} \tag{2.33a}$$

$$\wedge \qquad \beta = \frac{1}{4}\left(1+\alpha_f\right)^2 \tag{2.33b}$$

$$\wedge \qquad \gamma = \frac{1}{2} + \alpha_f \tag{2.33c}$$

where $\rho_\infty \in \left[0, \frac{1}{2}\right]$ is again the user-specified spectral radius in the high-frequency limit, i.e. the user-specified high-frequency dissipation.

Recalling that here $\alpha_m = 0$ and observing that Equation (2.33a) together with $\rho_\infty \in \left[0, \frac{1}{2}\right]$ can also be formulated as

$$0 \leq \alpha_f \leq \frac{1}{3}, \tag{2.34}$$

the HHT–α method can also be described in terms of the remaining parameter α_f. This is again illustrated in Figure 2.3 with point

$$\alpha_f = \frac{1}{3} \tag{2.35a}$$

corresponding, however, to a fixed

$$\rho_\infty = \frac{1}{2} \tag{2.35b}$$

stating the parameter choice for minimum low-frequency dissipation.

Newmark–β Method

The Newmark–β method constitutes the combination of WBZ–α method and HHT–α method, i.e. it emerges from the generalized–α method by

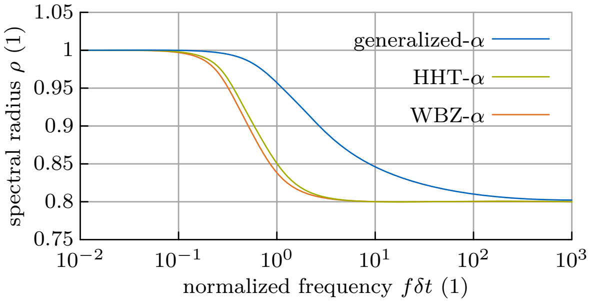

Figure 2.4 COMPARISON OF SPECTRAL RADII FROM GENERALIZED–α METHOD, WBZ–α METHOD AND HHT–α METHOD WITH RESPECTIVE $\rho_\infty = 0.8$ (CHUNG AND HULBERT 1993, FIGURE 2, P. 373).

fixing the parameters $\alpha_m = 0$ and $\alpha_f = 0$. For second order IVP's (2.4) it is defined as

$$\boldsymbol{\phi}^{n+1} = \boldsymbol{\phi}^n + \delta t\dot{\boldsymbol{\phi}}^n + \delta t^2\left(\left(\frac{1}{2}-\beta\right)\ddot{\boldsymbol{\phi}}^n + \beta\ddot{\boldsymbol{\phi}}^{n+1}\right) \tag{2.36a}$$

$$\dot{\boldsymbol{\phi}}^{n+1} = \dot{\boldsymbol{\phi}}^n + \delta t\left((1-\gamma)\ddot{\boldsymbol{\phi}}^n + \gamma\ddot{\boldsymbol{\phi}}^{n+1}\right) \tag{2.36b}$$

$$\boldsymbol{M}\ddot{\boldsymbol{\phi}}^{n+1} + \boldsymbol{C}\dot{\boldsymbol{\phi}}^{n+1} + \boldsymbol{K}\boldsymbol{\phi}^{n+1} = \boldsymbol{\psi}^{n+1} \tag{2.36c}$$

$$\begin{aligned}\boldsymbol{\phi}^0 &= \boldsymbol{\phi}_0\\ \dot{\boldsymbol{\phi}}^0 &= \dot{\boldsymbol{\phi}}_0\\ \ddot{\boldsymbol{\phi}}^0 &= \ddot{\boldsymbol{\phi}}_0\end{aligned} \tag{2.36d}$$

In more compact matrix notation this reads

$$\begin{aligned}&\begin{bmatrix}\mathbf{I} & \mathbf{0} & -\delta t^2\beta\mathbf{I}\\ \mathbf{0} & \mathbf{I} & -\delta t\gamma\mathbf{I}\\ \boldsymbol{K} & \boldsymbol{C} & \boldsymbol{M}\end{bmatrix}\begin{bmatrix}\boldsymbol{\phi}^{n+1}\\ \dot{\boldsymbol{\phi}}^{n+1}\\ \ddot{\boldsymbol{\phi}}^{n+1}\end{bmatrix}\\ &= \begin{bmatrix}\mathbf{I} & \delta t\mathbf{I} & \delta t^2\left(\frac{1}{2}-\beta\right)\mathbf{I}\\ \mathbf{0} & \mathbf{I} & \delta t(1-\gamma)\mathbf{I}\\ \mathbf{0} & \mathbf{0} & \mathbf{0}\end{bmatrix}\begin{bmatrix}\boldsymbol{\phi}^{n}\\ \dot{\boldsymbol{\phi}}^{n}\\ \ddot{\boldsymbol{\phi}}^{n}\end{bmatrix} + \begin{bmatrix}\mathbf{0}\\ \mathbf{0}\\ \mathbf{I}\end{bmatrix}\boldsymbol{\psi}^{n+1}\end{aligned} \tag{2.37a}$$

$$\begin{bmatrix}\boldsymbol{\phi}^{0}\\ \dot{\boldsymbol{\phi}}^{0}\\ \ddot{\boldsymbol{\phi}}^{0}\end{bmatrix} = \begin{bmatrix}\boldsymbol{\phi}_{0}\\ \dot{\boldsymbol{\phi}}_{0}\\ \ddot{\boldsymbol{\phi}}_{0}\end{bmatrix} \tag{2.37b}$$

i.e.

$$\boldsymbol{\Phi}^{n+1} = \boldsymbol{A}_{\mathrm{d}}\boldsymbol{\Phi}^{n} + \boldsymbol{B}_{\mathrm{d}}\boldsymbol{\psi}^{n+1} \tag{2.37c}$$

$$\boldsymbol{\Phi}^{0} = \boldsymbol{\Phi}_{0} \tag{2.37d}$$

where $\boldsymbol{\Phi}^n = \left[\boldsymbol{\phi}^n, \dot{\boldsymbol{\phi}}^n, \ddot{\boldsymbol{\phi}}^n\right]^{\mathrm{T}}$, $\boldsymbol{\Phi}_0 = \left[\boldsymbol{\phi}_0, \dot{\boldsymbol{\phi}}_0, \ddot{\boldsymbol{\phi}}_0\right]^{\mathrm{T}}$ and $\boldsymbol{A}_{\mathrm{d}}$ is called the discrete amplification matrix.

Once again, an eigenvalue analysis of the discrete amplification matrix $\boldsymbol{A}_{\mathrm{d}}$ for the simplest second order problem (2.6) leads to certain requirements on the choice of parameters β and γ. Thus, in the best case, the Newmark–β method is unconditionally stable and second-order accurate for

$$\beta \geq \frac{1}{4} \tag{2.38a}$$

$$\wedge \qquad \gamma = \frac{1}{2}. \tag{2.38b}$$

The demand for second order accuracy results in a loss of any numerical dissipation, i.e. zero artificial damping.

Furthermore, the best following of phase is given with

$$\beta = \frac{1}{4} \tag{2.39a}$$

$$\wedge \qquad \gamma = \frac{1}{2} \tag{2.39b}$$

resulting in the trapezoidal rule method.

Further Methods

Choosing $\rho_\infty = 1$ in (2.23), consequently $\alpha_m = \frac{1}{2}$, $\alpha_f = \frac{1}{2}$, $\beta = \frac{1}{4}$ and $\gamma = \frac{1}{2}$, the generalized–α method possesses no numerical dissipation and corresponds as such to the midpoint rule method "which is equivalent to the trapezoidal rule for linear problems" (Jansen, Whiting, and Hulbert 2000).

Alternatively, choosing $\alpha_m = 0$, $\alpha_f = 0$ and $\beta = \frac{1}{4}$ in (2.24), consequently $\gamma = \frac{1}{2}$, the generalized–α method possesses no numerical dissipation and corresponds as such to the trapezoidal rule method. It is the Newmark–β method with best following of phase.

Further choices of parameters are possible. For example $\alpha_m = 0$, $\alpha_f = 0$, $\beta = 0$ and $\gamma = \frac{1}{2}$ lead to Störmer's rule.

Generalized–α Method for 1st Order ODEs

The standard generalized–α method presented in passage Generalized–α Method (pp. 16 ff.) was originally developed as an one-step, three level, numerically dissipative time integration scheme particularly for second order IVP's. In Jansen, Whiting, and Hulbert (2000) this second order generalized–α method is now also adapted to first order IVP's by applying definition (2.21) to the second-order reformulation (2.9) of a linear first order IVP. This procedure looses the parameter β and results in an one-step, two level, numerically dissipative time integration scheme for first order IVP's.

For the linear, first order IVP (2.1) it is defined as

$$\boldsymbol{\phi}^{n+1} = \boldsymbol{\phi}^{n} + \delta t\left((1-\gamma)\dot{\boldsymbol{\phi}}^{n} + \gamma\dot{\boldsymbol{\phi}}^{n+1}\right) \tag{2.40a}$$

$$\dot{\boldsymbol{\phi}}^{n+1-\alpha_m} = \boldsymbol{A}\boldsymbol{\phi}^{n+1-\alpha_f} + \boldsymbol{B}\boldsymbol{\psi}\left(t^{n+1-\alpha_f}\right) \tag{2.40b}$$

$$\boldsymbol{\phi}^{0} = \boldsymbol{\phi}_0 \tag{2.40c}$$

$$\dot{\boldsymbol{\phi}}^{0} = \dot{\boldsymbol{\phi}}_0 = \boldsymbol{A}\boldsymbol{\phi}_0 + \boldsymbol{B}\boldsymbol{\psi}(t_0) \tag{2.40d}$$

along with

$$\dot{\boldsymbol{\phi}}^{n+1-\alpha_m} = (1-\alpha_m)\,\dot{\boldsymbol{\phi}}^{n+1} + \alpha_m\dot{\boldsymbol{\phi}}^{n} \tag{2.40e}$$

$$\boldsymbol{\phi}^{n+1-\alpha_f} = (1-\alpha_f)\,\boldsymbol{\phi}^{n+1} + \alpha_f\boldsymbol{\phi}^{n} \tag{2.40f}$$

$$t^{n+1-\alpha_f} = (1-\alpha_f)\,t^{n+1} + \alpha_f t^{n} \tag{2.40g}$$

In more compact matrix notation this reads

$$\begin{bmatrix} \mathbf{I} & -\delta t\gamma\mathbf{I} \\ -(1-\alpha_f)\boldsymbol{A} & (1-\alpha_m)\mathbf{I} \end{bmatrix} \begin{bmatrix} \boldsymbol{\phi}^{n+1} \\ \dot{\boldsymbol{\phi}}^{n+1} \end{bmatrix} = \begin{bmatrix} \mathbf{I} & \delta t(1-\gamma)\mathbf{I} \\ \alpha_f\boldsymbol{A} & -\alpha_m\mathbf{I} \end{bmatrix} \begin{bmatrix} \boldsymbol{\phi}^{n} \\ \dot{\boldsymbol{\phi}}^{n} \end{bmatrix} + \begin{bmatrix} \mathbf{0} \\ \boldsymbol{B} \end{bmatrix} \boldsymbol{\psi}\left(t^{n+1-\alpha_f}\right) \tag{2.41a}$$

$$\begin{bmatrix} \boldsymbol{\phi}^{0} \\ \dot{\boldsymbol{\phi}}^{0} \end{bmatrix} = \begin{bmatrix} \boldsymbol{\phi}_0 \\ \dot{\boldsymbol{\phi}}_0 \end{bmatrix} \tag{2.41b}$$

i.e.

$$\boldsymbol{\Phi}^{n+1} = \boldsymbol{A}_{\mathrm{d}}\boldsymbol{\Phi}^{n} + \boldsymbol{B}_{\mathrm{d}}\boldsymbol{\psi}\left(t^{n+1-\alpha_f}\right) \tag{2.41c}$$

$$\boldsymbol{\Phi}^{0} = \boldsymbol{\Phi}_0 \tag{2.41d}$$

where $\boldsymbol{\Phi}^n = \left[\boldsymbol{\phi}^n, \dot{\boldsymbol{\phi}}^n\right]^{\mathrm{T}}$, $\boldsymbol{\Phi}_0 = \left[\boldsymbol{\phi}_0, \dot{\boldsymbol{\phi}}_0\right]^{\mathrm{T}}$ and $\boldsymbol{A}_{\mathrm{d}}$ is called the discrete amplification matrix.

Again, eigenvalue analysis of the discrete amplification matrix $\boldsymbol{A}_{\mathrm{d}}$ for accordingly the simplest, first order problem (2.3) now leads to certain requirements on the choice of parameters α_m, α_f and γ. Thus, in the best case, the generalized–α method for first order IVP's is unconditionally stable, second-order accurate and possesses strictly controllable, maximum high-frequency dissipation for

$$\alpha_m = \frac{1}{2}\frac{3\rho_\infty - 1}{\rho_\infty + 1} \tag{2.42a}$$

$$\wedge \qquad \alpha_f = \frac{\rho_\infty}{\rho_\infty + 1} \tag{2.42b}$$

$$\wedge \qquad \gamma = \frac{1}{2} - \alpha_m + \alpha_f \tag{2.42c}$$

where $\rho_\infty \in [0, 1]$ is the user-specified spectral radius in the high-frequency limit, i.e. the user-specified high-frequency dissipation.

If just unconditional stability and second-order accuracy are demanded, it is sufficient to fulfill

$$\alpha_m \leq \alpha_f \leq \frac{1}{2} \tag{2.43a}$$

$$\wedge \qquad \gamma = \frac{1}{2} - \alpha_m + \alpha_f. \tag{2.43b}$$

The generalized–α method for first order IVP's can then also be described in terms of the two remaining parameters α_m and α_f. This could also be depicted in a Figure, where

$$\alpha_f = \frac{1}{4}\left(1 + 2\alpha_m\right) \tag{2.44}$$

would state the condition for parameter sets corresponding to the best case (2.42) with additional strictly controllable, maximum high-frequency dissipation.

Choosing $\alpha_m = 0$ and $\alpha_f = 0$ in (2.43), consequently $\gamma = \frac{1}{2}$, the generalized–α method for first order IVP's possesses no numerical dissipation and corresponds as such to the trapezoidal rule method.

Alternatively choosing $\rho_\infty = 0$ in (2.42), consequently $\alpha_m = -\frac{1}{2}$, $\alpha_f = 0$ and $\gamma = 1$, the generalized–α method for first order IVP's possesses maximum numerical dissipation and, in the linear case, corresponds as such to the BDF2 method (compare definition (2.10) with $N = 2$). Frequencies above $\frac{\delta t}{T}$ will be dissipated within one time step, a so called asymptotic annihilation (Shearer and Cesnik 2006, p. 3).

Conversely, choosing $\rho_\infty = 1$ in (2.42), consequently $\alpha_m = \frac{1}{2}$, $\alpha_f = \frac{1}{2}$ and $\gamma = \frac{1}{2}$, the generalized–α method for first order IVP's possesses no numerical dissipation and corresponds as such to the midpoint rule method "which is equivalent to the trapezoidal rule for linear problems" (Jansen, Whiting, and Hulbert 2000).

Consequently, a range of numerical time integrators in between is given setting any value $\rho_\infty \in [0, 1]$.

2.2 Temporal and Spatial Consistency Considerations on Partitioned Approaches

The following section outlines briefly the most important and non-neglectable aspects on temporal and spatial consistency of partitioned approaches. This means effects arising from the combination of different time integration schemes (temporal consistency) respectively different spatial discretization schemes along with non-matching meshes (spatial consistency) in the subsystems of a partitioned approach.

Already the suitable choice of time integration schemes, guaranteeing temporal consistency of the overall problem, is a demanding topic which is still under research and outside the scope of this work. Having said that, it nevertheless cannot simply be disregarded. For instance Joosten, Dettmer, and Perić (2010) present the analytical analysis of a simplest FSI problem (similar to model problem presented in Chapter 3 Model Problem, pp. 32 ff.) which is combining the second order generalized–α method in the structural subsystem (see Equation (2.21), p. 16) with the first order generalized–α method in the fluid subsystem (see Equation (2.40), p. 24). Their results demonstrate possible loss of temporal stability and accuracy up to complete failure of the approach if no special measures are taken.

Generalized–α methods are the common choice in computational solid mechanics and also on the up in computational fluid dynamics due to their well definable numerical dissipation properties. Despite that fact, generalized–α methods are not used in this work to specifically exclude the problem of temporal consistency. As illustrated with the example cited above, already the coupling of only two subsystems demands for special treatment. Coupling of three or more subsystems in possible combination with third- or higher-order subsystem dynamics quickly become unmanageable with such methods up to now.

As direct consequence, this work throughout uses the BDF2 combined with equidistant time stepping (see Equation (2.10), p. 11 with $N = 2$). As one-level, two-stage method, each level of derivative in the subsystems' dynamics is treated in the exact same manner. Guaranteeing temporal consistency therefore reduces to setting consistent initial values in all subsystems which can easily be realized. The temporal consistency includes the conservation of the second order accuracy in time coming with the BDF2. It should be pointed out that also the mesh updating scheme in the fluid subsystem uses the BDF2 for recalculating the mesh velocity to guarantee temporal consistency especially at the moving interface.

Furthermore, the loss of spatial consistency is also eliminated in this work. As presented subsequently, only the fluid subsystem (see Chapter 5 The Fluid (CFD) Subsystem, pp. 57 ff.) in fact involves a spatial discretization scheme. The applied structural SDoF (see Chapter 6 The Structural (CSM)

Subsystem, pp. 68 ff.) and control subsystems (see Chapter 8 The Controller (CLC) Subsystem, pp. 94 ff.) are however defined by pure ODE's without real spatial affiliation. Even changing to the native structural multi-degree of freedom subsystem involving its own spatial discretization scheme does not harm the spatial consistency. The same scheme as in the fluid subsystem in combination with matching interface meshes is used. A mapping operation as mentioned in the beginning therefore also becomes redundant. The issues will be taken up again later.

In summary, it can be stated that all numerical problems investigated in this work are exact in the sense of matching the respective monolithic solution. Further analysis e.g. on the temporal stability and accuracy as performed in Dettmer and Perić (2013, Section 3.2, pp. 6 ff.) becomes redundant.

2.3 Phenomenology of Vortex Shedding on Cylinders

Material from existing studies, in particular Lienhard (1966), Okajima (1982) and Blevins (1990), on the phenomenology of vortex shedding on rigid cylinders in cross-flows is collected in this brief section. At an earlier stage, it formed a basis for the design of the fluid subsystem (see Section 5 The Fluid (CFD) Subsystem, pp. 57 ff.) in the numerical experiments (see Section 4 The Experiment, pp. 53 ff.) investigated in this work.

The well-known Turek benchmark (Turek and Hron 2006) served as major inspiration for the design of the numerical experiments. The original setting contains a cylinder of circular cross-section which is in this work, however, changed to a square-shaped one. Square cylinders show uniquely defined separation points due to their sharp edges. Smooth circular cylinders or more general bluff bodies in contrast do not possess such distinct separation points. Therefore, the square cylinder is chosen to, amongst other things, reduce dependencies on the spatial discretization.

In the scope of this work the Reynolds number of the problem is given by

$$Re = \frac{v_{\text{in}} d}{\nu_{\text{F}}} \tag{2.45}$$

and the Strouhal number regarding the vortex shedding by

$$Sr = \frac{f_{\text{s}} d}{v_{\text{in}}} \tag{2.46}$$

with the cylinder diameter d, kinematic fluid viscosity ν_{F}, mean inlet velocity v_{in} and vortex shedding frequency f_{s}.

Figure 2.5 illustrates the different flow regimes arising on circular cylinders with varying Reynold number respectively inlet velocity.

With Figures 2.6 to 2.7 and 2.8 the comparison between Strouhal numbers of circular and square cylinders is given. For future reference the characteristic Reynolds numbers of $Re = 2$, 100 and 200 are highlighted in blue. They show relevant but not severe deviations between both shapes. This justifies the simple change from circular to square cylinder without modifying the overall behavior associated with the Turek benchmark.

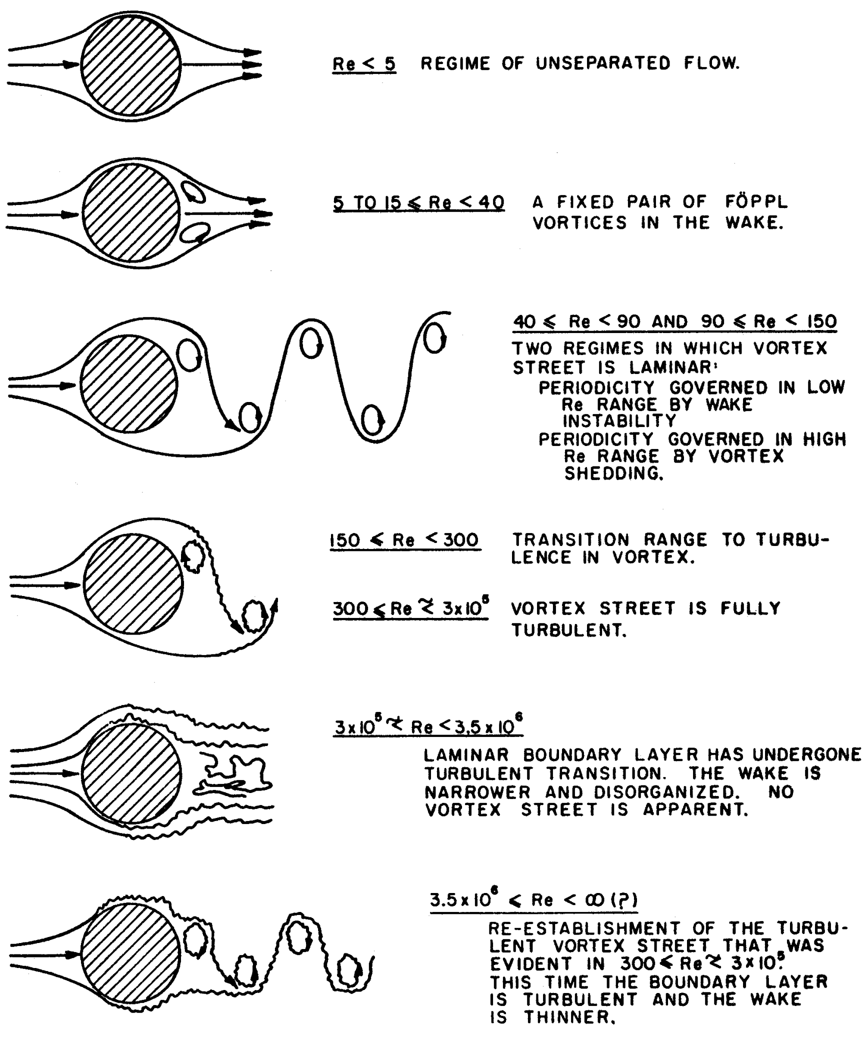

Figure 2.5 Different regimes of vortex shedding on circular cylinders (Lienhard 1966, Figure 1, p. 3).

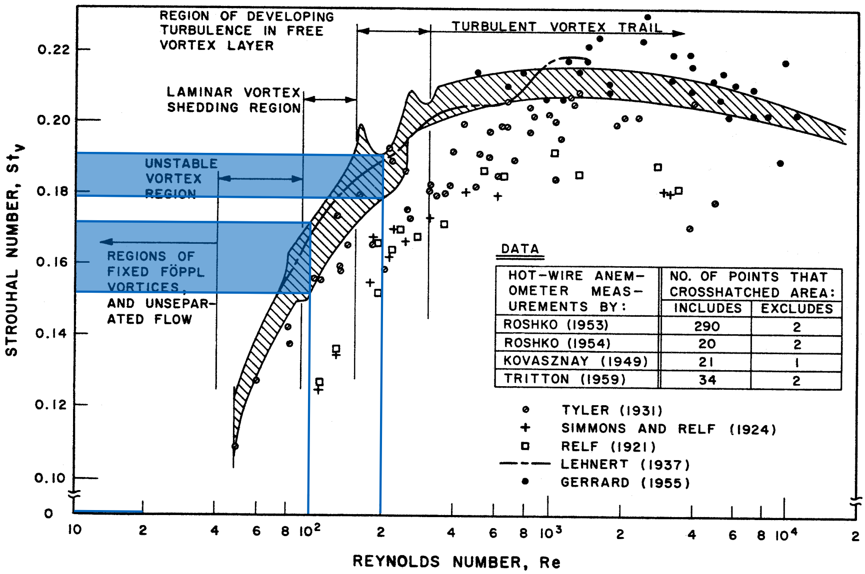

Figure 2.6 *Sr*-*Re* relationship for circular cylinders in $0 \leq Re \leq 2{\times}10^4$ (Lienhard 1966, Figure 3, p. 8).

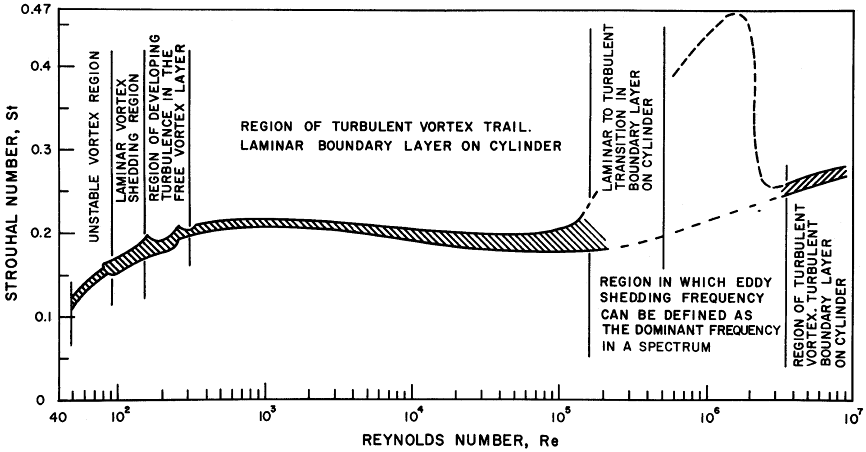

Figure 2.7 *Sr*-*Re* relationship for circular cylinders in $40 < Re < 10^7$ (Lienhard 1966, Figure 5, p. 12).

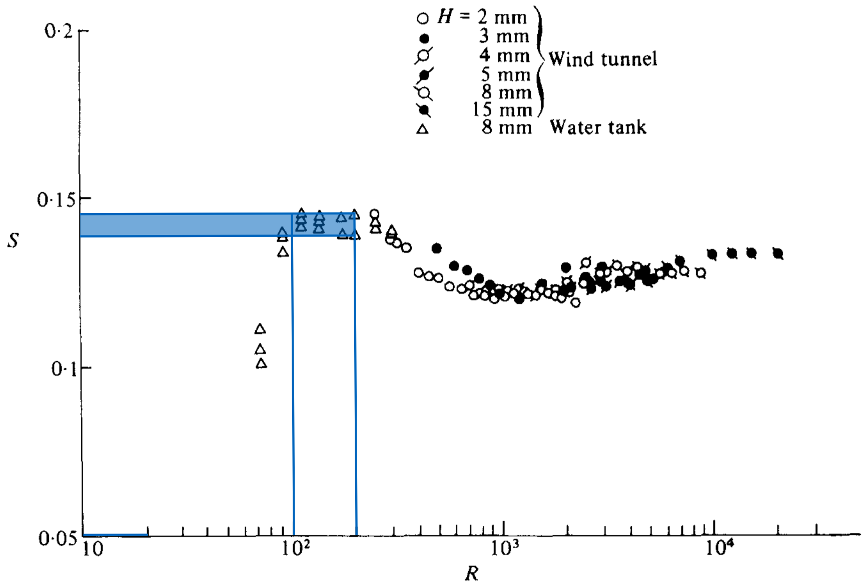

Figure 2.8 *Sr*-*Re* relationship for square cylinders in $0 \leq Re \leq 4{\times}10^4$ (Okajima 1982, Figure 2, p. 381).

2.4 Miscellaneous

Some further observations and insights which are worth mentioning are gathered in this section.

In FSCI simulations in the context of this work three levels of model fidelity have to be distinguished: the present "infinite-fidelity" real physics, the chosen high-fidelity mathematical model of the numerical experiments and the chosen low-fidelity mathematical model in the controller. Ideally, they would all three be identical which in practice, however, is unfeasible. Consequently, decreasing fidelity as illustrated by Figure 2.9 is the case.

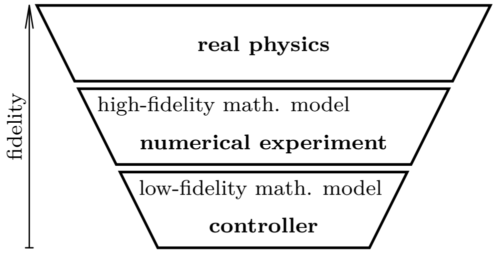

Figure 2.9 Levels of model fidelity in FSCI simulations.

It should further be noted that the influence of time step δt is not exhaustively examined. This applies especially to the finally used fluid (CFD) (see Chapter 5 The Fluid (CFD) Subsystem, pp. 57 ff.) and high-fidelity structural (CSM) subsystems (see Chapter 6 The Structural (CSM) Subsystem, pp. 68 ff.). Along with the low-fidelity structural (CSM) subsystem an overall time step of $\delta t = 0.01\,\mathrm{s}$ is used by default. This results in rather strong damping of higher eigenmodes in the fluid. Thus, the performed simulations can only cover basic dynamical effects related to lower modes. This, however, fits the needs of this work. With the high-fidelity structural (CSM) subsystem on the other hand a time step of $\delta t = 0.005\,\mathrm{s}$ turns out to be necessary primarily due to the mesh updating scheme in the fluid (CFD) subsystem.

Everything should be as simple as it can be, but not simpler.

—Albert Einstein (1879–1955)

3 Model Problem

3.1 Setup

Goal of this chapter is to carefully analyze the proposed solution procedures for FSI and FSCI problems (see Chapter 7 Fluid–Structure Interaction, pp. 79 ff. and Chapter 9 Fluid–Structure–Control Interaction, pp. 118 ff.) before they are finally employed in simulations in Part II Numerical Experiments (pp. 53 ff.) of this thesis. This analysis proves to be extremely costly and consequently unfeasible for highly multi-dimensional problems. The opaque superposition of many different effects does not allow for specific extraction of fundamental statements, in particular not analytical ones.

In the field of computational FSI it therefore became well established practice to fall back to highly simplified model problems, which represent only the most basic characteristics of actual FSI problems. Such model problems are for instance used in Dettmer (2015, pp. 9, 12) and Dettmer and Perić (2013, Section 3.1, pp. 4–6).

Point mass, linear damper (dashpot) and elastic spring assemble to the common setting, the linear, one-dimensional SDoF system

$$m\ddot{y} + c\dot{y} + ky = 0 \tag{3.1a}$$

with its initial conditions

$$\begin{aligned} y(0) &= y_0 \\ \dot{y}(0) &= \dot{y}_0. \end{aligned} \tag{3.1b}$$

This purely autonomous[1] IVP is sufficient for the analysis of a broad

[1] without external influences like disturbance $z(t)$ or control input $u(t)$

spectrum of solution schemes for incompressible FSI regarding properties like stability (convergence behavior), accuracy and high-freuqency damping. It explains very well the behavior of partitioned strategies for multi-dimensional FSI. (Dettmer 2015, pp. 9, 10; Dettmer and Perić 2013, Remark I, pp. 5, 6, Conclusion, pp. 20, 21; Joosten, Dettmer, and Perić 2010, 2009; Causin, Gerbeau, and Nobile 2005))

As a first analysis of the FSCI approaches employed in this work the classical SDoF system

$$m\ddot{y} + c\dot{y} + ky = u \tag{3.2a}$$

is extended by a representative state-feedback controller

$$u = -k_{\mathrm{R1}}y - k_{\mathrm{R2}}\dot{y} \tag{3.2b}$$

to the modified model problem of a controlled SDoF system

$$m\ddot{y} + (c + k_{\mathrm{R2}})\,\dot{y} + (k + k_{\mathrm{R1}})\,y = 0 \tag{3.2c}$$

with initial conditions

$$\begin{aligned} y(0) &= y_0 \\ \dot{y}(0) &= \dot{y}_0. \end{aligned} \tag{3.2d}$$

In the following it is simply referred to as model problem. An illustration can be found in Figure 3.1.

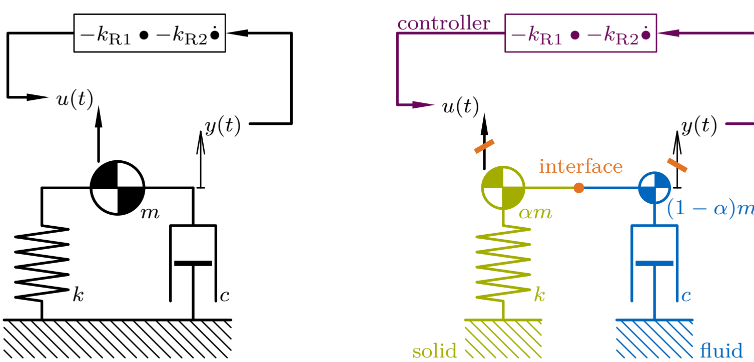

(a) Monolithic. **(b)** Towards partitioned.

Figure 3.1 Setup of model problem.

At this stage the system stays linear and in particular still one-dimensional. Reason for this is that the control input $u(t)$ is treated as an external influence on the SDoF system of type disturbance or force $z(t)$ not adding any new displacement degree of freedom. This assumption holds as long the later introduced u-output factor $f_u = 0$ (see Chapter 6 The Structural

(CSM) Subsystem, pp. 68 ff.). Conversely, $f_u \neq 0$ implies that the control input $u(t)$ adds an additional displacement degree of freedom, the root-point excitation. This case is only considered briefly in a later suggestion for a better suitable, modified model problem as well as in the numerical experiments.

A substantial observation is made in this work: Adding a controller, operating on the structure via force, adjusts the structural dynamics to desired ones rather than changing the overall physics of the coupled problem. As direct consequence the justifications made in literature concerning the FSI model problem are still valid for the expansion to the FSCI model problem. Therefore, model problem (3.2) is sufficient for the analysis of fundamental effects in partitioned coupling schemes for FSCI.

The key features of the employed model problem can be summarized as follows: The coupling of a first order ODE substituting the fluid and a second order ODE substituting the structure reproduces the FSI subproblem. With the additional coupling to the algebraic ODE (AODE) of the controller it extends to the full FSCI problem. Combination of viscosity and inertia in one subsystem (fluid) and stiffness/inertia in another (structure) also corresponds to key characteristics of FS(C)I problems. The main physics are still dominated by the FSI subproblem, since inertia is limited to fluid and structure and the controller is just adjusting the structural dynamics. Furthermore, pressure can be seen as Lagrangian multipliers enforcing the incompressibility constraint (continuity), i.e. the pressure does not directly drive the interaction. And the classical model problem (3.1) is already used exactly for the purposes of partitioned FSI approaches with fixed-point iterative coupling and Gauß-Seidel communication pattern by Joosten, Dettmer, and Perić (2010) and Joosten, Dettmer, and Perić (2009).

In the following first the BDF1 (see Equation (2.10) with $N = 1$) will be used for time integration of occurring ODE's. Thus, closed solutions and analytical statements can be derived. Whereas formulations using the BDFN with $N > 1$ can only be evaluated graphically.

3.2 Monolithic Solution

The time-continuous, monolithic description of the model problem is given with Equations (3.2c) and (3.2d). Together with the BDF1 in terms of Equation (2.10) with $N = 1$ this leads to the time-discrete, monolithic model problem respectively the monolithic solution

$$\begin{aligned}
&\left(m + (c + k_{\mathrm{R2}})\,\delta t + (k + k_{\mathrm{R1}})\,\delta t^2\right) y^{n+1} \\
&\qquad - \left(2m + (c + k_{\mathrm{R2}})\,\delta t\right) y^n + m y^{n-1} = 0 \\
\text{i.e.} \qquad & y^{n+1} = \frac{2m + (c + k_{\mathrm{R2}})\,\delta t}{m + (c + k_{\mathrm{R2}})\,\delta t + (k + k_{\mathrm{R1}})\,\delta t^2} y^n \\
&\qquad - \frac{m}{m + (c + k_{\mathrm{R2}})\,\delta t + (k + k_{\mathrm{R1}})\,\delta t^2} y^{n-1}
\end{aligned} \tag{3.3a}$$

and its discrete initial conditions

$$\begin{aligned}
y^{-1} &= y_0 - \delta t \dot{y}_0 \\
y^0 &= y_0.
\end{aligned} \tag{3.3b}$$

3.3 Stability Considerations

Meaningful physical properties are

$$\begin{aligned}
m &\geq 0 \\
c &\geq 0 \\
k &\geq 0.
\end{aligned} \tag{3.4}$$

However, the special case of all being zero at once is excluded since this would correspond to a "nonexistent system".

Those properties along with the time-continuous (3.2c, 3.2d) and time-discrete monolith (3.3) allow for the derivation of statements on the k_{R1}-k_{R2}-stability regions, i.e. on controller settings k_{R1} and k_{R2} for which the controlled SDoF system shows stable dynamics.

3.3.1 Time–Continuous Problem

First of all, the stability region in the k_{R1}-k_{R2}-plane for the time-continuous, monolithic model problem (3.2c, 3.2d) is considered.

The characteristic polynomial of the system

$$p(s) = ms^2 + (c + k_{\mathrm{R2}})\,s + (k + k_{\mathrm{R1}}) \tag{3.5}$$

is determined from Equation (3.2c). Its roots

$$\begin{aligned}
&\left\{ s \in \mathbb{C} \middle| p(s) = 0 \right\} \\
\Leftrightarrow \qquad & s_{1,2} = -\frac{c + k_{\mathrm{R2}}}{2m} \pm \sqrt{\left(\frac{c + k_{\mathrm{R2}}}{2m}\right)^2 - \frac{k + k_{\mathrm{R1}}}{m}}
\end{aligned} \tag{3.6}$$

denote the poles of the system.

In control theory it is distinguished between two basic stability definitions for time-continuous systems (Kotyczka and Gehring 2015; Lohmann 2015d): The controlled SDoF system is bounded-input, bounded-output (BIBO) stable if and only if both its poles lie in the negative complex half-plane. Furthermore, it is asymptotically stable if and only if both its eigenvalues lie in the negative complex half-plane. In general, all poles of a system denote eigenvalues of that system, but only controllable and observable eigenvalues are poles. Asymptotical stability is therefore in general stronger than BIBO stability. It covers BIBO stability as well as stability of internal dynamics which can not be recognized at the output.

Here, the second-order system possesses exactly two eigenvalues which are entirely specified by the two poles. Thus, asymptotical and BIBO stability coincide. The time-continuous, controlled SDoF system is asymptotical and BIBO stable

$$\begin{aligned} \Leftrightarrow \quad & s_{1,2} \in \left\{ s \in \mathbb{C} \,\middle|\, \mathrm{Re}\{s\} \leq 0 \right\} \\ \Leftrightarrow \quad & \max_{i=1,2} \left\{ \mathrm{Re}\left\{ s_i \right\} \right\} \leq 0. \end{aligned} \tag{3.7}$$

Consequently, the k_{R1}-k_{R2}-stability region results in

$$\begin{aligned} \Omega_{\mathrm{c}} &= \left\{ k_{\mathrm{R1}}, k_{\mathrm{R2}} \in \mathbb{R} \,\middle|\, \max_{i=1,2} \left\{ \mathrm{Re}\left\{ s_i \right\} \right\} \leq 0 \right\} \\ &= \left\{ k_{\mathrm{R1}}, k_{\mathrm{R2}} \in \mathbb{R} \,\middle|\, k_{\mathrm{R1}} + k \geq 0 \quad \wedge \quad \frac{k_{\mathrm{R2}} + c}{\delta t} \geq 0 \right\} \\ &= \left\{ k_{\mathrm{R1}}, k_{\mathrm{R2}} \in \mathbb{R} \,\middle|\, k_{\mathrm{R1}} \geq -k \quad \wedge \quad k_{\mathrm{R2}} \geq -c \right\}. \end{aligned} \tag{3.8}$$

It is illustrated in Figure 3.2.

3.3.2 Time–Discrete Problem

In the same way, now the stability region in the k_{R1}-k_{R2}-plane for the time-discrete, monolithic model problem (3.3) is considered.

The characteristic polynomial of the system

$$p(z) = \left(m + (c + k_{\mathrm{R2}})\, \delta t + (k + k_{\mathrm{R1}})\, \delta t^2 \right) z^2 - (2m + (c + k_{\mathrm{R2}})\, \delta t)\, z + m \tag{3.9}$$

is determined from Equation (3.3a). Its roots

$$
\begin{aligned}
& \left\{z \in \mathbb{C} \middle| p(z) = 0\right\} \\
\Leftrightarrow \qquad & z_{1,2} = \frac{2m + (c + k_{\mathrm{R2}})\,\delta t}{2\left(m + (c + k_{\mathrm{R2}})\,\delta t + (k + k_{\mathrm{R1}})\,\delta t^2\right)} \\
& \pm \sqrt{\left(\frac{2m + (c + k_{\mathrm{R2}})\,\delta t}{2\left(m + (c + k_{\mathrm{R2}})\,\delta t + (k + k_{\mathrm{R1}})\,\delta t^2\right)}\right)^2 - \frac{m}{m + (c + k_{\mathrm{R2}})\,\delta t + (k + k_{\mathrm{R1}})\,\delta t^2}}
\end{aligned}
\tag{3.10}
$$

denote the poles of the system.

The two basic stability definitions in control theory change inor the time-discrete case (Kotyczka 2013): The controlled SDoF system is bounded-input, bounded-output (BIBO) stable if and only if both its poles lie inside the unite circle. Furthermore, it is asymptotically stable if and only if both its eigenvalues lie inside the unite circle. The remaining statements on eigenvalues and poles respectively asymptotical and BIBO stability in general and in particular still hold.

With

$$z = \mathrm{e}^{s\delta t} \tag{3.11a}$$

and vice versa

$$s = \frac{1}{\delta t} \ln(z) \tag{3.11b}$$

the map between the time-continuous s- and the time-discrete z-plane is given. $\mathrm{e}^{s\delta t}$ herein corresponds to the exact amplification factor which is the result of going analytically from the initial value y^n to the final value y^{n+1} with time step δt and appropriate eigenvalue s (Kotyczka 2013).

The time-discrete, controlled SDoF system is asymptotical and BIBO stable

$$
\begin{aligned}
\Leftrightarrow \qquad & z_{1,2} \in \left\{z \in \mathbb{C} \middle| \, |z| \leq 1\right\} \\
\Leftrightarrow \qquad & \max_{i=1,2} \{|z_i|\} \leq 1.
\end{aligned}
\tag{3.12}
$$

Consequently, the k_{R1}-k_{R2}-stability region formulated in the z-plane results in

$$\Omega_{\mathrm{d}} = \left\{k_{\mathrm{R1}}, k_{\mathrm{R2}} \in \mathbb{R} \middle| \max_{i=1,2} \{|z_i|\} \leq 1\right\}. \tag{3.13a}$$

And mapped back to the s-plane this reads

$$
\begin{aligned}
\Omega_{\mathrm{d}} &= \left\{k_{\mathrm{R1}}, k_{\mathrm{R2}} \in \mathbb{R} \middle| \frac{1}{\delta t} \ln\left(\max_{i=1,2} \{|z_i|\}\right) \leq 0\right\} \\
&= \left\{k_{\mathrm{R1}}, k_{\mathrm{R2}} \in \mathbb{R} \middle| k_{\mathrm{R1}} + k \geq 0 \quad \wedge \quad \frac{k_{\mathrm{R2}} + c}{\delta t} \geq -(k_{\mathrm{R1}} + k)\right\} \\
&= \left\{k_{\mathrm{R1}}, k_{\mathrm{R2}} \in \mathbb{R} \middle| k_{\mathrm{R1}} \geq -k \quad \wedge \quad k_{\mathrm{R2}} \geq -c - \delta t\,(k_{\mathrm{R1}} + k)\right\}.
\end{aligned}
\tag{3.13b}
$$

The result is illustrated in Figure 3.2 as well.

Clearly recognizable in Figure 3.2 is the fact that the time-continuous k_{R1}-k_{R2}-stability region representing real physics gets extended to an apparently bigger, time-discrete k_{R1}-k_{R2}-stability region. But only real physics with its time-continuous k_{R1}-k_{R2}-stability region can be decisive for designing the controller. This must in particular receive attention when numerical parameter identification for the controller, e.g. in form of a co-simulation based optimization, is performed.

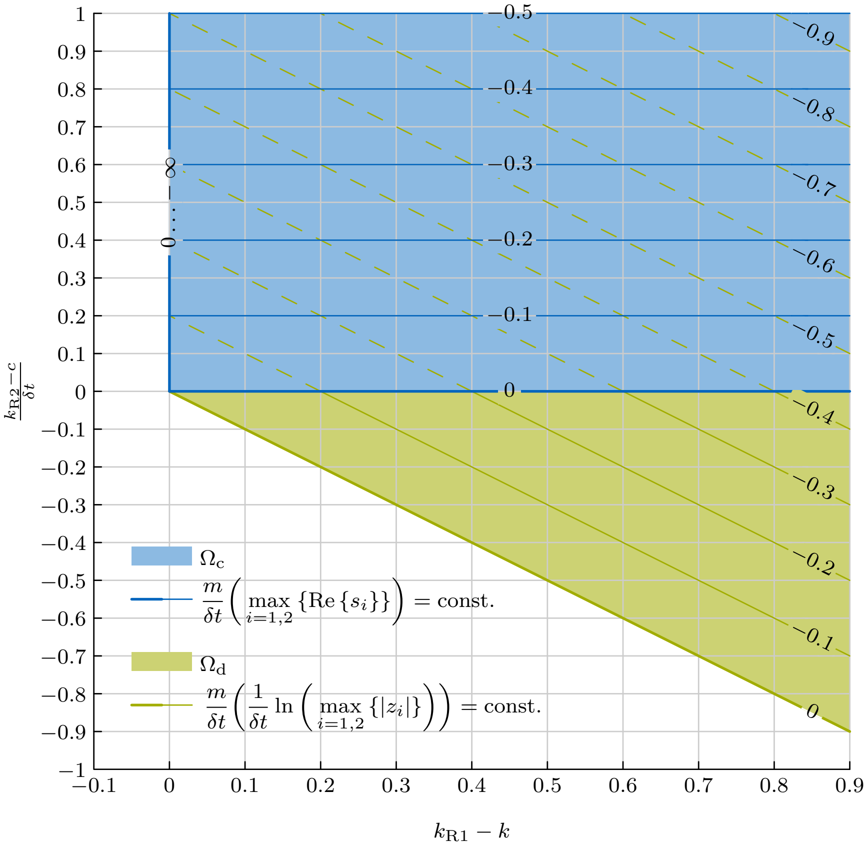

Figure 3.2 Stability regions of time-continuous and time-discrete model problem.

3.4 Partitioned Approach or Co–Simulation

Presented in the previous Chapter 1 Introduction (pp. 1 ff.) and more detailed in the later Chapters 7 Fluid–Structure Interaction (pp. 79 ff.)

and 9 Fluid–Structure–Control Interaction (pp. 118 ff.) this work employs one specific partitioned approach in three similar realizations. This chapter is particularly interested in the convergence properties and consequently stability of those schemes. For that purposes the model problem (3.2) was introduced.

3.4.1 Partitioning

The initial step of a partitioned approach is the decomposition of the multi-physics problem into single-physics subproblems and appropriate interface constraints covering the interactions. This is referred to as partitioning.

Preparational step for reaching a here suitable partitioning of model problem (3.2) is the reformulation of the ODE (3.2a)

$$\begin{aligned} & (\alpha m)\ddot{y} + ((1-\alpha)m)\,\ddot{y} + c\dot{y} + ky = u + z + z \\ \wedge \qquad & z + z = 0. \end{aligned} \tag{3.14}$$

In combination with Equations (3.2b) and (3.2d) this leads finally to the partitioned model problem. It may be pointed out that this is still describing the exact same dynamics.

$$((1-\alpha)m)\,\ddot{y}_{\mathrm{F}} + c\dot{y}_{\mathrm{F}} = z_{\mathrm{F}} \tag{3.15a}$$

is referred to as the fluid subsystem identified with the indix F,

$$(\alpha m)\ddot{y}_{\mathrm{S}} + ky_{\mathrm{S}} = u_{\mathrm{S}} + z_{\mathrm{S}} \tag{3.15b}$$

as the structural subsystem (index S) and

$$u_{\mathrm{C}} = -\,k_{\mathrm{R1}}y_{\mathrm{C}} - k_{\mathrm{R2}}\dot{y}_{\mathrm{C}} \tag{3.15c}$$

as controller subsystem (index C). The physical interaction is shiftet to the interface constraints (index I)

$$y_{\mathrm{F}} - y_{\mathrm{S}} = 0 \tag{3.15d}$$

$$z_{\mathrm{F}} + z_{\mathrm{S}} = 0 \tag{3.15e}$$

$$y_{\mathrm{S}} - y_{\mathrm{C}} = 0 \tag{3.15f}$$

$$u_{\mathrm{S}} - u_{\mathrm{C}} = 0. \tag{3.15g}$$

And initial conditions are given with

$$\begin{aligned} y_{\mathrm{S}}(0) &= y_0 \\ \dot{y}_{\mathrm{S}}(0) &= \dot{y}_0. \end{aligned} \tag{3.15h}$$

Thus, the structural domain is represented by the elastic spring k and the point mass share αm, the fluid domain by the linear damper (dashpot)

c and the point mass share $(1-\alpha)m$. The interface constraints cover the interactions between these two domains (FSI) and between structure and controller (FSCI). y describes the displacement which corresponds to the measured output. z is the disturbance (force) originating from the partitioning and u the control input equivalent here to a force acting on the system. The partitioning is illustrated in Figure 3.1b.

The appearing parameter $\alpha \in [0,1]$ describes the mass distribution between fluid and structural subsystem, i.e.

$$\begin{aligned} \frac{m_{\mathrm{S}}}{m} &= \alpha \\ \frac{m_{\mathrm{F}}}{m} &= 1-\alpha \\ \frac{m_{\mathrm{S}}}{m_{\mathrm{F}}} &= \frac{\alpha}{1-\alpha} \end{aligned} \tag{3.15i}$$

and allows to precisely quantify the added-mass effect. Also other "α"-parameters regarding damping c and stiffness k would be feasible (compare Dettmer (2015, Slide 12)). But at this stage only one paramter α associated with the mass m is considered. In the dominating FSI subproblem the convergence properties of ${}_{\beta}A$ depend simply only on this one parameter in the limit case $\delta t \to 0$ (Joosten, Dettmer, and Perić 2009, Section 3, p. 763). Conversely, for $\delta t \to \infty$ the "α"-parameter for the stiffness k gains main influence. This explains also the observation of better convergence behavior for large δt rather than small ones. The more accurate the time integration scheme the more relevant is this effect, i.e. the more dominant is the limit of ${}_{\beta}A$ for $\delta t \to 0$. Here only sufficiently small time steps are of interest to ensure a certain accuracy of the simulations especially with regard to control. Therefore, considering α is sufficient.

3.4.2 Temporal Discretization

Temporal discretization of the partitioned model problem (3.15) with the BDF1 (Equation (2.10) with $N=1$) leads to the discrete, partitioned model problem with the discrete fluid subsystem

$$\begin{aligned} & z_{\mathrm{F}}^{n+1} = \frac{(1-\alpha)m + c\delta t}{\delta t^2} y_{\mathrm{F}}^{n+1} - \frac{(1-\alpha)m + c\delta t}{\delta t^2} y_{\mathrm{F}}^{n} - \frac{(1-\alpha)m}{\delta t} \dot{y}_{\mathrm{F}}^{n} \\ \text{i.e.} \quad & z_{\mathrm{F}}^{n+1} = \mathcal{G}_{\mathrm{F}}\left(y_{\mathrm{F}}^{n+1}\right), \end{aligned} \tag{3.16a}$$

the discrete structural subsystem

$$\begin{aligned} y_{\mathrm{S}}^{n+1} &= \frac{\delta t^2}{\alpha m + k\delta t^2} z_{\mathrm{S}}^{n+1} + \frac{\delta t^2}{\alpha m + k\delta t^2} u_{\mathrm{S}}^{n+1} \\ &\quad + \frac{\alpha m}{\alpha m + k\delta t^2} y_{\mathrm{S}}^{n} + \frac{\alpha m \delta t}{\alpha m + k\delta t^2} \dot{y}_{\mathrm{S}}^{n} \\ \text{i.e.} \qquad y_{\mathrm{S}}^{n+1} &= \mathcal{G}_{\mathrm{S}} \left(z_{\mathrm{S}}^{n+1}, u_{\mathrm{S}}^{n+1} \right), \end{aligned} \tag{3.16b}$$

the discrete controller subsystem

$$\begin{aligned} u_{\mathrm{C}}^{n+1} &= -\frac{k_{\mathrm{R1}}\delta t + k_{\mathrm{R2}}}{\delta t} y_{\mathrm{C}}^{n+1} + \frac{k_{\mathrm{R2}}}{\delta t} y_{\mathrm{C}}^{n} \\ \text{i.e.} \qquad u_{\mathrm{C}}^{n+1} &= \mathcal{G}_{\mathrm{C}} \left(y_{\mathrm{C}}^{n+1} \right), \end{aligned} \tag{3.16c}$$

the discrete interface equations

$$\begin{aligned} y_{\mathrm{F}}^{n+1} - y_{\mathrm{S}}^{n+1} &= 0 \\ \text{i.e.} \qquad \mathcal{I}_{\mathrm{FS},y} \left(y_{\mathrm{F}}^{n+1}, y_{\mathrm{S}}^{n+1} \right) &= 0 \end{aligned} \tag{3.16d}$$

$$\begin{aligned} z_{\mathrm{F}}^{n+1} + z_{\mathrm{S}}^{n+1} &= 0 \\ \text{i.e.} \qquad \mathcal{I}_{\mathrm{FS},z} \left(z_{\mathrm{F}}^{n+1}, z_{\mathrm{S}}^{n+1} \right) &= 0 \end{aligned} \tag{3.16e}$$

$$\begin{aligned} y_{\mathrm{S}}^{n+1} - y_{\mathrm{C}}^{n+1} &= 0 \\ \text{i.e.} \qquad \mathcal{I}_{\mathrm{SC},y} \left(y_{\mathrm{S}}^{n+1}, y_{\mathrm{C}}^{n+1} \right) &= 0 \end{aligned} \tag{3.16f}$$

$$\begin{aligned} u_{\mathrm{S}}^{n+1} - u_{\mathrm{C}}^{n+1} &= 0 \\ \text{i.e.} \qquad \mathcal{I}_{\mathrm{SC},u} \left(u_{\mathrm{S}}^{n+1}, u_{\mathrm{C}}^{n+1} \right) &= 0 \end{aligned} \tag{3.16g}$$

and the discrete initial conditions

$$\begin{aligned} y_{\mathrm{S}}^{-1} &= y_0 - \delta t \dot{y}_0 \\ y_{\mathrm{S}}^{0} &= y_0. \end{aligned} \tag{3.16h}$$

The operators $\mathcal{G}$ and $\mathcal{I}$ describe the input-output relation for the specific subsystem and the interface constraint for the specific coupling, respectively.

The FSI subproblem, i.e. the coupling between fluid and structure converges to the solution of Equations (3.16a), (3.16b), (3.16d) and (3.16e). The emerging "fluid-structure (FS) subsystem" is given with

$$\begin{aligned} y_{\mathrm{S}}^{n+1} &= \frac{\delta t^2}{m + c\delta t + k\delta t^2} u_{\mathrm{S}}^{n+1} + \frac{m + c\delta t}{m + c\delta t + k\delta t^2} y_{\mathrm{S}}^{n} \\ &\quad + \frac{m\delta t}{m + c\delta t + k\delta t^2} \dot{y}_{\mathrm{S}}^{n} \\ \text{i.e.} \qquad y_{\mathrm{S}}^{n+1} &= \mathcal{G}_{\mathrm{FS}} \left(u_{\mathrm{S}}^{n+1} \right) \end{aligned} \tag{3.17}$$

which obviously corresponds to the BDF1-discretization of $m\ddot{y}_{\mathrm{S}} + c\dot{y}_{\mathrm{S}} + ky_{\mathrm{S}} = u_{\mathrm{S}}$ due to the consistent use of the BDF1 in all subsystems.

Accordingly, the converged solution of the SCI subproblem, i.e. the coupling between structure and controller fulfills Equations (3.16b), (3.16c), (3.16f) and (3.16g). This leads to a "structure-controller (SC) subsystem"

$$\begin{aligned} y_{\mathrm{S}}^{n+1} &= \frac{\delta t^2}{\alpha m + k_{\mathrm{R2}}\delta t + (k + k_{\mathrm{R1}})\,\delta t^2} z_{\mathrm{S}}^{n+1} \\ &\quad + \frac{\alpha m + k_{\mathrm{R2}}\delta t}{\alpha m + k_{\mathrm{R2}}\delta t + (k + k_{\mathrm{R1}})\,\delta t^2} y_{\mathrm{S}}^{n} \\ &\quad + \frac{\alpha m \delta t}{\alpha m + k_{\mathrm{R2}}\delta t + (k + k_{\mathrm{R1}})\,\delta t^2} \dot{y}_{\mathrm{S}}^{n} \\ \text{i.e.} \qquad y_{\mathrm{S}}^{n+1} &= \mathcal{G}_{\mathrm{SC}}\left(z_{\mathrm{S}}^{n+1}\right) \end{aligned} \tag{3.18}$$

which obviously meets the BDF1-discretization of $(\alpha m)\ddot{y}_{\mathrm{S}} + k y_{\mathrm{S}} = u_{\mathrm{S}} + z_{\mathrm{S}}$ with $u_{\mathrm{S}} = -k_{\mathrm{R1}} y_{\mathrm{S}} - k_{\mathrm{R2}} \dot{y}_{\mathrm{S}}$ respectively combined $\alpha m \ddot{y}_{\mathrm{S}} + k_{\mathrm{R2}}\dot{y}_{\mathrm{S}} + (k + k_{\mathrm{R1}})\, y_{\mathrm{S}} = z_{\mathrm{S}}$ again due to the consistent use of the BDF1 in all subsystems.

3.4.3 Fixed–Point Formulation

Partitioning (3.16) of the underlying monolithic system (3.3) illustrates well the second fundamental concept of partitioned approaches: The interactions of the multiple physical fields (multi-physics) are shifted to interface constraints. Those couple the resulting single-physics subsystems and need to be solved in order to provide the subsystems' inputs. Assuming this can be done each time step, in a third fundamental step of partitioned approaches the subsystems can then finally be ran independently and straight forward. However, the interface constraints are dependent on all subsystems' inputs and outputs. The outputs themselves again depend on the systems' inputs via input-output relations as part of the dynamics. This makes the overall solution process in general more complex.

In this work the interface constraints are solved iteratively which implies the solution of all involved single-physics subsystems in each iteration step. It becomes obvious that in case of multi degrees of freedom in numerical experiments the number of overall coupling iterations per time step is decisive for the efficiency of the solution procedures.

More precisely, the solution of the interface constraints (3.16d) to (3.16g) is formulated in terms of fixed-point iterations

$$^{k+1}y_{\mathrm{S}}^{n+1} = {}_{1}A\, {}^{k}y_{\mathrm{S}}^{n+1} + b^{n} \tag{3.19}$$

solving for the structural displacement y_{S}^{n+1} based on Gauß-Seidel communication patterns which can be read from Figures 9.1 (p. 120), 9.2 (p. 121) and 9.3 (p. 122). The simple form is the result of the linearity of the underlying model problem.

Formulation (3.19) can be further improved with a simplest form of relaxation

$$\begin{aligned} {}^{k+1}y_{\mathrm{S}}^{n+1} &= \beta \left({}_1A\,{}^{k}y_{\mathrm{S}}^{n+1} + b^n\right) + (1-\beta)\,{}^{k}y_{\mathrm{S}}^{n+1} \\ \text{i.e.} \qquad {}^{k+1}y_{\mathrm{S}}^{n+1} &= {}_{\beta}A\,{}^{k}y_{\mathrm{S}}^{n+1} + \beta b^n \end{aligned} \tag{3.20}$$

where β denotes the user-defined relaxation parameter.

Convergence behavior and stability are only determined by the relaxed iteration factor ${}_{\beta}A = 1 + \beta\,({}_1A - 1)$. It is exclusively dependent on the relaxation parameter β and the non-relaxed iteration factor ${}_1A$ containing the time step δt and the problem properties m, c, k and α. b^n does not change over all iterations $k = 1, \ldots, k_{\text{end}}$.

Convergence, i.e. reduction of the error in each iteration is guaranteed for

$$\left|{}_{\beta}A\right| < 1. \tag{3.21a}$$

In terms of the user-specifiable relaxation parameter β this demands for

$$\frac{2}{1 - {}_1A} = -\frac{2}{{}_1A - 1} < \beta < 0 \tag{3.21b}$$

in case of ${}_1A > 1$ and for

$$0 < \beta < \frac{2}{1 - {}_1A} \tag{3.21c}$$

in case of ${}_1A < 1$. The conditions are illustrated in Figure 3.3.

Figure 3.4 shows the convergence and divergence (failure) behavior for different values of the relaxed iteration factor ${}_{\beta}A$. In particular, with ${}_{\beta}A = 0$ in Figure 3.4a the optimal case of meeting the exact solution after only one iteration is given. An optimal relaxation factor of

$$\beta^* = \frac{1}{1 - {}_1A} \tag{3.22}$$

for ${}_1A \neq 1$ follows. It is also highlighted within Figure 3.3.

The solution of the iteration procedure is finally given as the result of Equation (3.20) along with Equation (3.22)

$$\lim_{k\to\infty} \left\{{}^{k}y_{\mathrm{S}}^{n+1}\right\} = \frac{b^n}{1 - {}_1A} \tag{3.23}$$

in accordance with Joosten, Dettmer, and Perić (2009, Equation (22), p. 762).

It can be concluded that for any ${}_1A \neq 1$ there exists a range of β's such that convergence is achieved. And even more, inside this range an optimal relaxation parameter β^* resulting in convergence within only one iteration can always be found.

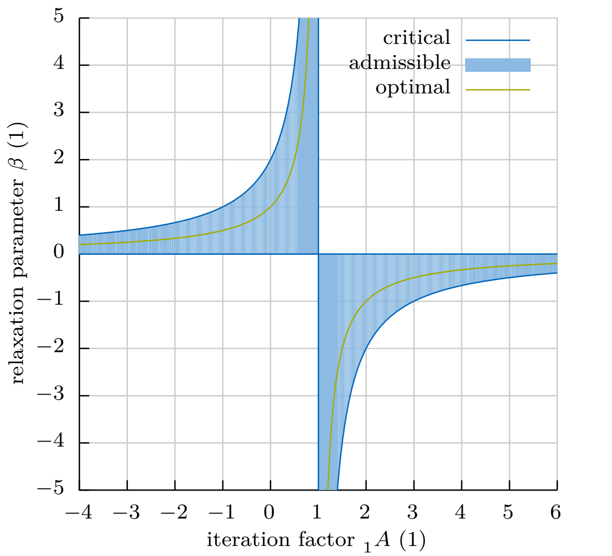

Figure 3.3 Relaxation of scalar fixed-point formulation.

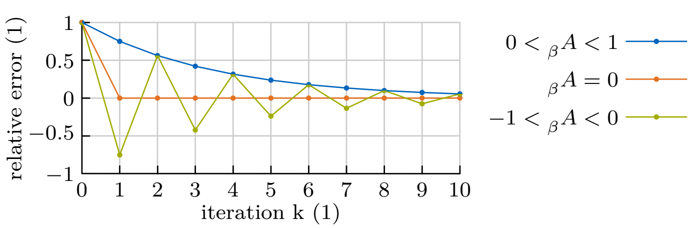

(a) Convergence.

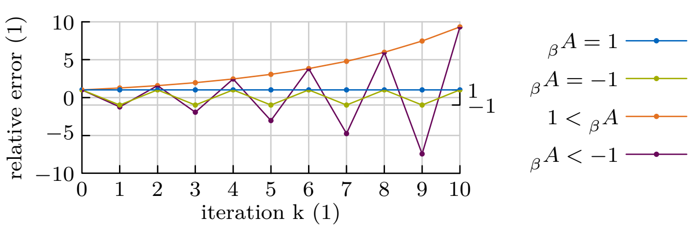

(b) Divergence.

Figure 3.4 Basic iteration behavior in scalar fixed-point formulation.

But "it should be emphasized that for multi-degree-of-freedom problems and long interfaces, evaluation of the optimal relaxation factor is non-unique even for linear problems" (Joosten, Dettmer, and Perić 2009, p. 769). Therefore, Aitken acceleration (see Küttler and Wall (2008) and Küttler (2009, Section 3.5, pp. 24–28 and Chapter 7, pp. 73–87)) is used in numerical experiments. In the present case of one linear degree of freedom this boils down to the optimal relaxation parameter.

For further details on fixed-point iteration, relaxation and Aitken acceleration, it is referred to literature for instance Küttler (2009, Section 3.5, pp. 24–28 and Chapter 7, pp. 73–87), Küttler and Wall (2008), Sicklinger (2014, Section 2.2, pp. 9–18) and Joosten, Dettmer, and Perić (2009).

Dettmer and Perić (2013, Equation (48), Section 3.4, p. 10) show that for FSI

$$\lim_{\substack{\delta t \to 0 \\ \alpha \to 0}} \{\beta^*\} = \lim_{\substack{\delta t \to 0 \\ \alpha \to 0}} \{\beta_{\text{crit}}\} = 0. \tag{3.24}$$

Consequently, a decreasing mass distribution $\alpha \to 0$ also demands a sufficiently smaller ($\beta \to 0$) relaxation parameter. But with this the sensitivity of the solution method concerning β increases. A drastically bigger amount of interface iterations is expected especially for the multi-degree of freedom case where an optimal relaxation parameter β^* with only one iteration does not exist. $\alpha = 0$ would require $\beta = 0$ which is inadmissible and thus leads to failure. The added-mass effect quantified by the mass distribution α is therefore crucial for the convergence behavior in the region of small δt's ($\delta t \to 0$) and convergence is getting more and more challenging as $\alpha \to 0$ (compare Dettmer (2015)).

Pseudo code implementations of the subsequently analyzed algorithms can be found in Chapter 9 Fluid–Structure–Control Interaction (pp. 118 ff.).

FSCI or no Nesting

In the context of this chapter the acronym FSCI also stands for the more specific iterative coupling scheme illustrated in Figure 9.1 and the corresponding Algorithm 9.1 (continued in 9.2). The Gauß-Seidel communication pattern is realized without nesting of any subproblems, i.e. the coupled problem is solved with a single fixed-point iteration loop. Applied without relaxation to model problem (3.16) the algorithm condenses down to

$$
\begin{aligned}
{}^{k+1}y_{\mathrm{S}}^{n+1} &\overset{(3.16b)}{=} \mathcal{G}_{\mathrm{S}}\left({}^{k}z_{\mathrm{S}}^{n+1}, {}^{k}u_{\mathrm{S}}^{n+1}\right)\\
&\overset{(3.16e),(3.16g)}{=} \mathcal{G}_{\mathrm{S}}\left(-{}^{k}z_{\mathrm{F}}^{n+1}, {}^{k}u_{\mathrm{C}}^{n+1}\right)\\
&\overset{(3.16a),(3.16c)}{=} \mathcal{G}_{\mathrm{S}}\left(-\mathcal{G}_{\mathrm{F}}\left({}^{k}y_{\mathrm{F}}^{n+1}\right), \mathcal{G}_{\mathrm{C}}\left({}^{k}y_{\mathrm{C}}^{n+1}\right)\right)\\
&\overset{(3.16d),(3.16f)}{=} \mathcal{G}_{\mathrm{S}}\left(-\mathcal{G}_{\mathrm{F}}\left({}^{k}y_{\mathrm{S}}^{n+1}\right), \mathcal{G}_{\mathrm{C}}\left({}^{k}y_{\mathrm{S}}^{n+1}\right)\right)\\
\text{i.e.}\quad {}^{k+1}y_{\mathrm{S}}^{n+1} &= -\frac{(1-\alpha)m + (c+k_{\mathrm{R2}})\,\delta t + k_{\mathrm{R1}}\delta t^2}{\alpha m + k\delta t^2}\,{}^{k}y_{\mathrm{S}}^{n+1} + b^n\\
\text{i.e.}\quad {}^{k+1}y_{\mathrm{S}}^{n+1} &= {}_{1}A_{\mathrm{FSCI}}\,{}^{k}y_{\mathrm{S}}^{n+1} + b^n.
\end{aligned}
\tag{3.25}
$$

The limit of the iteration factor

$$
\lim_{\delta t\to 0}\left\{{}_{1}A_{\mathrm{FSCI}}\right\} = \frac{\alpha-1}{\alpha} \tag{3.26}
$$

shows pure dependency on the mass distribution α.

Supplemented by relaxation the FSCI scheme reads

$$
\begin{aligned}
{}^{k+1}y_{\mathrm{S}}^{n+1} &= \beta\mathcal{G}_{\mathrm{S}}\left(-\mathcal{G}_{\mathrm{F}}\left({}^{k}y_{\mathrm{S}}^{n+1}\right), \mathcal{G}_{\mathrm{C}}\left({}^{k}y_{\mathrm{S}}^{n+1}\right)\right) + (1-\beta)\,{}^{k}y_{\mathrm{S}}^{n+1}\\
\text{i.e.}\quad {}^{k+1}y_{\mathrm{S}}^{n+1} &= -\frac{(\beta-\alpha)m + \beta\left((c+k_{\mathrm{R2}})\,\delta t + k_{\mathrm{R1}}\delta t^2\right) - (1-\beta)k\delta t^2}{\alpha m + k\delta t^2}\\
&\quad\cdot {}^{k}y_{\mathrm{S}}^{n+1} + \beta b^n\\
\text{i.e.}\quad {}^{k+1}y_{\mathrm{S}}^{n+1} &= {}_{\beta}A_{\mathrm{FSCI}}\,{}^{k}y_{\mathrm{S}}^{n+1} + \beta b^n.
\end{aligned}
\tag{3.27}
$$

And the limit of the iteration factor

$$
\lim_{\delta t\to 0}\left\{{}_{\beta}A_{\mathrm{FSCI}}\right\} = \frac{\alpha-\beta}{\alpha} \tag{3.28}
$$

now is obviously determined by the mass distribution α and the relaxation parameter β.

The optimal relaxation parameter (3.22) becomes

$$
\beta^{*}_{\mathrm{FSCI}} = \frac{\alpha m + k\delta t^2}{m + (c+k_{\mathrm{R2}})\,\delta t + (k+k_{\mathrm{R1}})\,\delta t^2}. \tag{3.29}
$$

Each summand in the denominator is positive non-equal to zero for physically relevant parameters (3.4) and stable controller setting (3.8. Thus, it can always be found. This supports the previously made statement.

[FS]CI or Nesting of FSI Sub–Problem

The acronym [FS]CI denotes the specific iterative coupling scheme illustrated in Figure 9.2 and the corresponding Algorithm 9.3 (continued in 9.4). The

Gauß-Seidel communication pattern is implemented with nesting of the FSI sub-problem made clear by bracketing [FS]. This means an inner fixed-point iteration loop solving the pure FSI sub-problem under constant control input is nested inside an outer fixed-point iteration finally solving the coupling between "FS" and fluid subsystem. The scheme is again applied to the model problem (3.16) without and with relaxation, respectively.

The inner FSI fixed-point iteration of the algorithm condenses down to

$$\begin{aligned}
{}^{k}_{m+1}y_{\mathrm{S}}^{n+1} &\overset{(3.16b)}{=} \mathcal{G}_{\mathrm{S}}\left({}^{k}_{m}z_{\mathrm{S}}^{n+1}, {}^{k}u_{\mathrm{S}}^{n+1} = \text{const.}\right)\\
&\overset{(3.16e)}{=} \mathcal{G}_{\mathrm{S}}\left(-{}^{k}_{m}z_{\mathrm{F}}^{n+1}, {}^{k}u_{\mathrm{S}}^{n+1} = \text{const.}\right)\\
&\overset{(3.16a)}{=} \mathcal{G}_{\mathrm{S}}\left(-\mathcal{G}_{\mathrm{F}}\left({}^{k}_{m}y_{\mathrm{F}}^{n+1}\right), {}^{k}u_{\mathrm{S}}^{n+1} = \text{const.}\right)\\
&\overset{(3.16d)}{=} \mathcal{G}_{\mathrm{S}}\left(-\mathcal{G}_{\mathrm{F}}\left({}^{k}_{m}y_{\mathrm{S}}^{n+1}\right), {}^{k}u_{\mathrm{S}}^{n+1} = \text{const.}\right)\\
\text{i.e.} \qquad {}^{k}_{m+1}y_{\mathrm{S}}^{n+1} &= -\frac{(1-\alpha)m + c\delta t}{\alpha m + k\delta t^2}\, {}^{k}_{m}y_{\mathrm{S}}^{n+1} + {}^{k}b^{n}\\
\text{i.e.} \qquad {}^{k}_{m+1}y_{\mathrm{S}}^{n+1} &= {}_{1}A_{\mathrm{FSI}}\, {}^{k}_{m}y_{\mathrm{S}}^{n+1} + {}^{k}b^{n}.
\end{aligned} \tag{3.30}$$

The limit of the inner iteration factor

$$\lim_{\delta t \to 0} \left\{ {}_{1}A_{\mathrm{FSI}} \right\} = \frac{\alpha - 1}{\alpha} \tag{3.31}$$

shows pure dependency on the mass distribution α.

Supplemented by relaxation the inner FSI part of the scheme reads

$$\begin{aligned}
{}^{k}_{m+1}y_{\mathrm{S}}^{n+1} &= \beta\mathcal{G}_{\mathrm{S}}\left(-\mathcal{G}_{\mathrm{F}}\left({}^{k}_{m}y_{\mathrm{S}}^{n+1}\right), {}^{k}u_{\mathrm{S}}^{n+1} = \text{const.}\right) + (1-\beta)\, {}^{k}_{m}y_{\mathrm{S}}^{n+1}\\
\text{i.e.} \qquad {}^{k}_{m+1}y_{\mathrm{S}}^{n+1} &= -\frac{(\beta-\alpha)m + c\delta t - (1-\beta)k\delta t^2}{\alpha m + k\delta t^2}\, {}^{k}_{m}y_{\mathrm{S}}^{n+1} + \beta\, {}^{k}b^{n}\\
\text{i.e.} \qquad {}^{k}_{m+1}y_{\mathrm{S}}^{n+1} &= {}_{\beta}A_{\mathrm{FSI}}\, {}^{k}_{m}y_{\mathrm{S}}^{n+1} + \beta\, {}^{k}b^{n}.
\end{aligned} \tag{3.32}$$

And the limit of the inner iteration factor

$$\lim_{\delta t \to 0} \left\{ {}_{\beta}A_{\mathrm{FSI}} \right\} = \frac{\alpha - \beta}{\alpha} \tag{3.33}$$

now is obviously determined by the mass distribution α and the relaxation parameter β.

The optimal relaxation parameter (3.22) becomes

$$\beta^{*}_{\mathrm{FSI}} = \frac{\alpha m + k\delta t^2}{m + c\delta t + k\delta t^2}. \tag{3.34}$$

It can always be found since each summand in the denominator is positive non-equal to zero for physically relevant parameters (3.4) independent of the controller setting. This supports again the previously made statement and additionally proofs the unrestricted stability of the pure FSI fixed-point iterations performed in Chapter 7 Fluid–Structure Interaction (pp. 79 ff.).

Assuming convergence the inner FSI fixed-point iteration can be substituted by the equivalent "FS subsystem" (3.17) for analyzing the outer [FS]CI fixed-point iteration. Consequently, this outer [FS]CI fixed-point iteration of the algorithm condenses down to

$$\begin{aligned}
{}^{k+1}y_{\mathrm{S}}^{n+1} &\overset{(3.17)}{=} \mathcal{G}_{\mathrm{FS}}\left({}^{k}u_{\mathrm{S}}^{n+1}\right) \\
&\overset{(3.16g)}{=} \mathcal{G}_{\mathrm{FS}}\left({}^{k}u_{\mathrm{C}}^{n+1}\right) \\
&\overset{(3.16c)}{=} \mathcal{G}_{\mathrm{FS}}\left(\mathcal{G}_{\mathrm{C}}\left({}^{k}y_{\mathrm{C}}^{n+1}\right)\right) \\
&\overset{(3.16f)}{=} \mathcal{G}_{\mathrm{FS}}\left(\mathcal{G}_{\mathrm{C}}\left({}^{k}y_{\mathrm{S}}^{n+1}\right)\right) \\
\text{i.e.} \qquad {}^{k+1}y_{\mathrm{S}}^{n+1} &= -\frac{k_{\mathrm{R}2}\delta t + k_{\mathrm{R}1}\delta t^2}{m + c\delta t + k\delta t^2}\,{}^{k}y_{\mathrm{S}}^{n+1} + b^n \\
\text{i.e.} \qquad {}^{k+1}y_{\mathrm{S}}^{n+1} &= {}_{1}A_{[\mathrm{FS}]\mathrm{CI}}\,{}^{k}y_{\mathrm{S}}^{n+1} + b^n.
\end{aligned} \tag{3.35}$$

The limit of the outer iteration factor

$$\lim_{\delta t \to 0} \left\{ {}_{1}A_{[\mathrm{FS}]\mathrm{CI}} \right\} = 0 \tag{3.36}$$

is always zero independently of the parameter setting.

Supplemented by relaxation the outer [FS]CI part of the scheme reads

$$\begin{aligned}
{}^{k+1}y_{\mathrm{S}}^{n+1} &= \beta\mathcal{G}_{\mathrm{FS}}\left(\mathcal{G}_{\mathrm{C}}\left({}^{k}y_{\mathrm{S}}^{n+1}\right)\right) + (1-\beta)\,{}^{k}y_{\mathrm{S}}^{n+1} \\
\text{i.e.} \qquad {}^{k+1}y_{\mathrm{S}}^{n+1} &= -\frac{\beta\left(k_{\mathrm{R}2}\delta t + k_{\mathrm{R}1}\delta t^2\right) - (1-\beta)(m + c\delta t + k\delta t^2)}{m + c\delta t + k\delta t^2}\,{}^{k}y_{\mathrm{S}}^{n+1} \\
&\quad + \beta b^n \\
\text{i.e.} \qquad {}^{k+1}y_{\mathrm{S}}^{n+1} &= {}_{\beta}A_{[\mathrm{FS}]\mathrm{CI}}\,{}^{k}y_{\mathrm{S}}^{n+1} + \beta b^n.
\end{aligned} \tag{3.37}$$

And the limit of the outer iteration factor

$$\lim_{\delta t \to 0} \left\{ {}_{\beta}A_{[\mathrm{FS}]\mathrm{CI}} \right\} = 1 - \beta \tag{3.38}$$

shows pure dependency on the relaxation parameter β.

The optimal relaxation parameter (3.22) becomes

$$\beta^{*}_{[\mathrm{FS}]\mathrm{CI}} = \frac{m + c\delta t + k\delta t^2}{m + (c + k_{\mathrm{R}2})\,\delta t + (k + k_{\mathrm{R}1})\,\delta t^2}. \tag{3.39}$$

Each summand in the denominator is positive non-equal to zero for physically relevant parameters (3.4) and stable controller setting (3.8). Thus, it can always be found. This supports again the previously made statement.

F[SC]I or Nesting of SCI Sub–Problem

The acronym F[SC]I denotes the specific iterative coupling scheme illustrated in Figure 9.3 and the corresponding Algorithm 9.5 (continued in 9.6). The Gauß-Seidel communication pattern is implemented with a nesting of the SCI sub-problem made clear by bracketing [SC]. This means an inner fixed-point iteration loop solving the pure SCI sub-problem under constant disturbance is nested inside an outer fixed-point iteration finally solving the coupling between fluid and "SC subsystem". The scheme is again applied to model problem (3.16) without and with relaxation, respectively.

The inner SCI fixed-point iteration of the algorithm condenses down to

$$\begin{aligned}
{}^{k}_{m+1}y^{n+1}_{\mathrm{S}} &\overset{(3.16b)}{=} \mathcal{G}_{\mathrm{S}}\left({}^{k}z^{n+1}_{\mathrm{S}} = \text{const.}, {}^{k}_{m}u^{n+1}_{\mathrm{S}}\right)\\
&\overset{(3.16g)}{=} \mathcal{G}_{\mathrm{S}}\left({}^{k}z^{n+1}_{\mathrm{S}} = \text{const.}, {}^{k}_{m}u^{n+1}_{\mathrm{C}}\right)\\
&\overset{(3.16c)}{=} \mathcal{G}_{\mathrm{S}}\left({}^{k}z^{n+1}_{\mathrm{S}} = \text{const.}, \mathcal{G}_{\mathrm{C}}\left({}^{k}_{m}y^{n+1}_{\mathrm{C}}\right)\right)\\
&\overset{(3.16f)}{=} \mathcal{G}_{\mathrm{S}}\left({}^{k}z^{n+1}_{\mathrm{S}} = \text{const.}, \mathcal{G}_{\mathrm{C}}\left({}^{k}_{m}y^{n+1}_{\mathrm{S}}\right)\right)\\
\text{i.e.}\qquad {}^{k}_{m+1}y^{n+1}_{\mathrm{S}} &= -\frac{k_{\mathrm{R2}}\delta t + k_{\mathrm{R1}}\delta t^2}{\alpha m + k\delta t^2}\,{}^{k}_{m}y^{n+1}_{\mathrm{S}} + {}^{k}b^{n}\\
\text{i.e.}\qquad {}^{k}_{m+1}y^{n+1}_{\mathrm{S}} &= {}_{1}A_{\mathrm{SCI}}\,{}^{k}_{m}y^{n+1}_{\mathrm{S}} + {}^{k}b^{n}.
\end{aligned}\tag{3.40}$$

The limit of the inner iteration factor

$$\lim_{\delta t\to 0}\left\{{}_{1}A_{\mathrm{SCI}}\right\} = 0 \tag{3.41}$$

is always zero independently of the parameter setting.

Supplemented by relaxation the inner SCI part of the scheme reads

$$\begin{aligned}
{}^{k}_{m+1}y^{n+1}_{\mathrm{S}} &= \beta\mathcal{G}_{\mathrm{S}}\left({}^{k}z^{n+1}_{\mathrm{S}} = \text{const.}, \mathcal{G}_{\mathrm{C}}\left({}^{k}_{m}y^{n+1}_{\mathrm{S}}\right)\right) + (1-\beta)\,{}^{k}_{m}y^{n+1}_{\mathrm{S}}\\
\text{i.e.}\qquad {}^{k}_{m+1}y^{n+1}_{\mathrm{S}} &= -\frac{\beta\left(k_{\mathrm{R2}}\delta t + k_{\mathrm{R1}}\delta t^2\right) - (1-\beta)(\alpha m + k\delta t^2)}{\alpha m + k\delta t^2}\,{}^{k}_{m}y^{n+1}_{\mathrm{S}}\\
&\quad + \beta\,{}^{k}b^{n}\\
\text{i.e.}\qquad {}^{k}_{m+1}y^{n+1}_{\mathrm{S}} &= {}_{\beta}A_{\mathrm{SCI}}\,{}^{k}_{m}y^{n+1}_{\mathrm{S}} + \beta\,{}^{k}b^{n}.
\end{aligned}\tag{3.42}$$

And the limit of the inner iteration factor

$$\lim_{\delta t\to 0}\left\{{}_{\beta}A_{\mathrm{SCI}}\right\} = 1-\beta \tag{3.43}$$

shows pure dependency on the relaxation parameter β.

The optimal relaxation parameter (3.22) becomes

$$\beta^{*}_{\mathrm{SCI}} = \frac{\alpha m + k\delta t^2}{\alpha m + k_{\mathrm{R2}}\delta t + (k + k_{\mathrm{R1}})\,\delta t^2}. \tag{3.44}$$

Summands αm and $(k + k_{\mathrm{R1}})\,\delta t^2$ in the denominator are positive non-equal to zero for physically relevant parameters (3.4) and stable controller setting (3.8). Thus, it can always be found by additionally requiring $k_{\mathrm{R2}}\delta t \neq -\left(\alpha m + (k + k_{\mathrm{R1}})\,\delta t^2\right)$. This supports the previous statement.

Assuming convergence the inner SCI fixed-point iteration can accordingly be substituted by the equivalent "SC subsystem" (3.18) for analyzing the outer F[SC]I fixed-point iteration. Consequently, this outer F[SC]I fixed-point iteration of the algorithm condenses down to

$$\begin{aligned}
{}^{k+1}y_{\mathrm{S}}^{n+1} &\overset{(3.18)}{=} \mathcal{G}_{\mathrm{SC}}\left({}^{k}z_{\mathrm{S}}^{n+1}\right) \\
&\overset{(3.16e)}{=} \mathcal{G}_{\mathrm{SC}}\left(-\,{}^{k}z_{\mathrm{F}}^{n+1}\right) \\
&\overset{(3.16a)}{=} \mathcal{G}_{\mathrm{SC}}\left(-\mathcal{G}_{\mathrm{S}}\left({}^{k}y_{\mathrm{F}}^{n+1}\right)\right) \\
&\overset{(3.16d)}{=} \mathcal{G}_{\mathrm{SC}}\left(-\mathcal{G}_{\mathrm{F}}\left({}^{k}y_{\mathrm{S}}^{n+1}\right)\right) \\
\text{i.e.}\qquad {}^{k+1}y_{\mathrm{S}}^{n+1} &= -\frac{(1-\alpha)m + c\delta t}{\alpha m + k_{\mathrm{R2}}\delta t + (k + k_{\mathrm{R1}})\,\delta t^2}\,{}^{k}y_{\mathrm{S}}^{n+1} + b^n \\
\text{i.e.}\qquad {}^{k+1}y_{\mathrm{S}}^{n+1} &= {}_{1}A_{\mathrm{F[SC]I}}\,{}^{k}y_{\mathrm{S}}^{n+1} + b^n.
\end{aligned} \tag{3.45}$$

The limit of the outer iteration factor

$$\lim_{\delta t \to 0}\left\{{}_{1}A_{\mathrm{F[SC]I}}\right\} = \frac{\alpha - 1}{\alpha} \tag{3.46}$$

shows pure dependency on the mass distribution α.

Supplemented by relaxation the outer F[SC]I part of the scheme reads

$$\begin{aligned}
{}^{k+1}y_{\mathrm{S}}^{n+1} &= \beta\mathcal{G}_{\mathrm{SC}}\left(-\mathcal{G}_{\mathrm{F}}\left({}^{k}y_{\mathrm{S}}^{n+1}\right)\right) + (1-\beta)\,{}^{k}y_{\mathrm{S}}^{n+1} \\
\text{i.e.}\quad {}^{k+1}y_{\mathrm{S}}^{n+1} &= -\,\frac{(\beta - \alpha)m + \beta c\delta t - (1-\beta)\left(k_{\mathrm{R2}}\delta t + (k + k_{\mathrm{R1}})\,\delta t^2\right)}{\alpha m + k_{\mathrm{R2}}\delta t + (k + k_{\mathrm{R1}})\,\delta t^2} \\
&\quad \cdot {}^{k}y_{\mathrm{S}}^{n+1} + \beta b^n \\
\text{i.e.}\quad {}^{k+1}y_{\mathrm{S}}^{n+1} &= {}_{\beta}A_{\mathrm{F[SC]I}}\,{}^{k}y_{\mathrm{S}}^{n+1} + \beta b^n.
\end{aligned} \tag{3.47}$$

And the limit of the outer iteration factor

$$\lim_{\delta t \to 0}\left\{{}_{\beta}A_{\mathrm{F[SC]I}}\right\} = \frac{\alpha - \beta}{\alpha} \tag{3.48}$$

now is obviously determined by the mass distribution α and the relaxation parameter β.

The optimal relaxation parameter (3.22) becomes

$$\beta^*_{\mathrm{F[SC]I}} = \frac{\alpha m + k_{\mathrm{R2}}\delta t + (k + k_{\mathrm{R1}})\,\delta t^2}{m + (c + k_{\mathrm{R2}})\,\delta t + (k + k_{\mathrm{R1}})\,\delta t^2} \tag{3.49}$$

It always exists since each summand in the denominator is positive non-equal to zero for physically relevant parameters (3.4) and stable controller setting (3.8). This supports again the previously made statement.

3.5 Résumé

Algorithms 9.1 to 9.6 and Figures 9.1 to 9.3 in Chapter 9 Fluid–Structure–Control Interaction (pp. 118 ff.) present the three realizations of the iterative partitioned coupling scheme suggested for the numerical experiments in Part II Numerical Experiments (pp. 53 ff.) of this work. In this chapter a much simpler model problem is introduced. It is representative for the convergence behavior and stability of the original multi-degree of freedom simulations in case of structural force control, i.e. if control input u states a Neumann BC of the structure. All three algorithms proof unrestrictedly stable under this model problem requiring physically relevant parameters and stable controller settings. For the linear model problem even an optimal relaxation factor can be determined each time. This is not applicable to the numerical experiments. Therefore, Aitken acceleration is applied for finding the best relaxation parameter in each iteration.

The used model problem is not able to sufficiently represent convergence behavior and stability of multi-degree of freedom simulations subject to structural displacement control, i.e. in cases where control input u states a Dirichlet BC of the structure. First numerical experiments indeed show a drastical influence on the fluid flow around the excited root-point leading to instabilities. Therefore, an advanced model problem has to be developed covering additional properties: The first-order ODE of the fluid subsystem has also to be capable of reproducing internal feedback effects. Those, probably causing the instabilities, arise from the forced excitation mostly working in opposite direction to the freely adjusting oscillations of the structure. Furthermore, the second-order ODE of the structural subsystem has to fully cover the root-point excitation.

So far, analysis of convergence behavior and stability is covered with the autonomous model problem, i.e. with the pure IVP formulation. But the model problem can likely be extended in further analyses: Adding some prescribed periodic disturbance in the fluid subsystem might allow for some explanations on the effects of the parameter scaling highlighted in Chapter 7 Fluid–Structure Interaction (pp. 79 ff.). Measurement of the iteration count with different grades of non-linearity quantified by $f_{1,2,3,4}$ could be performed on the model problem after modifying the linear stiffness ky and viscosity $c\dot{y}$ terms to non-linear ones like for instance $\left(k\dot{y}^{f_1}\right) y^{f_2}$ and $\left(cy^{f_3}\right) \dot{y}^{f_4}$ and employing Aitken acceleration. Comparisons with the multi-degree of freedom cases might allow for classification of its subsystems with respect to $f_{1,2,3,4}$ as well. Thus, further conclusions could be drawn. At this point it should also be noted that only iterations involving the fluid subsystem are regarded to be numerically expensive within this work.

Part II

Numerical Experiments

The world we have made as a result of the level of thinking we have done thus far creates problems that we can't solve at the same level as the level we created them at.

—Albert Einstein (1879–1955)

4 The Experiment

Originally, the present thesis was initiated and motivated by the intention of further assessing co-simulation, i.e. the implementation of partitioned coupling schemes, for large FSCI problems. Once more, it should be noted that FSCI in the context of this work denotes the specific multi-physical problem: interaction of fluid, structure and controller for the structure.

This second part of the thesis takes up exactly on those original intentions: Multi-degree of freedom simulations, hereinafter referred to as numerical experiments, are performed. Their main objective is investigating proposed FSCI schemes in a multi-degree of freedom environment for verifying unrestricted stability concluded with a single-degree of freedom model problem in Chapter 3 Model Problem (pp. 32 ff.). The addressed schemes are presented in Algorithms 9.1 (p. 123) to 9.6 (p. 128) along with Figures 9.1 (p. 120) to 9.3 (p. 122) in Chapter 9 Fluid–Structure–Control Interaction (pp. 118 ff.).

A secondary goal is the demonstration of exclusive basic principles in control theory. Especially, limitations of applied simple control strategies are explored by stressing the assumption of linear dynamics. This is accomplished within the numerical experiments by a parameter scaling with the factor q. It is introduced at a later stage.

Consideration and rejection of various experimental setups in the beginning of this work finally converged to the one setup illustrated by Figure 4.1. It shows a modification of the well-known Turek benchmark (Turek and Hron 2006) which itself is based on Wall and Ramm (1998) and Wall (1999). As originally mere FSI benchmark with a circular cylinder it is adapted to a full computational FSCI experiment. Furthermore, the circular cylinder is replaced by a square one. Section 2.3 Phenomenology of Vortex Shedding

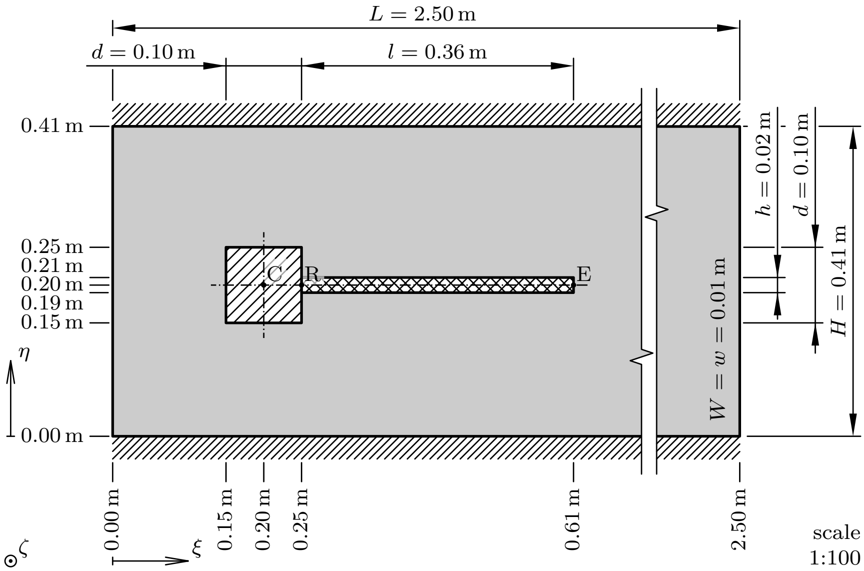

Figure 4.1 Setup of the numerical experiments including dimensions.

on Cylinders (pp. 27 ff.) provides background information.

The final two-dimensional setup attaches an elastic flag of dimensions $l \times h$ to the rigid square cylinder of diameter d. This structure is by intention placed non-symmetrically in a laminar incompressible channel flow. The channel has dimensions $H \times L$. In Figure 4.1 the character C, R and E mark the center of the square cylinder, the root- and the end-point of the flag, respectively.

First of all, the physics of pure FSI with the given setup is described. Figure 4.2 shows an example. For FSI experiments the root-point attachment of the elastic flag is constantly fixed. As soon as the channel flow exceeds a certain critical Reynolds number, periodic vortex shedding from the cylinder is setting in. For details on this phenomenon it is again referred to Section 2.3 Phenomenology of Vortex Shedding on Cylinders (pp. 27 ff.) and therein especially to Figure 2.8 (p. 30). The emerging high and low pressure regions are washed downstream with the main flow (see especially Figure 4.2b). At certain points they hit the elastic flag forcing it to oscillate. Those structural motions in turn affect the fluid flow and linked characteristic quantities like e.g. the vortex shedding frequency. Therefore, data like in Figure 2.8 (p. 30) for the pure square cylinder anyway can only state approximate values in case of FSI due to attachment and motion of the flag. Pure FSI is investigated as sub-problem of FSCI within Chapter 7 Fluid–Structure Interaction (pp. 79 ff.).

Full FSCI differentiates from FSI as described above in a closed-loop

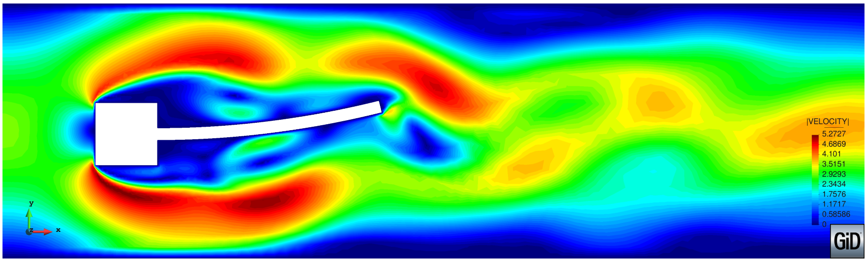

(a) Velocity field.

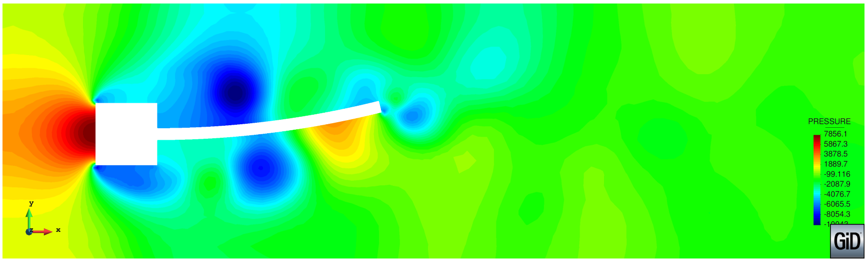

(b) Pressure field.

Figure 4.2 Example of FSI with low-fidelity structural (CSM) subsystem and parameter scaling $q = 10^1$ at $t = 14.73\,\mathrm{s}$.

controller actively influencing the dynamics of the structure. Its object is suppressing or at least reducing the oscillation amplitude at end-point E. Displacement and force control of the structure are distinguished. In displacement control, control input u denotes a Dirichlet BC at point R, i.e. it acts as root-point excitation. Originally intended, the complete simulation framework already provides the implementation of displacement control. But due to encountered difficulties presented later investigations are for now limited to FSCI with force control. This implies control input u denotes a Neumann BC, i.e. the structure is influenced simply in terms of a prescribed force. The attachment of the flag at point R stays constantly fixed similar to FSI. FSCI is extensively presented in Chapter 9 Fluid–Structure–Control Interaction (pp. 118 ff.).

It is stressed that in the following presented and used spatial and temporal discretizations are knowingly chosen rather rough. An outcome of physically meaningful numbers can therefore by no means be expected. This is also emphasized by the mesh convergence studies seen in Figures 5.3 (p. 61) and 6.3 (p. 71). Nevertheless, the main dynamic phenomenons decisive with respect to this work are captured while minimizing the numerical effort.

The remainder of this part can be outlined as follows: Chapters 5 The Fluid (CFD) Subsystem (pp. 57 ff.) and 6 The Structural (CSM)

Subsystem (pp. 68 ff.) give detailed descriptions of the fluid (CFD) and structural (CSM) subsystems. Chapter 7 Fluid–Structure Interaction (pp. 79 ff.) couples of both subsystems to the FSI. Resultant findings are needed to derive the closed-loop controller subsystem (CLC) in Chapter 8 The Controller (CLC) Subsystem (pp. 94 ff.) which is in Chapter 9 Fluid–Structure–Control Interaction (pp. 118 ff.) finally coupled to the FSI subsystems to the full FSCI.

5 The Fluid (Computational Fluid Dynamics) Subsystem

An intrinsic advantage of co-simulation – coupled approaches – is the modularity the method necessarily implies. Partitioning the multi-physics system into single-physics subsystems, exchanging information via common interfaces, allows separate consideration at first. Thus, each physical field or subsystem can be designed, modeled, implemented, validated and evaluated on its own. Also the application of different fidelity models is unproblematic. Afterwards the subsystems can again be coupled together step-by-step to the multi-physical problem. This procedure can also include the coupling of pseudo-subsystems missing own dynamics and sending only well-defined information for testing of either specific subsystems or the coupling logic. Finally, the real physical subsystems are used. Further details on this extensively followed gradual procedure will be presented in Chapter 9 Fluid–Structure–Control Interaction (pp. 118 ff.).

The previously mentioned modularity of coupled approaches also reflects in the structure of this and subsequent chapters. The subsystems will first be introduced in an isolated manner and then coupled together to FSI and FSCI simulations. This chapter covers now all aspects on the fluid subsystem. In the presented numerical experiments its dynamics are dominating the solution. It is also the most expensive one in terms of modeling and numerical effort. Fluid and computational fluid dynamics (CFD) as well as subsystem, client and model are used synonymously within this work.

The fluid (CFD) subsystem covers the channel flow which is modeled by the Navier-Stokes equations (NSE) along with incompressible Newtonian fluid of constant density ρ_F and constant kinematic viscosity ν_F. Situated in the laminar regime turbulence can be neglected. Shape and dimensions of the resulting fluid domain can again be found in Figure 4.1 (gray area, p. 54). The more detailed configuration including the BC's is illustrated by Figure 5.1. Those are treated in the following.

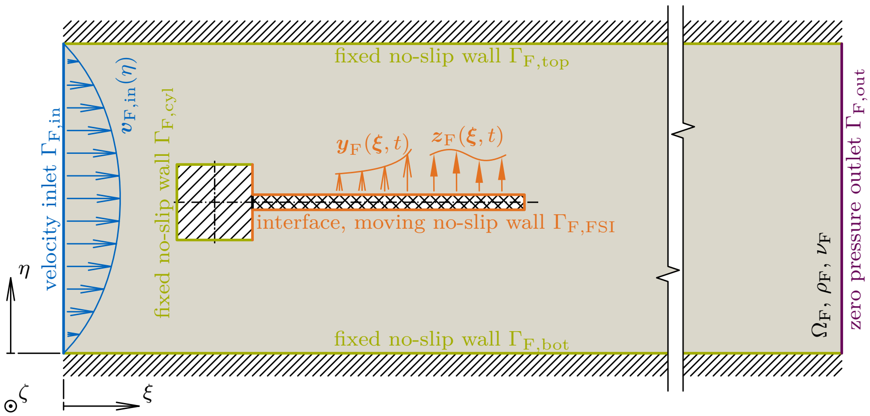

Figure 5.1 FLUID (CFD) SUBSYSTEM OF NUMERICAL EXPERIMENTS.

Top wall $\Gamma_{\mathrm{F,top}}$ and bottom wall $\Gamma_{\mathrm{F,bot}}$ constitute the channel's sidewalls as well as the non-interface part of the surface of the rigid cylinder $\Gamma_{\mathrm{F,cyl}}$ are specified as non-moving no-slip walls. The remaining part of the cylinder surface together with the surface of the elastic flag denotes the actual FSI interface $\Gamma_{\mathrm{F,FSI}}$ which is set as moving no-slip wall. Its motion is given with the displacements $\boldsymbol{y}_{\mathrm{F}}$ respectively the velocities $\dot{\boldsymbol{y}}_{\mathrm{F}}$. Actual driving force of the channel flow is the time-constant velocity profile

$$\boldsymbol{v}_{\mathrm{F,in}}(\eta) = \begin{pmatrix} \frac{3}{2} v_{\mathrm{in}} 4 \frac{\eta}{H} \left(1 - \frac{\eta}{H}\right) \\ 0 \end{pmatrix} = \begin{pmatrix} v_{\max} 4 \frac{\eta}{H} \left(1 - \frac{\eta}{H}\right) \\ 0 \end{pmatrix} \tag{5.1}$$

prescribed at the channel inlet $\Gamma_{\mathrm{F,in}}$ along with the zero-mean value pressure outlet $\Gamma_{\mathrm{F,out}}$. The initial and boundary value problem (IBVP) of the fluid is finally completed by the IC's zero-velocity and zero-pressure, i.e. $\boldsymbol{x}_{\mathrm{F}}(\boldsymbol{\xi}, t=0) = \mathbf{0}$ throughout the entire domain Ω_{F}. Therefore, also the disturbances disappear at the beginning, i.e. $\boldsymbol{z}_{\mathrm{F}}(\boldsymbol{\xi}, t=0) = \mathbf{0}$.

Turek and Hron (2006) propose three different parameter settings for the fluid in their benchmark which are also adopted here. They are summarized in Table 5.1. Settings CFD1 and CFD2 imply under-critical Reynolds numbers. No vortex shedding is present leading to a steady-state like infinite solutions. Setting CFD3 with an over-critical Reynolds number on the contrary shows vortex shedding, i.e. strongly unsteady fluid flow. The basic solution behavior and snapshots of the resulting fields can be seen in Figures 5.6/5.7 and 5.8/5.9, respectively. For the further FSI and FSCI simulations within this work only parameter setting CFD3 is considered.

Table 5.1 Parameter settings for fluid (CFD) subsystem.

parameter	*setting and value*			*unit*
	CFD1	*CFD2*	***CFD3***	
ρ_{F}	1000	1000	**1000**	kg/m^3
ν_{F}	0.001	0.001	**0.001**	m^2/s
v_{in}	0.2	1	**2**	m/s
Re	20	100	**200**	1

Initially, this work was started using the open source tool OpenFOAM 2.2 (Weller 2004) for implementing the fluid (CFD) subsystem. Its solvers are based on a segregated finite volume (FV) formulation with BDF2 time integration. Among other things obsolescence, missing accuracy and unresolved bugs, but especially instabilities of flow and mesh solvers and missing spatial consistency with FE-formulated structures led to exclusion of OpenFOAM as the fluid solver. Nevertheless, temporal consistency is met. Furthermore, it should be noted that a block-structured mesh as optimal prerequisite was used (compare Sicklinger, Lerch, Wüchner, and Bletzinger (2015)).

Throughout this work the open source tool Kratos Multi-Physics (Dadvand and Rossi 2007a,b) is used by now. It is developed at the Centre Internacional de Mètodes Numèrics a l'Enginyeria (International Center for Numerical Methods in Engineering, CIMNE) of the Universitat Politècnica de Catalunya (Technical University of Catalonia, UPC) in Barcelona (Spain), a partner of the Chair of Structural Analysis. Three appropriate solvers are currently available. Considering accuracy, temporal consistency with BDF2, spatial consistency with FE-formulated structures and the capability of providing additional derivative information needed in the IJCSA (Sicklinger, Belsky, Engelmann, Elmqvist, Olsson, Wüchner, and Bletzinger 2014; Sicklinger 2014) the solver based on a coupled finite element (FE) formulation with variational multiscale (VMS) stabilization and BDF2 time integration is chosen. Some further impacts regarding the last argument and IJCSA will be discussed in the final Part III Conclusion and Outlook starting on page 162. Convergence criteria for velocities and pressures of relative 10^{-9} and absolute 10^{-12} are specified.

Substantial problem of finite element (FE) formulated incompressible flows are numerical instabilities "which are a consequence of the incompressibility constraint and the effect of the convective term in the equations for convection-dominated flows" (Dalmau 2016, Subsection 1.1.2, pp. 3, 4). At solver level this appears as a zero block in the equation system which laxly said has to be filled up. Mathematically this is reached by stabilizing the fluid formulation. As already stated above this is done with the VMS method. (Dalmau 2016) gives with paragraph 1 on page 7 a brief introduction:

> "Variational multiscale (VMS) methods [...] provide a theoretical framework for the design of stabilized finite element formulations based on the separation of the solution into resolved and unresolved parts, which is achieved through the definition of large scale and small scale solution spaces. The projection of the original equations onto the large scale space gives an equivalent problem that depends on the small scale variables, while the projection of the original equations onto the small scale space is used to motivate a model for the effect of the small scale variables, which are not solved, to the large scale solution."

For further details on the FE-formulation and stabilization of fluids the interested reader is referred to literature. In particular, the derivations of the used FE-formulation and VMS stabilization are for instance found in Chapter 2 Variational Multiscale Stabilization for Turbulent Flow Problems (pp. 7 ff.) of Dalmau (2016) and Rossi and Dadvand (2015).

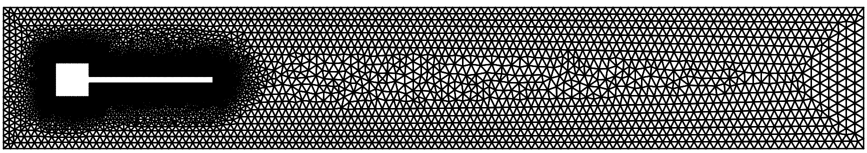

(a) COMPLETE VIEW.

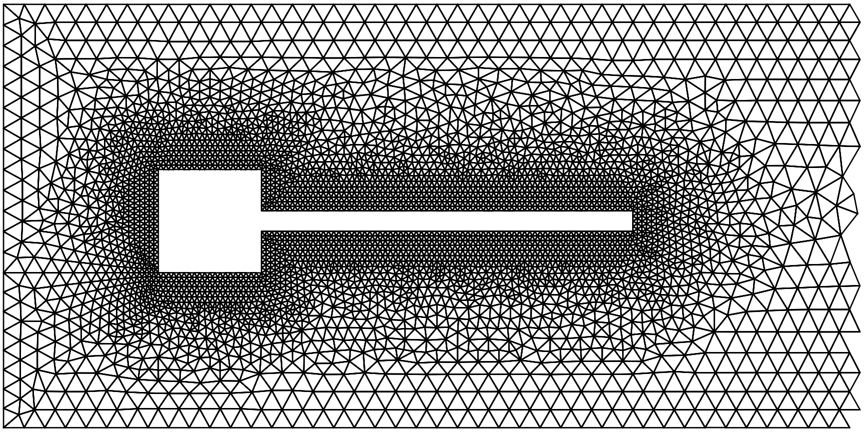

(b) ZOOMED VIEW.

Figure 5.2 MESH FOR FLUID (CFD) SUBSYSTEM.

The pre-processing step meshing of the fluid domain Ω_F is done using the pre- and post-processing tool GiD ((unknown) 1998) as well as the pre-processing tool Pointwise (Chawner and Steinbrenner 1984). 10′515 3-node (2D) triangular elements (triangles) with 5′505 nodes form the resulting unstructured mesh shown in Figure 5.2. Its elements' edge sizes grow from 0.005 m at the inner boundaries of cylinder and flag to 0.02 m at the outer boundaries of top wall, bottom wall, inlet and outlet. The mesh convergence study presented in Figure 5.3 clearly shows the insufficient resolution of the fluid domain which was chosen in order to keep the numerical costs to a minimum. Consequently, outcome of the simulations can not represent physically meaningful numbers. Nevertheless, the interesting fundamental physical phenomenons are captured. Therefore, conclusions on the ability of the applied approach and schemes can still be drawn. The transferability of those statements to more detailed and in consequence numerically more expensive simulations is guaranteed.

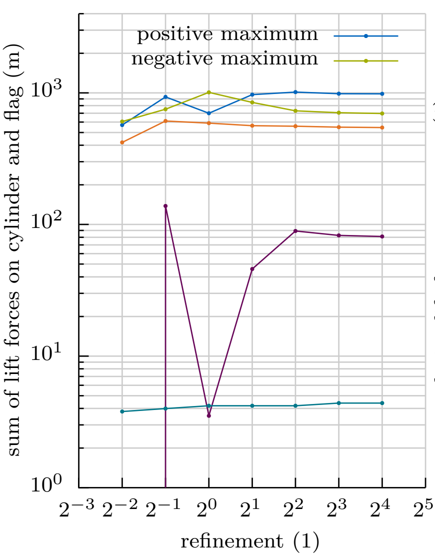

(a) Sums of lift forces on cylinder and flag.

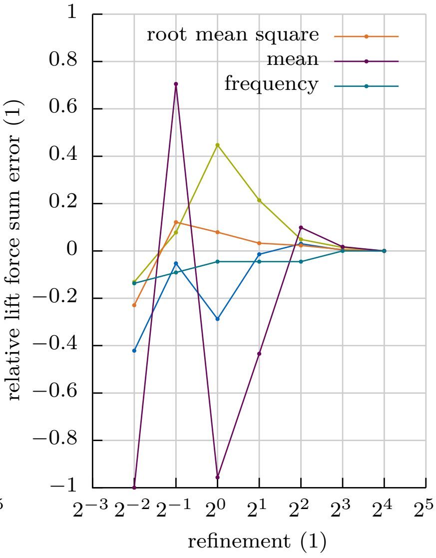

(b) Relative lift force sum errors.

Figure 5.3 Mesh convergence study for fluid (CFD) subsystem.

For performing FSI and FSCI simulations with the fluid (CFD) model presented thus far the ability of deforming the FSI interface $\Gamma_{F,FSI}$ still needs to be implemented. An embedded or an arbitrary Lagrangian-Eulerian (ALE) formulation is possible. This work employs the second one due to better resolution of surface phenomenons at the obstacle cylinder with elastic flag. Herein, the deformation of a boundary is enabled by moving the boundary nodes and distributing this deformation over the complete fluid domain by accordingly deforming the remainder of the fluid mesh. This task is handled by a mesh updating scheme. The ones used here are the linear and non-linear version of the structural similarity mesh solver presented in Mini (2014, especially Section 3.2 Treating the Mesh Similar to a Solid, pp. 61 ff.). Those treat the mesh similar to a linear respectively non-linear solid (pseudo-structure). Both apply the BDF2 for recalculating the velocities at the FSI interface. Therefore, temporal consistency in the co-simulations is also retained at this point. For the resulting mesh displacement field in Ω_F homogeneous Dirichlet BC's are specified at all boundaries except the FSI interface $\Gamma_{\mathrm{F,FSI}}$. Here inhomogeneous Dirichlet BC's result naturally from the prescribed interface displacements $\boldsymbol{y}_\mathrm{F}$. An example of a resulting mesh deformation is given in Figure 5.4. Associated velocity and pressure fields are shown in Figure 4.2 (p. 55).

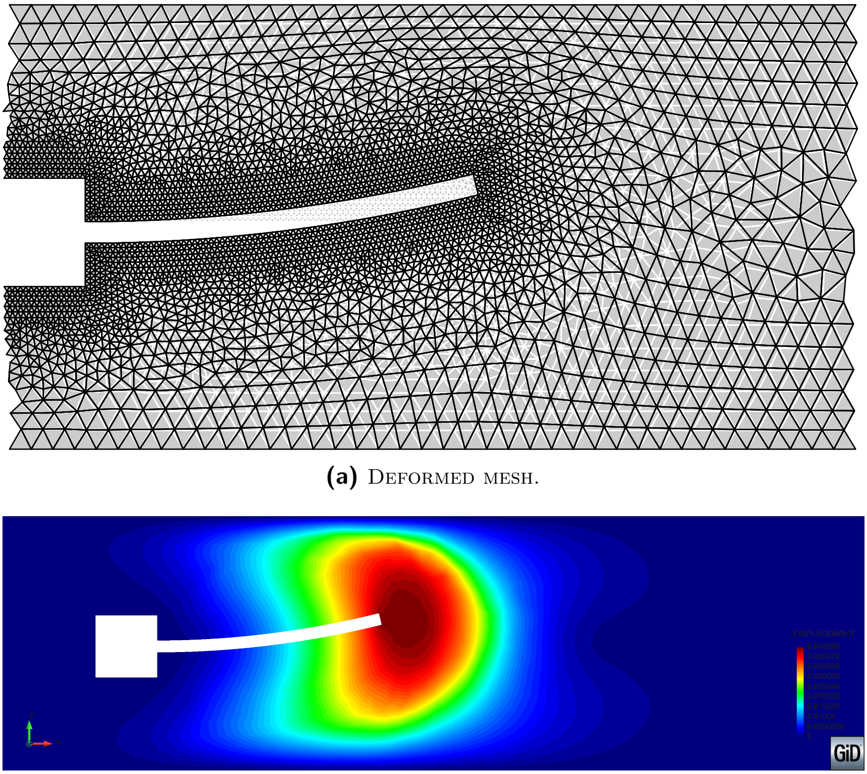

(a) DEFORMED MESH.

(b) MESH DISPLACEMENT FIELD.

Figure 5.4 EXAMPLE OF FLUID (CFD) MESH DEFORMATION IN FSI WITH LOW-FIDELITY STRUCTURAL (CSM) SUBSYSTEM AND PARAMETER SCALING $q = 10^1$ AT $t = 14.73\,\mathrm{s}$.

The coupling at the final stage of the co-simulation only sees a black box fluid (CFD) subsystem as illustrated by Figure 5.5. It is interacting with its environment via input $\boldsymbol{U}_{\mathrm{F}} = \boldsymbol{y}_{\mathrm{F}}$ prescribing the deformation (displacement) of the interface $\Gamma_{\mathrm{F,FSI}}$ and output $\boldsymbol{Y}_{\mathrm{F}} = \boldsymbol{z}_{\mathrm{F}}$ giving the fluid reaction (disturbance) at the FSI interface $\Gamma_{\mathrm{F,FSI}}$. Internal dynamics of the fluid, represented by the state variable $\boldsymbol{X}_{\mathrm{F}} = \boldsymbol{x}_{\mathrm{F}}$ denoting all velocities $\boldsymbol{v}$ and pressures $\boldsymbol{p}$ in the complete domain Γ_{F}, and other implementation details are hidden inside this black box.

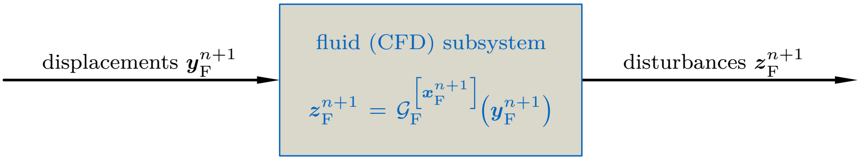

Figure 5.5 Block diagram of fluid (CFD) subsystem.

For the sake of completeness also the comparisons made between the four mentioned solvers are presented here. They can be seen in Figures 5.6 and 5.7. Therein, it can also be recognized that the applied solver shows satisfying accuracy if taking the solution of the coupled FE-formulated VMS-stabilized WBZ–α-time integrated solver as a reference. Snapshots of associated fields resulting from this solver can be seen in Figures 5.8 and 5.9.

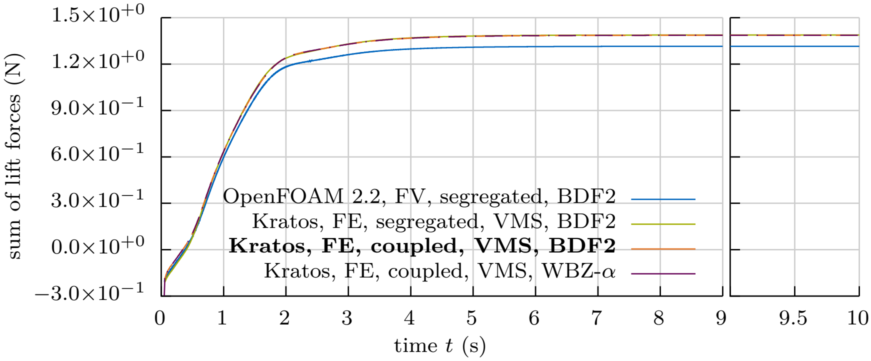

(a) CFD1 TEST.

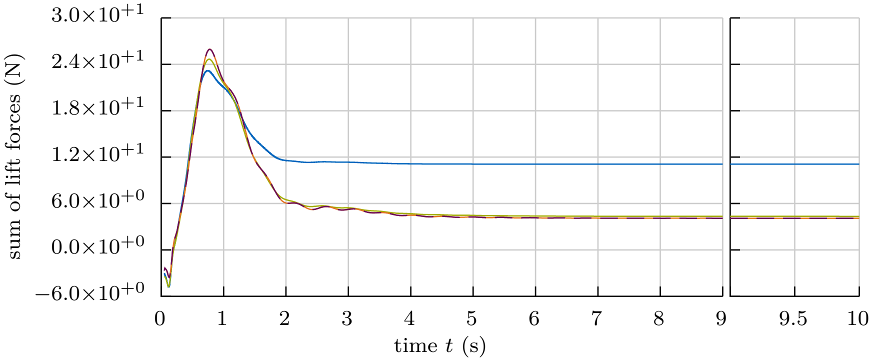

(b) CFD2 TEST.

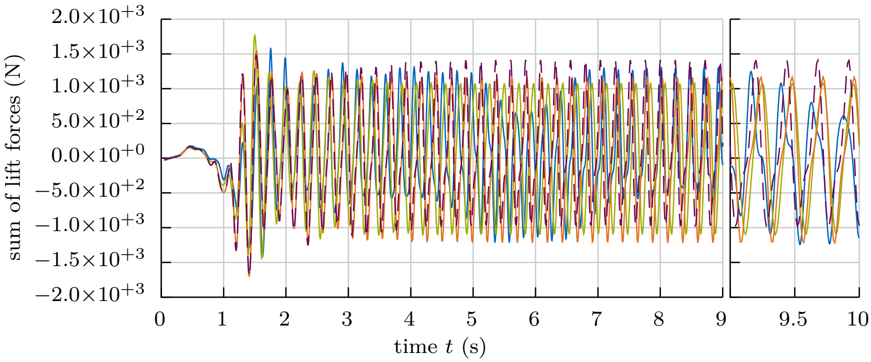

(c) CFD3 TEST.

Figure 5.6 SUM OF LIFT FORCES ON CYLINDER AND FLAG IN CFD TESTS FOR COMPARISON OF CFD SOLVERS.

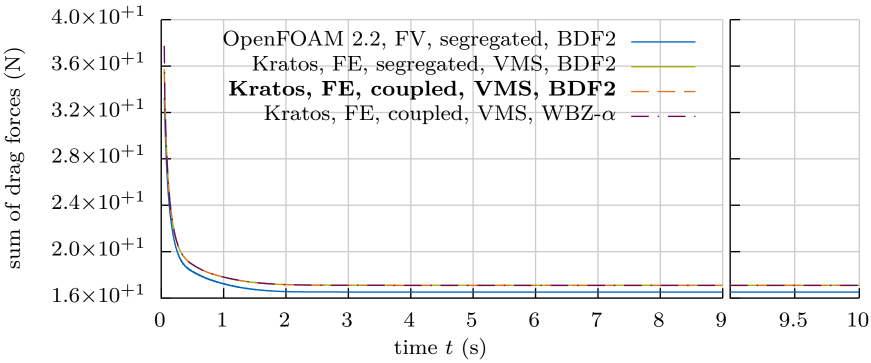

(a) CFD1 test.

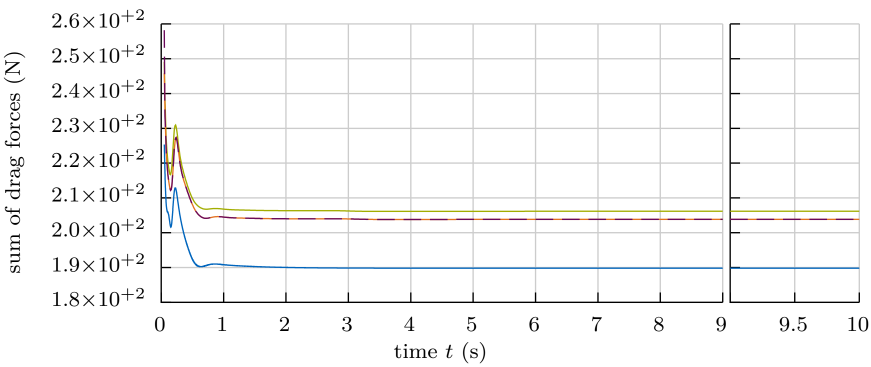

(b) CFD2 test.

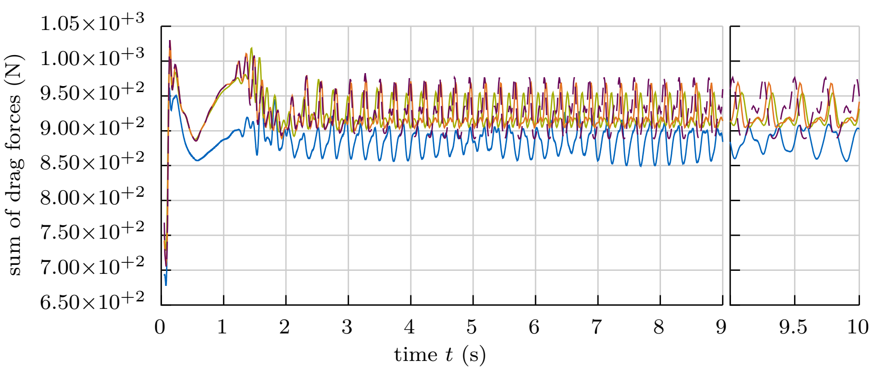

(c) CFD3 test.

Figure 5.7 Sum of drag forces on cylinder and flag in CFD tests for comparison of CFD solvers.

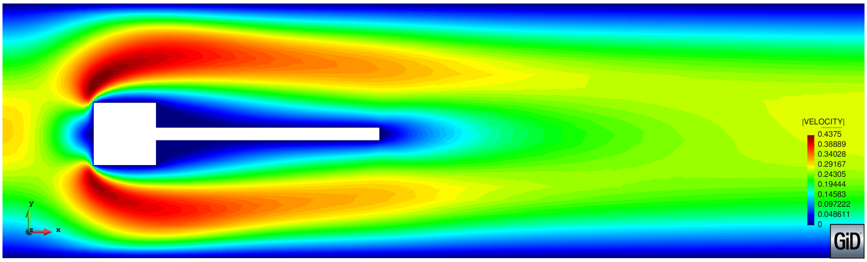

(a) CFD1 TEST.

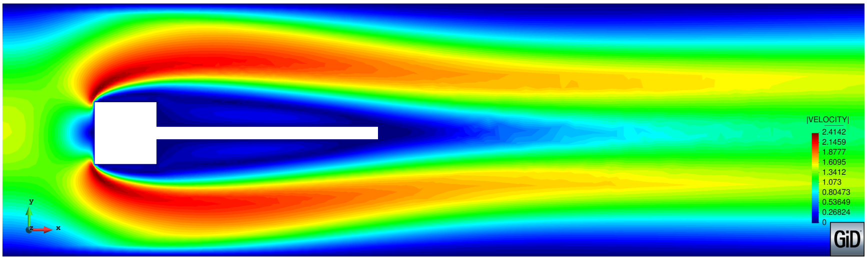

(b) CFD2 TEST.

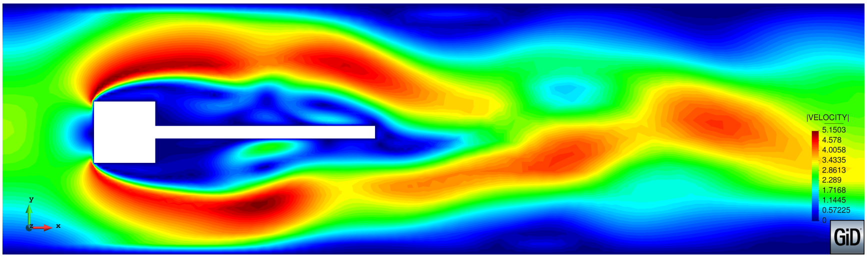

(c) CFD3 TEST.

Figure 5.8 VELOCITY FIELDS OF CFD TESTS WITH USED FLUID (CFD) SOLVER AT $t = 9.96\,\mathrm{s}$.

(a) CFD1 test.

(b) CFD2 test.

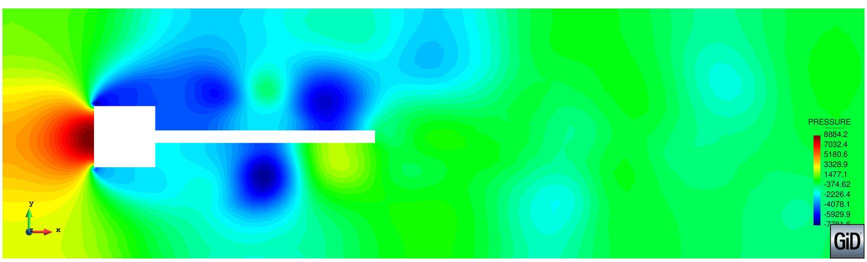

(c) CFD3 test.

Figure 5.9 Pressure fields of CFD tests with used fluid (CFD) solver at $t = 9.96\,\mathrm{s}$.

Any intelligent fool can make things bigger, more complex, and more violent. It takes a touch of genius – and a lot of courage to move in the opposite direction.

—Ernst Friedrich Schumacher (1911–1977)

6 The Structural (Computational Solid Mechanics) Subsystem

The following chapter is presenting full details on the structural (CSM) subsystem. It states the second module for the FSI and FSCI co-simulations performed in this work. In comparison to the fluid (CFD) subsystem presented in the previous chapter this one is far less expensive especially in terms of modeling and numerical effort. Equivalently, also here structure, solid and computational solid mechanics (CSM) as well as subsystem, client or model are used synonymously.

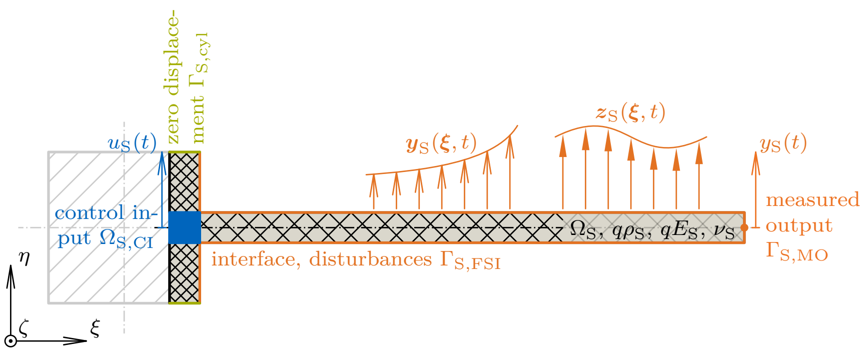

Figure 6.1 High-fidelity structural (CSM) subsystem of the numerical experiments.

The structural subsystem is modeling the physics of the elastic flag attached to the rigid cylinder. Strictly speaking, two distinct CSM models are developed and applied: a high-fidelity multi-degree of freedom (MDoF) finite element (FE) model complying exactly with the originally suggested

CSM model of Turek and Hron (2006) and a low-fidelity single degree of freedom (SDoF) based one with distribution of its single displacement DoF over the actual structural domain along with the control input. Further details will follow.

In pure FSI the structure is subject to disturbances (forces) $\boldsymbol{z}_{\mathrm{S}}(\boldsymbol{\xi}, t)$ at the FSI interface stemming from the fluid. They are causing structural deformations. In FSCI an additional control input $u_{\mathrm{S}}(t)$ determined by a closed-loop controller (CLC) tries to compensate those deformations. It acts as root-point excitation on the flag. Therefore, both models, low- and high-fidelity, already include the necessary implementations for displacement control. In the low-fidelity CSM model an additional so-called u-output factor f_u is introduced: While the structure undergoes the exact control input $1 \cdot u_{\mathrm{S}}(t)$ in its dynamics the fluid on the other hand sees the displacements of a scaled control input $f_u \cdot u_{\mathrm{S}}(t)$, i.e. f_u scales the impact of the incoming control input on the actual outgoing displacements as seen by the fluid. Specifying $f_u = 0$ results in pure force control: Control input $u_{\mathrm{S}}(t)$ is fully acting on the structure without causing any related displacements influencing the fluid. It should also be pointed out that the FSI interface next to the wet surface of the flag contains some parts of the cylinder surface in order to realize the root-point excitation in combination with an ALE-formulation of the fluid.

Original plannings at the beginning of the thesis also scheduled the implementation of additional low-fidelity CSM models: transitional single and triple degree of freedom and rotational single and triple degree of freedom. Those were rejected. In the following at first the final high-fidelity MDoF model is introduced and afterwards the low-fidelity SDoF model is derived from that.

6.1 High–Fidelity Model

Figure 6.1 shows the detailed configuration of the high-fidelity structural (CSM) model including all BC's. Its domain Ω_{S} consists of two distinct parts: The main one (coarsely cross-hatched) corresponds to the elastic flag. It is characterized by compressible Saint Venant-Kirchhoff material with constant Young's modulus qE_{S}, constant Poisson's Ratio ν_{S} and constant density $q\rho_{\mathrm{S}}$ in the undeformed configuration. The parameter scaling factor q included in mass and stiffness is needed for the parameter scaling tests performed along with the FSI simulations. They are specified in Chapter 7 Fluid–Structure Interaction (pp. 79 ff.). To some extend the structural domain Ω_{S} also consists of a part of the originally rigid cylinder (finely crosshatched). This serves for continuous distribution of the root-point excitation along the back side of the cylinder to match the ALE-formulation of the fluid. Material parameters are changed here to zero Poisson's Ratio $\nu_{\mathrm{S}} = 0$ to neglect buckling deformations of the cylinder backsides in ξ-direction and zero density $q\rho_{\mathrm{S}} = 0$ to exclude inertial effects like micro-oscillations in that part of the domain. Therefore, it states some kind of pseudo-material. Corresponding dimensions and the intentionally non-symmetric placement in the channel flow can be seen in Figure 4.1.

Homogenous Dirichlet BC's at top and bottom of the cylinder $\Gamma_{\mathrm{S,cyl}}$ along with inhomogenous ones $[0, u_{\mathrm{S}}(t), 0]^{\mathrm{T}}$ at cylinder part $\Omega_{\mathrm{S,CI}}$ support the modeling of the root-point excitation and its linear distribution along the backside of the cylinder. Neumann BC's at the FSI interface $\Gamma_{\mathrm{S,FSI}}$ are given by the disturbances (forces) $\boldsymbol{z}_{\mathrm{S}}(\boldsymbol{\xi}, t)$ coming from the fluid. Zero-displacement and zero-velocity IC's in the entire domain Ω_{S}, i.e. $\boldsymbol{x}_{\mathrm{S}}(\boldsymbol{\xi}, t = 0) = \mathbf{0}$ finally complete the IBVP. Therefore, also interface displacements and measured output vanish at the beginning $\boldsymbol{y}_{\mathrm{S}}(\boldsymbol{\xi}, t = 0) = \mathbf{0}$ and $y_{\mathrm{S}}(t = 0) = 0$.

Table 6.1 Parameter settings for high-fidelity structural (CSM) subsystem.

parameter	*value*			*unit*
	CSM1	***CSM2***	*CSM3*	
ρ_{S}	1000	**1000**	1000	$\mathrm{kg/m^3}$
E_{S}	1.4	**5.6**	1.4	$10^6\ \mathrm{N/m^2}$
ν_{S}	0.4	**0.4**	0.4	1
q	—	$\mathbf{10^{6\ldots-3}}$	—	1
g	2	**2**	2	$\mathrm{m/s^2}$

In accordance with Turek and Hron (2006) three different parameter settings CSM1, CSM2 and CSM 3 are used. They are summarized in Table 6.1. Figure 6.10 at the end of this chapter shows results for CSM model tests with those parameter settings as suggested by Turek and Hron (2006): CSM1 and CSM2 denote static tests while CSM3 is dynamic. In each the structure is subject to self load with gravity g missing any fluid. Only parameter setting CSM2 will be considered further for the low-fidelity CSM model, FSI and FSCI.

Originally, the FE tool Carat++ ((unknown) 2008) developed by the Chair of Structural Analysis at the Technical University of Munich was intended for use. Missing possibilities to implement inhomogeneous BC's next to other difficulties however led to a change to the open source FE tool Kratos Multiphysics (Dadvand and Rossi 2007a,b) which is better fitting these purposes. In expectation of large structural deformations demanding a geometrical non-linear formulation fully integrated 4-noded (2D) total Lagrangian displacement elements are chosen. Until now only implicit time integration with the generalized–α method is available harming temporal consistency. Spatial consistency along with the FE-formulated fluid however

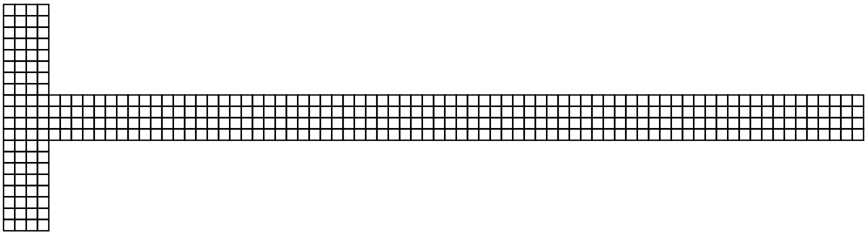

Figure 6.2 Mesh for high-fidelity structural (CSM) subsystem.

is met. Convergence criteria for displacements and residuals of relative 10^{-9} and absolute 10^{-12} are specified. 465 nodes and 368 4-node (2D) quad elements (quadrilaterals) of equal size 0.005 m × 0.005 m form the used structured mesh presented in Figure 6.2. A mesh convergence study is performed with the parameter setting CSM2. Corresponding results in Figure 6.3 show errors of around 5 % for positive and negative maximum, root mean square, negative mean and frequency. Thus, it can be concluded that the mesh has sufficient resolution for not only covering basic effects but also for returning physically meaningful numbers.

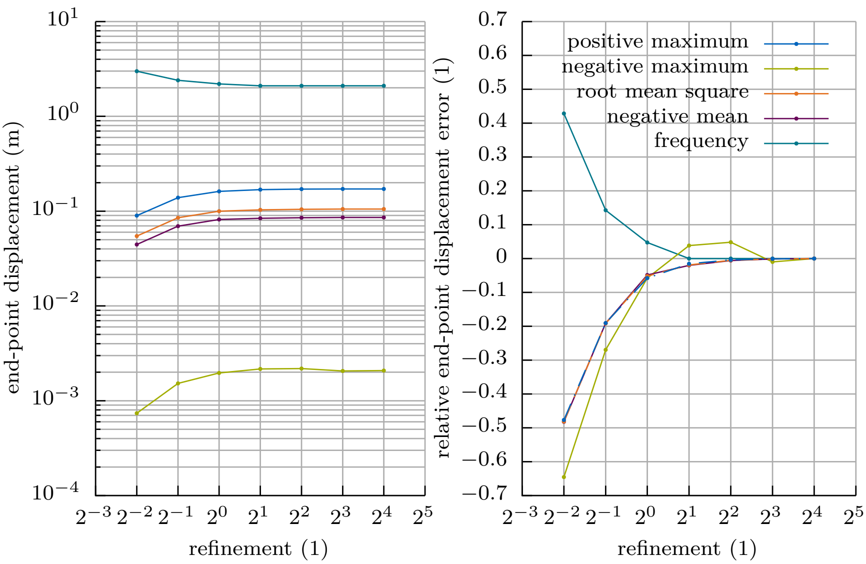

(a) End-point displacement.

(b) Relative error of end-point displacement.

Figure 6.3 Mesh convergence study for high-fidelity structural (CSM) subsystem.

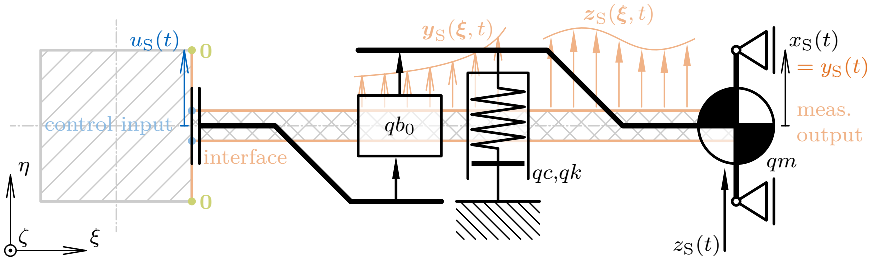

Figure 6.4 Low-fidelity structural (CSM) subsystem of the numerical experiments.

6.2 Low–Fidelity Model

A low-fidelity SDoF CSM model as illustrated in Figure 6.4 is derived from the previously introduced high-fidelity MDoF model. Its main purpose is next to a guarantee of structural and temporal consistency to have a well-defined structural behavior from control theory's perspective and to gain better insights in the underlying dynamical effects in FSI and FSCI. This will partly be taken up again in the introductory words of Chapter 8 The Controller (CLC) Subsystem (pp. 94 ff.). The low-fidelity structure is principally defined by two displacements: the single state $x_S(t)$ stating also the displacement of end-poind E $y_S(t) = x_S(t)$ and the control input $u_S(t)$ defining the displacement at root-point R. The dynamics of $x_S(t)$ are based on a simple linear second-order ODE and $u_S(t)$ is calculated by the controller. Therefore, no spatial affiliation is involved. The original BC's are included in the simplification process. Distributed interface displacements $\boldsymbol{y}_S(\boldsymbol{\xi}, t)$ between R and E finally seen by the fluid are extrapolated by a quadratic ansatz. Consequently, the low-fidelity CSM model only needs a surface mesh seen in Figure 7.2. The disturbances $\boldsymbol{z}_S(\boldsymbol{\xi}, t)$ distributed over the FSI interface are integrated to one single disturbance $z_S(t)$ acting on the replacing SDoF system. IC's are accordingly set to zero, i.e. $x_S(t=0) = 0$ and $\dot{x}_S(t=0) = 0$. Therefore, again also $\boldsymbol{y}_S(\boldsymbol{\xi}, t=0) = \boldsymbol{0}$ and $y_S(t=0) = 0$. The impact of $u_S(t)$ (displacement or force control) is adjusted by the already mentioned u-output factor f_u. It is set to zero for pure force control. The subsystem is implemented in form of an own C++ dynamics code providing BDF2 and generalized–α time integration.

The low-fidelity CSM model reduces the real physics to

$$(qm)\ddot{x}_S + (qk)x_S = (qb_2)\,\ddot{u}_S + (qb_0)\,u_S + z_S \tag{6.1}$$

where q denotes the parameter scaling factor for the subsequent parameter scaling tests. The single state $x_S(t)$ is directly stating the displacement of end-point E and therefore also corresponds to the measured output $y_S = x_S$

required by the controller. The concentrated mass m and spring stiffness k substitute the real system mass and system stiffness, respectively. The concentrated input coefficients b_2 and b_0 associated to $u_\mathrm{S}(t)$ replace the real root-point excitation.

The complete spatial distribution of the interface displacements $\boldsymbol{y}_\mathrm{S}(\boldsymbol{\xi}, t)$ is determined by the root-point excitation $u_\mathrm{S}(t)$ at position $\boldsymbol{\xi}_\mathrm{R}$ and end-point displacement respectively state $x_\mathrm{S}(t)$ at $\boldsymbol{\xi}_\mathrm{E}$. Along the baseline (dotdashed straight connection of R and E in the undeformed configuration) a quadratic ansatz in ξ-direction

$$y_\mathrm{S}(\xi, t) = A(t)\,(\xi - \xi_\mathrm{R})^2 + B(t)\,(\xi - \xi_\mathrm{R}) + C(t) \tag{6.2a}$$

is applied. Appropriate Dirichtlet BC's

$$y_\mathrm{S}(\xi = \xi_\mathrm{R}, t) = f_u u_\mathrm{S}(t) \tag{6.2b}$$

and

$$y_\mathrm{S}(\xi = \xi_\mathrm{R} + l, t) = x_\mathrm{S}(t) \tag{6.2c}$$

directly follow from the definition. f_u is the mentioned u-output factor controlling the influence of the control input on the interface displacements. Only vertical movement (η-direction) of the flag along the backside of the cylinder and therefore conservation of the right angle reflects in the Neumann BC

$$y'_\mathrm{S}(\xi = \xi_\mathrm{R}, t) = 0. \tag{6.2d}$$

Inserting all BC's in the ansatz leads to the final spatial distribution

$$\begin{aligned} y_\mathrm{S}(\xi, t) &= \left[1 - \left(\frac{\xi - \xi_\mathrm{R}}{l}\right)^2\right] f_u u_\mathrm{S}(t) + \left[\left(\frac{\xi - \xi_\mathrm{R}}{l}\right)^2\right] x_\mathrm{S}(t) \\ \text{i.e.} \quad y_\mathrm{S}(\xi, t) &= y_u(\xi) f_u u_\mathrm{S}(t) + y_x(\xi) x_\mathrm{S}(t) \end{aligned} \tag{6.2e}$$

along baseline RE with both resulting shape functions $y_u(\xi) = 1 - \left(\frac{\xi - \xi_\mathrm{R}}{l}\right)^2$ and $y_x(\xi) = \left(\frac{\xi - \xi_\mathrm{R}}{l}\right)^2$ plotted in Figure 6.5.

The principle of virtual work (PvW) is formulated with distributed sectional mass $\mu = \rho w h$ and distributed sectional stiffness κ

$$\begin{aligned} \int_{\xi_\mathrm{R}}^{\xi_\mathrm{R}+l} & -\mu \ddot{y}_\mathrm{S}(\xi, t)\delta y_\mathrm{S}(\xi, t) - \kappa y_\mathrm{S}(\xi, t)\delta y_\mathrm{S}(\xi, t)\,\mathrm{d}\xi \\ & + \sum_i z_{\eta\mathrm{S}}(\boldsymbol{\xi}_i, t)\delta y_\mathrm{S}(\xi_i, t) = 0. \end{aligned} \tag{6.3a}$$

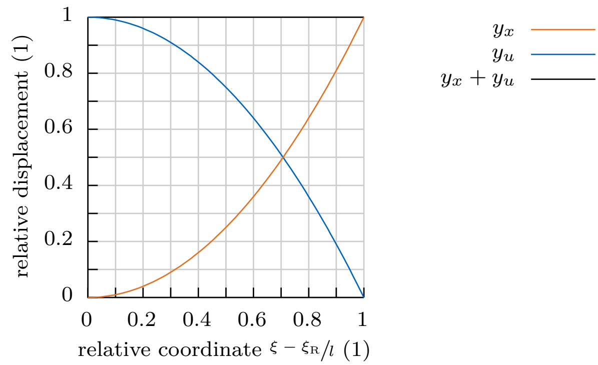

Figure 6.5 SHAPE FUNCTIONS OF LOW-FIDELITY STRUCTURAL (CSM) SUBSYSTEM.

Resolved, this results in

$$\begin{aligned}
&\mu \int_{\xi_R}^{\xi_R+l} y_x^2(\xi)\,\mathrm{d}\xi\ \ddot{x}_S + \kappa \int_{\xi_R}^{\xi_R+l} y_x^2(\xi)\,\mathrm{d}\xi\ x_S \\
&\quad = -\mu \int_{\xi_R}^{\xi_R+l} y_x(\xi) y_u(\xi)\,\mathrm{d}\xi\ \ddot{u}_S \\
&\quad\quad - \kappa \int_{\xi_R}^{\xi_R+l} y_x(\xi) y_u(\xi)\,\mathrm{d}\xi\ u_S \\
&\quad\quad + \sum_i y_x(\xi_i) z_{\eta S}(\boldsymbol{\xi}_i, t) \\
\text{i.e.}\quad &\frac{\mu l}{5}\ddot{x}_S + \frac{\kappa l}{5} x_S \\
&\quad = -\mu \frac{2l}{15}\ddot{u}_S - \kappa \frac{2l}{15} u_S + \sum_i \left(\frac{\xi_i - \xi_R}{l}\right)^2 z_{\eta S}(\boldsymbol{\xi}_i, t)
\end{aligned} \tag{6.3b}$$

what has to be equivalent to Equation (6.1).

Additionally, the stiffness of the low-fidelity flag is obtained from the static displacement of a cantilever beam: For $u_S(t) \equiv 0$ and $z_S(t) \equiv \widehat{z}_S =$ const. the displacement of end-point E is $\widehat{x}_S = \hat{z}_S / \frac{3EI_\xi}{l^3}$ (Gross, Hauger, Schröder, and Wall 2014, Number 6 in Table 4.3, pp. 138–141) which has to be equivalent to $\widehat{x}_S = \frac{\hat{z}_S}{k}$ stemming from Equation (6.1). Therefore, $\kappa = \frac{15EI_\xi}{l^4}$ with the area moment of inertia $I_\xi = \frac{Ewh^3}{12}$ (Gross, Hauger, Schröder, and Wall 2014, Rectangle in Table 4.1, pp. 102, 103).

Thus, parameters and disturbance for the low-fidelity CSM model are finally obtained as

$$m = \frac{\mu l}{5} = \frac{\rho w h l}{5} \tag{6.4a}$$

$$k = \frac{\kappa l}{5} = \frac{3E_\mathrm{S} I_\xi}{l^3} = \frac{E_\mathrm{S} w h^3}{4l^3} \tag{6.4b}$$

$$b_2 = -\frac{2\mu l}{15} = \frac{2\rho w h l}{15} \tag{6.4c}$$

$$b_0 = -\frac{2\kappa l}{15} = -\frac{2E_\mathrm{S} I_\xi}{l^3} = \frac{E_\mathrm{S} w h^3}{6l^3} \tag{6.4d}$$

and

$$z_\mathrm{S}(t) = \sum_i \left(\frac{\xi_i - \xi_\mathrm{R}}{l}\right)^2 z_{\eta\mathrm{S}}(\boldsymbol{\xi}_i, t). \tag{6.4e}$$

Baseline displacement $y_\mathrm{S}(\xi, t)$ has to be projected onto the actual distributed FSI interface seen by the fluid. It is shown in Figure 7.2). As already mentioned two segments have to be distinguished: the back side of the cylinder (vertical left) and the flag surface (horizontal and vertical right).

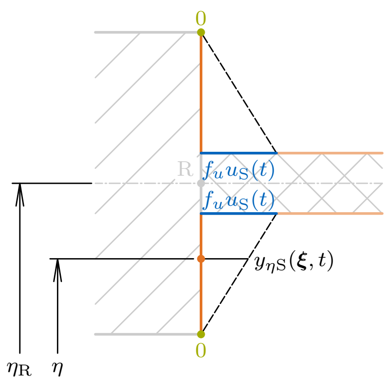

Figure 6.6 Projection of baseline displacement to cylinder surface in low-fidelity structural (CSM) subsystem.

The projection to the cylinder backside is given by linear distributions from $y_\mathrm{S}(\xi_\mathrm{R}, t) = f_u u(t)$ to 0 as illustrated with Figure 6.6. For the upper cylinder backside

$$y_{\eta\mathrm{S}}(\boldsymbol{\xi}, t) = \left[1 - \frac{\eta - \left(\eta_\mathrm{R} + \frac{h}{2}\right)}{\frac{d}{2} - \frac{h}{2}}\right] f_u u_\mathrm{S}(t) \tag{6.5a}$$

and for the lower cylinder backside

$$y_{\eta\mathrm{S}}(\boldsymbol{\xi}, t) = \left[1 - \frac{\left(\eta_\mathrm{R} - \frac{h}{2}\right) - \eta}{\frac{d}{2} - \frac{h}{2}}\right] f_u u_\mathrm{S}(t). \tag{6.5b}$$

Displacements in ξ-direction are blocked

$$y_{\xi\mathrm{S}}(\boldsymbol{\xi}, t) = 0. \tag{6.5c}$$

The displacements of all points on the cylinder backside are given with $\boldsymbol{y}_{\mathrm{S}} = [y_{\xi\mathrm{S}}, y_{\eta\mathrm{S}}]^{\mathrm{T}}$.

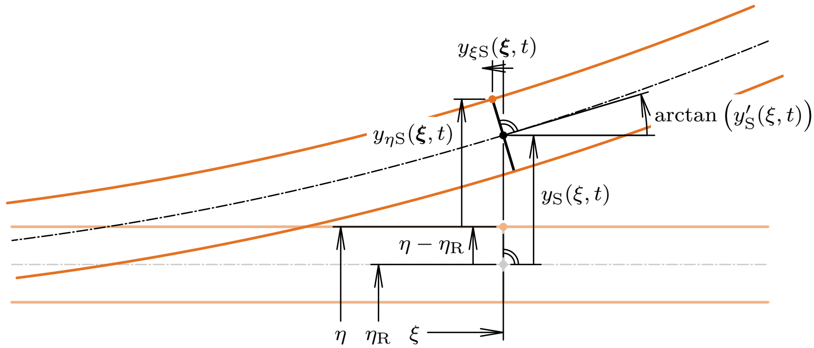

Figure 6.7 Projection of baseline displacement to flag surface in low-fidelity structural (CSM) subsystem.

The projection to the flag surface including modeling of sectional rotations can be seen in Figure 6.7. Displacements $\boldsymbol{y}_{\mathrm{S}} = [y_{\xi\mathrm{S}}, y_{\eta\mathrm{S}}]^{\mathrm{T}}$ are composed of

$$y_{\xi\mathrm{S}}\left(\boldsymbol{\xi}, t\right) = -\frac{y'_{\mathrm{S}}\left(\xi, t\right)}{\sqrt{1 + y'^{2}_{\mathrm{S}}\left(\xi, t\right)}}\left(\eta - \eta_{\mathrm{R}}\right) \tag{6.6a}$$

and

$$y_{\eta\mathrm{S}}\left(\boldsymbol{\xi}, t\right) = y_{\mathrm{S}}\left(\xi, t\right) - \left(1 - \frac{1}{\sqrt{1 + y'^{2}_{\mathrm{S}}\left(\xi, t\right)}}\right)\left(\eta - \eta_{\mathrm{R}}\right). \tag{6.6b}$$

Finally, the time-discrete low-fidelity CSM model is given with the adapted time-discretization (3.16b) of the structural subsystem in the model problem (see Chapter 3 Model Problem, pp. 32 ff.). In order to simplify the design of the controller in Chapter 8 The Controller (CLC) Subsystem (pp. 94 ff.) the input parameter for $\ddot{u}_{\mathrm{S}}$ is further set to zero, i.e. $b_2 = 0$. Resulting final parameters are summed up in Table 6.2.

Equivalent to the fluid (CFD) subsystem introduced in the previous chapter the final FSI and FSCI co-simulations also here only see the black box structural (CSM) subsystem with its inputs $\boldsymbol{U}_{\mathrm{S}}$ and outputs $\boldsymbol{Y}_{\mathrm{S}}$ as illustrated by Figure 6.8 completely independent from the fidelity level of the model. Input $\boldsymbol{z}_{\mathrm{S}}$ contains the disturbances on the FSI interface coming from the fluid and input $u_{\mathrm{S}}(t)$ the control input, i.e. the root-point excitation stemming from the closed-loop controller. Output $\boldsymbol{y}_{\mathrm{S}}$ carries the displacements of the FSI interface and output $y_{\mathrm{S}}(t)$ the measured output for the controller equivalent to the displacement of end-point E. All implementational details like fidelity level and accompanying internal dynamics $\boldsymbol{X}_{\mathrm{S}}$ are hidden inside the black box.

Table 6.2 Parameter settings for low-fidelity structural (CSM) subsystem.

parameter	*value*			*unit*
	CSM1	***CSM2***	*CSM3*	
m	—	**0.0144**	—	kg
k	—	**2.400549**	—	N/m
b_2	—	**0**	—	kg
b_0	—	**1.600366**	—	N/m
q	—	$\mathbf{10^{6\ldots-3}}$	—	1
f_u	—	**0**	—	1

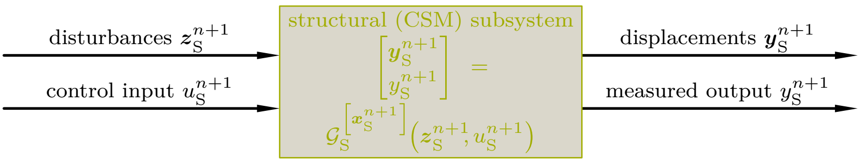

Figure 6.8 Block diagram of structural (CSM) subsystem.

For the sake of completeness results of the high-fidelity CSM model tests with parameter settings CSM1, CSM2 and CSM3 as suggested in Turek and Hron (2006) are shown. They can be found in Figures 6.9 and 6.10.

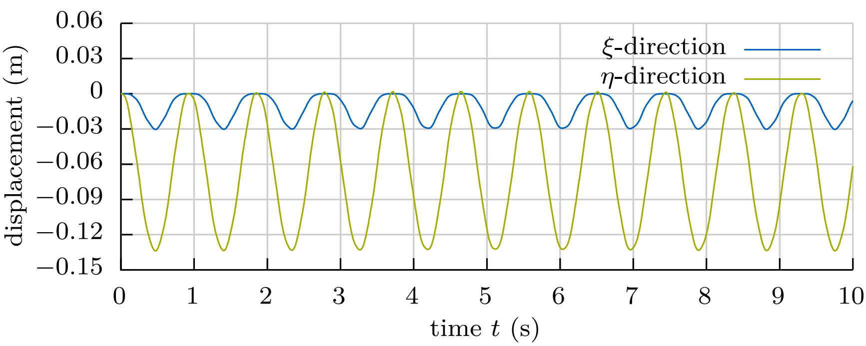

Figure 6.9 End-point displacement in dynamic CSM3 test with high-fidelity structural (CSM) subsystem.

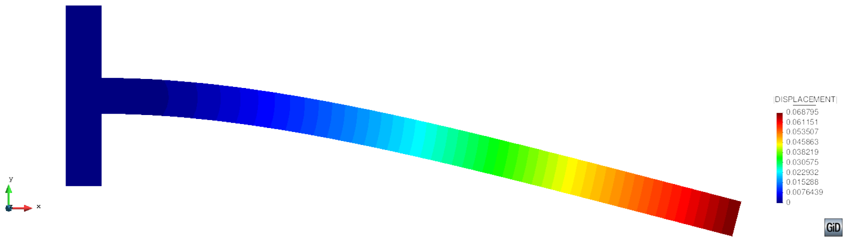

(a) STATIC CSM1 TEST WITH A DISPLACEMENT OF $-0.0074415\,\mathrm{m}$ IN ξ-DIRECTION, $-0.068296\,\mathrm{m}$ IN η-DIRECTION AND $0.068701\,\mathrm{m}$ ABSOLUTE AT END-POINT E.

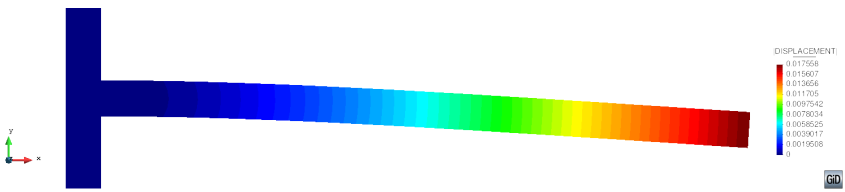

(b) STATIC CSM2 TEST WITH A DISPLACEMENT OF $-0.00048546\,\mathrm{m}$ IN ξ-DIRECTION, $-0.017536\,\mathrm{m}$ IN η-DIRECTION AND $0.017543\,\mathrm{m}$ ABSOLUTE AT END-POINT E.

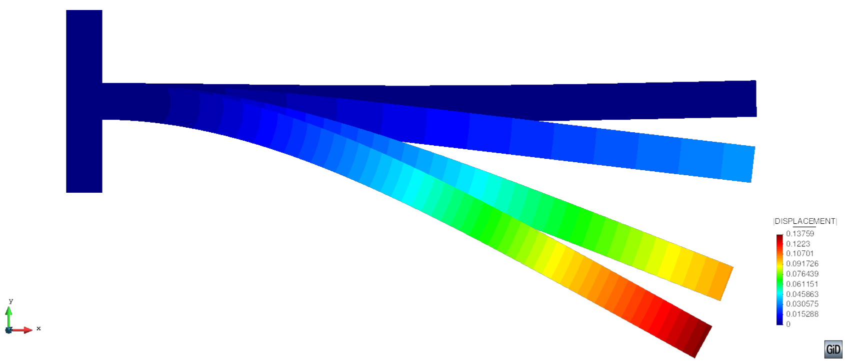

(c) DYNAMIC CSM3 TEST AT $t = 4.67\,\mathrm{s}$ (BACK), $4.82\,\mathrm{s}$, $4.97\,\mathrm{s}$ AND $5.12\,\mathrm{s}$ (FRONT).

Figure 6.10 DISPLACEMENT FIELDS OF CSM TESTS WITH HIGH-FIDELITY STRUCTURAL (CSM) SUBSYSTEM.

Der Urquell aller technischen Errungenschaften ist die göttliche Neugier und der Spieltrieb des bastelnden und grübelnden Forschers und nicht minder die konstruktive Phantasie des technischen Erfinders. [...] Sollen sich auch alle schämen, die gedankenlos sich der Wunder der Wissenschaft und Technik bedienen, und nicht mehr davon geistig erfasst haben als die Kuh von der Botanik der Pflanzen, die sie mit Wohlbehagen frisst.

—Albert Einstein (1879–1955)

7 Fluid–Structure Interaction

FSI short for fluid-structure interaction identifies the multi-physics of fluid and structure. The single-physics field fluid is interfering with the single-physics field solid and vice versa. It denotes one subproblem of fluid-structure-control interaction (FSCI) as introduced by this work. Therefore, it can also be closer referred to as the FSI developing freely while FSCI indicates a FSI influenced by a controller. In FSCI exploring the pure FSI also states a major subtask in the development and design of the structural controller based on classical linear theory. Key prerequisite is the fundamental understanding of the underlying dynamics. Further details on this will be given in Chapter 8 The Controller (CLC) Subsystem (pp. 94 ff.).

This chapter is investigating the FSCI subproblem class FSI with two fundamental intentions: First, it is shown that the coupled scheme without controller can deliver a meaningful system response at all. And secondly, a basis for the development of a control law and subsequent design of the controller is provided. During an early stage of this work some first FSCI simulations of a controlled system, expected to stable, were performed. But even with testing a variety of further parameter sets the coupled dynamics always diverged, i.e. the simulations permanently failed. In order to investigate the causes behind this the FSI parameter scaling tests as presented in the following were designed. With those the reasons for previous failure could finally be identified underlining the conclusion that a fundamental understanding of the underlying dynamical effects in the interaction is crucial in order to appropriately design a controller.

This work applies a partitioned approach (co-simulation) with iterative coupling based on a fixed-point formulation on the displacements. It is

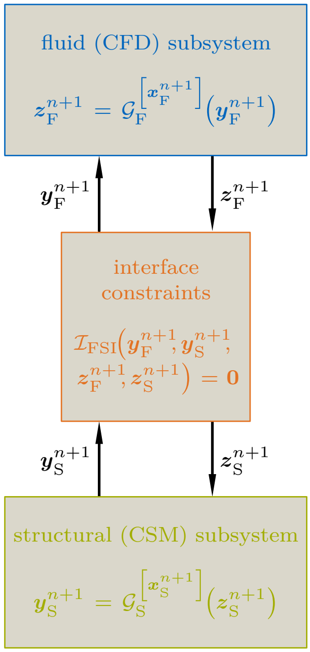

Figure 7.1 BLOCK DIAGRAM OF FSI CO-SIMULATION.

supplemented by Aitken acceleration (Küttler and Wall 2008; Küttler 2009) to get an optimal choice of relaxation parameter each iteration. Thus, the computational FSI problem is formulated in terms of a fluid (CFD) subsystem and a structural (CSM) subsystem coupled by interface constraints replacing the actual interaction.

The fluid (CFD) subsystem

$$\left.\begin{aligned} \mathcal{F}_F\left(\boldsymbol{x}_F^{n+1}, \boldsymbol{y}_F^{n+1}\right) &= \boldsymbol{0} \\ \boldsymbol{z}_F^{n+1} &= \mathcal{G}_F\left(\boldsymbol{x}_F^{n+1}, \boldsymbol{y}_F^{n+1}\right) \end{aligned}\right\} \boldsymbol{z}_F^{n+1} = \mathcal{G}_F^{[\boldsymbol{x}_F^{n+1}]}\left(\boldsymbol{y}_F^{n+1}\right) \tag{7.1}$$

and the structural (CSM) subsystem

$$\left.\begin{aligned} \mathcal{F}_S\left(\boldsymbol{x}_S^{n+1}, \boldsymbol{z}_S^{n+1}\right) &= \boldsymbol{0} \\ \boldsymbol{y}_S^{n+1} &= \mathcal{G}_S\left(\boldsymbol{x}_S^{n+1}, \boldsymbol{z}_S^{n+1}\right) \end{aligned}\right\} \boldsymbol{y}_S^{n+1} = \mathcal{G}_S^{[\boldsymbol{x}_S^{n+1}]}\left(\boldsymbol{z}_S^{n+1}\right) \tag{7.2}$$

are established in Chapters 5 The Fluid (CFD) Subsystem (pp. 57 ff.) and 6 The Structural (CSM) Subsystem (pp. 68 ff.), respectively. Hereby control input $u_S^{n+1} \equiv 0$ and measured output y_S^{n+1} is only captured for analysis purposes. The FSI problem is completed by interface constraints

$$\mathcal{I}_{\boldsymbol{z}}\left(\boldsymbol{z}_F^{n+1}, \boldsymbol{z}_S^{n+1}\right) = \boldsymbol{z}_F^{n+1} + \boldsymbol{z}_S^{n+1} = \boldsymbol{0} \tag{7.3a}$$

balancing the disturbances (forces) and

$$\mathcal{I}_{\boldsymbol{y}}\left(\boldsymbol{y}_{\mathrm{F}}^{n+1},\boldsymbol{y}_{\mathrm{S}}^{n+1}\right)=\boldsymbol{y}_{\mathrm{F}}^{n+1}-\boldsymbol{y}_{\mathrm{S}}^{n+1}=\mathbf{0} \tag{7.3b}$$

enforcing the kinematic compatibility at the FSI interface $\Gamma_{\mathrm{F/S,FSI}}=\Omega_{\mathrm{F}}\cap\Omega_{\mathrm{S}}$ between both subsystems. They can be summarized to

$$\mathcal{I}_{\mathrm{FSI}}\left(\boldsymbol{y}_{\mathrm{F}}^{n+1},\boldsymbol{y}_{\mathrm{S}}^{n+1},\boldsymbol{z}_{\mathrm{F}}^{n+1},\boldsymbol{z}_{\mathrm{S}}^{n+1}\right)=\mathbf{0}. \tag{7.3c}$$

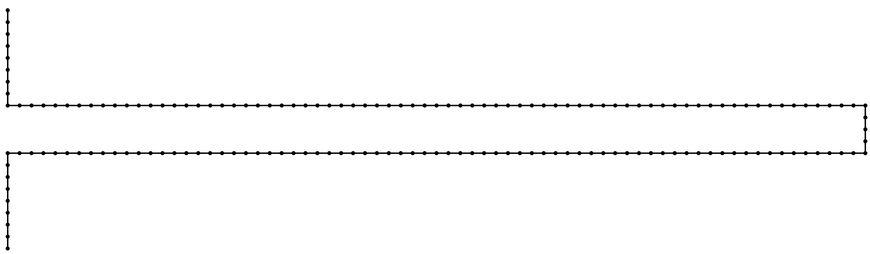

Figure 7.2 MATCHING INTERFACE MESHES OF FLUID (CFD) AND STRUCTURAL (CSM) SUBSYSTEM.

The discrete FSI interface with matching interface meshes of fluid (CFD) and structural (CSM) subsystem can be seen in Figure 7.2. Possessing additionally equal spatial discretizations reduces mapping operations between fluid and structural fields to simple copy operations, i.e. renders them redundant. They are already left out in formulation 7.3 of the interface constraints. Figure 7.1 shows the block diagram of the underlying Gauß-Seidel (GS) communication pattern. The resulting coupling algorithm is presented as pseudo code in Algorithm 7.1. For the numerical experiments it is implemented in the open source tool enhanced multi-physics interface research engine (EMPIRE) (Sicklinger and Wang 2013) developed at the Chair of Structural Analysis at the Technical University of Munich.

Main purpose of this chapter is the investigation of the FSI parameter scaling tests. In those the basic mass and stiffness properties of the structure (ρ_{S} and E_{S} respectively m and k) are scaled with the parameter scaling factor q while keeping the impact of the disturbances unscaled. With this an inversely scaled ($^{1}/_{q}$) structural response arrives in case of ideal linear behavior of the coupled problem. Expected deviations from this ideal behavior allow for conclusions on the real underlying dynamical behavior. This reflects the main idea and intention behind the FSI parameter scaling tests.

Up to now extensive investigations of FSCI are limited to the low-fidelity structural (CSM) model. Thus, only this one is considered during the FSI parameter scaling tests. This implies the additional advantage of relatively well behaving Aitken factors resulting from the single structural degree of

Algorithm 7.1 PSEUDO CODE OF PARTITIONED SCHEME FOR FSI CO-SIMULATION.

`// initialize states, i.e. set ICs...`
$^{k_{\mathrm{end}}}\boldsymbol{x}_{\mathrm{F}}^{0} \longleftarrow \boldsymbol{x}_{\mathrm{F}}^{\mathrm{init}}$
$^{k_{\mathrm{end}}}\boldsymbol{x}_{\mathrm{S}}^{0} \longleftarrow \boldsymbol{x}_{\mathrm{S}}^{\mathrm{init}}$
`// initialize displacements...`
$^{k_{\mathrm{end}}}\boldsymbol{y}_{\mathrm{S}}^{0} \longleftarrow \boldsymbol{y}_{\mathrm{S}}^{\mathrm{init}}$
`// do co-simulation...`
`// time loop...`
for $n \longleftarrow 0$ *to* $n \longleftarrow n_{\mathrm{end}} - 1$ **do**
    `// predict displacements...`
    $^{0}\boldsymbol{y}_{\mathrm{S}}^{n+1} \longleftarrow {}^{k_{\mathrm{end}}}\boldsymbol{y}_{\mathrm{S}}^{n}$
    `// interface iteration loop, i.e. FSI loop...`
    for $k \longleftarrow 0$ *to* $k \longleftarrow k_{\max}$ **do**
        `// map displacements from solid to fluid...`
        $^{k}\boldsymbol{y}_{\mathrm{F}}^{n+1} \longleftarrow \mathcal{M}_{\boldsymbol{y}}\left({}^{k}\boldsymbol{y}_{\mathrm{S}}^{n+1}\right)$
        `// solve fluid...`
        $^{k}\boldsymbol{z}_{\mathrm{F}}^{n+1} \longleftarrow \mathcal{G}_{\mathrm{F}}^{\left[{}^{k}\boldsymbol{x}_{\mathrm{F}}^{n+1}\right]}\left({}^{k}\boldsymbol{y}_{\mathrm{F}}^{n+1}\right)$
        `// map forces from fluid to solid...`
        $^{k}\boldsymbol{z}_{\mathrm{S}}^{n+1} \longleftarrow \mathcal{M}_{\boldsymbol{z}}\left({}^{k}\boldsymbol{z}_{\mathrm{F}}^{n+1}\right)$
        `// solve solid...`
        $^{k}\boldsymbol{y}_{\mathrm{S}}^{n+1} \longleftarrow \mathcal{G}_{\mathrm{S}}^{\left[{}^{k}\boldsymbol{x}_{\mathrm{S}}^{n+1}\right]}\left({}^{k}\boldsymbol{z}_{\mathrm{S}}^{n+1}\right)$
        `// calculate residuum of displacements...`
        $^{k}\mathcal{R}_{\boldsymbol{y}}^{n+1} \longleftarrow {}^{k}\boldsymbol{y}_{\mathrm{S}}^{n+1} - {}^{k-1}\boldsymbol{y}_{\mathrm{S}}^{n+1}$
        `// check for convergence...`
        $^{k}\varepsilon^{n+1} \longleftarrow \left\|{}^{k}\mathcal{R}_{\boldsymbol{y}}^{n+1}\right\|$
        if $^{k}\varepsilon^{n+1} < {}^{\max}\varepsilon$ **then**
            `break`
        end if
        `// update Aitken factor...`
        if $k = 0$ **then**
            $^{0}\beta^{n+1} \longleftarrow {}^{\mathrm{init}}\beta$
        else
            if $\dim\left\{{}^{k}\mathcal{R}_{\boldsymbol{y}}^{n+1}\right\} = 1$ **then**
                $^{k}\beta^{n+1} \longleftarrow {}^{k-1}\beta^{n+1}\frac{{}^{k-1}\mathcal{R}_{\boldsymbol{y}}^{n+1}}{{}^{k-1}\mathcal{R}_{\boldsymbol{y}}^{n+1} - {}^{k}\mathcal{R}_{\boldsymbol{y}}^{n+1}}$
            else
                $^{k}\beta^{n+1} \longleftarrow {}^{k-1}\beta^{n+1}\frac{{}^{k-1}\mathcal{R}_{\boldsymbol{y}}^{n+1\,\mathrm{T}}\left({}^{k-1}\mathcal{R}_{\boldsymbol{y}}^{n+1} - {}^{k}\mathcal{R}_{\boldsymbol{y}}^{n+1}\right)}{\left\|{}^{k-1}\mathcal{R}_{\boldsymbol{y}}^{n+1} - {}^{k}\mathcal{R}_{\boldsymbol{y}}^{n+1}\right\|^{2}}$
            end if
        end if
        `// update displacements...`
        $^{k+1}\boldsymbol{y}_{\mathrm{S}}^{n+1} \longleftarrow {}^{k}\boldsymbol{y}_{\mathrm{S}}^{n+1} + {}^{k}\beta^{n+1}\,{}^{k}\mathcal{R}_{\boldsymbol{y}}^{n+1}$
    end for
end for

freedom (DoF). If not noted otherwise in Table 7.1 the FSI parameter scaling tests with the low-fidelity structural (CSM) subsystem use the following standard settings next to the ones already given with the introduction of the respective subsystems: The fluid (CFD) subsystem uses the non-linear version of the structural similarity mesh updating scheme. A maximum of 40 interface iterations is allowed to attain the set absolute convergence criteria of 10^{-9}. Time step size is equally $\delta t = 0.01$. The structural (CSM) subsystem starts not until $3 \cdot \delta t = 0.03\,\mathrm{s}$ to avoid faulty disturbances outputted by the fluid (CFD) subsystem for the first steps. The simulations run $1500 \cdot \delta t = 15.00\,\mathrm{s}$ which are evaluated from $t_1 = 1000 \cdot \delta t = 10.00\,\mathrm{s}$ to $t_2 = 1500 \cdot \delta t = 15.00\,\mathrm{s}$. Used parameter scaling factors can be found in Table 7.1 presenting the simulation log.

Table 7.1 LOG OF FSI PARAMETER SCALING TEST WITH LOW-FIDELITY STRUCTURAL (CSM) SUBSYSTEM.

coupling scheme	*parameter scaling factor q*									
	10^6	10^5	10^4	10^3	10^2	10^1	10^0	10^{-1}	10^{-2}	10^{-3}
FSI	✓	✓	✓	✓	✗[f],✓[ab]	✓[a]	✓[a]	✓[ae]	✓[ac]	✓[ade]

[a] change to linear mesh updating scheme in fluid (CFD) subsystem

[b] start structural (CSM) subsystem after $303 \cdot \delta t = 3.03\,\mathrm{s}$, increase simulation time to 20 s and evaluate from $t_1 = 1500 \cdot \delta t = 15.00\,\mathrm{s}$ to $t_2 = 2000 \cdot \delta t = 20.00\,\mathrm{s}$

[c] increase absolute convergence criterion to 10^{-6}

[d] increase absolute convergence criterion to $2{\times}10^{-5}$

[e] maximal number of 40 interface iterations reached

[f] mesh updating scheme in fluid (CFD) subsystem fails due to large deformations of structural (CSM) subsystem for different settings

The results of all performed simulations (see log in Table 7.1) are presented and evaluated in terms of the disturbance $z_\mathrm{F}(t)$ and the measured output $y_\mathrm{S}(t)$. Both only denote signals and not complete fields. In the present case of the low-fidelity SDoF structure they sufficiently represent trends of the developing fields and the underlying dynamics. This is questionable in case of the high-fidelity MDoF structure where e.g. the simple measurement of an end-point displacement (measured output) can not be sufficient to represent the actually distributed structural displacements and the more complex dynamics. Time responses of the chosen signals $z_\mathrm{F}(t)$ and $y_\mathrm{S}(t)$ are included in Figures 9.11 (p. 139) to 9.20 (p. 148) in Chapter 9 Fluid–Structure–Control Interaction (pp. 118 ff.). Runtime iteration counts are provided in Figures 9.21 (p. 151) to 9.29 (p. 159) of the same chapter. In order to draw final conclusions the shown results are condensed further down to four figures presented and explained in the following.

Trends of disturbance $z_\mathrm{F}(t)$ and measured output $y_\mathrm{S}(t)$ with respect to the parameter scaling factor q are displayed in Figures 7.3a and 7.3b, respectively. Illustrated are the positive maximum

$$\max_{t\in[t_1,t_2]} \{\square(t)\}\,, \tag{7.4a}$$

the negative maximum

$$\max_{t\in[t_1,t_2]} \{-\square(t)\}\,, \tag{7.4b}$$

the root mean square

$$\sqrt{\frac{1}{t_2-t_1}\int_{t_1}^{t_2} \square^2(t)\,\mathrm{d}t} \tag{7.4c}$$

and the absolute mean

$$\left|\frac{1}{t_2-t_1}\int_{t_1}^{t_2} \square(t)\,\mathrm{d}t\right|. \tag{7.4d}$$

The variety of time-independent characteristics is chosen to guarantee a sufficient reliability of subsequently derived statements. For instance the mean value on its own is only capable of reflecting trends in the static displacement part.

The Fourier analyses of disturbance $z_\mathrm{F}(t)$ and measured output $y_\mathrm{S}(t)$ are presented in Figures 7.4 and 7.5, respectively. Normalized power spectral densities (PSD's)

$$\frac{\left|\mathcal{F}\left\{\square(t)\Big|_{t_1}^{t_2}\right\}\right|^2}{\max\limits_f\left\{\left|\mathcal{F}\left\{\square(t)\Big|_{t_1}^{t_2}\right\}\right|^2\right\}} \tag{7.5}$$

corresponding to frequency-dependent energy contents are plotted in vertical direction for all parameter scaling factors in horizontal direction (interpolation between discrete q-values) resulting in a contour plot. Decisive are regions with dense contour lines indicating main frequencies of the coupled system. Absolute values of the PSD are not of interest here.

Figures 7.3, 7.4 and 7.5 obviously support the following conclusion: The range of parameter scaling factor q subdivides into two main regions.

In the range from $q = 10^\infty$ to approximately 10^2 the coupled system shows indeed the discussed ideal linear behavior. The disturbance from the fluid on the structure stays constant independent of q and the measured output and consequently all structural displacements are accordingly scaling with $^1/_q$. The structure is mainly moving with its own single eigenfrequency and only partially with the first and second vortex shedding frequency of the fluid. Those fluid eigenfrequencies are shifted to multiples of the structural eigenfrequency. I.e. the structure is dominating here. This region is optimal in terms of the controller design of Chapter 8 The Controller

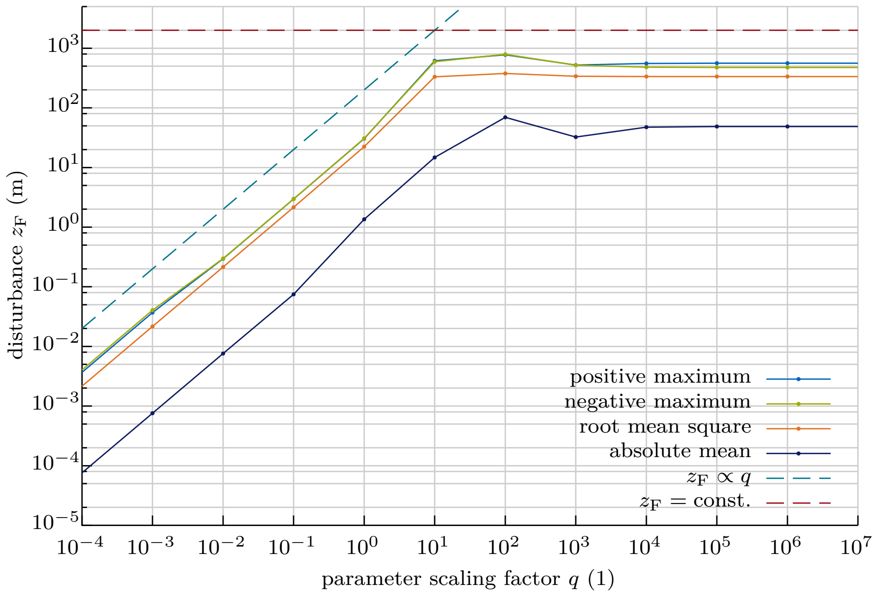

(a) Disturbance.

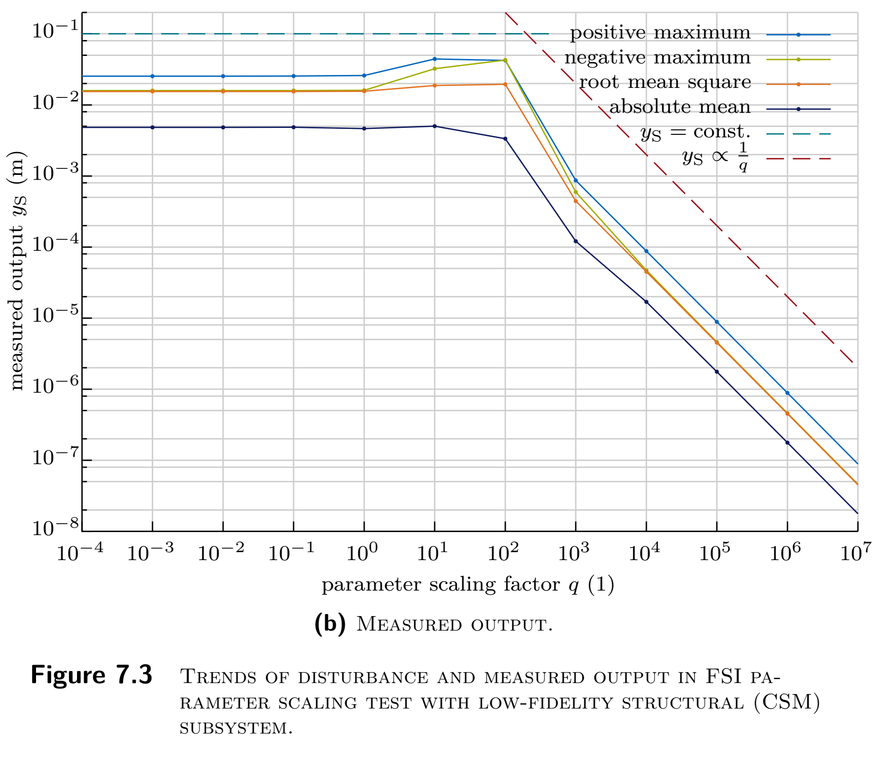

(b) Measured output.

Figure 7.3 Trends of disturbance and measured output in FSI parameter scaling test with low-fidelity structural (CSM) subsystem.

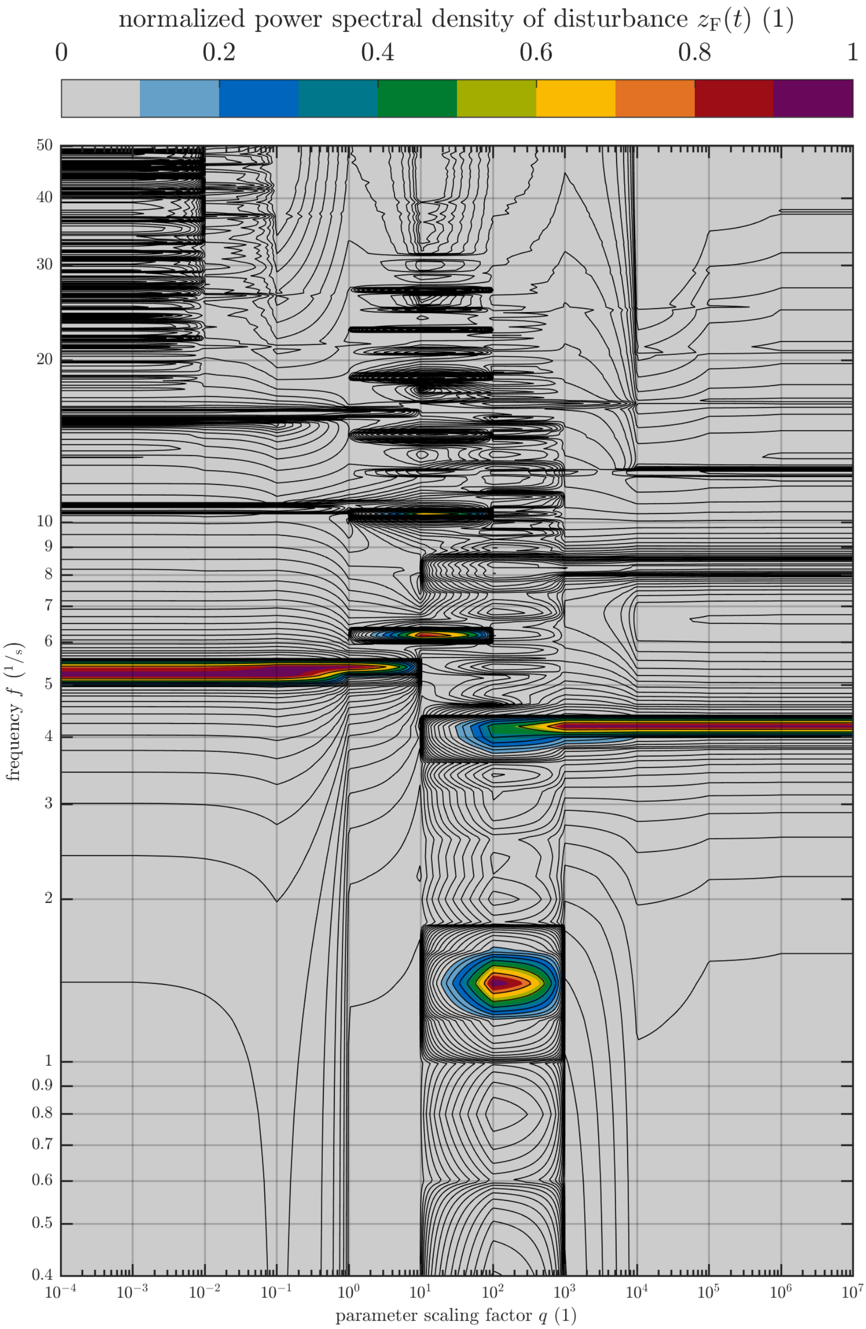

Figure 7.4 Fourier analysis of disturbance in FSI parameter scaling test with low-fidelity structural (CSM) subsystem.

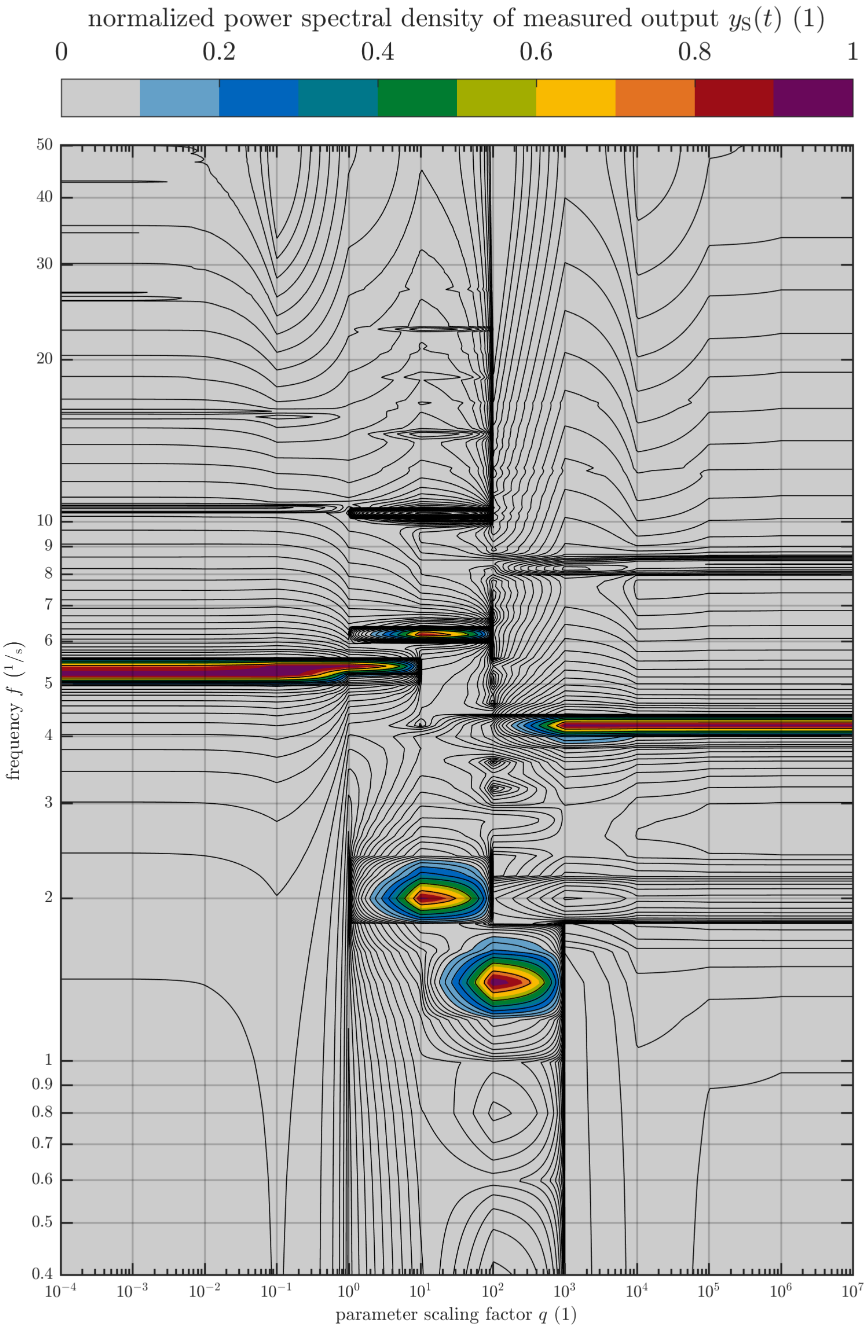

Figure 7.5 Fourier analysis of measured output in FSI parameter scaling test with low-fidelity structural (CSM) subsystem.

(CLC) Subsystem (pp. 94 ff.) since the influence of the fluid can simply be substituted with the recorded disturbance. The Aitken factor, i.e. the dynamically adopting relaxation factor also stays nearly constant in this region. Therewith a best initial Aitken factor can be determined by simply starting a simulation, stopping it after some time steps and taking a second arriving Aitken factor of one of the last simulated time steps as the future initial one.

The second region is ranging from $q \approx 10^1$ to $10^{-\infty}$. It is characterized by strongly non-linear behavior of the coupled dynamics. Independent of the actual parameter scaling in the structure the measured output respectively the displacements stay constant. The disturbance (force) from the fluid on the structure is simply adopting proportional to q. Thus, the fluid is absolutely dominating this region forcing the structure (even with controller as seen later) to the always same displacements. In the Fourier analyses neither eigendynamics of structure nor structural influence on the fluid's vortex shedding frequencies can be identified. One main fluid frequency is developing. The design of a structural controller for this region is challenging. With force control and hypothetically unbounded control input a reduction of the displacement is feasible. Displacement control implying a strongly bounded control input seems impossible. It is not surprising that the standard controllers originally designed for the other linear region fail here as shown subsequently in Chapter 9 Fluid–Structure–Control Interaction (pp. 118 ff.). Perhaps fluid control with direct adjustment of the fluid flow can be more effective here. Concerning the Aitken factors in this region, no clear trend is identifiable.

For the parameter range from $q \approx 10^2$ to approximately 10^1 a kind of transfer region can be observed. To this effect a superelevation of the measured output and connected displacements is observed reflecting as well in special settings during the co-simulation as noted in Table 7.1. This gives an indication towards a synchronization process.

It must be pointed out that also the FSI simulations can only deliver results as qualitative as the underlying subsystems. In consequence of harm induced by the fluid (CFD) subsystem, physically meaningful quantities can not be produced. Nevertheless, the underlying dynamical effects and their trends are well covered and based on that reliable conclusions can be drawn. The reduction of the structure to a simple SDoF system furthermore delivers valuable insights in the coupled system dynamics which can also be assigned to MDoF structures. However, further investigations with the high-fidelity structure are indispensable. Also the rather rough resolution in the parameter space should be considered.

For the sake of completeness test cases FSI1, FSI2 and FSI3 as suggested by Turek and Hron (2006) but employing this work's deviating CFD model (with square cylinder) are presented. Their results are shown in Figures 7.6 to 7.9: Different inlet velocities v_{in} lead to different vortex shedding frequencies causing the excitation of different structural modes and therefore delivering different coupled system responses. Here, only the coupling of the first-order-generalized–α fluid solver and the second-order-generalized–α structural solver is successful. This results in loss of temporal consistency, since the mesh updating scheme in the fluid (CFD) subsystem still applies the BDF2. In the coupling of the default BDF2 fluid solver and the second-order-generalized–α structural solver the convergence of the interface iterations fails. Furthermore, some small changes to the standard settings are made: The time step size is halved ($\delta t = 0.005\,\mathrm{s}$). Convergence criteria are relaxed to reduce the numerical effort in these purely illustrative simulations (relative 10^{-3} for the interface iterations, relative 10^{-6}/absolute 10^{-9} for the fluid velocities/pressures, relative 10^{-6}/absolute 10^{-9} for the structural displacements/residuals). $\alpha_f = 0$ and $\alpha_m = -1$ are chosen as generalized–α parameters in both subsystems. The structural (CSM) subsystem starts not until $1000 \cdot \delta t = 5.000\,\mathrm{s}$ to let the fluid flow fully develop first. In consequence of the increased interface residuals the time responses of the interface disturbances show extreme fluctuations and are not plotted here.

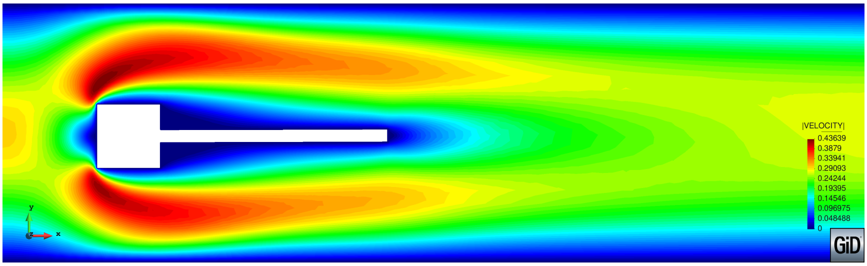

(a) FSI1 TEST.

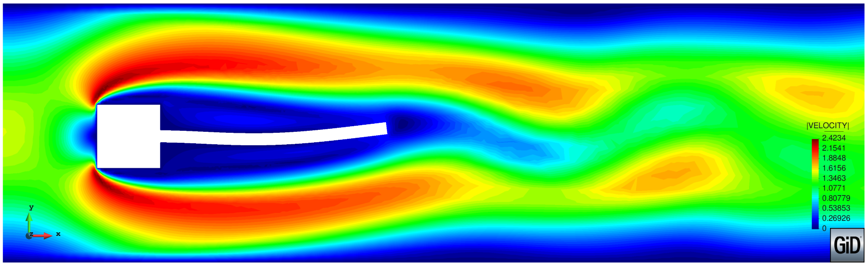

(b) FSI2 TEST.

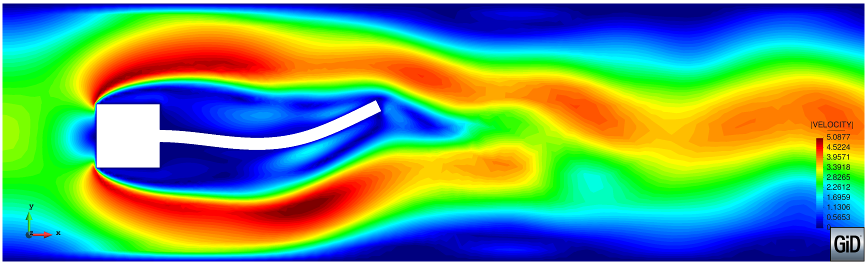

(c) FSI3 TEST.

Figure 7.6 VELOCITY FIELDS OF FSI TESTS WITH HIGH-FIDELITY STRUCTURAL (CSM) SUBSYSTEM AT $t = 14.95\,\mathrm{s}$.

(a) FSI1 test.

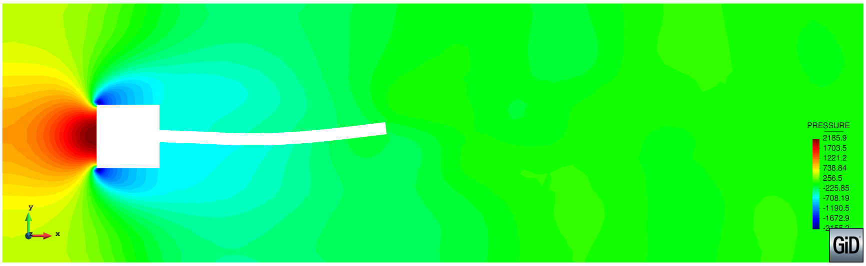

(b) FSI2 test.

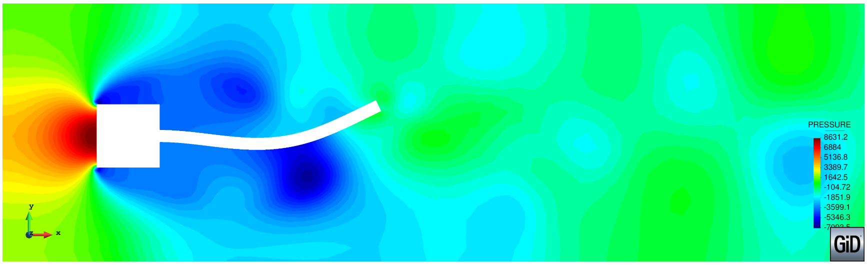

(c) FSI3 test.

Figure 7.7 Pressure fields of FSI tests with high-fidelity structural (CSM) subsystem at $t = 14.95\,\mathrm{s}$.

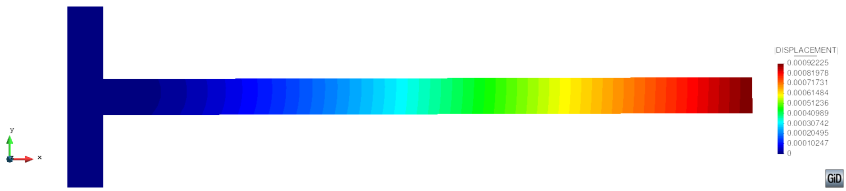

(a) FSI1 TEST.

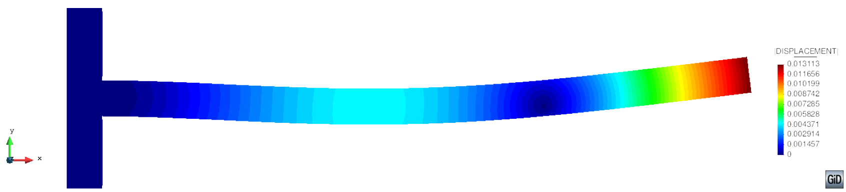

(b) FSI2 TEST.

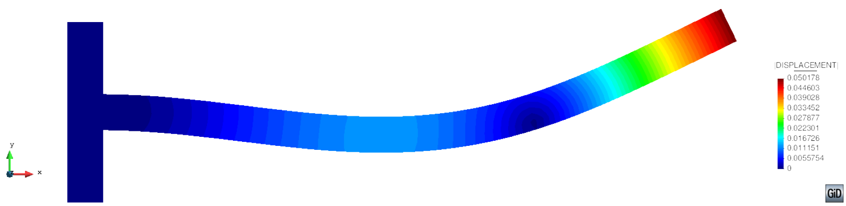

(c) FSI3 TEST.

Figure 7.8 DISPLACEMENT FIELDS OF FSI TESTS WITH HIGH-FIDELITY STRUCTURAL (CSM) SUBSYSTEM AT $t = 14.95\,\mathrm{s}$.

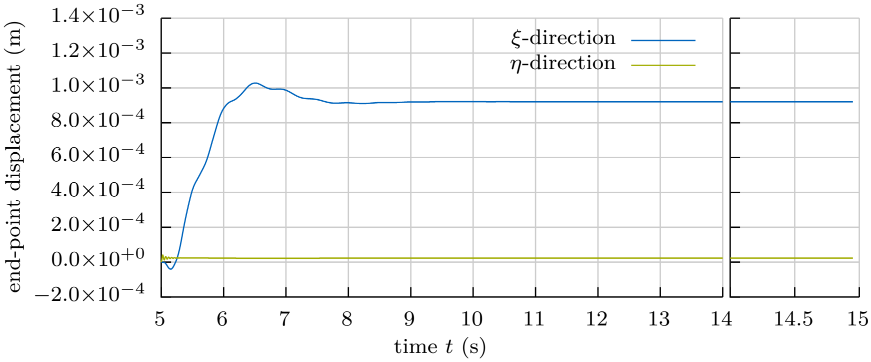

(a) FSI1 test.

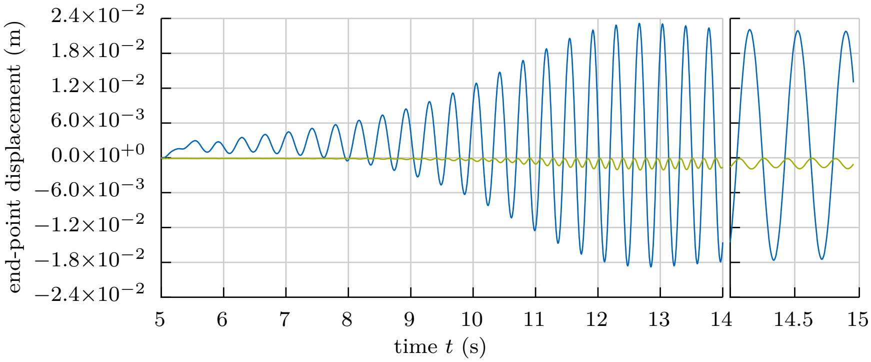

(b) FSI2 test.

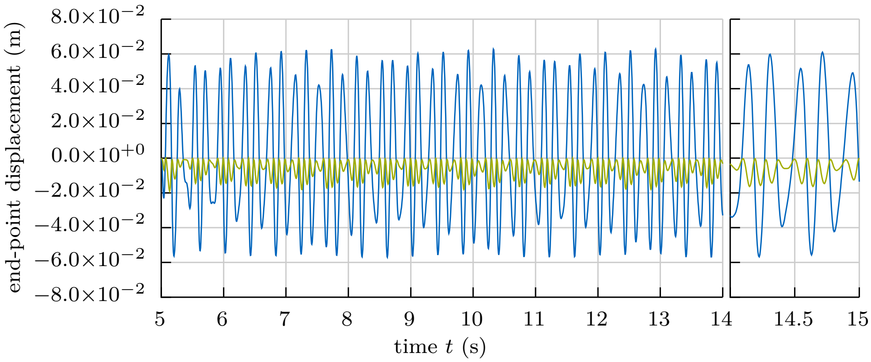

(c) FSI3 test.

Figure 7.9 End-point displacements in FSI with high-fidelity structural (CSM) subsystem tests.

8 The Controller (Closed–Loop Control) Subsystem

8.1 References on Control Theory and Introduction

The analysis and output-feedback control of linear lumped-parameter single-input single-output (SISO) systems in Laplace or frequency domain constitutes the most classical branch in control theory. Introductions can for instance be found in Lohmann (2015c), Unbehauen (2008), King (2007) or Lunze (2014a). (Ger. *Die Analyse und Eingrößenregelung von linearen konzentriert-prarameterischen Systemen im Laplace- bzw. Frequenzbereich stellt den klassischten Bereich der Regelungstechnik dar. Einführungen sind zum Beispiel in Lohmann (2015c), Unbehauen (2008), King (2007) oder Lunze (2014a) zu finden.*)

An introduction to issues in systems theory like state-space representation, controllability, observability, meaning of eigenvalues and eigenvectors etc. is for example given in Lohmann (2015d), Kotyczka and Gehring (2015), Unbehauen (2007), King (2008), Lunze (2014a) or Lunze (2014b). (Ger. *Eine Einführung in Fragestellungen der Systemtheory wie Zustandsraumdarstellung bzw. Zustandsraummodelle, Steuerbarkeit, Beobachtbarkeit, Bedeutung von Eigenwerten und -vektoren usw. wird zum Beispiel in Lohmann (2015d), Kotyczka and Gehring (2015), Unbehauen (2007), King (2008), Lunze (2014a) oder Lunze (2014b) gegeben.*)

Among others Lohmann (2015a), Kotyczka and Gehring (2015), Unbehauen (2007), King (2008) and Lunze (2014b) deal with state-feedback control in the time domain. This includes constant state-feedback and reference feedforward control for linear systems. (Ger. *Unter anderem Lohmann (2015a), Kotyczka and Gehring (2015), Unbehauen (2007), King (2008) und*

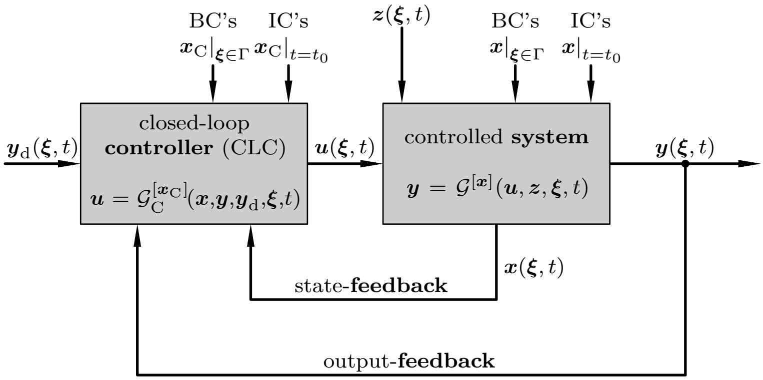

Figure 8.1 Block diagram of general closed-loop control from a control theory point of view.

Lunze (2014b) befassen sich mit der Zustandsregelung im Zeitbereich. Dies beinhaltet auch die konstante Zustandsrückführung und Führungsgrößenaufschaltung für lineare Systeme.)

An optimal state-feedback control law can be stated with respect to a quadratic cost functional and an infinite control interval. This is also known as linear quadratic regulator (LQR). See e.g. Lohmann (2015b), Kotyczka and Gehring (2015), King (2008) or Lunze (2014b). (Ger. *Ein optimales Zustandsregelgesetz kann bezüglich quadratischem Gütemaß und unendlichem Steuerintervall angegeben werden. Dies ist auch unter dem Namen Linear-Quadratischer Regler (LQR) bekannt. Siehe z.B. Lohmann (2015b), Kotyczka and Gehring (2015), King (2008) oder Lunze (2014b).*)

Aspects on disturbance feedforward control (disturbance rejection) including constant disturbance feedforward control are for instance covered in Lohmann (2015a), Lohmann (1997), Kotyczka and Gehring (2015) as well as Lunze (2014b). (Ger. *Aspekte bezüglich Störgrößenaufschaltung (Störgrößenunterdrückung) inklusive konstanter Störgrößenaufschaltung werden beispielsweise in Lohmann (2015a), Lohmann (1997), Kotyczka and Gehring (2015) oder auch Lunze (2014b) behandelt.*)

Unbehauen (2007) and King (2008) exclusively address state observer design while Lohmann (2015a), Kotyczka and Gehring (2015) and Lunze (2014b) also include disturbance models and disturbance observers. (Ger. *Unbehauen (2007) und King (2008) befassen sich ausschließlich mit dem Zustandsbeobachterentwurf während Lohmann (2015a), Kotyczka and Gehring (2015) und Lunze (2014b) auch Störmodelle und Störgrößenbeobachter einbeziehen.*)

For an introduction to control of distributed-parameter systems it is exemplarily referred to the works of Franke (1987), Krstic and Smyshlyaev (2008) and Deutscher (2012). (Ger. *Als Einstieg in die Regelung von verteilt-*

parametrischen Systemen wird beispielhaft auf die Werke von Franke (1987), Krstic and Smyshlyaev (2008) und Deutscher (2012) verwiesen.)

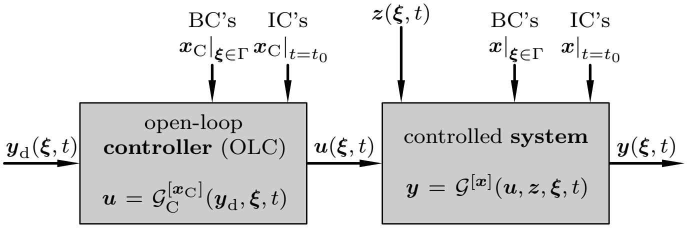

Figure 8.2 Block diagram of general open-loop control from a control theory point of view.

Figure 8.1 and Figure 8.2 illustrate the difference between closed-loop control (CLC, Ger. *Regelung*) and open-loop control (OLC, Ger. *Steuerung*): CLC in contrast to OLC involves the continuous feedback of actual system quantities. Therefore, the controller possesses information about the actual state of the controlled system at any time. It is distinguished between output-feedback (Ger. *Ausgangsrückführung*, outer branch in Figure 8.1) and state-feedback (Ger. *Zustandsrückführung*, inner branch in Figure 8.1).

This work uses the following standard terminology presented for the most general case: The closed-loop controller (Ger. *Regler*)

$$\left.\begin{aligned} \mathcal{F}_\mathrm{C}(\boldsymbol{x}_\mathrm{C},\boldsymbol{x},\boldsymbol{y},\boldsymbol{y}_\mathrm{d},\boldsymbol{\xi},t) &= \boldsymbol{0} \\ \boldsymbol{y} &= \mathcal{G}_\mathrm{C}(\boldsymbol{x}_\mathrm{C},\boldsymbol{x},\boldsymbol{y},\boldsymbol{y}_\mathrm{d},\boldsymbol{\xi},t) \end{aligned}\right\} \boldsymbol{u} = \mathcal{G}_\mathrm{C}^{[\boldsymbol{x}_\mathrm{C}]}(\boldsymbol{x},\boldsymbol{y},\boldsymbol{y}_\mathrm{d},\boldsymbol{\xi},t) \tag{8.1}$$

acts on the controlled system (Ger. *Regelstrecke*)

$$\left.\begin{aligned} \mathcal{F}(\boldsymbol{x},\boldsymbol{u},\boldsymbol{z},\boldsymbol{\xi},t) &= \boldsymbol{0} \\ \boldsymbol{y} &= \mathcal{G}(\boldsymbol{x},\boldsymbol{u},\boldsymbol{z},\boldsymbol{\xi},t) \end{aligned}\right\} \boldsymbol{y} = \mathcal{G}^{[\boldsymbol{x}]}(\boldsymbol{u},\boldsymbol{z},\boldsymbol{\xi},t) \tag{8.2}$$

stating the actual physical process or system which should be controlled through control input $\boldsymbol{u}(\boldsymbol{\xi},t)$ (Ger. *Steuergröße*). It constantly receives feedback of state $\boldsymbol{x}(\boldsymbol{\xi},t)$ (Ger. *Zustandsgröße*, state-feedback) and/or measured output $\boldsymbol{y}(\boldsymbol{\xi},t)$ (Ger. *Regelgröße*, output-feedback) from the controlled system. It additionally receives the desired output $\boldsymbol{y}_\mathrm{d}(\boldsymbol{\xi},t)$ (Ger. *Führungsgröße*) constituting the target behavior for the measured output. Disturbance $\boldsymbol{z}(\boldsymbol{\xi},t)$ (Ger. *Störgröße*) covers all known and/or unknown disturbing environmental impacts on the controlled system. The initial boundary value problems (IBVP's) of controller and controlled system are completed by initial conditions (IC's, $\boldsymbol{x}_\mathrm{C}|_{t=t_0}$ and $\boldsymbol{x}|_{t=t_0}$) and boundary conditions (BC's, $\boldsymbol{x}_\mathrm{C}|_{\boldsymbol{\xi}\in\Gamma}$ and $\boldsymbol{x}|_{\boldsymbol{\xi}\in\Gamma}$).

The objective of output- and state-feedback control is to stabilize the dynamics of the controlled system as well as to compensate initial value disturbances (Ger. *Anfangswertstörungen*). Objective of disturbance feedforward control, however, is the compensation of unknown respectively known or estimated steady disturbances (Ger. *Dauerstörungen*). Combination of both, feedback and feedforward control, is also possible. This is for instance done in this work's LQS controller.

As already introduced several times before this work focuses exclusively on closed-loop structural control. This means that a closed-loop controller manipulates the dynamics of the structure via displacement or force control as explained in Chapter 6 The Structural (CSM) Subsystem (pp. 68 ff.). The fluid dynamics are only affected indirectly. A direct approach doing fluid control would for instance be the suppression of vortex shedding by manipulating the cylinder boundary layer per micro jets.

As previously stated, so far only FSCI in combination with the low-fidelity structural (CSM) subsystem is considered. Accordingly, this chapter only deals with the design and implementation of control laws and controller (CLC) subsystems for the low-fidelity CSM model. In fact, the low-fidelity model was specifically designed in order to reduce the control effort in FSCI for first investigations and a fundamental understanding. The simple single degree of freedom (SDoF) dynamics permit treatment of the actually non-linear distributed-parameter system as a linear time-invariant lumped-parameter system. Classical control theory can be applied. The consideration as a distributed-parameter system certainly becomes necessary with a change to the high-fidelity structure.

For the subsequently presented derivations of control laws the operation in the linear range of the parameter scaling factor q is assumed (see Chapter 7 Fluid–Structure Interaction, pp. 79 ff.). Therefore, the controllers are in general expected to fail in the transfer and especially in the strongly non-linear parameter range. Nevertheless, it will turn out that the applied controllers are able to extend the linear parameter range over one or two decades (see Chapter 9 Fluid–Structure–Control Interaction, pp. 118 ff.).

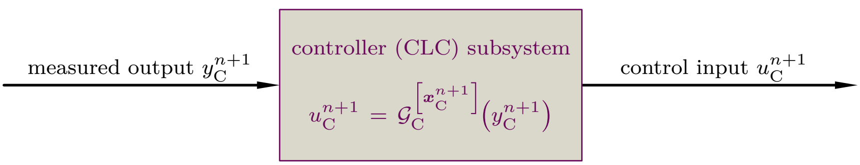

Figure 8.3 BLOCK DIAGRAM OF CONTROLLER (CLC) SUBSYSTEM.

According to the previously introduced fluid (CFD) and structural (CSM) subsystems the coupling in the co-simulation sees again only the black-box controller (CLC) subsystem interacting with its environment via input and output as illustrated in Figure 8.3. The input is constituted by measured output $\boldsymbol{U}_{\mathrm{C}} = y_{\mathrm{C}}$ capturing the end-point displacement of the structure respectively its single degree of freedom. Output $\boldsymbol{Y}_{\mathrm{C}} = u_{\mathrm{C}}$

denotes the actual control input for the structure corresponding to a root-point excitation respectively a force in case of u-output factor $f_u = 0$. Any controller dynamics (8.11/8.13) (LQR), (8.18/8.20) (LQI) or (8.31/8.33) (LQS), states $\boldsymbol{X}_\mathrm{C} = x_\mathrm{C}$ and further implementational details are covert inside the black box.

The following sections present detailed derivations of three control laws and their respective implementations in controller (CLC) subsystems, namely LQR, LQI and LQS. They are successively employed and analyzed in the FSCI simulations of Chapter 9 Fluid–Structure–Control Interaction (pp. 118 ff.). Controllers LQI and LQS denote enhancements of the respective priorly presented controller. For convenience, this chapter misses a consistent indexing with C referring to the controller (CLC) subsystem. Furthermore, the intended compensation of the end-point displacement reflects in a desired output of $y_\mathrm{d}(t) \equiv 0$. Thus, specification of feedforward matrices $\boldsymbol{M}_u$ and $\boldsymbol{M}_{\boldsymbol{x}}$ is redundant.

8.2 State–Feedback Control (LQR)

This section implements state-feedback control following a state observer. The controller state-feedback matrix is specified via linear-quadratic regulator (LQR) approach. The observer output-feedback matrix is set via pole placement approach. Figure 8.4 shows the underlying block diagram from a control theory point of view.

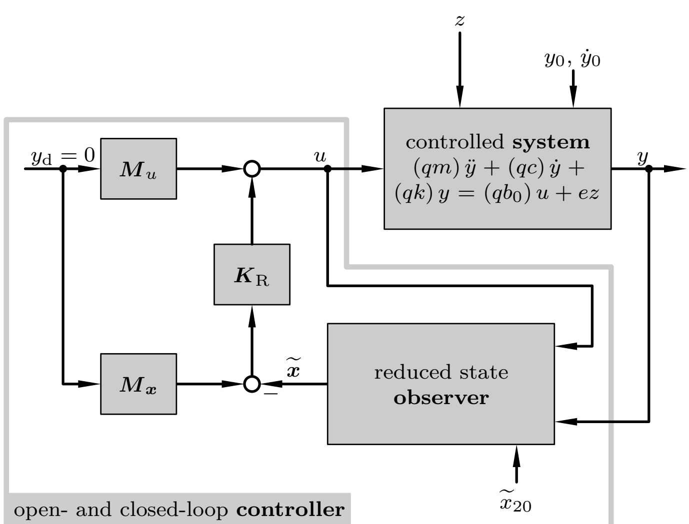

Figure 8.4 Block diagram of LQR controller (CLC) subsystem from a control theory point of view.

The controlled system is stated by

$$(qm)\,\ddot{y} + (qc)\,\dot{y} + (qk)\,y = (qb_0)\,u + ez \tag{8.3}$$

with measured output y, control input u and disturbance z. q denotes again the parameter scaling factor for the scaling tests. As already announced, for the final parameter exploration afterwards disturbance z will be substituted by recordings from the FSI simulations. This is possible assuming an operation in the linear q-range. In regard to Figure 2.9 (p. 30), it should be noted that the mathematical model of the controller is here completely equivalent to the mathematical model of the low-fidelity structure in the numerical experiments. This special case was the original intention for the design of a low-fidelity structural (CSM) subsystem.

By defining states $x_1 := y$ and $x_2 := \dot{y}$ in $\boldsymbol{x} = [x_1, x_2]^{\mathrm{T}}$ Equation (8.3) can be rewritten as state-space representation with differential equation

$$\begin{bmatrix} \dot{x}_1 \\ \dot{x}_2 \end{bmatrix} = \begin{bmatrix} 0 & 1 \\ -\frac{k}{m} & -\frac{c}{m} \end{bmatrix} \begin{bmatrix} x_1 \\ x_2 \end{bmatrix} + \begin{bmatrix} 0 \\ \frac{b_0}{m} \end{bmatrix} u + \begin{bmatrix} 0 \\ \frac{e}{qm} \end{bmatrix} z \tag{8.4a}$$

$$\text{i.e.} \qquad \dot{\boldsymbol{x}} = \boldsymbol{A}\boldsymbol{x} + \boldsymbol{B}u + \boldsymbol{E}z$$

and output equation

$$y = \begin{bmatrix} 1 & 0 \end{bmatrix} \begin{bmatrix} x_1 \\ x_2 \end{bmatrix} \tag{8.4b}$$

$$\text{i.e.} \qquad y = \boldsymbol{C}\boldsymbol{x}.$$

Obviously, the system is fully controllable, i.e. each state (x_1 and x_2) can be accessed via control input u, and fully observable, i.e. each state (x_1 and x_2) appears in measured output y. Therefore state-feedback control and state observation will be possible.

The scheduled control law for the state-feedback controller reads

$$\begin{aligned} u &= -k_{\mathrm{R}1}x_1 - k_{\mathrm{R}2}x_2 \\ \text{i.e.} \qquad u &= -\boldsymbol{K}_{\mathrm{R}}\boldsymbol{x} \end{aligned} \tag{8.5}$$

where $\boldsymbol{K}_{\mathrm{R}} = [k_{\mathrm{R}1}, k_{\mathrm{R}2}]$ is the constant state-feedback matrix. Its weights $k_{\mathrm{R}1}$ and $k_{\mathrm{R}2}$ are determined via the LQR approach. This involves user-definable weights $\boldsymbol{Q} \in \mathbb{R}^{2,2}$ related to state $\boldsymbol{x}$ and $r \in \mathbb{R}^{1,1}$ for control input u. With an appropriate choice $\boldsymbol{Q} \neq \boldsymbol{Q}(q)$ and $r \neq r(q)$ the state-feedback matrix becomes independent from q since also $\boldsymbol{A} \neq \boldsymbol{A}(q)$, $\boldsymbol{B} \neq \boldsymbol{B}(q)$ and $\boldsymbol{C} \neq \boldsymbol{C}(q)$.

During later co-simulations y will be directly accessible which corresponds very well to an assumption that in reality only y is measurable. Thus, first state $x_1 = y$ is also directly known. The second state needs estimation

$x_2 \approx \widetilde{x}_2$ based on the measurements of the first state by a reduced state observer. Quantity $\widetilde{\square}$ with tilde represents here the estimation of exact quantity $\square$. Omitting the influence of disturbance z, state-space differential equation (8.4a) can be split up in a part for measurement y and a part for estimation $\widetilde{x}_2$

$$\begin{aligned} \dot{\widetilde{\boldsymbol{x}}} &= \boldsymbol{A}\widetilde{\boldsymbol{x}} + \boldsymbol{B}u \\ \text{i.e.} \qquad \left[\begin{array}{c} \dot{y} \\ \hline \dot{\widetilde{x}}_2 \end{array}\right] &= \left[\begin{array}{c|c} 0 & 1 \\ \hline -\frac{k}{m} & -\frac{c}{m} \end{array}\right] \left[\begin{array}{c} y \\ \hline \widetilde{x}_2 \end{array}\right] + \left[\begin{array}{c} 0 \\ \hline \frac{b_0}{m} \end{array}\right] u \\ \text{i.e.} \qquad \left[\begin{array}{c} \dot{y} \\ \hline \dot{\widetilde{x}}_2 \end{array}\right] &= \left[\begin{array}{c|c} a_{11} & a_{12} \\ \hline a_{21} & a_{22} \end{array}\right] \left[\begin{array}{c} y \\ \hline \widetilde{x}_2 \end{array}\right] + \left[\begin{array}{c} b_1 \\ \hline b_2 \end{array}\right] u \end{aligned} \tag{8.6a}$$

with

$$\begin{aligned} &a_{11} = 0 &&\wedge\quad a_{12} = 1 &&\wedge\quad b_1 = 0 \\ &a_{21} = -\tfrac{k}{m} &&\wedge\quad a_{22} = -\tfrac{c}{m} &&\wedge\quad b_2 = \tfrac{b_0}{m}. \end{aligned} \tag{8.6b}$$

From this the reduced state observer

$$\begin{aligned} \dot{\underline{\widetilde{x}}}_2 &= a_{\mathrm{B}}\underline{\widetilde{x}}_2 + b_{\mathrm{B}}u + e_{\mathrm{B}}y \\ \widetilde{x}_2 &= \underline{\widetilde{x}}_2 + k_{\mathrm{B}}y \end{aligned} \tag{8.7a}$$

along with

$$\begin{aligned} a_{\mathrm{B}} &= a_{22} - k_{\mathrm{B}}a_{12} = -\frac{c}{m} - k_{\mathrm{B}} \\ b_{\mathrm{B}} &= b_2 - k_{\mathrm{B}}b_1 = \frac{b_0}{m} \\ e_{\mathrm{B}} &= (a_{22} - k_{\mathrm{B}}a_{12})\,k_{\mathrm{B}} + (a_{21} - k_{\mathrm{B}}a_{11}) = \left(-\frac{c}{m} - k_{\mathrm{B}}\right)k_{\mathrm{B}} - \frac{k}{m} \end{aligned} \tag{8.7b}$$

can be formulated.

Its required value for the output-feedback matrix (here only factor) k_{B} is determined via the fictive system

$$\left.\begin{aligned} \dot{x}_{\mathrm{f}} &= a_{22}x_{\mathrm{f}} + a_{12}u_{\mathrm{f}} \\ u_{\mathrm{f}} &= -k_{\mathrm{B}}x_{\mathrm{f}} \end{aligned}\right\} \dot{x}_{\mathrm{f}} = a_{\mathrm{Rf}}x_{\mathrm{f}} \tag{8.8}$$

with $a_{\mathrm{Rf}} = a_{22} - a_{12}k_{\mathrm{B}} = -\frac{c}{m} - k_{\mathrm{B}}$ and placement of the single eigenvalue

$$s - a_{\mathrm{Rf}} \stackrel{!}{=} s - \lambda_{\mathrm{B}} \qquad \Leftrightarrow \qquad k_{\mathrm{B}} = -\frac{c}{m} - \lambda_{\mathrm{B}} \tag{8.9}$$

where $\mathbb{R} \stackrel{!}{\ni} \lambda_{\mathrm{B}} \stackrel{!}{\ll} \mathrm{Re}\{\lambda\} = -\frac{c}{2m} \leq 0$.

The final time discretization of the reduced observer and *deactivated* controller

$$\begin{aligned} x_1 &= y \\ \dot{\underline{\widetilde{x}}}_2 &= a_{\mathrm{B}}\underline{\widetilde{x}}_2 + b_{\mathrm{B}}u + e_{\mathrm{B}}y \\ \widetilde{x}_2 &= \underline{\widetilde{x}}_2 + k_{\mathrm{B}}y \\ u &= 0 \end{aligned} \tag{8.10}$$

$$\text{i.e.} \qquad \dot{\underline{\widetilde{x}}}_2 = a_{\mathrm{B}}\underline{\widetilde{x}}_2 + e_{\mathrm{B}}y$$

with the BDFN (Equation (2.10), p. 11) reads

$$\begin{aligned} x_1^{n+1} &= y^{n+1} \\ [\mathrm{LHS}]\, \underline{\widetilde{x}}_2^{n+1} &= -\sum_{l=0}^{N-1}\left(\widehat{\alpha}_{n-l}\underline{\widetilde{x}}_2^{n-l}\right) + [\mathrm{RHS}]\, y^{n+1} \\ \widetilde{x}_2^{n+1} &= \underline{\widetilde{x}}_2^{n+1} + k_{\mathrm{B}}y^{n+1} \\ u^{n+1} &= 0 \end{aligned} \tag{8.11a}$$

where

$$\begin{aligned} [\mathrm{LHS}] &= \widehat{\alpha}_{n+1} - a_{\mathrm{B}} = \widehat{\alpha}_{n+1} + \frac{c}{m} + k_{\mathrm{B}} \\ [\mathrm{RHS}] &= e_{\mathrm{B}} = -\left(\frac{c}{m} + k_{\mathrm{B}}\right)k_{\mathrm{B}} - \frac{k}{m}. \end{aligned} \tag{8.11b}$$

The final time discretization of the reduced observer and *activated* controller

$$\begin{aligned} x_1 &= y \\ \dot{\underline{\widetilde{x}}}_2 &= a_{\mathrm{B}}\underline{\widetilde{x}}_2 + b_{\mathrm{B}}u + e_{\mathrm{B}}y \\ \widetilde{x}_2 &= \underline{\widetilde{x}}_2 + k_{\mathrm{B}}y \\ u &= -k_{\mathrm{R1}}x_1 - k_{\mathrm{R2}}\widetilde{x}_2 \end{aligned} \tag{8.12}$$

$$\text{i.e.} \qquad \dot{\underline{\widetilde{x}}}_2 = \left(a_{\mathrm{B}} - b_{\mathrm{B}}k_{\mathrm{R2}}\right)\underline{\widetilde{x}}_2 + \left(e_{\mathrm{B}} - b_{\mathrm{B}}\left(k_{\mathrm{R1}} + k_{\mathrm{R2}}k_{\mathrm{B}}\right)\right)y$$

becomes

$$\begin{aligned} x_1^{n+1} &= y^{n+1} \\ [\mathrm{LHS}]\, \underline{\widetilde{x}}_2^{n+1} &= -\sum_{l=0}^{N-1}\left(\widehat{\alpha}_{n-l}\underline{\widetilde{x}}_2^{n-l}\right) + [\mathrm{RHS}]\, y^{n+1} \\ \widetilde{x}_2^{n+1} &= \underline{\widetilde{x}}_2^{n+1} + k_{\mathrm{B}}y^{n+1} \\ u^{n+1} &= -k_{\mathrm{R1}}x_1^{n+1} - k_{\mathrm{R2}}\widetilde{x}_2^{n+1} \end{aligned} \tag{8.13a}$$

where

$$
\begin{aligned}
[\text{LHS}] &= \widehat{\alpha}_{n+1} - a_\text{B} + b_\text{B} k_\text{R2} = \widehat{\alpha}^{n+1} + \frac{c}{m} + k_\text{B} + \frac{b_0}{m} k_\text{R2} \\
[\text{RHS}] &= e_\text{B} - b_\text{B}\left(k_\text{R1} + k_\text{R2} k_\text{B}\right) \\
&= -\left(\frac{c}{m} + k_\text{B}\right) k_\text{B} - \frac{k}{m} - \frac{b_0}{m}\left(k_\text{R1} + k_\text{R2} k_\text{B}\right).
\end{aligned}
\tag{8.13b}
$$

A parameter exploration for observer and controller is done in MATLAB and Simulink (Little and Moler 1984a,b) using the recorded disturbance z from previously performed FSI simulations. The resulting final parameter settings are summarized in Table 8.1. For the actual implementation in an own C++ code Figure 8.5 shows a simplified block diagram from control theory point of view.

Table 8.1 Parameter settings for LQR controller (CLC) subsystem.

component	*parameter*	*value*	*unit*
controlled system	m	0.0144	kg
	c	0	Ns/m
	k	2.400549	N/m
	b_0	−1.600366	N/m
	e	0.01	1
state-feedback	$\boldsymbol{Q}$	$\mathbf{I}$	—
	r	1	—
	k_R1	−0.3028	1
	k_R2	−1.0027	s
state observer	λ_B	−2000	rad/s
	k_B	2000	rad/s

8.3 State– and Integral Output–Feedback Control (LQI)

This section implements state- and integral output-feedback control following a state observer. It is an extension to the LQR control law from previous Section 8.2 State–Feedback Control (LQR) (pp. 98 ff.). The controller feedback matrix covering the state-feedback matrix and the integral output-feedback matrix is specified by extended state-space model and attached linear-quadratic regulator (LQR) approach. The observer output-feedback matrix is defined via pole placement approach. The acronym LQI is used in context of this work and e.g. also within MATLAB/Simulink (Little and Moler 1984a,b) to identify the LQR controller with integral extension. The

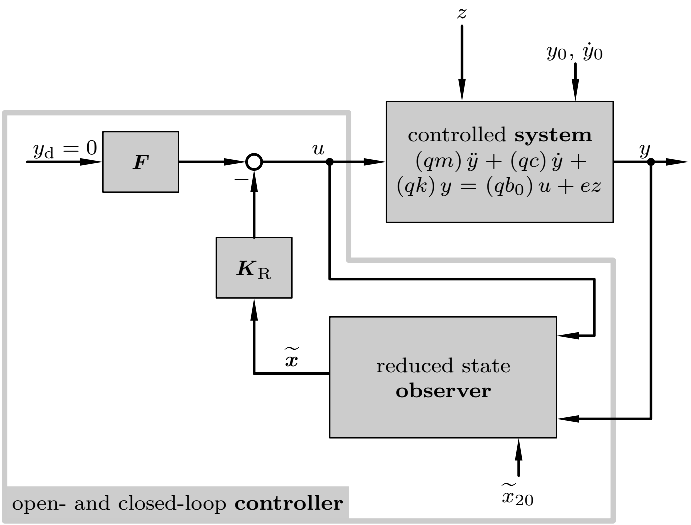

Figure 8.5 Simplified block diagram of LQR controller (CLC) subsystem from a control theory point of view.

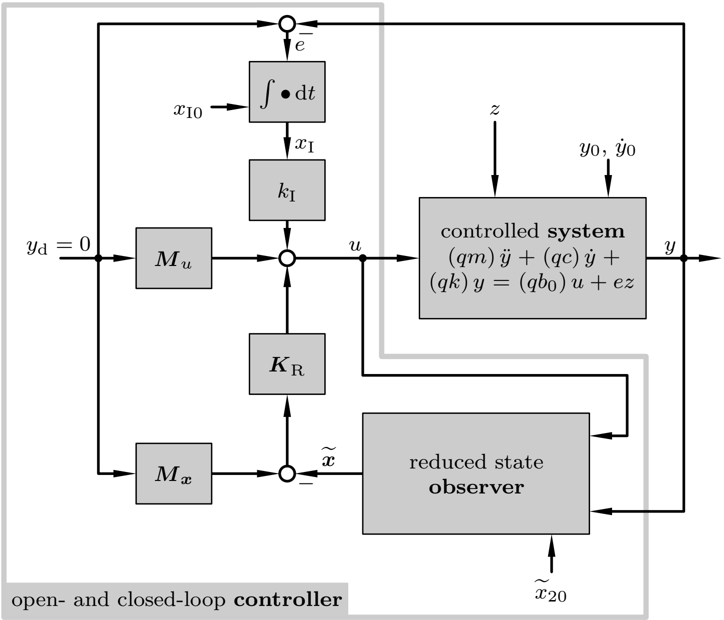

Figure 8.6 Block diagram of LQI controller (CLC) subsystem from a control theory point of view.

underlying block diagram from a control theory point of view can be seen in Figure 8.6.

State-space representation (8.4) of the controlled system (8.3) and its state-feedback control law (8.5) are enhanced by integral output-feedback

$$\begin{aligned} & u = -k_{\mathrm{R}1}x_1 - k_{\mathrm{R}2}x_2 + k_{\mathrm{I}}x_{\mathrm{I}} \\ \text{i.e.}\qquad & u = -\boldsymbol{K}_{\mathrm{R}}\boldsymbol{x} + k_{\mathrm{I}}x_{\mathrm{I}} \\ \text{i.e.}\qquad & u = -\overline{\boldsymbol{K}}\overline{\boldsymbol{x}} \end{aligned} \tag{8.14}$$

using $\overline{\boldsymbol{x}} = \left[\boldsymbol{x}^{\mathrm{T}}, x_{\mathrm{I}}\right]^{\mathrm{T}} = [x_1, x_2, x_{\mathrm{I}}]^{\mathrm{T}}$, $\overline{\boldsymbol{K}} = [\boldsymbol{K}_{\mathrm{R}}, -k_{\mathrm{I}}] = [k_1, k_2, -k_{\mathrm{I}}]$ and the additional pseudo state

$$\begin{aligned} & x_{\mathrm{I}} = x_{\mathrm{I}0} + \int_{t_0}^{t} -y \,\mathrm{d}\tau \\ \text{i.e.}\qquad & \dot{x}_{\mathrm{I}} = -y \end{aligned} \tag{8.15}$$

to the extended state-space model with differential equation

$$\begin{aligned} & \begin{bmatrix} \dot{x}_1 \\ \dot{x}_2 \\ \dot{x}_{\mathrm{I}} \end{bmatrix} = \begin{bmatrix} 0 & 1 & 0 \\ -\frac{k}{m} & -\frac{c}{m} & 0 \\ -1 & 0 & 0 \end{bmatrix} \begin{bmatrix} x_1 \\ x_2 \\ x_{\mathrm{I}} \end{bmatrix} + \begin{bmatrix} 0 \\ \frac{b_0}{m} \\ 0 \end{bmatrix} u + \begin{bmatrix} 0 \\ \frac{e}{qm} \\ 0 \end{bmatrix} z \\ \text{i.e.}\qquad & \begin{bmatrix} \dot{\boldsymbol{x}} \\ \dot{x}_{\mathrm{I}} \end{bmatrix} = \begin{bmatrix} \boldsymbol{A} & \boldsymbol{0} \\ -\boldsymbol{C} & 0 \end{bmatrix} \begin{bmatrix} \boldsymbol{x} \\ x_{\mathrm{I}} \end{bmatrix} + \begin{bmatrix} \boldsymbol{B} \\ 0 \end{bmatrix} u + \begin{bmatrix} \boldsymbol{E} \\ 0 \end{bmatrix} z \\ \text{i.e.}\qquad & \dot{\overline{\boldsymbol{x}}} = \overline{\boldsymbol{A}}\overline{\boldsymbol{x}} + \overline{\boldsymbol{B}}u + \overline{\boldsymbol{E}}z \end{aligned} \tag{8.16a}$$

and output equation

$$\begin{aligned} & y = \begin{bmatrix} 1 & 0 & 0 \end{bmatrix} \begin{bmatrix} x_1 \\ x_2 \\ x_{\mathrm{I}} \end{bmatrix} \\ \text{i.e.}\qquad & y = \overline{\boldsymbol{C}}\overline{\boldsymbol{x}}. \end{aligned} \tag{8.16b}$$

The dedicated extended state-feedback matrix $\overline{\boldsymbol{K}} = [k_{\mathrm{R}1}, k_{\mathrm{R}2}, -k_{\mathrm{I}}]$ with weights $k_{\mathrm{R}1}$, $k_{\mathrm{R}2}$ and k_{I} is equally determined via linear-quadratic regulator (LQR) approach but by using the extended state-space model. Again choosing the required weights $\overline{\boldsymbol{Q}} \in \mathbb{R}^{3,3}$ related to $\overline{\boldsymbol{x}}$ and $\overline{r} \in \mathbb{R}^{1,1}$ related to u independent from q also the extended state-feedback matrix itself becomes independent from q.

As before only y is accessible respectively measurable and the first state is therefore directly known $x_1 = y$. The additional integral pseudo state identifies no real physical state. That is why its initial value is rather a choice of the user than related to the physical problem. In this way, direct calculation of x_I is possible. Again only the second state with unknown physical initial value needs an estimation $x_2 \approx \widetilde{x}_2$ and the state observer boils down to the reduced one derived in Equations 8.6 (p. 100) to 8.9 (p. 100).

The final time discretization of the reduced observer and *deactivated* controller

$$\begin{aligned} x_1 &= y \\ \dot{x}_\mathrm{I} &= -y \\ \dot{\underline{\widetilde{x}}}_2 &= a_\mathrm{B}\underline{\widetilde{x}}_2 + b_\mathrm{B}u + e_\mathrm{B}y \\ \widetilde{x}_2 &= \underline{\widetilde{x}}_2 + k_\mathrm{B}y \\ u &= 0 \end{aligned} \tag{8.17}$$

$$\text{i.e.} \qquad \dot{\underline{\widetilde{x}}}_2 = a_\mathrm{B}\underline{\widetilde{x}}_2 + e_\mathrm{B}y$$

with the BDFN (Equation (2.10), p. 11) reads

$$\begin{aligned} x_1^{n+1} &= y^{n+1} \\ \widehat{\alpha}_{n+1}x_\mathrm{I}^{n+1} &= -\sum_{l=0}^{N-1}\left(\widehat{\alpha}_{n-l}x_\mathrm{I}^{n-l}\right) - y^{n+1} \\ [\mathrm{LHS}]\,\underline{\widetilde{x}}_2^{n+1} &= -\sum_{l=0}^{N-1}\left(\widehat{\alpha}_{n-l}\underline{\widetilde{x}}_2^{n-l}\right) + [\mathrm{RHS}]\,y^{n+1} \\ \widetilde{x}_2^{n+1} &= \underline{\widetilde{x}}_2^{n+1} + k_\mathrm{B}y^{n+1} \\ u^{n+1} &= 0 \end{aligned} \tag{8.18a}$$

where

$$\begin{aligned} [\mathrm{LHS}] &= \widehat{\alpha}_{n+1} - a_\mathrm{B} = \widehat{\alpha}_{n+1} + \frac{c}{m} + k_\mathrm{B} \\ [\mathrm{RHS}] &= e_\mathrm{B} = -\left(\frac{c}{m} + k_\mathrm{B}\right)k_\mathrm{B} - \frac{k}{m}. \end{aligned} \tag{8.18b}$$

The final time discretization of reduced observer and *activated* controller

$$\begin{aligned} x_1 &= y \\ \dot{x}_\mathrm{I} &= -y \\ \dot{\underline{\widetilde{x}}}_2 &= a_\mathrm{B}\underline{\widetilde{x}}_2 + b_\mathrm{B}u + e_\mathrm{B}y \\ \widetilde{x}_2 &= \underline{\widetilde{x}}_2 + k_\mathrm{B}y \\ u &= -k_\mathrm{R1}x_1 - k_\mathrm{R2}\widetilde{x}_2 + k_\mathrm{I}x_\mathrm{I} \end{aligned} \tag{8.19}$$

$$\begin{aligned} \text{i.e.} \qquad \dot{\underline{\widetilde{x}}}_2 &= \left(a_\mathrm{B} - b_\mathrm{B}k_\mathrm{R2}\right)\underline{\widetilde{x}}_2 \\ &\quad + \left(e_\mathrm{B} - b_\mathrm{B}\left(k_\mathrm{R1} + k_\mathrm{R2}k_\mathrm{B}\right)\right)y + \left(b_\mathrm{B}k_\mathrm{I}\right)x_\mathrm{I} \end{aligned}$$

becomes

$$
\begin{aligned}
x_1^{n+1} &= y^{n+1} \\
\widehat{\alpha}_{n+1} x_{\mathrm{I}}^{n+1} &= -\sum_{l=0}^{N-1} \left(\widehat{\alpha}_{n-l} x_{\mathrm{I}}^{n-l}\right) - y^{n+1} \\
[\mathrm{LHS}]\, \underline{\widetilde{x}}_2^{n+1} &= -\sum_{l=0}^{N-1} \left(\widehat{\alpha}_{n-l} \underline{\widetilde{x}}_2^{n-l}\right) + [\mathrm{RHS}]\, y^{n+1} + (b_{\mathrm{B}} k_{\mathrm{I}})\, x_{\mathrm{I}}^{n+1} \\
\widetilde{x}_2^{n+1} &= \underline{\widetilde{x}}_2^{n+1} + k_{\mathrm{B}} y^{n+1} \\
u^{n+1} &= -k_{\mathrm{R1}} x_1^{n+1} - k_{\mathrm{R2}} \widetilde{x}_2^{n+1} + k_{\mathrm{I}} x_{\mathrm{I}}
\end{aligned}
\tag{8.20a}
$$

where

$$
\begin{aligned}
[\mathrm{LHS}] &= \widehat{\alpha}_{n+1} - a_{\mathrm{B}} + b_{\mathrm{B}} k_{\mathrm{R2}} = \widehat{\alpha}^{n+1} + \frac{c}{m} + k_{\mathrm{B}} + \frac{b_0}{m} k_{\mathrm{R2}} \\
[\mathrm{RHS}] &= e_{\mathrm{B}} - b_{\mathrm{B}} \left(k_{\mathrm{R1}} + k_{\mathrm{R2}} k_{\mathrm{B}}\right) \\
&= -\left(\frac{c}{m} + k_{\mathrm{B}}\right) k_{\mathrm{B}} - \frac{k}{m} - \frac{b_0}{m} \left(k_{\mathrm{R1}} + k_{\mathrm{R2}} k_{\mathrm{B}}\right).
\end{aligned}
\tag{8.20b}
$$

Again a parameter exploration for observer and controller is performed via MATLAB and Simulink (Little and Moler 1984a,b) under usage of recorded disturbances z from FSI simulations. The resulting final parameter settings are summarized in Table 8.2. Figure 8.7 shows a simplified block diagram from a control theory point of view for the implementation in an own C++ code.

Table 8.2 Parameter settings for LQI controller (CLC) subsystem.

component	*parameter*	*value*	*unit*
controlled system	m	0.0144	kg
	c	0	Ns/m
	k	2.400549	N/m
	b_0	−1.600366	N/m
	e	0.01	1
state- and integral	$\overline{\boldsymbol{Q}}$	$\mathbf{I}$	—
output-feedback	$\overline{r}$	1	—
	k_{R1}	−0.7944	1
	k_{R2}	−1.0071	s
	k_{I}	−1.0000	1/s
state observer	λ_{B}	−2000	1/s
	k_{B}	2000	1/s

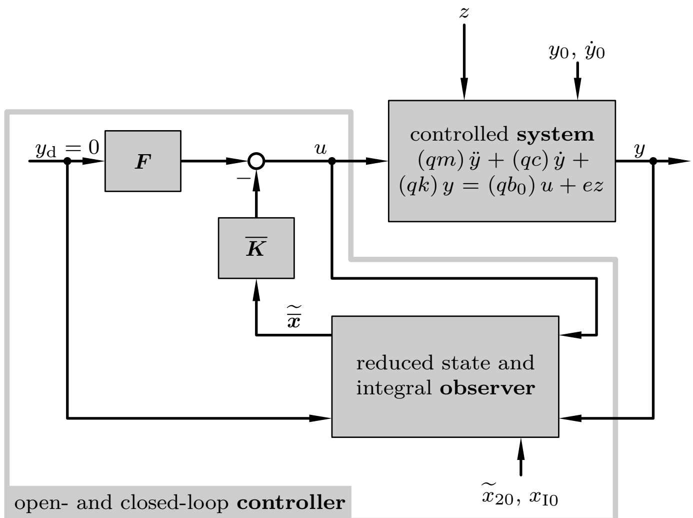

Figure 8.7 Simplified block diagram of LQI controller (CLC) subsystem from a control theory point of view.

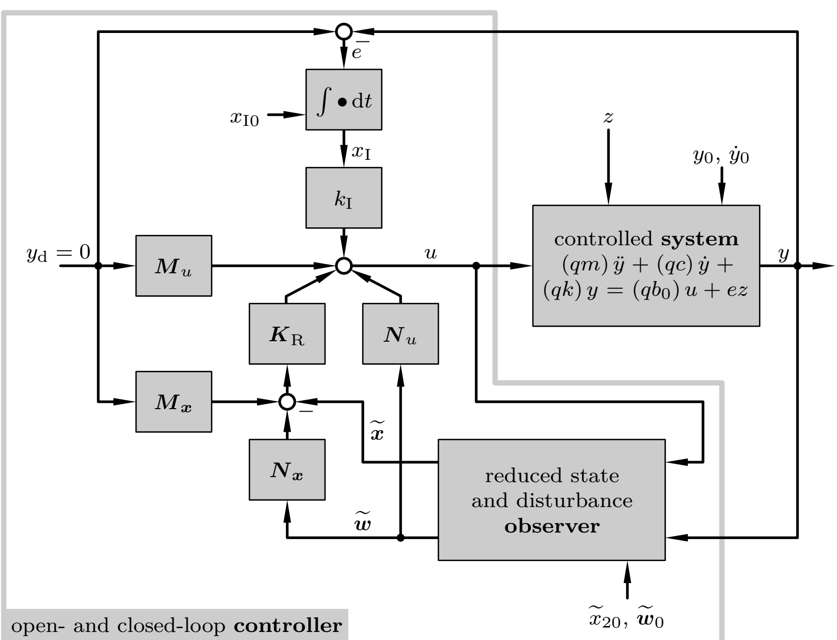

Figure 8.8 Block diagram of LQS controller (CLC) subsystem from a control theory point of view.

8.4 State– and Integral Output–Feedback and Constant Disturbance Feedforward Control (LQS)

This section implements state- and integral output-feedback and constant disturbance feedforward control following an integrated state and disturbance observer as further extension to the LQR and LQI controllers from the previous Sections 8.2 State–Feedback Control (LQR) (pp. 98) ff.) and 8.3 ... and Integral Output–Feedback Control (LQI) (pp. 102 ff.). The controller (state- and integral output-) feedback matrix is set via extended state-space model and linear-quadratic regulator (LQR) approach. The feedforward matrices are determined via constant feedforward approach. And the state and disturbance observer output-feedback matrix is finally defined by pole placement. The acronym LQS only used within this thesis identifies the LQI controller enhanced by disturbance feedforward. The underlying block diagram from a control theory point of view is presented in Figure 8.8. Especially for the mathematical derivations in this section the open-source computer algebra system SageMath (Stein 2005) is used.

State- and integral output-feedback control law (8.14) is extended by constant disturbance feedforward

$$
\begin{aligned}
& u = \boldsymbol{K}_\mathrm{R}\left(\boldsymbol{N}_{\boldsymbol{x}}\boldsymbol{w} - \boldsymbol{x}\right) + \boldsymbol{N}_u\boldsymbol{w} + k_\mathrm{I}x_\mathrm{I} \\
\text{i.e.}\qquad & u = -\boldsymbol{K}_\mathrm{R}\boldsymbol{x} - \boldsymbol{K}_\mathrm{S}\boldsymbol{w} + k_\mathrm{I}x_\mathrm{I} \\
\text{i.e.}\qquad & u = -\widehat{\boldsymbol{K}}\widehat{\boldsymbol{x}} + k_\mathrm{I}x_\mathrm{I}
\end{aligned}
\tag{8.21}
$$

using $\widehat{\boldsymbol{x}} = \left[\boldsymbol{x}^\mathrm{T}, \boldsymbol{w}^\mathrm{T}\right]^\mathrm{T} = \left[x_1, x_2, w_1, w_2, w_3, w_4, w_5\right]^\mathrm{T}$, $\widehat{\boldsymbol{K}} = \left[\boldsymbol{K}_\mathrm{R}, \boldsymbol{K}_\mathrm{S}\right]$, $\boldsymbol{K}_\mathrm{S} = -\left(\boldsymbol{K}_\mathrm{R}\boldsymbol{N}_{\boldsymbol{x}} + \boldsymbol{N}_u\right)$ and the disturbance model (state-space representation) with differential equation

$$
\begin{aligned}
& \begin{bmatrix} \dot{w}_1 \\ \dot{w}_2 \\ \dot{w}_3 \\ \dot{w}_4 \\ \dot{w}_5 \end{bmatrix} = \begin{bmatrix} 0 & 1 & 0 & 0 & 0 \\ -\left(2\pi f_1\right)^2 & 0 & 0 & 0 & 0 \\ 0 & 0 & 0 & 1 & 0 \\ 0 & 0 & -\left(2\pi f_2\right)^2 & 0 & 0 \\ 0 & 0 & 0 & 0 & 0 \end{bmatrix} \begin{bmatrix} w_1 \\ w_2 \\ w_3 \\ w_4 \\ w_5 \end{bmatrix} \\
\text{i.e.}\qquad & \dot{\boldsymbol{w}} = \boldsymbol{W}\boldsymbol{w}
\end{aligned}
\tag{8.22a}
$$

and output equation

$$
\begin{aligned}
& z = \begin{bmatrix} 1 & 0 & 1 & 0 & 1 \end{bmatrix}\boldsymbol{w} \\
\text{i.e.}\qquad & z = \boldsymbol{Z}\boldsymbol{w}
\end{aligned}
\tag{8.22b}
$$

where $\boldsymbol{w} = \left[w_1, w_2, w_3, w_4, w_5\right]^\mathrm{T}$ are the disturbance states and z is the disturbance finally acting on the controlled system.

This disturbance model is based on observations made during the FSI simulations (see Chapter 7 Fluid–Structure Interaction, pp. 79 ff.). It is derived from a detailed analysis of the z-data recorded in the linear range of parameter scaling factor q. This reflects the standard approach in classical control theory: Only the FSCI sub-problem SCI with recorded or modeled disturbance substituting the actual fluid is considered. It proves that the disturbance behavior is dominated by the superposition of two undamped oscillating modes z_1 and z_2 with frequencies f_1 and f_2 and one undamped constant mode z_3

$$\ddot{z}_1 + (2\pi f_1)^2\, z_1 = 0 \tag{8.23a}$$
$$\ddot{z}_2 + (2\pi f_2)^2\, z_2 = 0 \tag{8.23b}$$
$$\dot{z}_3 = 0 \tag{8.23c}$$
$$z = z_1 + z_2 + z_3. \tag{8.23d}$$

Definition of disturbance states $w_1 := z_1$, $w_2 := \dot{z}_1$, $w_3 := z_2$, $w_4 := \dot{z}_2$, $w_5 := z_3$ allows the reformulation as state-space model (8.22). An extraction of initial values $w_{10} = z_{10}$, $w_{20} = \dot{z}_{10}$, $w_{30} = z_{20}$, $w_{40} = \dot{z}_{20}$, $w_{50} = z_{30}$ specifying the amount of each mode on outputted disturbance z is not necessary. This will be carried out by the disturbance observer.

State-feedback weights $k_{\mathrm{R}1}$, $k_{\mathrm{R}2}$ and integral output-feedback weight k_{I} are specified equivalent to Section 8.3 … and Integral Output–Feedback Control (LQI) (pp. 102 ff.).

The constant feedforward matrices $\boldsymbol{N_x} \in \mathbb{R}^{2,5}$ and $\boldsymbol{N}_u \in \mathbb{R}^{1,5}$ are defined via constant feedforward approach

$$\boldsymbol{N_x} = \begin{bmatrix} 0 & 0 & 0 & 0 & 0 \\ 0 & 0 & 0 & 0 & 0 \end{bmatrix} = \boldsymbol{0} \tag{8.24a}$$
$$\boldsymbol{N}_u = \begin{bmatrix} -\frac{e}{b_0} & 0 & -\frac{e}{b_0} & 0 & -\frac{e}{b_0} \end{bmatrix}. \tag{8.24b}$$

It follows $\boldsymbol{K}_{\mathrm{S}} = \left[\frac{e}{b_0}, 0, \frac{e}{b_0}, 0, \frac{e}{b_0}\right]$.

System model (8.4), disturbance model (8.22) and control law (8.21) are combined to an overall state-space model describing the ideally disturbed and controlled system with differential equation

$$\begin{bmatrix} \dot{x}_1 \\ \dot{x}_2 \\ \dot{w}_1 \\ \dot{w}_2 \\ \dot{w}_3 \\ \dot{w}_4 \\ \dot{w}_5 \end{bmatrix} = \begin{bmatrix} 0 & 1 & 0 & 0 & 0 & 0 & 0 \\ -\frac{k}{m} & -\frac{c}{m} & \frac{e}{m} & 0 & \frac{e}{m} & 0 & \frac{e}{m} \\ 0 & 0 & 0 & 1 & 0 & 0 & 0 \\ 0 & 0 & -(2\pi f_1)^2 & 0 & 0 & 0 & 0 \\ 0 & 0 & 0 & 0 & 0 & 1 & 0 \\ 0 & 0 & 0 & 0 & -(2\pi f_2)^2 & 0 & 0 \\ 0 & 0 & 0 & 0 & 0 & 0 & 0 \end{bmatrix} \begin{bmatrix} x_1 \\ x_2 \\ w_1 \\ w_2 \\ w_3 \\ w_4 \\ w_5 \end{bmatrix} + \begin{bmatrix} 0 \\ \frac{b_0}{m} \\ 0 \\ 0 \\ 0 \\ 0 \\ 0 \end{bmatrix} u$$

$$\text{i.e.} \qquad \begin{bmatrix} \dot{\boldsymbol{x}} \\ \dot{\boldsymbol{w}} \end{bmatrix} = \begin{bmatrix} \boldsymbol{A} & \boldsymbol{EZ} \\ \boldsymbol{0} & \boldsymbol{W} \end{bmatrix} \begin{bmatrix} \boldsymbol{x} \\ \boldsymbol{w} \end{bmatrix} + \begin{bmatrix} \boldsymbol{B} \\ \boldsymbol{0} \end{bmatrix} u$$

$$\text{i.e.} \qquad \dot{\widehat{\boldsymbol{x}}} = \widehat{\boldsymbol{A}}\widehat{\boldsymbol{x}} + \widehat{\boldsymbol{B}}u, \tag{8.25a}$$

output equation for measured output y

$$y = \begin{bmatrix} 1 & 0 & 0 & 0 & 0 & 0 & 0 \end{bmatrix} \widehat{\boldsymbol{x}}$$

$$\text{i.e.} \qquad y = \begin{bmatrix} \boldsymbol{C} & \boldsymbol{0} \end{bmatrix} \begin{bmatrix} \boldsymbol{x} \\ \boldsymbol{w} \end{bmatrix} \tag{8.25b}$$

$$\text{i.e.} \qquad y = \widehat{\boldsymbol{C}}\widehat{\boldsymbol{x}},$$

output equation for disturbance z

$$z = \begin{bmatrix} 0 & 0 & 1 & 0 & 1 & 0 & 1 \end{bmatrix} \widehat{\boldsymbol{x}}$$

$$\text{i.e.} \qquad z = \begin{bmatrix} \boldsymbol{0} & \boldsymbol{Z} \end{bmatrix} \begin{bmatrix} \boldsymbol{x} \\ \boldsymbol{w} \end{bmatrix} \tag{8.25c}$$

$$\text{i.e.} \qquad z = \widehat{\boldsymbol{Z}}\widehat{\boldsymbol{x}}$$

and control law

$$u = -\begin{bmatrix} k_{\mathrm{R}1} & k_{\mathrm{R}2} & \frac{e}{b_0} & 0 & \frac{e}{b_0} & 0 & \frac{e}{b_0} \end{bmatrix} \widehat{\boldsymbol{x}} + k_{\mathrm{I}} x_{\mathrm{I}}$$

$$\text{i.e.} \qquad u = -\begin{bmatrix} \boldsymbol{K}_{\mathrm{R}} & \boldsymbol{K}_{\mathrm{S}} \end{bmatrix} \begin{bmatrix} \boldsymbol{x} \\ \boldsymbol{w} \end{bmatrix} + k_{\mathrm{I}} x_{\mathrm{I}} \tag{8.25d}$$

$$\text{i.e.} \qquad u = -\widehat{\boldsymbol{K}}\widehat{\boldsymbol{x}} + k_{\mathrm{I}} x_{\mathrm{I}}.$$

y is accessible in the co-simulation respectively measurable in reality. First state $x_1 = y$ is therefore directly known. The unphysical integral state x_I with user-defined initial value can directly be computed. As before, the second state with unknown physical initial value needs an estimation $x_2 \approx \widetilde{x}_2$. As well, the newly defined disturbance states with unknown physical initial values must be estimated $\boldsymbol{w} \approx \widetilde{\boldsymbol{w}}$. A reduced state- and disturbance observer which includes the reduced state observer from Sections 8.2 State–Feedback Control (LQR) (pp. 98 ff.) and 8.3 … and Integral Output–Feedback Control (LQI) (pp. 102 ff.) is formulated. For this purpose the overall model (8.25) is split up into the measurable part y and the estimated part $\widetilde{\widetilde{\boldsymbol{x}}}_2 = \left[\widetilde{x}_2, \widetilde{\boldsymbol{w}}^\mathrm{T}\right]^\mathrm{T}$

$$\dot{\widetilde{\widetilde{\boldsymbol{x}}}} = \widehat{\boldsymbol{A}}\widetilde{\widetilde{\boldsymbol{x}}} + \widehat{\boldsymbol{B}}u$$

$$\text{i.e.} \qquad \left[\begin{array}{c} \dot{y} \\ \hline \dot{\widetilde{\widetilde{\boldsymbol{x}}}}_2 \end{array}\right] = \left[\begin{array}{c|c} \widehat{a}_{11} & \widehat{\boldsymbol{A}}_{12} \\ \hline \widehat{\boldsymbol{A}}_{21} & \widehat{\boldsymbol{A}}_{22} \end{array}\right] \left[\begin{array}{c} y \\ \hline \widetilde{\widetilde{\boldsymbol{x}}}_2 \end{array}\right] + \left[\begin{array}{c} \widehat{b}_1 \\ \hline \widehat{\boldsymbol{B}}_2 \end{array}\right] u \tag{8.26a}$$

and

$$u = -\widehat{\boldsymbol{K}}\widetilde{\widetilde{\boldsymbol{x}}} + k_\mathrm{I} x_\mathrm{I}$$

$$\text{i.e.} \qquad u = -\left[\begin{array}{c|c} \widehat{k}_1 & \widehat{\boldsymbol{K}}_2 \end{array}\right] \left[\begin{array}{c} y \\ \hline \widetilde{\widetilde{\boldsymbol{x}}}_2 \end{array}\right] + k_\mathrm{I} x_\mathrm{I} \tag{8.26b}$$

with

$$\widehat{a}_{11} = 0 \qquad \wedge \qquad \widehat{\boldsymbol{A}}_{12} = \begin{bmatrix} 1 & 0 & 0 & 0 & 0 & 0 \end{bmatrix}, \tag{8.26c}$$

$$\widehat{\boldsymbol{A}}_{21} = \begin{bmatrix} -\frac{k}{m} \\ 0 \\ 0 \\ 0 \\ 0 \\ 0 \end{bmatrix} \qquad \wedge \qquad \widehat{\boldsymbol{A}}_{22} = \begin{bmatrix} -\frac{c}{m} & \frac{e}{m} & 0 & \frac{e}{m} & 0 & \frac{e}{m} \\ 0 & 0 & 1 & 0 & 0 & 0 \\ 0 & -(2\pi f_1)^2 & 0 & 0 & 0 & 0 \\ 0 & 0 & 0 & 0 & 1 & 0 \\ 0 & 0 & 0 & -(2\pi f_2)^2 & 0 & 0 \\ 0 & 0 & 0 & 0 & 0 & 0 \end{bmatrix}, \tag{8.26d}$$

$$\widehat{b}_1 = 0 \qquad \wedge \qquad \widehat{\boldsymbol{B}}_2 = \begin{bmatrix} \frac{b_0}{m} \\ 0 \\ 0 \\ 0 \\ 0 \\ 0 \end{bmatrix} \tag{8.26e}$$

and

$$\widehat{k}_1 = k_{\mathrm{R}1} \qquad \wedge \qquad \widehat{\boldsymbol{K}}_2 = \begin{bmatrix} k_{\mathrm{R}2} & \frac{e}{b_0} & 0 & \frac{e}{b_0} & 0 & \frac{e}{b_0} \end{bmatrix}. \tag{8.26f}$$

Result is the reduced state and disturbance observer

$$\begin{aligned} \dot{\underline{\widetilde{\widehat{\boldsymbol{x}}}}}_2 &= \boldsymbol{A}_\mathrm{B}\underline{\widetilde{\widehat{\boldsymbol{x}}}}_2 + \boldsymbol{B}_\mathrm{B}u + \boldsymbol{E}_\mathrm{B}y \\ \widetilde{\widehat{\boldsymbol{x}}}_2 &= \underline{\widetilde{\widehat{\boldsymbol{x}}}}_2 + \boldsymbol{K}_\mathrm{B}y \end{aligned} \tag{8.27a}$$

with

$$\begin{aligned} \boldsymbol{A}_\mathrm{B} &= \widehat{\boldsymbol{A}}_{22} - \boldsymbol{K}_\mathrm{B}\widehat{\boldsymbol{A}}_{12} \\ &= \begin{bmatrix} -\frac{c}{m} - k_{\mathrm{B}1} & \frac{e}{m} & 0 & \frac{e}{m} & 0 & \frac{e}{m} \\ -k_{\mathrm{B}2} & 0 & 1 & 0 & 0 & 0 \\ -k_{\mathrm{B}3} & -\left(2\pi f_1\right)^2 & 0 & 0 & 0 & 0 \\ -k_{\mathrm{B}4} & 0 & 0 & 0 & 1 & 0 \\ -k_{\mathrm{B}5} & 0 & 0 & -\left(2\pi f_2\right)^2 & 0 & 0 \\ -k_{\mathrm{B}6} & 0 & 0 & 0 & 0 & 0 \end{bmatrix}, \end{aligned} \tag{8.27b}$$

$$\boldsymbol{B}_\mathrm{B} = \widehat{\boldsymbol{B}}_2 - \boldsymbol{K}_\mathrm{B}\widehat{b}_1 = \begin{bmatrix} \frac{b_0}{m} \\ 0 \\ 0 \\ 0 \\ 0 \\ 0 \end{bmatrix} \tag{8.27c}$$

and

$$\begin{aligned} \boldsymbol{E}_\mathrm{B} &= \left(\widehat{\boldsymbol{A}}_{22} - \boldsymbol{K}_\mathrm{B}\widehat{\boldsymbol{A}}_{12}\right)\boldsymbol{K}_\mathrm{B} + \left(\widehat{\boldsymbol{A}}_{21} - \boldsymbol{K}_\mathrm{B}\widehat{a}_{11}\right) \\ &= \begin{bmatrix} -\frac{k}{m} - \frac{c}{m}k_{\mathrm{B}1} + \frac{e}{m}\left(k_{\mathrm{B}2} + k_{\mathrm{B}4} + k_{\mathrm{B}6}\right) - k_{\mathrm{B}1}^2 \\ k_{\mathrm{B}3} - k_{\mathrm{B}1}k_{\mathrm{B}2} \\ -\left(2\pi f_1\right)^2 k_{\mathrm{B}2} - k_{\mathrm{B}1}k_{\mathrm{B}3} \\ k_{\mathrm{B}5} - k_{\mathrm{B}1}k_{\mathrm{B}4} \\ -\left(2\pi f_2\right)^2 k_{\mathrm{B}4} - k_{\mathrm{B}1}k_{\mathrm{B}5} \\ -k_{\mathrm{B}1}k_{\mathrm{B}6} \end{bmatrix}. \end{aligned} \tag{8.27d}$$

Its output-feedback matrix $\boldsymbol{K}_\mathrm{B} = [k_{\mathrm{B}1}, k_{\mathrm{B}2}, k_{\mathrm{B}3}, k_{\mathrm{B}4}, k_{\mathrm{B}5}, k_{\mathrm{B}6}]^\mathrm{T}$ is defined via the fictive system

$$\left.\begin{aligned} \dot{\boldsymbol{x}}_\mathrm{f} &= \widehat{\boldsymbol{A}}_{22}^\mathrm{T}\boldsymbol{x}_\mathrm{f} + \widehat{\boldsymbol{A}}_{12}^\mathrm{T}u_\mathrm{f} \\ u_\mathrm{f} &= -\boldsymbol{K}_\mathrm{B}^\mathrm{T}\boldsymbol{x}_\mathrm{f} \end{aligned}\right\} \dot{\boldsymbol{x}}_\mathrm{f} = \widehat{\boldsymbol{A}}_\mathrm{Rf}\boldsymbol{x}_\mathrm{f} \tag{8.28}$$

with $\widehat{\boldsymbol{A}}_\mathrm{Rf} = \widehat{\boldsymbol{A}}_{22}^\mathrm{T} - \widehat{\boldsymbol{A}}_{12}^\mathrm{T}\boldsymbol{K}_\mathrm{B}^\mathrm{T}$ and pole placement

$$\det\left(s\mathbf{I} - \widehat{\boldsymbol{A}}_\mathrm{Rf}\right) \stackrel{!}{=} \prod_{i=1}^{6}(s - \lambda_{\mathrm{B}i}) \qquad \Leftrightarrow \qquad \boldsymbol{K}_\mathrm{B} = \ldots \tag{8.29}$$

where either $\lambda_{\mathrm{B}i} \stackrel{!}{\in} \mathbb{R}$ or $\lambda_{\mathrm{B}i} \stackrel{!}{\in} \mathbb{C}$ and pairwise complex conjugate and for all $\mathrm{Re}\{\lambda_{\mathrm{B}i}\} \stackrel{!}{\ll} \mathrm{Re}\{\lambda_j\} = \left\{-\frac{c}{m}, 0, 0, 0, 0, 0\right\} \leq 0$ with $i, j = 1, \ldots, 6$.

The final time discretization of the reduced observer and *deactivated* controller

$$\begin{aligned} x_1 &= y \\ \dot{x}_\mathrm{I} &= -y \\ \dot{\underline{\widetilde{\widehat{\boldsymbol{x}}}}}_2 &= \boldsymbol{A}_\mathrm{B}\underline{\widetilde{\widehat{\boldsymbol{x}}}}_2 + \boldsymbol{B}_\mathrm{B}u + \boldsymbol{E}_\mathrm{B}y \\ \widetilde{\widehat{\boldsymbol{x}}}_2 &= \underline{\widetilde{\widehat{\boldsymbol{x}}}}_2 + \boldsymbol{K}_\mathrm{B}y \\ u &= 0 \end{aligned} \tag{8.30}$$

$$\text{i.e.} \qquad \dot{\underline{\widetilde{\widehat{\boldsymbol{x}}}}}_2 = \boldsymbol{A}_\mathrm{B}\underline{\widetilde{\widehat{\boldsymbol{x}}}}_2 + \boldsymbol{E}_\mathrm{B}y$$

with the BDFN (Equation (2.10), p. 11) reads

$$\begin{aligned} x_1^{n+1} &= y^{n+1} \\ \widehat{\alpha}_{n+1}x_\mathrm{I}^{n+1} &= -\sum_{l=0}^{N-1}\left(\widehat{\alpha}_{n-l}x_\mathrm{I}^{n-l}\right) - y^{n+1} \\ [\mathrm{LHS}]\,\underline{\widetilde{\widehat{\boldsymbol{x}}}}_2^{n+1} &= -\sum_{l=0}^{N-1}\left(\widehat{\alpha}_{n-l}\underline{\widetilde{\widehat{\boldsymbol{x}}}}_2^{n-l}\right) + [\mathrm{RHS}]\,y^{n+1} \\ \widetilde{\widehat{\boldsymbol{x}}}_2^{n+1} &= \underline{\widetilde{\widehat{\boldsymbol{x}}}}_2^{n+1} + \boldsymbol{K}_\mathrm{B}y^{n+1} \\ u^{n+1} &= 0 \end{aligned} \tag{8.31a}$$

where

$$[\mathrm{LHS}] = \widehat{\alpha}_{n+1}\mathbf{I} - \boldsymbol{A}_{\mathrm{B}} = \widehat{\alpha}_{n+1}\mathbf{I} - \widehat{\boldsymbol{A}}_{22} + \boldsymbol{K}_{\mathrm{B}}\widehat{\boldsymbol{A}}_{12}$$
$$= \begin{bmatrix} \widehat{\alpha}_{n+1} + \frac{c}{m} + k_{\mathrm{B1}} & -\frac{e}{m} & 0 & -\frac{e}{m} & 0 & -\frac{e}{m} \\ k_{\mathrm{B2}} & \widehat{\alpha}_{n+1} & -1 & 0 & 0 & 0 \\ k_{\mathrm{B3}} & (2\pi f_1)^2 & \widehat{\alpha}_{n+1} & 0 & 0 & 0 \\ k_{\mathrm{B4}} & 0 & 0 & \widehat{\alpha}_{n+1} & -1 & 0 \\ k_{\mathrm{B5}} & 0 & 0 & (2\pi f_2)^2 & \widehat{\alpha}_{n+1} & 0 \\ k_{\mathrm{B6}} & 0 & 0 & 0 & 0 & \widehat{\alpha}_{n+1} \end{bmatrix} \tag{8.31b}$$

and

$$[\mathrm{RHS}] = \boldsymbol{E}_{\mathrm{B}} = \left(\widehat{\boldsymbol{A}}_{22} - \boldsymbol{K}_{\mathrm{B}}\widehat{\boldsymbol{A}}_{12}\right)\boldsymbol{K}_{\mathrm{B}} + \left(\widehat{\boldsymbol{A}}_{21} - \boldsymbol{K}_{\mathrm{B}}\widehat{a}_{11}\right)$$
$$= \begin{bmatrix} -\frac{k}{m} - \frac{c}{m}k_{\mathrm{B1}} + \frac{e}{m}\left(k_{\mathrm{B2}} + k_{\mathrm{B4}} + k_{\mathrm{B6}}\right) - k_{\mathrm{B1}}^2 \\ k_{\mathrm{B3}} - k_{\mathrm{B1}}k_{\mathrm{B2}} \\ -\left(2\pi f_1\right)^2 k_{\mathrm{B2}} - k_{\mathrm{B1}}k_{\mathrm{B3}} \\ k_{\mathrm{B5}} - k_{\mathrm{B1}}k_{\mathrm{B4}} \\ -\left(2\pi f_2\right)^2 k_{\mathrm{B4}} - k_{\mathrm{B1}}k_{\mathrm{B5}} \\ -k_{\mathrm{B1}}k_{\mathrm{B6}} \end{bmatrix}. \tag{8.31c}$$

The final time discretization of the reduced observer and *activated* controller

$$\begin{aligned} x_1 &= y \\ \dot{x}_{\mathrm{I}} &= -y \\ \dot{\underline{\widetilde{\widetilde{\boldsymbol{x}}}}}_2 &= \boldsymbol{A}_{\mathrm{B}}\underline{\widetilde{\widetilde{\boldsymbol{x}}}}_2 + \boldsymbol{B}_{\mathrm{B}}u + \boldsymbol{E}_{\mathrm{B}}y \\ \widetilde{\widetilde{\boldsymbol{x}}}_2 &= \underline{\widetilde{\widetilde{\boldsymbol{x}}}}_2 + \boldsymbol{K}_{\mathrm{B}}y \\ u &= -\widehat{k}_1 x_1 - \widehat{\boldsymbol{K}}_2\widetilde{\widetilde{\boldsymbol{x}}}_2 + k_{\mathrm{I}}x_{\mathrm{I}} \end{aligned} \tag{8.32}$$

$$\text{i.e.} \quad \begin{aligned} \dot{\underline{\widetilde{\widetilde{x}}}}_2 = {} & \left(\boldsymbol{A}_{\mathrm{B}} - \boldsymbol{B}_{\mathrm{B}}\widehat{\boldsymbol{K}}_2\right)\underline{\widetilde{\widetilde{\boldsymbol{x}}}}_2 \\ & + \left(\boldsymbol{E}_{\mathrm{B}} - \boldsymbol{B}_{\mathrm{B}}\left(\widehat{k}_1 + \widehat{\boldsymbol{K}}_2\boldsymbol{K}_{\mathrm{B}}\right)\right)y + \left(\boldsymbol{B}_{\mathrm{B}}k_{\mathrm{I}}\right)x_{\mathrm{I}} \end{aligned}$$

becomes

$$
\begin{aligned}
x_1^{n+1} &= y^{n+1} \\
\widehat{\alpha}_{n+1} x_{\mathrm{I}}^{n+1} &= -\sum_{l=0}^{N-1} \left(\widehat{\alpha}_{n-l} x_{\mathrm{I}}^{n-l}\right) - y^{n+1} \\
[\mathrm{LHS}]\, \underline{\widetilde{\widehat{\boldsymbol{x}}}}_2^{n+1} &= -\sum_{l=0}^{N-1} \left(\widehat{\alpha}_{n-l} \underline{\widetilde{\widehat{\boldsymbol{x}}}}_2^{n-l}\right) + [\mathrm{RHS}]\, y^{n+1} + \left(\boldsymbol{B}_{\mathrm{B}} k_{\mathrm{I}}\right) x_{\mathrm{I}}^{n+1} \\
\widetilde{\widehat{\boldsymbol{x}}}_2^{n+1} &= \underline{\widetilde{\widehat{\boldsymbol{x}}}}_2^{n+1} + \boldsymbol{K}_{\mathrm{B}} y^{n+1} \\
u^{n+1} &= -\widehat{k}_1 x_1^{n+1} - \widehat{\boldsymbol{K}}_2 \widetilde{\widehat{\boldsymbol{x}}}_2^{n+1} + k_{\mathrm{I}} x_{\mathrm{I}}
\end{aligned}
\tag{8.33a}
$$

with

$$
\begin{aligned}
[\mathrm{LHS}] &= \widehat{\alpha}_{n+1} \mathbf{I} - \boldsymbol{A}_{\mathrm{B}} + \boldsymbol{B}_{\mathrm{B}} \widehat{\boldsymbol{K}}_2 \\
&= \widehat{\alpha}_{n+1} \mathbf{I} - \widehat{\boldsymbol{A}}_{22} + \boldsymbol{K}_{\mathrm{B}} \widehat{\boldsymbol{A}}_{12} + \left(\widehat{\boldsymbol{B}}_2 - \boldsymbol{K}_{\mathrm{B}} \widehat{b}_1\right) \widehat{\boldsymbol{K}}_2
\end{aligned}
$$

$$
= \begin{bmatrix}
\widehat{\alpha}_{n+1} + \frac{c}{m} + \frac{b_0}{m} k_{\mathrm{R}2} + k_{\mathrm{B}1} & 0 & 0 & 0 & 0 & 0 \\
k_{\mathrm{B}2} & \widehat{\alpha}_{n+1} & -1 & 0 & 0 & 0 \\
k_{\mathrm{B}3} & (2\pi f_1)^2 & \widehat{\alpha}_{n+1} & 0 & 0 & 0 \\
k_{\mathrm{B}4} & 0 & 0 & \widehat{\alpha}_{n+1} & -1 & 0 \\
k_{\mathrm{B}5} & 0 & 0 & (2\pi f_2)^2 & \widehat{\alpha}_{n+1} & 0 \\
k_{\mathrm{B}6} & 0 & 0 & 0 & 0 & \widehat{\alpha}_{n+1}
\end{bmatrix}
\tag{8.33b}
$$

and

$$
\begin{aligned}
[\mathrm{RHS}] &= \boldsymbol{E}_{\mathrm{B}} - \boldsymbol{B}_{\mathrm{B}} \left(\widehat{k}_1 + \widehat{\boldsymbol{K}}_2 \boldsymbol{K}_{\mathrm{B}}\right) \\
&= \left(\widehat{\boldsymbol{A}}_{22} - \boldsymbol{K}_{\mathrm{B}} \widehat{\boldsymbol{A}}_{12}\right) \boldsymbol{K}_{\mathrm{B}} + \left(\widehat{\boldsymbol{A}}_{21} - \boldsymbol{K}_{\mathrm{B}} \widehat{a}_{11}\right) \\
&\quad - \left(\widehat{\boldsymbol{B}}_2 - \boldsymbol{K}_{\mathrm{B}} \widehat{b}_1\right) \left(\widehat{k}_1 + \widehat{\boldsymbol{K}}_2 \boldsymbol{K}_{\mathrm{B}}\right) \\
&= \begin{bmatrix}
-\frac{k}{m} - \frac{c}{m} k_{\mathrm{B}1} - \frac{b_0}{m} \left(k_{\mathrm{R}1} + k_{\mathrm{R}2} k_{\mathrm{B}1}\right) - k_{\mathrm{B}1}^2 \\
k_{\mathrm{B}3} - k_{\mathrm{B}1} k_{\mathrm{B}2} \\
-(2\pi f_1)^2 k_{\mathrm{B}2} - k_{\mathrm{B}1} k_{\mathrm{B}3} \\
k_{\mathrm{B}5} - k_{\mathrm{B}1} k_{\mathrm{B}4} \\
-(2\pi f_2)^2 k_{\mathrm{B}4} - k_{\mathrm{B}1} k_{\mathrm{B}5} \\
-k_{\mathrm{B}1} k_{\mathrm{B}6}
\end{bmatrix} .
\end{aligned}
\tag{8.33c}
$$

Once more a parameter exploration for observer and controller in MATLAB and Simulink (Little and Moler 1984a,b) using recorded disturbances

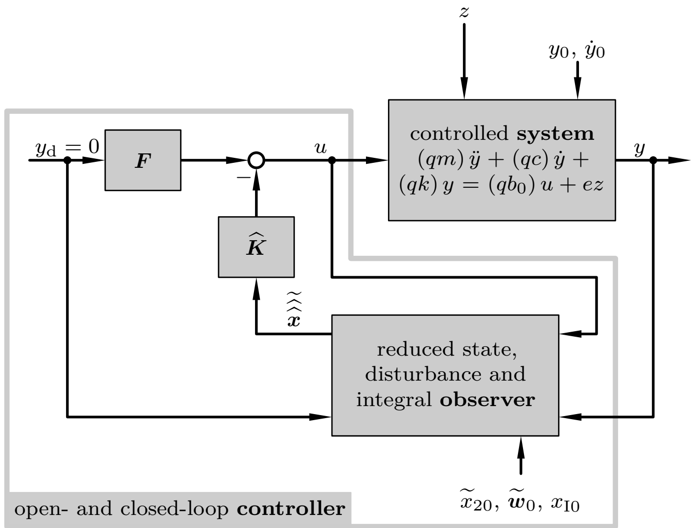

Figure 8.9 SIMPLIFIED BLOCK DIAGRAM OF LQS CONTROLLER (CLC) SUBSYSTEM FROM A CONTROL THEORY POINT OF VIEW.

z is done. Resulting final parameter settings are summarized in Table 8.3. For implementational purposes Figure 8.9 shows a simplified block diagram from a control theory point of view.

Table 8.3 PARAMETER SETTINGS FOR LQS CONTROLLER (CLC) SUBSYSTEM.

component	*parameter*	*value*	*unit*
controlled system	m	0.0144	kg
	c	0	Ns/m
	k	2.400549	N/m
	b_0	-1.600366	N/m
	e	0.01	1
state- and integral output-feedback	$\widehat{\boldsymbol{Q}}$	$\mathbf{I}$	—
	$\widehat{r}$	1	—
	k_{R1}	-0.7944	1
	k_{R2}	-1.0071	s
	k_{I}	-1.0000	1/s
state and disturbance observer	f_1	4.1221	1/s
	f_2	8.2617	1/s
	λ_{B1}	-2000	1/s
	$\lambda_{\mathrm{B2,3}}$	$-20 \pm \mathrm{j}2\pi f_1$	1/s
	$\lambda_{\mathrm{B4,5}}$	$-20 \pm \mathrm{j}2\pi f_2$	1/s
	λ_{B6}	-200	1/s
	k_{B1}	2.2800×10^3	1/s
	k_{B2}/q	2.2076×10^5	N/m
	k_{B3}/q	3.1931×10^7	N/ms
	k_{B4}/q	-4.4382×10^5	N/m
	k_{B5}/q	2.1604×10^7	N/ms
	k_{B6}/q	1.0560×10^6	N/m

Wege enstehen dadurch, dass man sie geht.

Franz Kafka

—Franz Kafka (1883–1924)

9 Fluid–Structure–Control Interaction

This very last chapter is now finally dedicated to full fluid-structure-control interaction, briefly written as FSCI, bearing the initial intentions of this work. FSCI in this context characterizes the multi-physical problem involving fluid, structure and closed-loop structural control: Fluid and structure form a classical FSI problem as introduced by Chapter 7 Fluid–Structure Interaction (pp. 79 ff.) in which however the dynamical behavior of the structure is adapted by a controller. Implied sub-problems are the already mentioned fluid-structure interaction (FSI) and structure-control interaction (SCI). The enclosed FSI is governing the underlying dynamics and physics while SCI on the other hand is only used for derivation and implementation of appropriate control laws (see Chapter 8 The Controller (CLC) Subsystem, pp. 94 ff.).

A first intention of this chapter is to investigate the exemplarily implemented LQR, LQI and LQS controller (CLC) subsystems within the full FSCI. Their control laws are derived in the preceding Chapter 8 The Controller (CLC) Subsystem (pp. 94 ff.) by decoupling the SCI sub-problem from the actual FSCI and substituting the fluid (CFD) subsystem with the appropriate recorded FSI disturbance. This procedure assumes an operation of the coupled system in the linear parameter scaling factor range. As already shown in Chapter 7 Fluid–Structure Interaction (pp. 79 ff.) the actual dominating FSI (sub-) problem can get strongly non-linear dependent on the parameter scaling factor q. Therefore, an operational range for each control law and controller (CLC) subsystem in terms of q will be assessed. For this purpose, again extensive parameter scaling tests are performed. Additional arising dynamical effects differing FSCI from FSI will also be developed. The second main intention of this final chapter is the implementation and a subsequent assessment of partitioned schemes for computational FSCI. The simple model problem of Chapter3 Model Problem (pp. 32 ff.) already predicted unconditional stability (convergence) for all schemes. Besides, the numerical effort is measured and analyzed allowing for comparison and ranking between the suggested schemes. This includes also the evaluation of necessity of nesting.

9.1 Implementation of Partitioned Schemes

In the following solution procedures for this work's FSCI problem class are proposed. They denote partitioned approaches (co-simulations) with iterative coupling formulated in terms of fixed-point iterations on the interface displacements, measured output inclusive. Aitken acceleration according to Küttler and Wall (2008) and Küttler (2009) is employed. Thus, computational FSCI is implemented as 3-code coupling of fluid (CFD), structural (CSM) and controller (CLC) subsystem. Interface constraints enforce the balance of disturbances $\boldsymbol{z}$ and the kinematic compatibility in the displacements $\boldsymbol{y}$ at the FSI interface as well as the kinematic compatibility of the measured output y and the control input u at the SCI interface. Three different schemes are proposed, namely FSCI, F[SC]I and [FS]CI. FSCI typifies a scheme with simple interface iteration loop while F[SC]I and [FS]CI mark schemes with an outer loop nesting the respective sub-problem FSI or SCI in an inner loop.

Chapter 5 The Fluid (CFD) Subsystem (pp. 57 ff.) establishes the fluid (CFD) subsystem

$$\left.\begin{aligned} \mathcal{F}_{\mathrm{F}}\left(\boldsymbol{x}_{\mathrm{F}}^{n+1}, \boldsymbol{y}_{\mathrm{F}}^{n+1}\right) = \mathbf{0} \\ \boldsymbol{z}_{\mathrm{F}}^{n+1} = \mathcal{G}_{\mathrm{F}}\left(\boldsymbol{x}_{\mathrm{F}}^{n+1}, \boldsymbol{y}_{\mathrm{F}}^{n+1}\right) \end{aligned}\right\} \; \boldsymbol{z}_{\mathrm{F}}^{n+1} = \mathcal{G}_{\mathrm{F}}^{\left[\boldsymbol{x}_{\mathrm{F}}^{n+1}\right]}\left(\boldsymbol{y}_{\mathrm{F}}^{n+1}\right), \tag{9.1a}$$

Chapter 6 The Structural (CSM) Subsystem (pp. 68 ff.) the structural (CSM) subsystem(s)

$$\left.\begin{aligned} \mathcal{F}_{\mathrm{S}}\left(\boldsymbol{x}_{\mathrm{S}}^{n+1}, \boldsymbol{z}_{\mathrm{S}}^{n+1}, u_{\mathrm{S}}^{n+1}\right) = \mathbf{0} \\ \boldsymbol{y}_{\mathrm{S}}^{n+1} = \mathcal{G}_{\mathrm{S}}\left(\boldsymbol{x}_{\mathrm{S}}^{n+1}, \boldsymbol{z}_{\mathrm{S}}^{n+1}, u_{\mathrm{S}}^{n+1}\right) \end{aligned}\right\} \; \boldsymbol{y}_{\mathrm{S}}^{n+1} = \mathcal{G}_{\mathrm{S}}^{\left[\boldsymbol{x}_{\mathrm{S}}^{n+1}\right]}\left(\boldsymbol{z}_{\mathrm{S}}^{n+1}, u_{\mathrm{S}}^{n+1}\right) \tag{9.1b}$$

and Chapter 8 The Controller (CLC) Subsystem (pp. 94 ff.) the controller (CLC) subsystem(s)

$$\left.\begin{aligned} \mathcal{F}_{\mathrm{C}}\left(\boldsymbol{x}_{\mathrm{C}}^{n+1}, y_{\mathrm{C}}^{n+1}\right) = \mathbf{0} \\ \boldsymbol{u}_{\mathrm{C}}^{n+1} = \mathcal{G}_{\mathrm{C}}\left(\boldsymbol{x}_{\mathrm{C}}^{n+1}, y_{\mathrm{C}}^{n+1}\right) \end{aligned}\right\} \; u_{\mathrm{C}}^{n+1} = \mathcal{G}_{\mathrm{C}}^{\left[\boldsymbol{x}_{\mathrm{C}}^{n+1}\right]}\left(y_{\mathrm{C}}^{n+1}\right). \tag{9.1c}$$

The interface constraints for the simple loop of scheme FSCI are specified as

$$
\begin{aligned}
\mathcal{I}_{\boldsymbol{y}}\left(\boldsymbol{y}_{\mathrm{F}}^{n+1}, \boldsymbol{y}_{\mathrm{S}}^{n+1}\right) &= \boldsymbol{y}_{\mathrm{F}} - \boldsymbol{y}_{\mathrm{S}}^{n+1} = \mathbf{0} \\
\mathcal{I}_{\boldsymbol{z}}\left(\boldsymbol{z}_{\mathrm{F}}^{n+1}, \boldsymbol{z}_{\mathrm{S}}^{n+1}\right) &= \boldsymbol{z}_{\mathrm{F}}^{n+1} + \boldsymbol{z}_{\mathrm{S}}^{n+1} = \mathbf{0} \\
\mathcal{I}_{y}\left(y_{\mathrm{S}}^{n+1}, y_{\mathrm{C}}^{n+1}\right) &= y_{\mathrm{S}}^{n+1} - y_{\mathrm{C}}^{n+1} = 0 \\
\mathcal{I}_{u}\left(u_{\mathrm{S}}^{n+1}, u_{\mathrm{C}}^{n+1}\right) &= u_{\mathrm{S}}^{n+1} - u_{\mathrm{C}}^{n+1} = 0
\end{aligned}
\tag{9.2}
$$

$$
\text{i.e.} \qquad \mathcal{I}_{\mathrm{FSCI}}\left(\boldsymbol{y}_{\mathrm{F}}^{n+1}, \boldsymbol{y}_{\mathrm{S}}^{n+1}, \boldsymbol{z}_{\mathrm{F}}^{n+1}, \boldsymbol{z}_{\mathrm{S}}^{n+1}, y_{\mathrm{S}}^{n+1}, y_{\mathrm{C}}^{n+1}, u_{\mathrm{S}}^{n+1}, u_{\mathrm{C}}^{n+1}\right) = \mathbf{0}.
$$

This results in coupling Algorithm 9.1 (continued 9.2). The block diagram of the underlying Gauß-Seidel (GS) communication pattern can be seen in Figure 9.1.

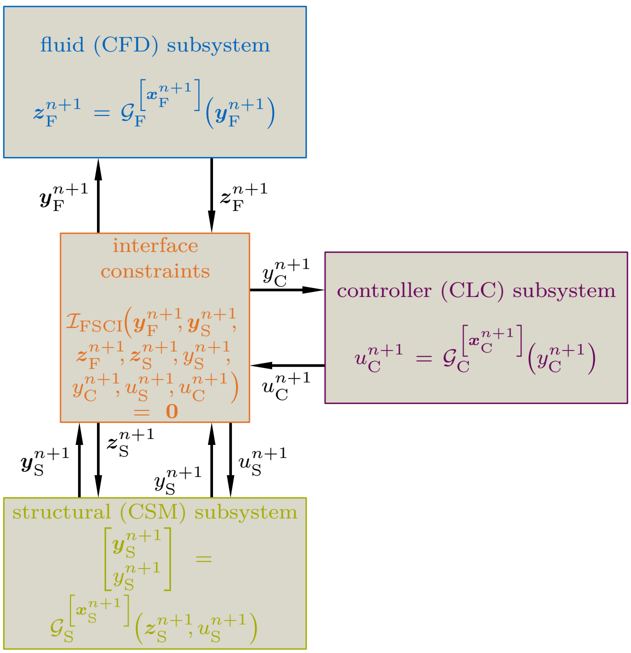

Figure 9.1 BLOCK DIAGRAM OF FSCI CO-SIMULATION WITH FSCI SCHEME.

Scheme [FS]CI defines the interface constraints for its inner FSI loop as

$$
\begin{aligned}
\mathcal{I}_{\boldsymbol{y}}\left(\boldsymbol{y}_{\mathrm{F}}^{n+1}, \boldsymbol{y}_{\mathrm{S}}^{n+1}\right) &= \boldsymbol{y}_{\mathrm{F}} - \boldsymbol{y}_{\mathrm{S}}^{n+1} = \mathbf{0} \\
\mathcal{I}_{\boldsymbol{z}}\left(\boldsymbol{z}_{\mathrm{F}}^{n+1}, \boldsymbol{z}_{\mathrm{S}}^{n+1}\right) &= \boldsymbol{z}_{\mathrm{F}}^{n+1} + \boldsymbol{z}_{\mathrm{S}}^{n+1} = \mathbf{0}
\end{aligned}
\tag{9.3a}
$$

$$
\text{i.e.} \qquad \mathcal{I}_{\mathrm{FSI}}\left(\boldsymbol{y}_{\mathrm{F}}^{n+1}, \boldsymbol{y}_{\mathrm{S}}^{n+1}, \boldsymbol{z}_{\mathrm{F}}^{n+1}, \boldsymbol{z}_{\mathrm{S}}^{n+1}\right) = \mathbf{0}
$$

and for its outer [FS]CI loop as

$$
\begin{aligned}
\mathcal{I}_y\left(y_{\mathrm{S}}^{n+1}, y_{\mathrm{C}}^{n+1}\right) &= y_{\mathrm{S}}^{n+1} - y_{\mathrm{C}}^{n+1} = 0 \\
\mathcal{I}_u\left(u_{\mathrm{S}}^{n+1}, u_{\mathrm{C}}^{n+1}\right) &= u_{\mathrm{S}}^{n+1} - u_{\mathrm{C}}^{n+1} = 0 \\
\text{i.e.} \qquad \mathcal{I}_{[\mathrm{FS}]\mathrm{CI}}\left(y_{\mathrm{S}}^{n+1}, y_{\mathrm{C}}^{n+1}, u_{\mathrm{S}}^{n+1}, u_{\mathrm{C}}^{n+1}\right) &= \mathbf{0}.
\end{aligned}
\tag{9.3b}
$$

The result is coupling Algorithm 9.3 (continued 9.4). Figure 9.2 shows the block diagram of the underlying Gauß-Seidel (GS) communication pattern.

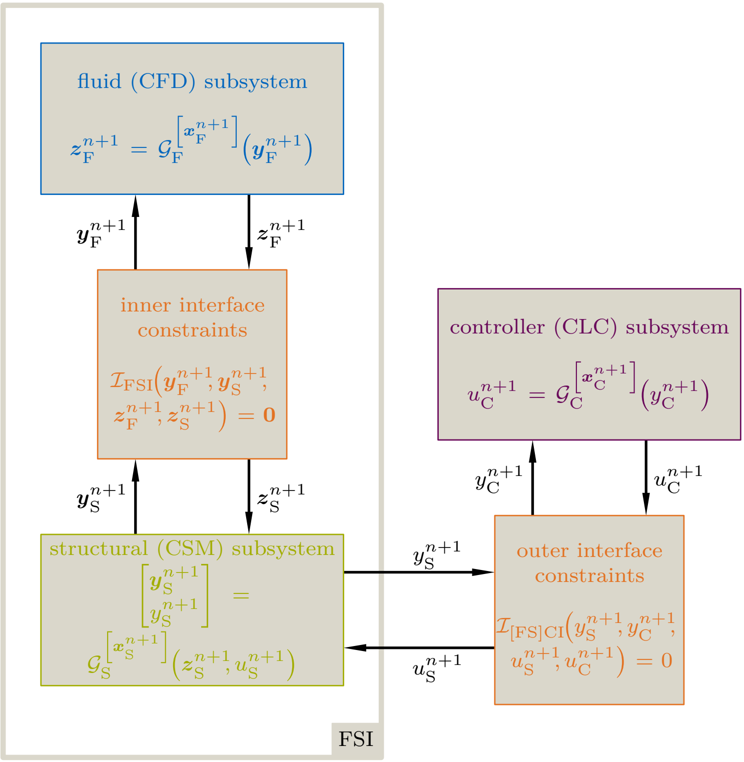

Figure 9.2 Block diagram of FSCI co-simulation with [FS]CI scheme.

Scheme F[SC]I implements

$$
\begin{aligned}
\mathcal{I}_y\left(y_{\mathrm{S}}^{n+1}, y_{\mathrm{C}}^{n+1}\right) &= y_{\mathrm{S}}^{n+1} - y_{\mathrm{C}}^{n+1} = 0 \\
\mathcal{I}_u\left(u_{\mathrm{S}}^{n+1}, u_{\mathrm{C}}^{n+1}\right) &= u_{\mathrm{S}}^{n+1} - u_{\mathrm{C}}^{n+1} = 0 \\
\text{i.e.} \qquad \mathcal{I}_{\mathrm{SCI}}\left(y_{\mathrm{S}}^{n+1}, y_{\mathrm{C}}^{n+1}, u_{\mathrm{S}}^{n+1}, u_{\mathrm{C}}^{n+1}\right) &= \mathbf{0}
\end{aligned}
\tag{9.4a}
$$

as the interface constraints for its inner SCI loop and

$$\begin{aligned} \mathcal{I}_{\boldsymbol{y}}\left(\boldsymbol{y}_{\mathrm{F}}^{n+1}, \boldsymbol{y}_{\mathrm{S}}^{n+1}\right) &= \boldsymbol{y}_{\mathrm{F}} - \boldsymbol{y}_{\mathrm{S}}^{n+1} = \mathbf{0} \\ \mathcal{I}_{\boldsymbol{z}}\left(\boldsymbol{z}_{\mathrm{F}}^{n+1}, \boldsymbol{z}_{\mathrm{S}}^{n+1}\right) &= \boldsymbol{z}_{\mathrm{F}}^{n+1} + \boldsymbol{z}_{\mathrm{S}}^{n+1} = \mathbf{0} \\ \text{i.e.} \qquad \mathcal{I}_{\mathrm{F[SC]I}}\left(\boldsymbol{y}_{\mathrm{F}}^{n+1}, \boldsymbol{y}_{\mathrm{S}}^{n+1}, \boldsymbol{z}_{\mathrm{F}}^{n+1}, \boldsymbol{z}_{\mathrm{S}}^{n+1}\right) &= \mathbf{0} \end{aligned} \tag{9.4b}$$

as the ones for its outer F[SC]I loop. Coupling Algorithm 9.5 (continued 9.6) is the outcome. The underlying Gauß-Seidel (GS) communication pattern is illustrated with the block diagram in Figure 9.3.

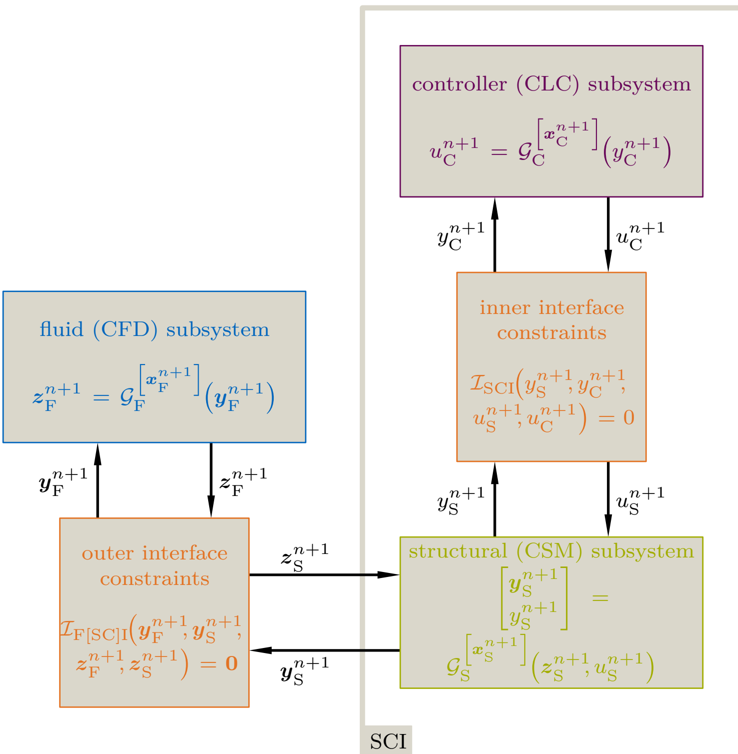

Figure 9.3 Block diagram of FSCI co-simulation with F[SC]I scheme.

Two distinct interfaces can be identified, FSI and SCI, reflecting the respective sub-problems. The SCI interface simply links the signals y and u between structural (CSM) and controller (CLC) subsystem and therefore possesses no spatial distribution. The FSI interface however identifies the spatially distributed common boundary of fluid (CFD) and structural (CSM) subsystem with the associated fields $\boldsymbol{z}$ and $\boldsymbol{y}$ (compare Chapter 7 Fluid–Structure Interaction, pp. 79 ff.). Its matching interface meshes have

Algorithm 9.1 PSEUDO CODE OF PARTITIONED SCHEME FSCI FOR FSCI CO-SIMULATION.

`// initialize states, i.e. set ICs...`
$^{k_{\text{end}}}\boldsymbol{x}_{\text{F}}^{0} \longleftarrow \boldsymbol{x}_{\text{F}}^{\text{init}}$
$^{k_{\text{end}}}\boldsymbol{x}_{\text{S}}^{0} \longleftarrow \boldsymbol{x}_{\text{S}}^{\text{init}}$
$^{k_{\text{end}}}\boldsymbol{x}_{\text{C}}^{0} \longleftarrow \boldsymbol{x}_{\text{C}}^{\text{init}}$

`// initialize displacements and measured output...`
$^{k_{\text{end}}}\boldsymbol{y}_{\text{S}}^{0} \longleftarrow \boldsymbol{y}_{\text{S}}^{\text{init}}$
$^{k_{\text{end}}}y_{\text{S}}{}^{0} \longleftarrow y_{\text{S}}^{\text{init}}$

`// do co-simulation...`
`// time loop...`
for $n \longleftarrow 0$ *to* $n \longleftarrow n_{\text{end}} - 1$ **do**
- `// predict displacements and measured output...`
- $^{0}\boldsymbol{y}_{\text{S}}^{n+1} \longleftarrow {}^{k_{\text{end}}}\boldsymbol{y}_{\text{S}}^{n}$
- $^{0}y_{\text{S}}^{n+1} \longleftarrow {}^{k_{\text{end}}}y_{\text{S}}^{n}$
- `// interface iteration loop, i.e. FSCI loop...`
- **for** $k \longleftarrow 0$ *to* $k \longleftarrow k_{\max}$ **do**
  - `// map displacements from solid to fluid...`
  - `// and copy measured output from solid to controller...`
  - $^{k}\boldsymbol{y}_{\text{F}}^{n+1} \longleftarrow \mathcal{M}_{\boldsymbol{y}}\left({}^{k}\boldsymbol{y}_{\text{S}}^{n+1}\right)$
  - $^{k}y_{\text{C}}{}^{n+1} \longleftarrow {}^{k}y_{\text{S}}{}^{n+1}$
  - `// solve fluid and controller in parallel...`
  - $^{k}\boldsymbol{z}_{\text{F}}^{n+1} \longleftarrow \mathcal{G}_{\text{F}}^{\left[{}^{k}\boldsymbol{x}_{\text{F}}^{n+1}\right]}\left({}^{k}\boldsymbol{y}_{\text{F}}^{n+1}\right)$
  - $^{k}u_{\text{C}}^{n+1} \longleftarrow \mathcal{G}_{\text{C}}^{\left[{}^{k}\boldsymbol{x}_{\text{C}}^{n+1}\right]}\left({}^{k}y_{\text{C}}^{n+1}\right)$
  - `// map forces from fluid to solid...`
  - `// and copy control input from controller to solid...`
  - $^{k}\boldsymbol{z}_{\text{S}}^{n+1} \longleftarrow \mathcal{M}_{\boldsymbol{z}}\left({}^{k}\boldsymbol{z}_{\text{F}}^{n+1}\right)$
  - $^{k}u_{\text{S}}^{n+1} \longleftarrow {}^{k}u_{\text{C}}^{n+1}$
  - `// solve solid...`
  - $\begin{bmatrix} {}^{k}\boldsymbol{y}_{\text{S}}^{n+1} \\ {}^{k}y_{\text{S}}^{n+1} \end{bmatrix} \longleftarrow \mathcal{G}_{\text{S}}^{\left[{}^{k}\boldsymbol{x}_{\text{S}}^{n+1}\right]}\left({}^{k}\boldsymbol{z}_{\text{S}}^{n+1}, {}^{k}u_{\text{S}}^{n+1}\right)$
  - `// calculate residuum of displacements and measured output...`
  - $^{k}\mathcal{R}_{\boldsymbol{y}}^{n+1} \longleftarrow {}^{k}\boldsymbol{y}_{\text{S}}^{n+1} - {}^{k-1}\boldsymbol{y}_{\text{S}}^{n+1}$
  - $^{k}\mathcal{R}_{y}^{n+1} \longleftarrow {}^{k}y_{\text{S}}^{n+1} - {}^{k-1}y_{\text{S}}^{n+1}$
  - $^{k}\mathcal{R}_{\boldsymbol{y},y}^{n+1} := \begin{bmatrix} {}^{k}\mathcal{R}_{\boldsymbol{y}}^{n+1} \\ {}^{k}\mathcal{R}_{y}^{n+1} \end{bmatrix}$
  - `// check for convergence...`
  - $^{k}\varepsilon^{n+1} \longleftarrow \left\| {}^{k}\mathcal{R}_{\boldsymbol{y},y}^{n+1} \right\|$
  - **if** $^{k}\varepsilon^{n+1} < {}^{\max}\varepsilon$ **then**
    - `break`
  - **end if**
  - $\vdots$
- $\vdots$

Algorithm 9.2 Pseudo code of partitioned scheme FSCI for FSCI co-simulation (continued).

⋮

⋮

`// update Aitken factor`

if $k = 0$ **then**

$\quad {}^{0}\beta^{n+1} \longleftarrow {}^{\text{init}}\beta$

else

$$\quad {}^{k}\beta^{n+1} \longleftarrow {}^{k-1}\beta^{n+1} \frac{{}^{k-1}\mathcal{R}_{\boldsymbol{y},y}^{n+1\,\mathrm{T}} \left({}^{k-1}\mathcal{R}_{\boldsymbol{y},y}^{n+1} - {}^{k}\mathcal{R}_{\boldsymbol{y},y}^{n+1} \right)}{\left\| {}^{k-1}\mathcal{R}_{\boldsymbol{y},y}^{n+1} - {}^{k}\mathcal{R}_{\boldsymbol{y},y}^{n+1} \right\|^{2}}$$

end if

`// update displacements and measured output...`

${}^{k+1}\boldsymbol{y}_{\mathrm{S}}^{n+1} \longleftarrow {}^{k}\boldsymbol{y}_{\mathrm{S}}^{n+1} + {}^{k}\beta^{n+1}\,{}^{k}\mathcal{R}_{\boldsymbol{y}}^{n+1}$

${}^{k+1}y_{\mathrm{S}}^{n+1} \longleftarrow {}^{k}y_{\mathrm{S}}^{n+1} + {}^{k}\beta^{n+1}\,{}^{k}\mathcal{R}_{y}^{n+1}$

end for

end for

already been shown in Figure 7.2 (p. 81). Consequently redundant mapping operations are all left out in formulations (9.2), (9.3) and (9.4) of respective interface constraints.

For the subsequently presented numerical experiments the proposed schemes are again implemented in the open source tool Enhanced Multi Physics Interface Research Engine (EMPIRE) (Sicklinger and Wang 2013) developed at the Chair of Structural Analysis at the Technical University of Munich. Extensive testing of all schemes is performed in stages. Therefore, dummy subsystems are used next to the previously presented ones. Those send well-defined output data for testing of coupling logic and data handling. An additional dummy fluid (CFD) subsystem implements the modified idealized piston problem from Sicklinger (2014) allowing a verification of the fully coupled problem with the monolithic solution. Dummy subsystems are step by step upgraded and finally exchanged with the actual subsystems to verify correct functionality. In particular, the realization of the root-point excitation is tested within FS"C"I simulations containing the actual structural (CSM) and fluid (CFD) but only a dummy controller (CLC) subsystem which is simply prescribing a sinusoidal control input. No test results are presented here but to get a feel for the effort behind this task: Two fluid (CFD), three solid (CSM) and four controller (CLC) subsystems in three partitioned schemes request $2 \cdot 3 \cdot 4 \cdot 3 = 72$ test scenarios before beginning the actual numerical experiments.

Algorithm 9.3 Pseudo code of partitioned scheme [FS]CI for FSCI co-simulation.

`// initialize states, i.e. set ICs...`
${}^{k_\text{end}}_{m_\text{end}}\boldsymbol{x}^0_\text{F} \longleftarrow \boldsymbol{x}^\text{init}_\text{F}$
${}^{k_\text{end}}_{m_\text{end}}\boldsymbol{x}^0_\text{S} \longleftarrow \boldsymbol{x}^\text{init}_\text{S}$
${}^{k_\text{end}}\boldsymbol{x}^0_\text{C} \longleftarrow \boldsymbol{x}^\text{init}_\text{C}$
`// initialize displacements and measured output...`
${}^{k_\text{end}}_{m_\text{end}}\boldsymbol{y}^0_\text{S} \longleftarrow \boldsymbol{y}^\text{init}_\text{S}$
${}^{k_\text{end}}_{m_\text{end}}y^0_\text{S} \longleftarrow y^\text{init}_\text{S}$
`// do co-simulation...`
`// time loop...`
for $n \longleftarrow 0$ *to* $n \longleftarrow n_\text{end} - 1$ **do**
  `// predict displacements and measured output...`
  ${}^{0}_{m_\text{end}}\boldsymbol{y}^{n+1}_\text{S} \longleftarrow {}^{k_\text{end}}_{m_\text{end}}\boldsymbol{y}^{n}_\text{S}$
  ${}^{0}_{m_\text{end}}y^{n+1}_\text{S} \longleftarrow {}^{k_\text{end}}_{m_\text{end}}y^{n}_\text{S}$
  `// outer interface iteration loop, i.e. [FS]CI loop...`
  for $k \longleftarrow 0$ *to* $k \longleftarrow k_\text{max}$ **do**
    `// copy measured output from solid to controller...`
    ${}^{k}y^{n+1}_\text{C} \longleftarrow {}^{k}_{m_\text{end}}y^{n+1}_\text{S}$
    `// solve controller...`
    ${}^{k}u^{n+1}_\text{C} \longleftarrow \mathcal{G}_\text{C}^{\left[{}^{k}\boldsymbol{x}^{n+1}_\text{C}\right]}\left({}^{k}y^{n+1}_\text{C}\right)$
    `// copy control input from controller to solid...`
    ${}^{k}u^{n+1}_\text{S} \longleftarrow {}^{k}u^{n+1}_\text{C}$
    `// predict displacements...`
    ${}^{k}_{0}\boldsymbol{y}^{n+1}_\text{S} \longleftarrow {}^{k}_{m_\text{end}}\boldsymbol{y}^{n+1}_\text{S}$
    `// inner interface iteration loop, i.e. FSI loop...`
    for $m \longleftarrow 0$ *to* $m \longleftarrow m_\text{max}$ **do**
      `// map displacements from solid to fluid...`
      ${}^{k}_{m}\boldsymbol{y}^{n+1}_\text{F} \longleftarrow \mathcal{M}_{\boldsymbol{y}}\left({}^{k}_{m}\boldsymbol{y}^{n+1}_\text{S}\right)$
      `// solve fluid...`
      ${}^{k}_{m}\boldsymbol{z}^{n+1}_\text{F} \longleftarrow \mathcal{G}_\text{F}^{\left[{}^{k}_{m}\boldsymbol{x}^{n+1}_\text{F}\right]}\left({}^{k}_{m}\boldsymbol{y}^{n+1}_\text{F}\right)$
      `// map forces from fluid to solid...`
      ${}^{k}_{m}\boldsymbol{z}^{n+1}_\text{S} \longleftarrow \mathcal{M}_{\boldsymbol{z}}\left({}^{k}_{m}\boldsymbol{z}^{n+1}_\text{F}\right)$
      `// solve solid...`
      $\begin{bmatrix} {}^{k}_{m}\boldsymbol{y}^{n+1}_\text{S} \\ {}^{k}_{m}y^{n+1}_\text{S} \end{bmatrix} \longleftarrow \mathcal{G}_\text{S}^{\left[{}^{k}_{m}\boldsymbol{x}^{n+1}_\text{S}\right]}\left({}^{k}_{m}\boldsymbol{z}^{n+1}_\text{S}, {}^{k}u^{n+1}_\text{S}\right)$
      `// calculate residuum of displacements...`
      ${}^{k}_{m}\mathcal{R}^{n+1}_{\boldsymbol{y}} \longleftarrow {}^{k}_{m}\boldsymbol{y}^{n+1}_\text{S} - {}^{k}_{m-1}\boldsymbol{y}^{n+1}_\text{S}$
      ⋮
    ⋮
  ⋮

Algorithm 9.4 PSEUDO CODE OF PARTITIONED SCHEME [FS]CI FOR FSCI CO-SIMULATION (CONTINUED).

⋮
⋮
⋮
`// check for inner convergence...`
${}^{k}_{m}\varepsilon^{n+1} \longleftarrow \left\| {}^{k}_{m}\mathcal{R}_{\boldsymbol{y}}^{n+1} \right\|$
if ${}^{k}_{m}\varepsilon^{n+1} < {}_{\max}\varepsilon$ **then**
  `break`
end if

`// update inner Aitken factor...`
if $m = 0$ **then**
  ${}^{k}_{0}\beta^{n+1} \longleftarrow {}_{\mathrm{init}}\beta$
else
  if $\dim \left\{ {}^{k}_{m}\mathcal{R}_{\boldsymbol{y}}^{n+1} \right\} = 1$ **then**
    ${}^{k}_{m}\beta^{n+1} \longleftarrow {}^{k}_{m-1}\beta^{n+1} \frac{{}^{k}_{m-1}\mathcal{R}_{\boldsymbol{y}}^{n+1}}{{}^{k}_{m-1}\mathcal{R}_{\boldsymbol{y}}^{n+1} - {}^{k}_{m}\mathcal{R}_{\boldsymbol{y}}^{n+1}}$
  else
    ${}^{k}_{m}\beta^{n+1} \longleftarrow {}^{k}_{m-1}\beta^{n+1} \frac{{}^{k}_{m-1}\mathcal{R}_{\boldsymbol{y}}^{n+1\,\mathrm{T}} \left({}^{k}_{m-1}\mathcal{R}_{\boldsymbol{y}}^{n+1} - {}^{k}_{m}\mathcal{R}_{\boldsymbol{y}}^{n+1} \right)}{\left\| {}^{k}_{m-1}\mathcal{R}_{\boldsymbol{y}}^{n+1} - {}^{k}_{m}\mathcal{R}_{\boldsymbol{y}}^{n+1} \right\|^2}$
  end if
end if

`// update displacements...`
${}^{k}_{m+1}\boldsymbol{y}_{\mathrm{S}}^{n+1} \longleftarrow {}^{k}_{m}\boldsymbol{y}_{\mathrm{S}}^{n+1} + {}^{k}_{m}\beta^{n+1}\, {}^{k}_{m}\mathcal{R}_{\boldsymbol{y}}^{n+1}$
end for

`// calculate residuum of measured output...`
${}^{k}\mathcal{R}_{y}^{n+1} \longleftarrow {}^{k}_{m_{\mathrm{end}}}y_{\mathrm{S}}{}^{n+1} - {}^{k-1}_{m_{\mathrm{end}}}y_{\mathrm{S}}{}^{n+1}$

`// check for outer convergence...`
${}^{k}\varepsilon^{n+1} \longleftarrow \left\| {}^{k}\mathcal{R}_{y}^{n+1} \right\|$
if ${}^{k}\varepsilon^{n+1} < {}^{\max}\varepsilon$ **then**
  `break`
end if

`// update outer Aitken factor...`
if $k = 0$ **then**
  ${}^{0}\beta^{n+1} \longleftarrow {}^{\mathrm{init}}\beta$
else
  ${}^{k}\beta^{n+1} \longleftarrow {}^{k-1}\beta^{n+1} \frac{{}^{k-1}\mathcal{R}_{y}^{n+1}}{{}^{k-1}\mathcal{R}_{y}^{n+1} - {}^{k}\mathcal{R}_{y}^{n+1}}$
end if

`// update displacements and measured output...`
${}^{k+1}_{m_{\mathrm{end}}}\boldsymbol{y}_{\mathrm{S}}^{n+1} \longleftarrow {}^{k}_{m_{\mathrm{end}}}\boldsymbol{y}_{\mathrm{S}}^{n+1}$
${}^{k+1}_{m_{\mathrm{end}}}y_{\mathrm{S}}{}^{n+1} \longleftarrow {}^{k}_{m_{\mathrm{end}}}y_{\mathrm{S}}{}^{n+1} + {}^{k}\beta^{n+1}\, {}^{k}\mathcal{R}_{y}^{n+1}$
end for
end for

Algorithm 9.5 Pseudo code of partitioned scheme F[SC]I for FSCI co-simulation.

`// initialize states, i.e. set ICs...`
${}^{k_\text{end}}\boldsymbol{x}_\text{F}^{0} \longleftarrow \boldsymbol{x}_\text{F}^\text{init}$
${}^{k_\text{end}}_{m_\text{end}}\boldsymbol{x}_\text{S}^{0} \longleftarrow \boldsymbol{x}_\text{S}^\text{init}$
${}^{k_\text{end}}_{m_\text{end}}\boldsymbol{x}_\text{C}^{0} \longleftarrow \boldsymbol{x}_\text{C}^\text{init}$
`// initialize displacements and measured output...`
${}^{k_\text{end}}_{m_\text{end}}\boldsymbol{y}_\text{S}^{0} \longleftarrow \boldsymbol{y}_\text{S}^\text{init}$
${}^{k_\text{end}}_{m_\text{end}}y_\text{S}^{0} \longleftarrow y_\text{S}^\text{init}$
`// do co-simulation...`
`// time loop...`
for $n \longleftarrow 0$ *to* $n \longleftarrow n_\text{end} - 1$ **do**
    `// predict displacements and measured output...`
    ${}^{0}_{m_\text{end}}\boldsymbol{y}_\text{S}^{n+1} \longleftarrow {}^{k_\text{end}}_{m_\text{end}}\boldsymbol{y}_\text{S}^{n}$
    ${}^{0}_{m_\text{end}}y_\text{S}^{n+1} \longleftarrow {}^{k_\text{end}}_{m_\text{end}}y_\text{S}^{n}$
    `// outer interface iteration loop, i.e. F[SC]I loop...`
    for $k \longleftarrow 0$ *to* $k \longleftarrow k_\text{max}$ **do**
        `// map displacements from solid to fluid...`
        ${}^{k}\boldsymbol{y}_\text{F}^{n+1} \longleftarrow \mathcal{M}_{\boldsymbol{y}}\left({}^{k}_{m_\text{end}}\boldsymbol{y}_\text{S}^{n+1}\right)$
        `// solve fluid...`
        ${}^{k}\boldsymbol{z}_\text{F}^{n+1} \longleftarrow \mathcal{G}_\text{F}^{\left[{}^{k}\boldsymbol{x}_\text{F}^{n+1}\right]}\left({}^{k}\boldsymbol{y}_\text{F}^{n+1}\right)$
        `// map forces from fluid to solid...`
        ${}^{k}\boldsymbol{z}_\text{S}^{n+1} \longleftarrow \mathcal{M}_{\boldsymbol{z}}\left({}^{k}\boldsymbol{z}_\text{F}^{n+1}\right)$
        `// predict measured output...`
        ${}^{k}_{0}y_\text{S}^{n+1} \longleftarrow {}^{k}_{m_\text{end}}y_\text{S}^{n+1}$
        `// inner interface iteration loop, i.e. SCI loop...`
        for $m \longleftarrow 0$ *to* $m \longleftarrow m_\text{max}$ **do**
            `// copy measured output from solid to controller...`
            ${}^{k}_{m}y_\text{C}^{n+1} \longleftarrow {}^{k}_{m}y_\text{S}^{n+1}$
            `// solve controller...`
            ${}^{k}_{m}u_\text{C}^{n+1} \longleftarrow \mathcal{G}_\text{C}^{\left[{}^{k}_{m}\boldsymbol{x}_\text{C}^{n+1}\right]}\left({}^{k}_{m}y_\text{C}^{n+1}\right)$
            `// copy control input from controller to solid...`
            ${}^{k}_{m}u_\text{S}^{n+1} \longleftarrow {}^{k}_{m}u_\text{C}^{n+1}$
            `// solve solid...`
            $\begin{bmatrix} {}^{k}_{m}\boldsymbol{y}_\text{S}^{n+1} \\ {}^{k}_{m}y_\text{S}^{n+1} \end{bmatrix} \longleftarrow \mathcal{G}_\text{S}^{\left[{}^{k}_{m}\boldsymbol{x}_\text{S}^{n+1}\right]}\left({}^{k}\boldsymbol{z}_\text{S}^{n+1}, {}^{k}_{m}u_\text{S}^{n+1}\right)$
            `// calculate residuum of measured output...`
            ${}^{k}_{m}\mathcal{R}_{y}^{n+1} \longleftarrow {}^{k}_{m}y_\text{S}^{n+1} - {}^{k}_{m-1}y_\text{S}^{n+1}$
            $\vdots$
        $\vdots$
    $\vdots$

Algorithm 9.6 PSEUDO CODE OF PARTITIONED SCHEME F[SC]I FOR FSCI CO-SIMULATION (CONTINUED).

⋮

⋮

⋮

`// check for inner convergence...`

$^{k}_{m}\varepsilon^{n+1} \longleftarrow \left\| ^{k}_{m}\mathcal{R}^{n+1}_{y} \right\|$

if $^{k}_{m}\varepsilon^{n+1} < {}_{\max}\varepsilon$ **then**

`break`

end if

`// update inner Aitken factor...`

if $m = 0$ **then**

$^{k}_{0}\beta^{n+1} \longleftarrow {}_{\text{init}}\beta$

else

$^{k}_{m}\beta^{n+1} \longleftarrow {}^{k}_{m-1}\beta^{n+1} \frac{^{k}_{m-1}\mathcal{R}^{n+1}_{y}}{^{k}_{m-1}\mathcal{R}^{n+1}_{y} - {}^{k}_{m}\mathcal{R}^{n+1}_{y}}$

end if

`// update measured output...`

$^{k}_{m+1}y^{n+1}_{\mathrm{S}} \longleftarrow {}^{k}_{m}y^{n+1}_{\mathrm{S}} + {}^{k}_{m}\beta^{n+1}\, {}^{k}_{m}\mathcal{R}^{n+1}_{y}$

end for

`// calculate residuum of displacements...`

$^{k}\mathcal{R}^{n+1}_{\boldsymbol{y}} \longleftarrow {}^{k}_{m_{\text{end}}}\boldsymbol{y}^{n+1}_{\mathrm{S}} - {}^{k-1}_{m_{\text{end}}}\boldsymbol{y}^{n+1}_{\mathrm{S}}$

`// check for outer convergence...`

$^{k}\varepsilon^{n+1} \longleftarrow \left\| ^{k}\mathcal{R}^{n+1}_{\boldsymbol{y}} \right\|$

if $^{k}\varepsilon^{n+1} < {}^{\max}\varepsilon$ **then**

`break`

end if

`// update outer Aitken factor...`

if $k = 0$ **then**

$^{0}\beta^{n+1} \longleftarrow {}^{\text{init}}\beta$

else

if $\dim \left\{ ^{k}\mathcal{R}^{n+1}_{\boldsymbol{y}} \right\} = 1$ **then**

$^{k}\beta^{n+1} \longleftarrow {}^{k-1}\beta^{n+1} \frac{^{k-1}\mathcal{R}^{n+1}_{\boldsymbol{y}}}{^{k-1}\mathcal{R}^{n+1}_{\boldsymbol{y}} - {}^{k}\mathcal{R}^{n+1}_{\boldsymbol{y}}}$

else

$^{k}\beta^{n+1} \longleftarrow {}^{k-1}\beta^{n+1} \frac{^{k-1}\mathcal{R}^{n+1\,\mathrm{T}}_{\boldsymbol{y}} \left(^{k-1}\mathcal{R}^{n+1}_{\boldsymbol{y}} - {}^{k}\mathcal{R}^{n+1}_{\boldsymbol{y}} \right)}{\left\| ^{k-1}\mathcal{R}^{n+1}_{\boldsymbol{y}} - {}^{k}\mathcal{R}^{n+1}_{\boldsymbol{y}} \right\|^{2}}$

end if

end if

`// update displacements and measured output...`

$^{k+1}_{m_{\text{end}}}\boldsymbol{y}^{n+1}_{\mathrm{S}} \longleftarrow {}^{k}_{m_{\text{end}}}\boldsymbol{y}^{n+1}_{\mathrm{S}} + {}^{k}\beta^{n+1}\, {}^{k}\mathcal{R}^{n+1}_{\boldsymbol{y}}$

$^{k+1}_{m_{\text{end}}}y^{n+1}_{\mathrm{S}} \longleftarrow {}^{k}_{m_{\text{end}}}y^{n+1}_{\mathrm{S}}$

end for

end for

9.2 Assessment of Closed–Loop Control Laws

Here exemplarily the three chosen closed-loop control laws LQR, LQI and LQS are investigated within full FSCI co-simulations. They are derived for the SCI sub-problem with prescribed disturbance in Chapter 8 The Controller (CLC) Subsystem (pp. 94 ff.). The assessment is again accomplished with parameter scaling tests identical to FSI. For explanations it is therefore referred to Chapter 7 Fluid–Structure Interaction (pp. 79 ff.). Up to now the extensive investigations of FSCI are still restricted to the low-fidelity structural (CSM) model. This implies again well behaving Aitken factors resulting from the single structural degree of freedom.

Table 9.1 LOG OF FSCI PARAMETER SCALING TEST WITH LOW-FIDELITY STRUCTURAL (CSM) SUBSYSTEM.

control law	*coupling scheme*	*parameter scaling factor q*									
		10^{6}	10^{5}	10^{4}	10^{3}	10^{2}	10^{1}	10^{0}	10^{-1}	10^{-2}	10^{-3}
LQR	FSCI	✓	✓	✓	✓	✓	✗[h]	✓[a]	✓[af]	✓[ad]	✓[aef]
	[FS]CI	✓	✓	✓	✓	✓	✗[h]	✓[af]	✓[ag]	✓[ad]	✓[aeg]
	F[SC]I	✓	✓	✓	✓	✓	✗[h]	✓[a]	✓[af]	✓[adf]	✓[aef]
LQI	FSCI	✓	✓	✓	✓	✓	✗[h]	✓[a]	✓[af]	✓[ad]	✓[aef]
	[FS]CI	✓	✓	✓	✓	✓	✗[h]	✓[a]	✓[ag]	✓[ad]	✓[aeg]
	F[SC]I	✓	✓	✓	✓	✓	✗[h]	✓[a]	✓[af]	✓[adf]	✓[aef]
LQS	FSCI	✓[b]	✓[b]	✓[b]	✓[c]	✓[c]	✓[c]	✗[h]	✗[h]	✓[df]	✓[ef]

[a] change to linear mesh updating scheme in fluid (CFD) subsystem
[b] decrease absolute convergence criterion to 10^{-15}
[c] decrease absolute convergence criterion to 10^{-12}
[d] increase absolute convergence criterion to 10^{-6}
[e] increase absolute convergence criterion to 2×10^{-5}
[f] maximal number of 40 simple/outer interface iterations reached
[g] maximal number of 40 inner interface iterations reached
[h] mesh updating scheme in fluid (CFD) subsystem fails due to large deformations of structural (CSM) subsystem for different settings

If not noted otherwise in Table 9.1 the FSCI parameter scaling tests with the low-fidelity structural (CSM) subsystem use the following standard settings: The fluid (CFD) subsystem employs the non-linear version of the structural similarity mesh updating scheme. A maximum of 40 simple/inner/outer interface iterations is allowed to attain the specified absolute convergence criteria of 10^{-9}. Time step size is consistently $\delta t = 0.01$. The structural (CSM) subsystem starts not until $3 \cdot \delta t = 0.03\,\text{s}$ to avoid wrong disturbances outputted by the fluid (CFD) subsystem for the first steps. The simulations run $1500 \cdot \delta t = 15.00\,\mathrm{s}$ which are evaluated from $t_1 = 1000 \cdot \delta t = 10.00\,\mathrm{s}$ to $t_2 = 1500 \cdot \delta t = 15.00\,\mathrm{s}$. Used parameter scaling factors can be found in Table 9.1 presenting the simulation log. For now FSCI investigations are restricted to force control, i.e. a u-output factor $f_u = 0$ is set. These standard settings matching the FSI ones are completed by the specific settings of the subsystems.

The results of the FSCI parameter scaling tests are again evaluated in terms of the representative signal quantities disturbance z and measured y. For details it is referred to Chapter 7 Fluid–Structure Interaction (pp. 79 ff.). Time responses can be found in Figures 9.11 (p. 139) for a parameter scaling of $q = 10^6$ through 9.20 (p. 148) for $q = 10^{-3}$. FSI results are included for comparison.

Figure 9.4 (p. 132) illustrates trends with respect to parameter scaling factor q for the relative disturbance

$$\frac{z_{\mathrm{FSI}}(t)}{z_{\mathrm{FSCI}}(t)} \tag{9.5a}$$

and the relative measured output

$$\frac{y_{\mathrm{FSCI}}(t)}{y_{\mathrm{FSI}}(t)}. \tag{9.5b}$$

I.e. the first one states the disturbance from FSI relative to the one from FSCI and the latter one the measured output from FSCI relative to the one from FSI. Expected are values for the relative measured output smaller than one indicating the intended reduction of the structural displacements towards FSI, respectively, the success of the particular control law. For values bigger than one the control law is graded as failed. A relative disturbance of one shows the independence of the arriving disturbance from the impact of the controller. This is expected for the upper q-range according to the assumptions for the derivations of the control laws. Values bigger or smaller than one indicate de- or increase, respectively. The plotted characteristics are specified in Equation (7.4) (p. 84).

Fourier analyses of disturbances and measured outputs for control laws LQR, LQI and LQS are presented in Figures 9.5 (p. 133) to 9.10 (p. 138). For explanations it is again referred to Chapter 7 Fluid–Structure Interaction (pp. 79 ff.).

It should be pointed out that in all aforementioned figures blanc space indicates failure of the respective control law rather than missing data. An illustration of consequently diverging dynamics would be meaningless. Long time simulations with accordingly higher numerical effort would further more clearly show the diverging responses.

Obviously, all control laws are successful within the linear q-range according to expectations. Furthermore, they are even able to extend this linear q-range by one (LQR and LQI) or two (LQS) decades into the transfer and non-linear ranges. Thus, the closed-loop control possesses a linearizing effect on the dynamics. Reductions to around 30 % for LQR, 20 to 10 % for LQI and 0.2 to 0.1 % for LQS are achieved. The values are estimated on the positive and negative maxima reflecting the maximum deflections in both directions.

Time responses and derived results cover well the basic functionality of the distinct control laws: LQR only intends to stabilize (problem is already stable) and to compensate initial value disturbances. The steady disturbance, however, corresponds to continuously disturbed initial values. Thus, LQR is not able to follow and just slightly reduces the deflections due to increased modal damping. LQI additionally possesses an integrator which in particular accounts for longtime static-like deflections. This can be nicely observed by comparing time responses of LQI and LQR. The disturbance model in the LQS control law finally captures main parts of the steady disturbance allowing for much better, sufficient compensation.

In the strongly non-linear q-range where the coupled dynamics are absolutely dominated by the fluid all control laws fail. The system response with LQR even corresponds exactly to the pure FSI response. Thus, LQR completely misses any impact. Coupled dynamics with LQI and LQS tend to long-term divergence. This can probably be traced back to the integrator continuously accumulating a static-like error which can however never be compensated finally resulting in a slow drift off.

The assumption made for the control law design finally proofs right: In the linear q-range all relative disturbances turn out equal to one, i.e. the forces are clearly similar to the pure FSI ones. In the transfer range a slight increase of the disturbances can be observed.

In all control laws (LQR, LQI and LQS) the state-feedback based on the LQR approach maintains the original structural eigenfrequency, i.e. the original imaginary part of both eigenvalues is retained. This corresponds to minimization of system constraints in order to keep control input and energetic effort as little as possible. This can nicely be observed in the respective illustrations of the Fourier Analyses. In order additionally minimize the state amplitudes both eigenvalues are shifted in negative direction, i.e. the modal damping reflecting in the negative real part is increased. The eigenvalues are said to become faster. All these aspects arise from the quadratic cost functional in the LQR approach.

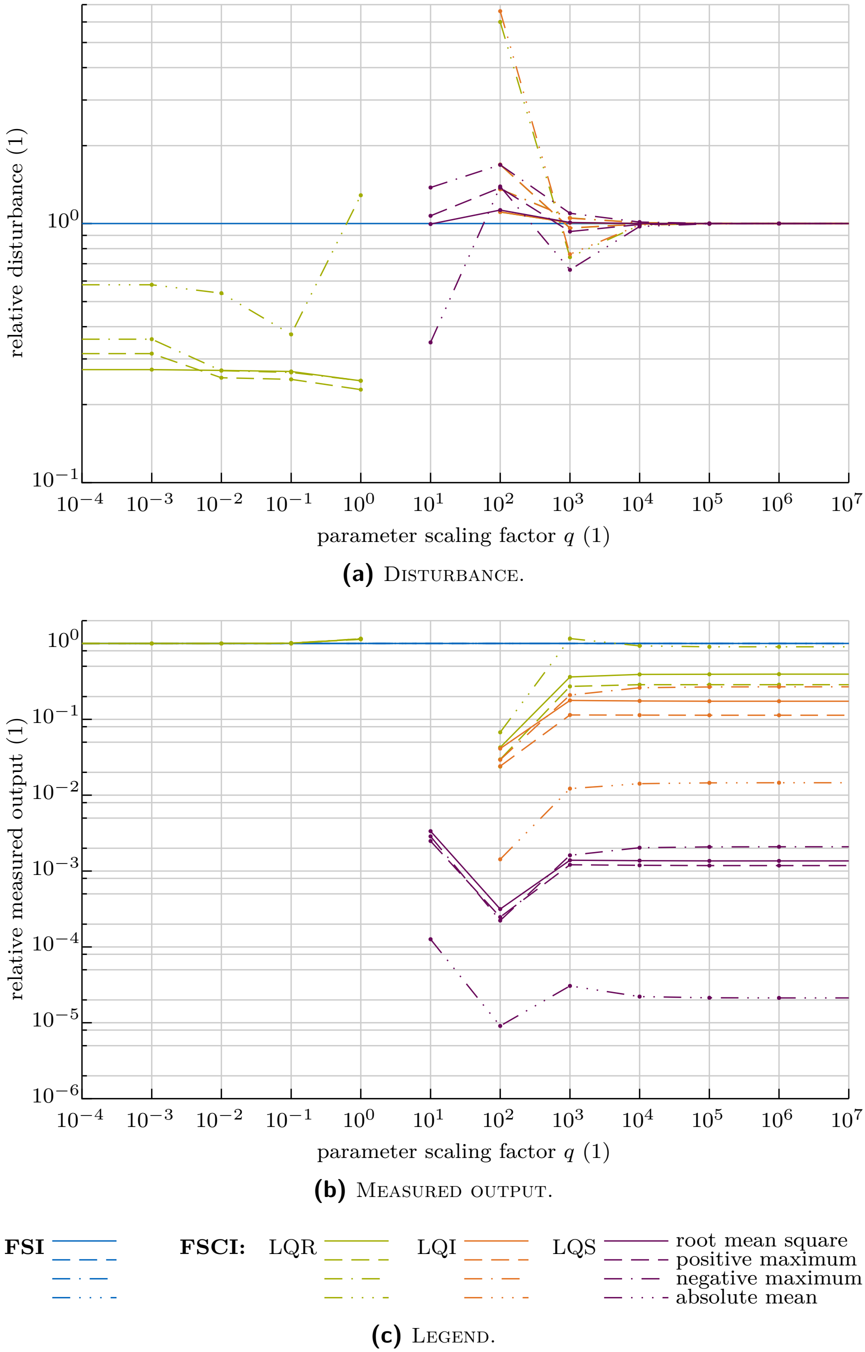

Figure 9.4 Trends of disturbance and measured output in FSCI parameter scaling tests with low-fidelity structural (CSM) subsystem.

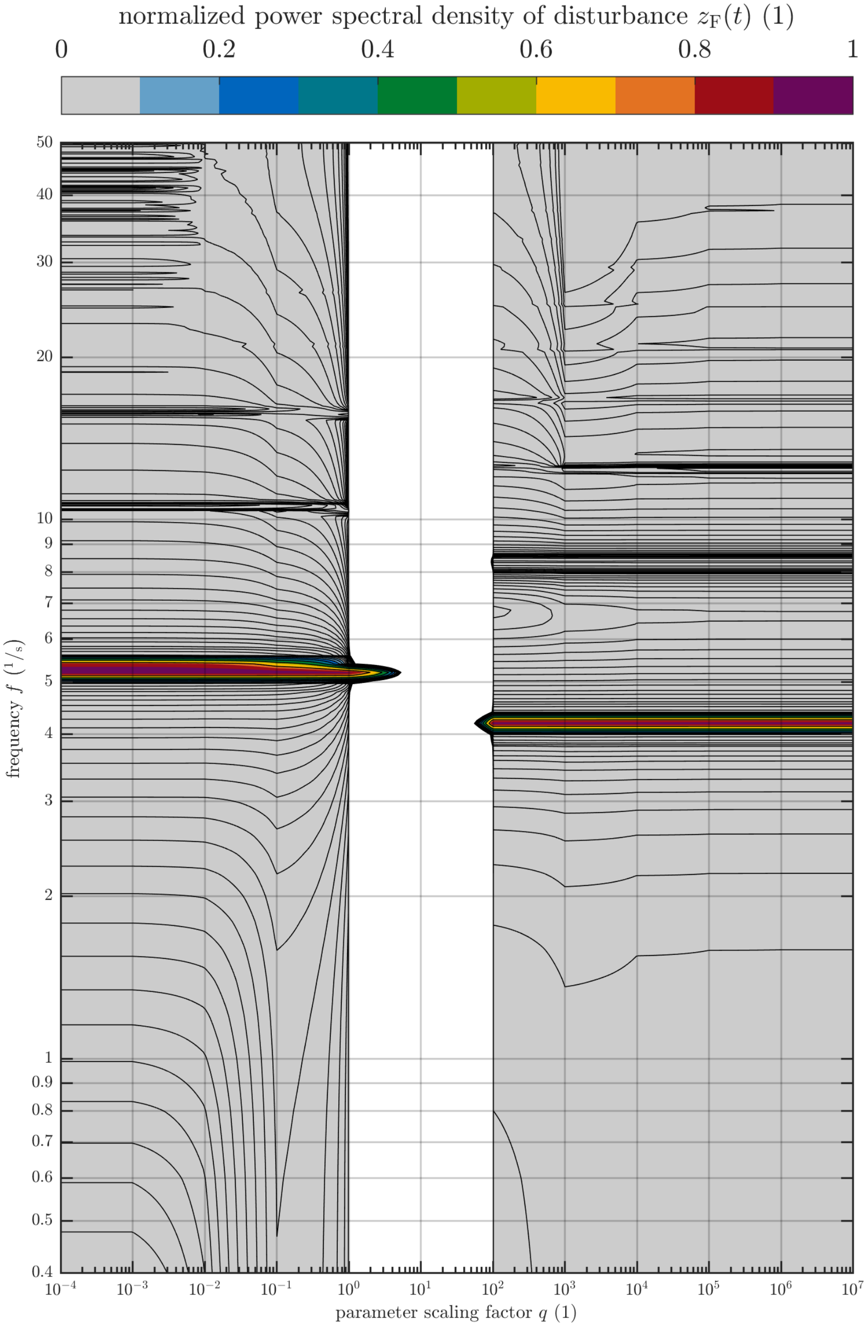

Figure 9.5 Fourier analysis of disturbance in FSCI parameter scaling test with LQR controller (CLC) subsystem and low-fidelity structural (CSM) subsystem.

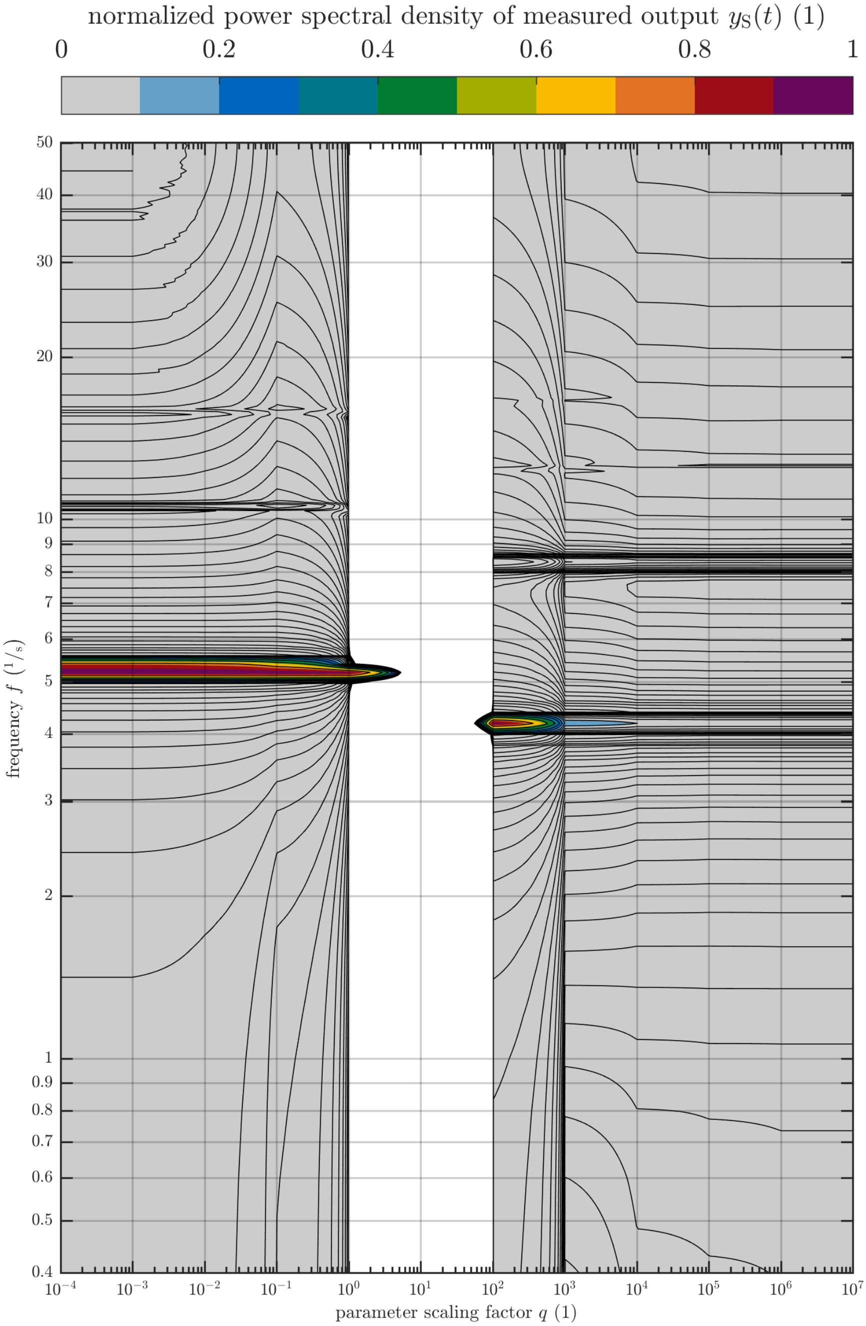

Figure 9.6 Fourier analysis of measured output in FSCI parameter scaling test with LQR controller (CLC) subsystem and low-fidelity structural (CSM) subsystem.

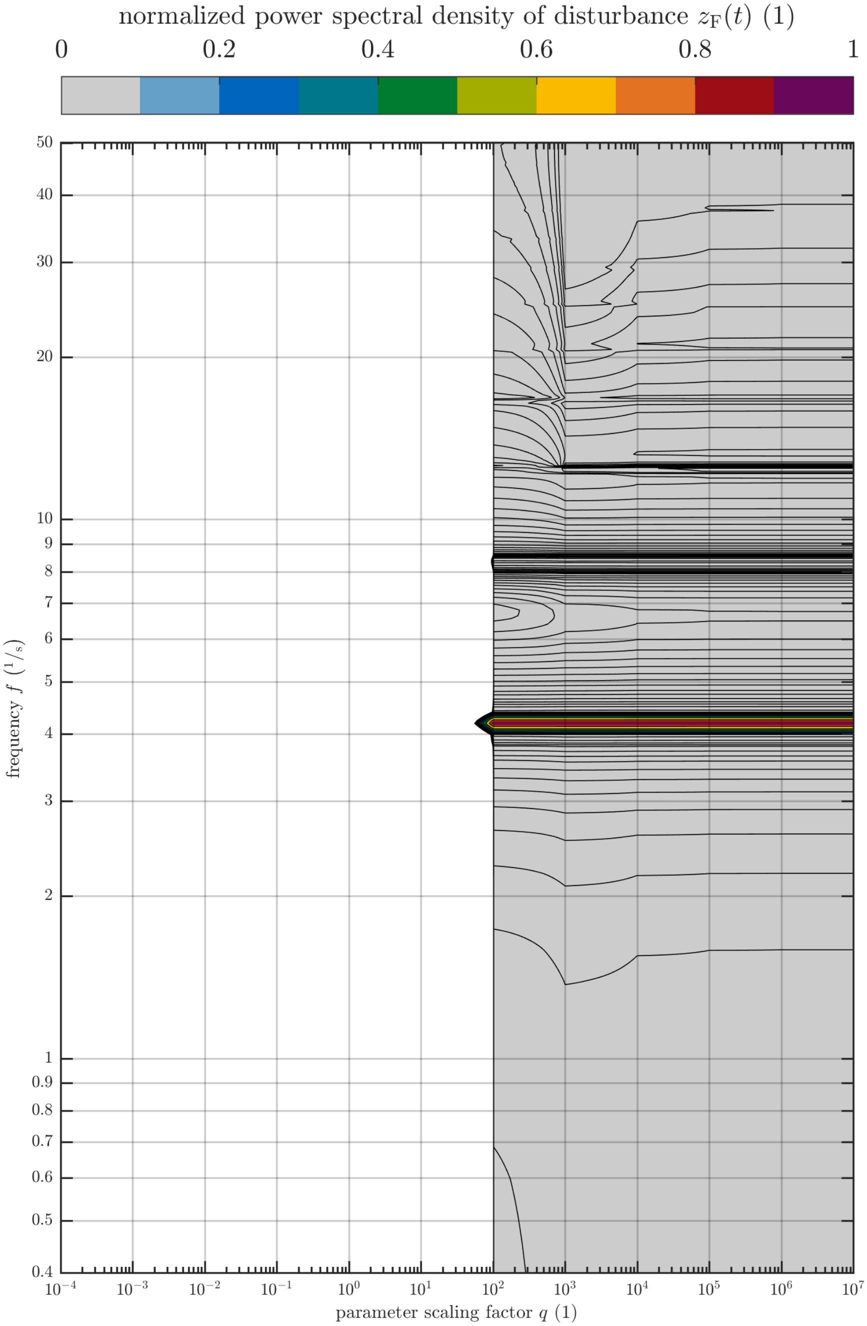

Figure 9.7 Fourier analysis of disturbance in FSCI parameter scaling test with LQI controller (CLC) subsystem and low-fidelity structural (CSM) subsystem.

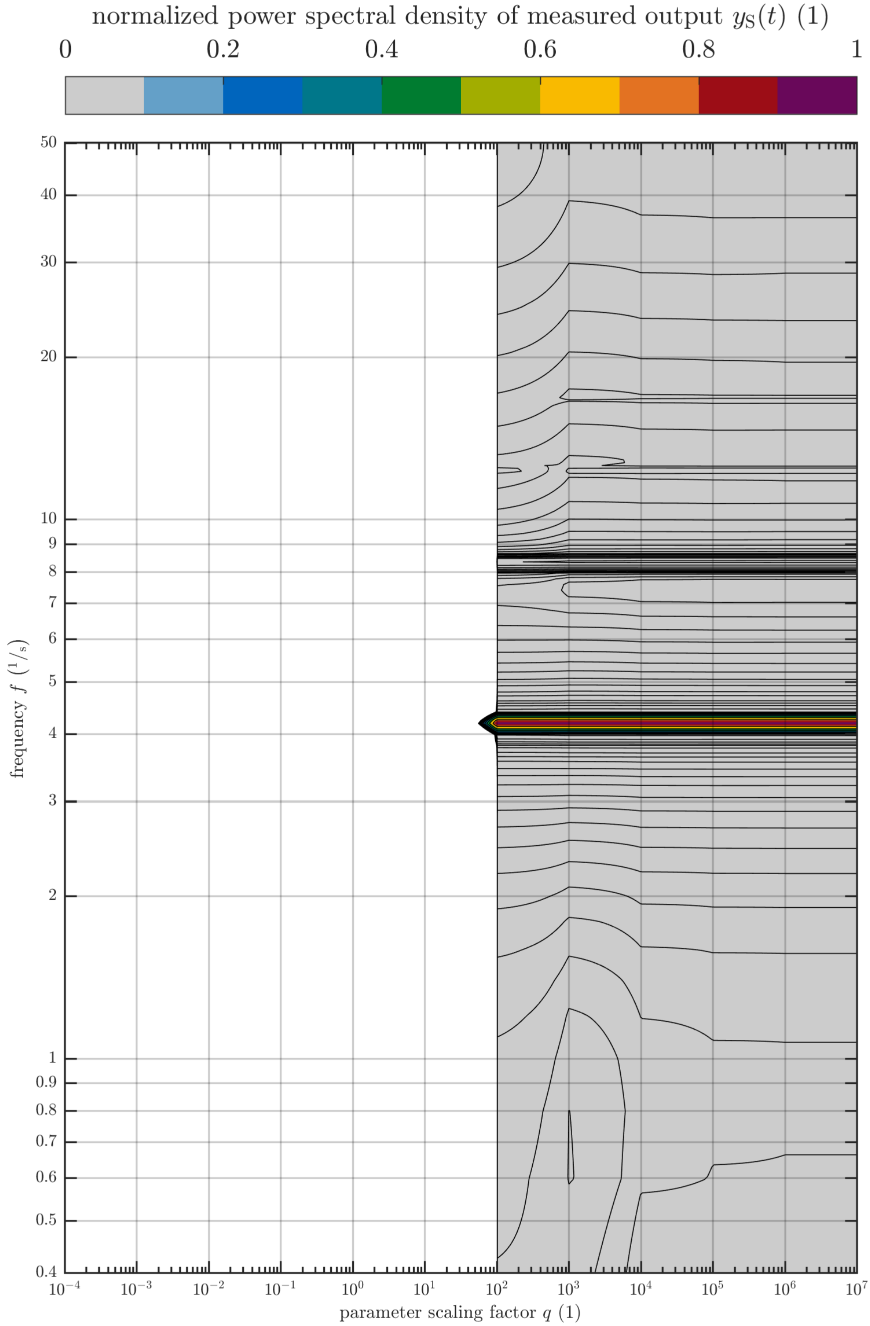

Figure 9.8 Fourier analysis of measured output in FSCI parameter scaling test with LQI controller (CLC) subsystem and low-fidelity structural (CSM) subsystem.

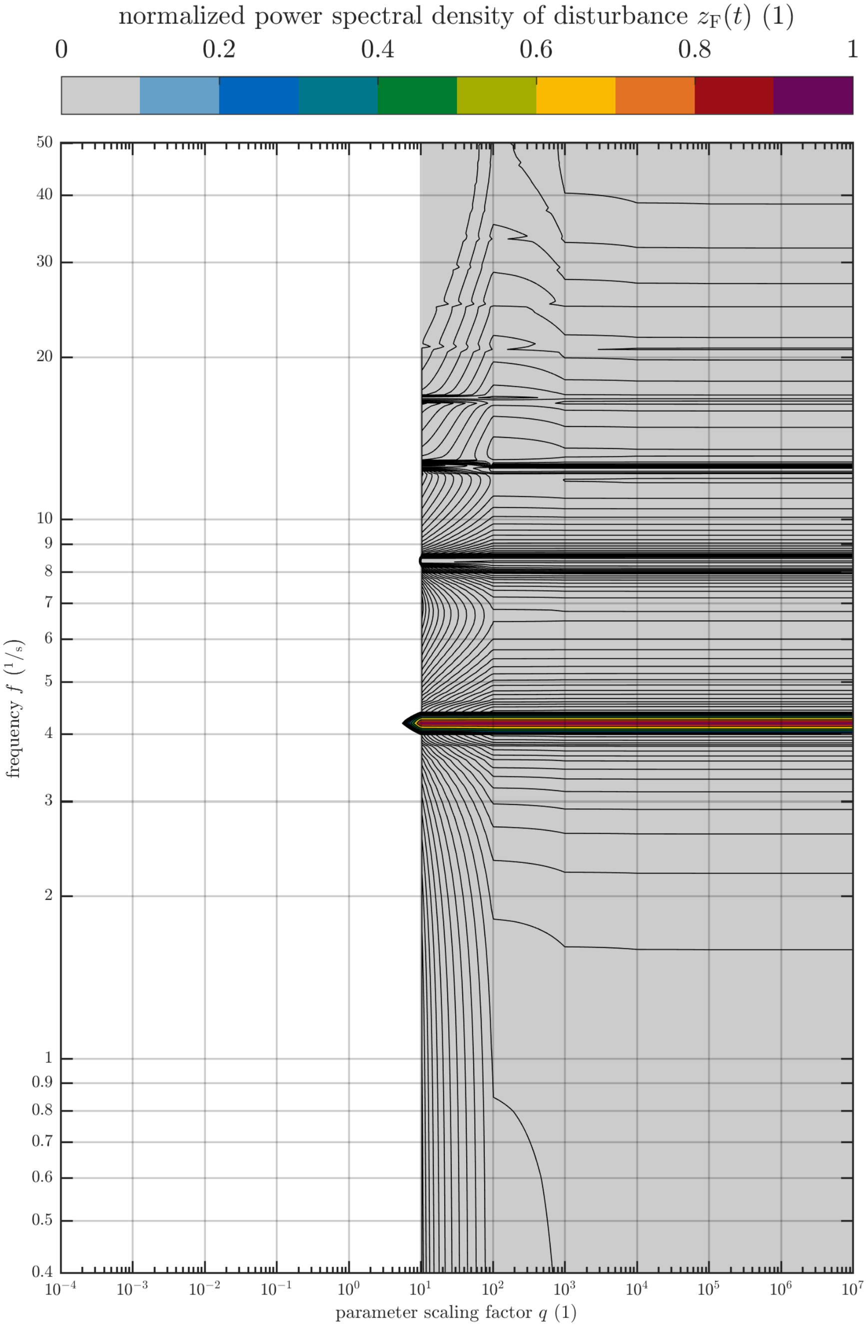

Figure 9.9 Fourier analysis of disturbance in FSCI parameter scaling test with LQS controller (CLC) subsystem and low-fidelity structural (CSM) subsystem.

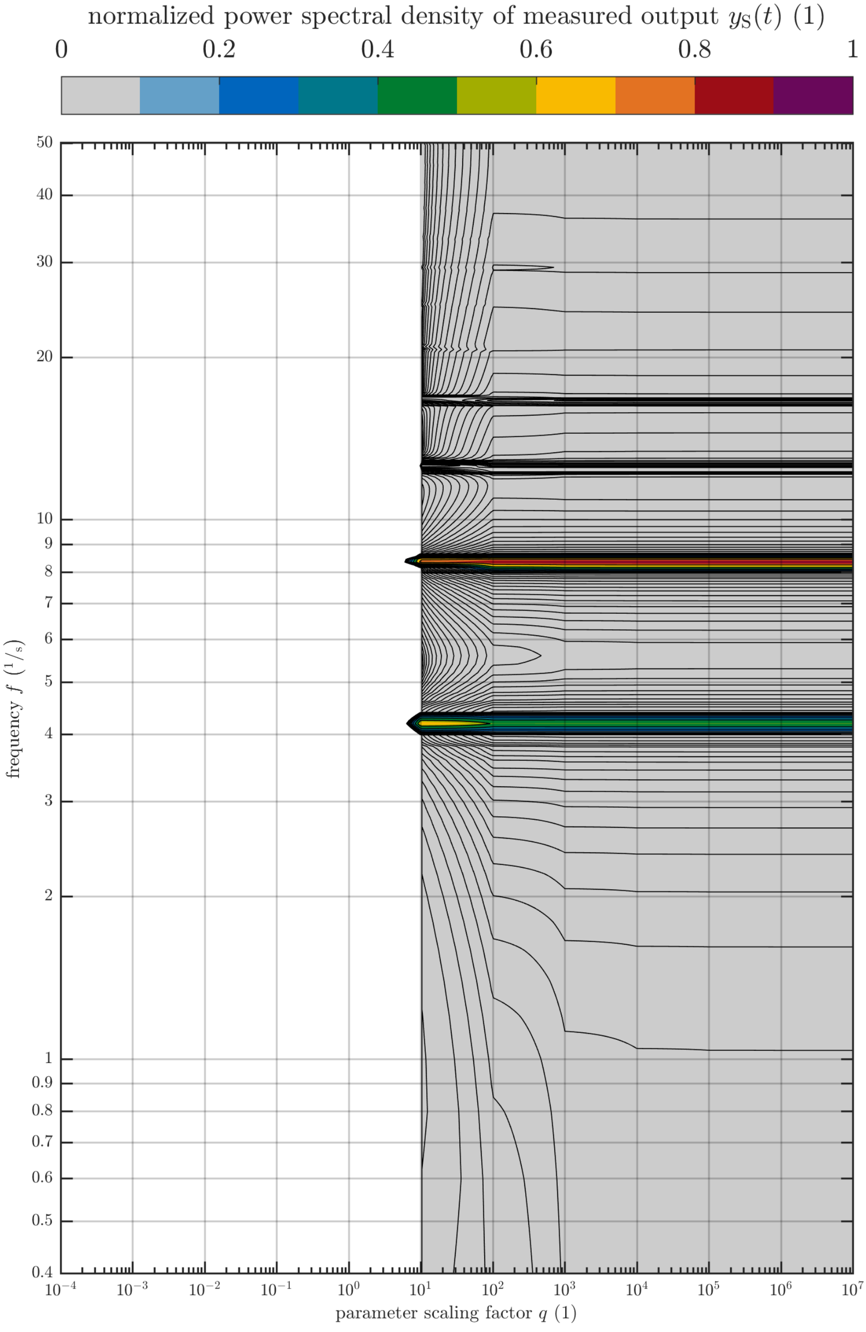

Figure 9.10 Fourier analysis of measured output in FSCI parameter scaling test with LQS controller (CLC) subsystem and low-fidelity structural (CSM) subsystem.

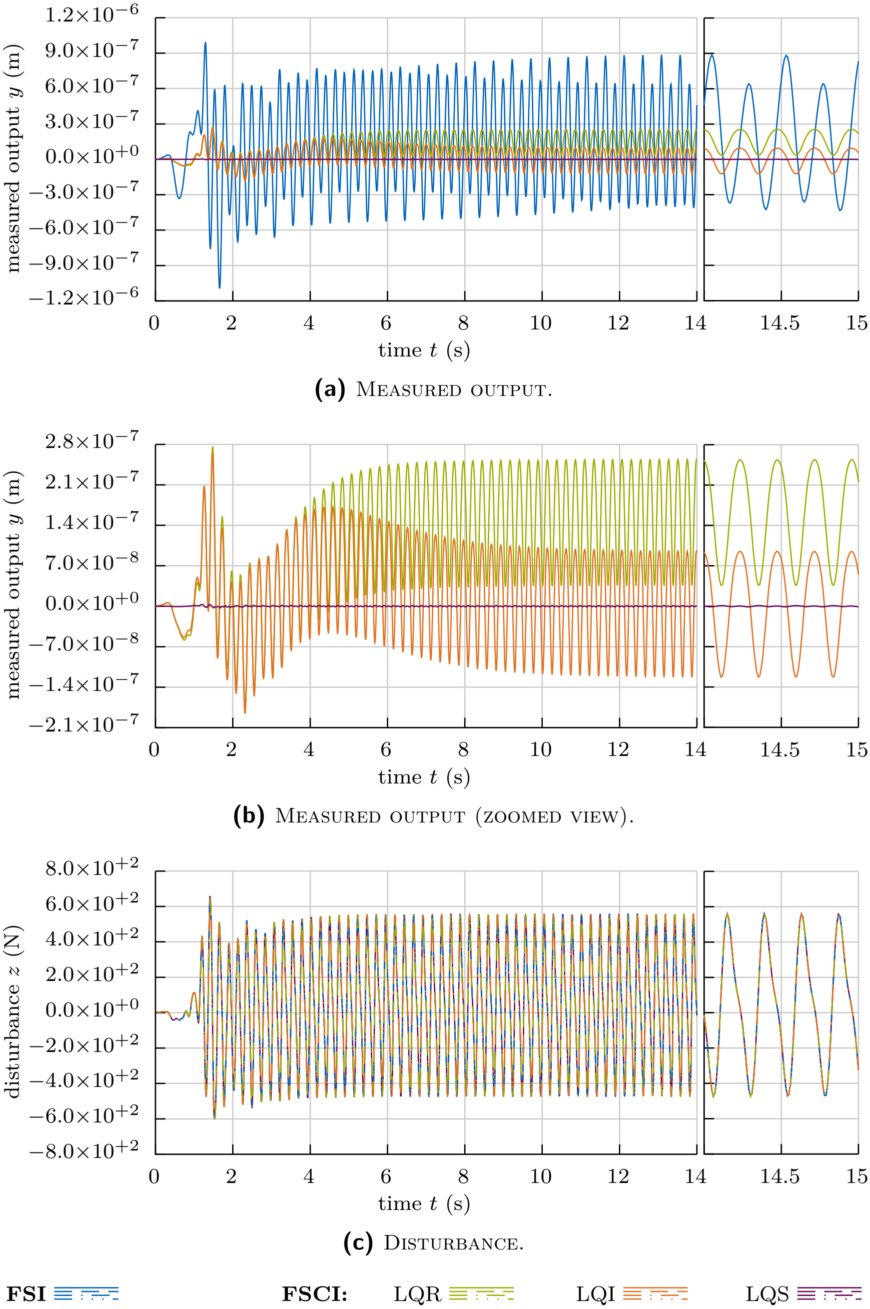

(a) Measured output.

(b) Measured output (zoomed view).

(c) Disturbance.

(d) Legend.

Figure 9.11 Measured outputs and disturbances in FSCI's with low-fidelity structural (CSM) subsystem scaled by $q = 10^6$.

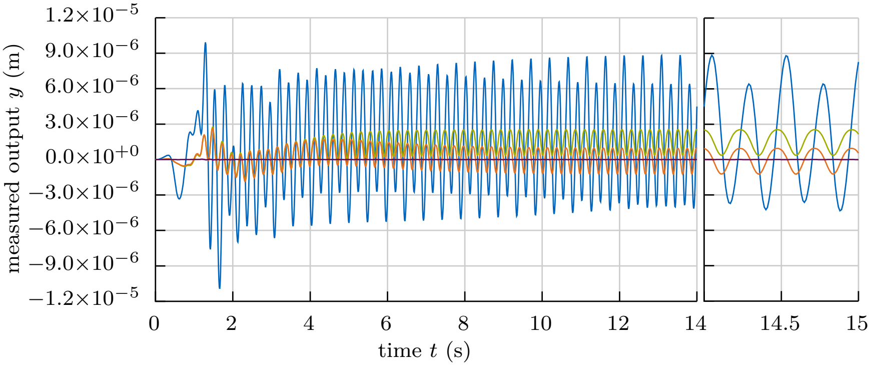

(a) MEASURED OUTPUT.

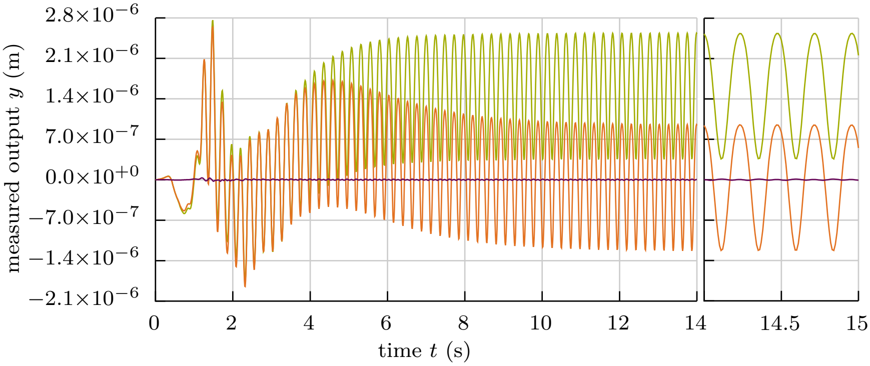

(b) MEASURED OUTPUT (ZOOMED VIEW).

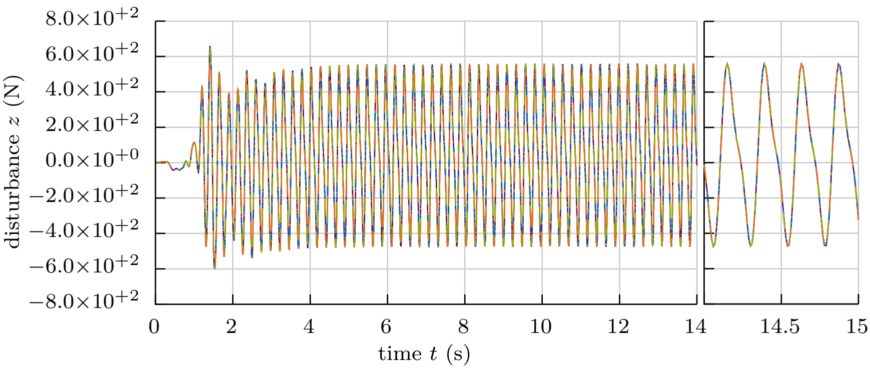

(c) DISTURBANCE.

FSI **FSCI:** LQR LQI LQS

(d) LEGEND.

Figure 9.12 MEASURED OUTPUTS AND DISTURBANCES IN FSCI'S WITH LOW-FIDELITY STRUCTURAL (CSM) SUBSYSTEM SCALED BY $q = 10^5$.

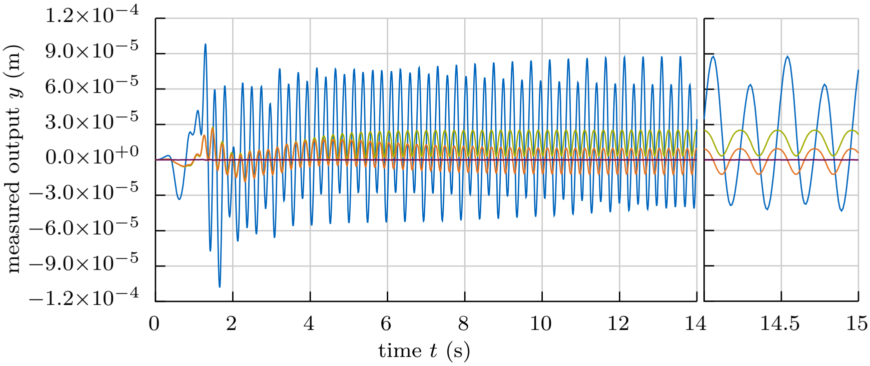

(a) Measured output.

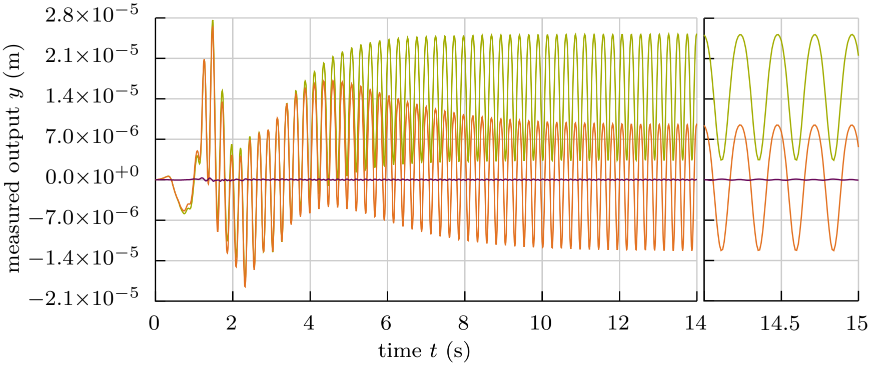

(b) Measured output (zoomed view).

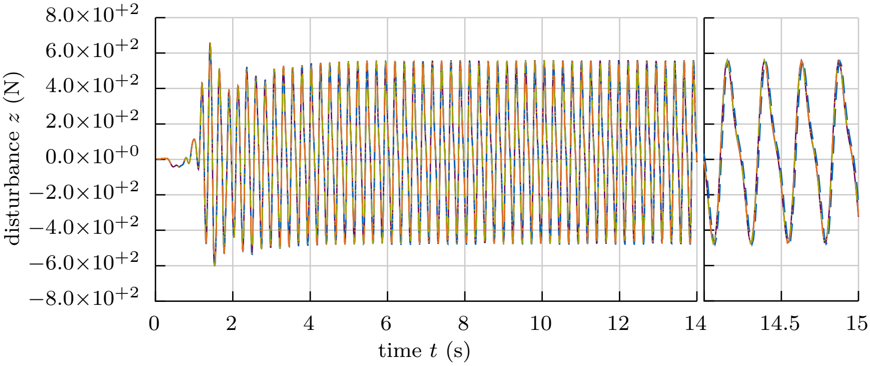

(c) Disturbance.

FSI **FSCI:** LQR LQI LQS

(d) Legend.

Figure 9.13 Measured outputs and disturbances in FSCI's with low-fidelity structural (CSM) subsystem scaled by $q = 10^4$.

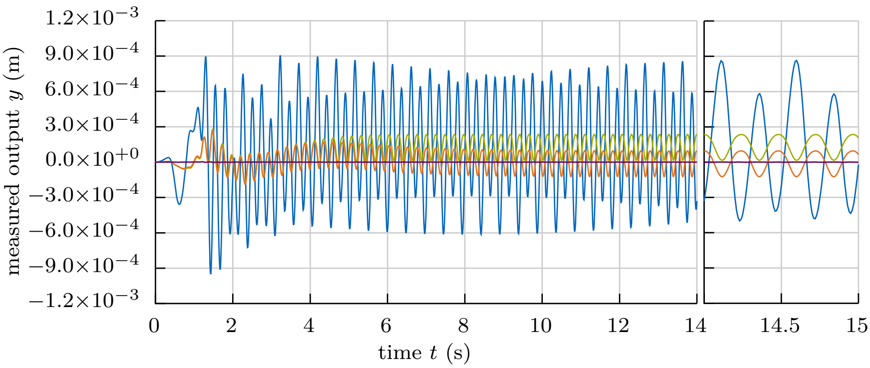

(a) Measured output.

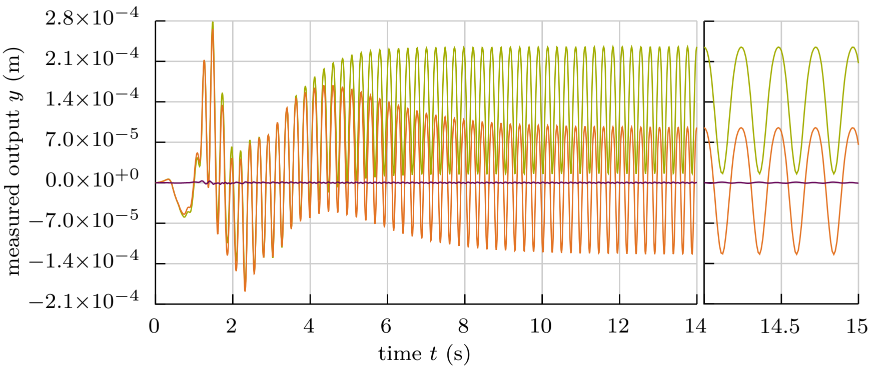

(b) Measured output (zoomed view).

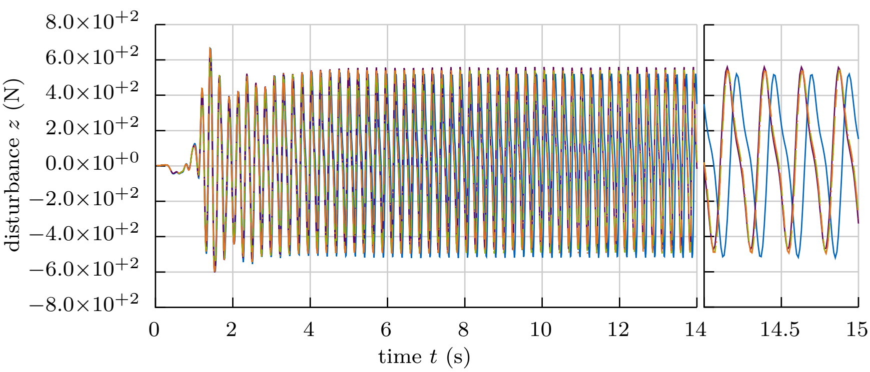

(c) Disturbance.

FSI **FSCI:** LQR LQI LQS

(d) Legend.

Figure 9.14 Measured outputs and disturbances in FSCI's with low-fidelity structural (CSM) subsystem scaled by $q = 10^3$.

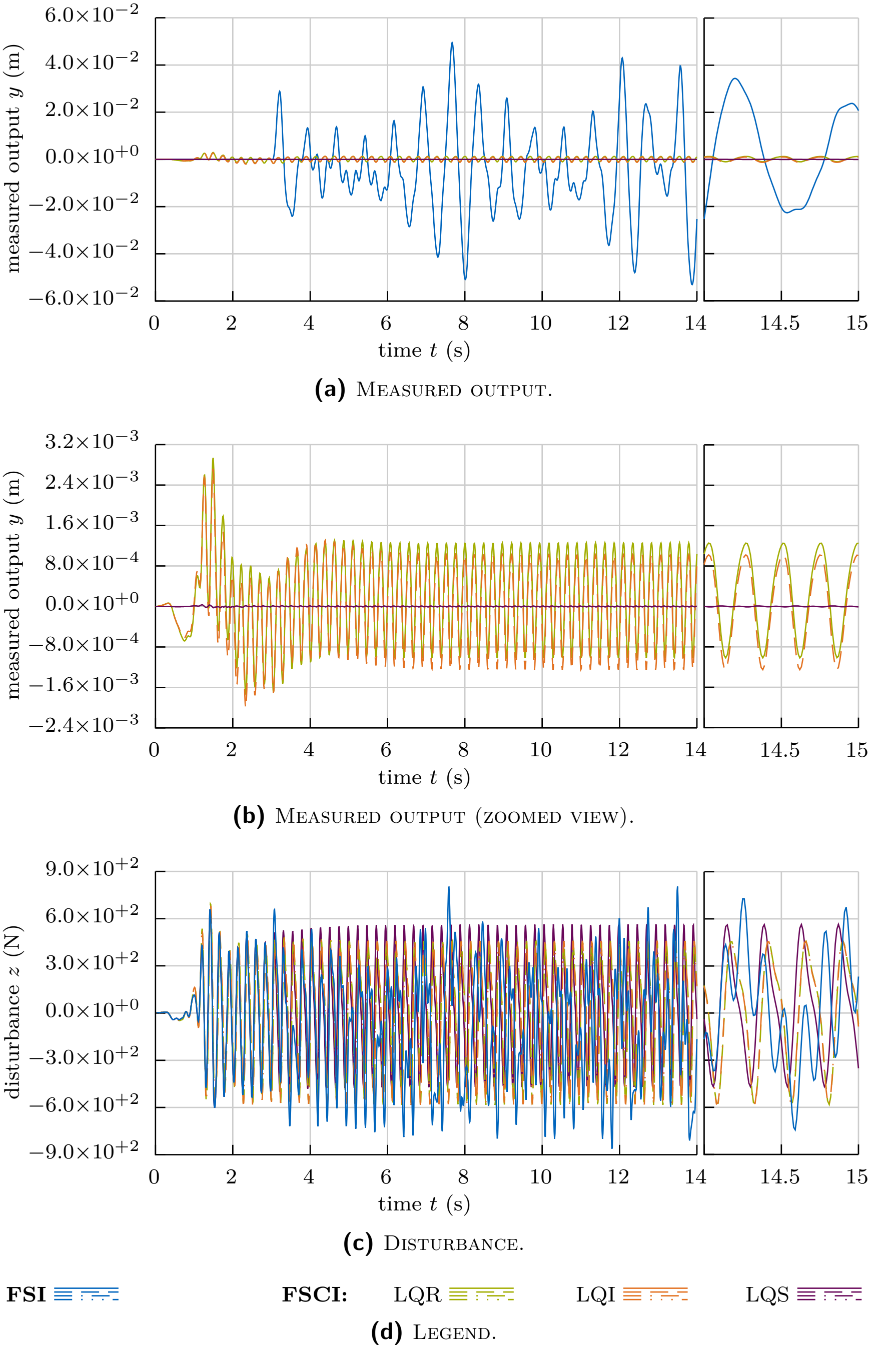

Figure 9.15 Measured outputs and disturbances in FSCI's with low-fidelity structural (CSM) subsystem scaled by $q = 10^2$.

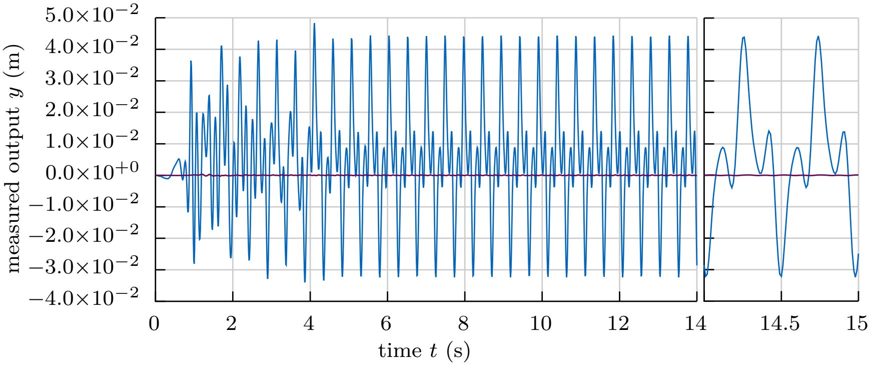

(a) MEASURED OUTPUT.

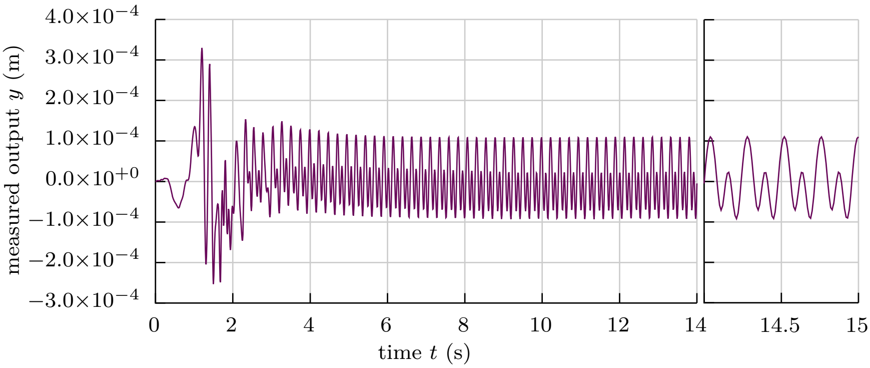

(b) MEASURED OUTPUT (ZOOMED VIEW).

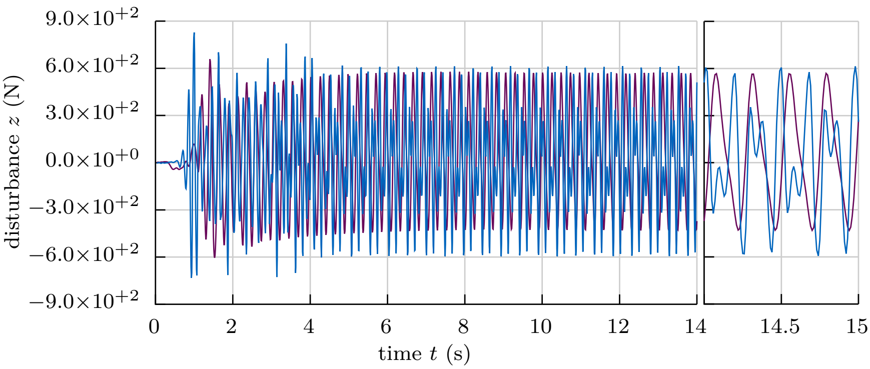

(c) DISTURBANCE.

FSI **FSCI:** LQR LQI LQS

(d) LEGEND.

Figure 9.16 MEASURED OUTPUTS AND DISTURBANCES IN FSCI'S WITH LOW-FIDELITY STRUCTURAL (CSM) SUBSYSTEM SCALED BY $q = 10^1$.

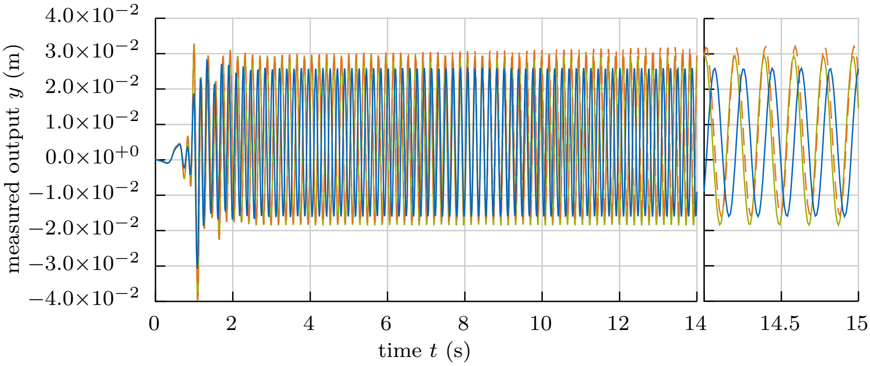

(a) MEASURED OUTPUT.

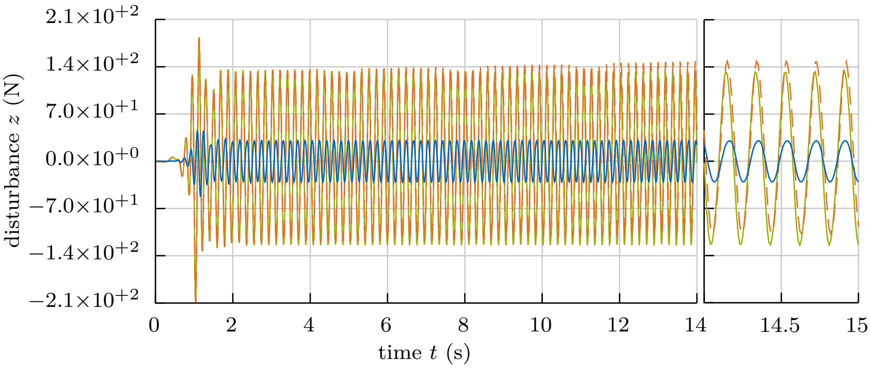

(b) DISTURBANCE.

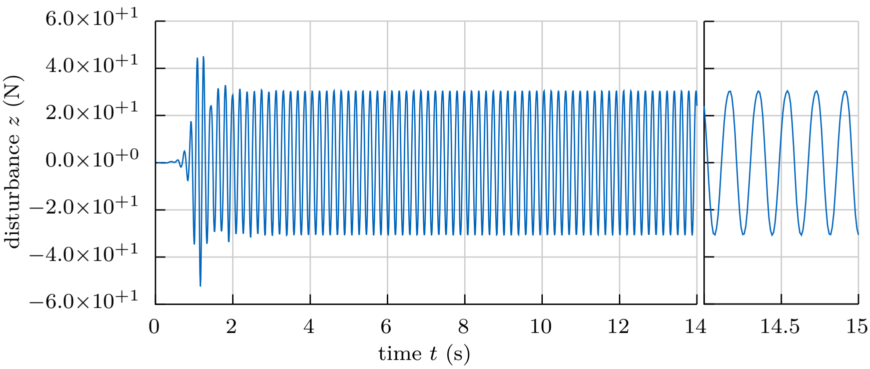

(c) DISTURBANCE (ZOOMED VIEW).

FSI **FSCI:** LQR LQI LQS

(d) LEGEND.

Figure 9.17 MEASURED OUTPUTS AND DISTURBANCES IN FSCI'S WITH LOW-FIDELITY STRUCTURAL (CSM) SUBSYSTEM SCALED BY $q = 10^0$.

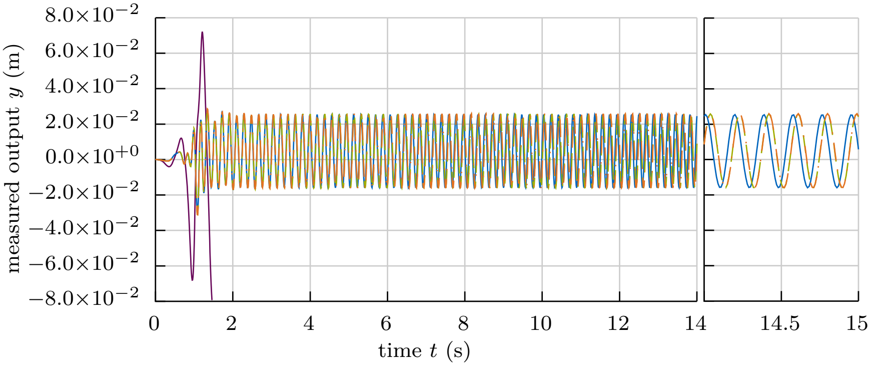

(a) Measured output.

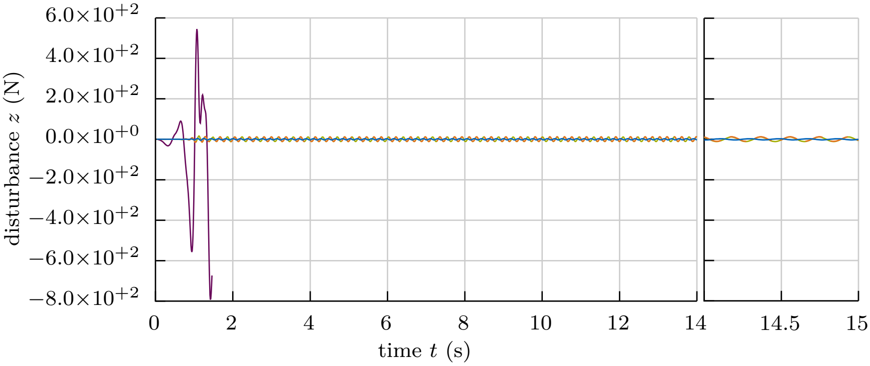

(b) Disturbance.

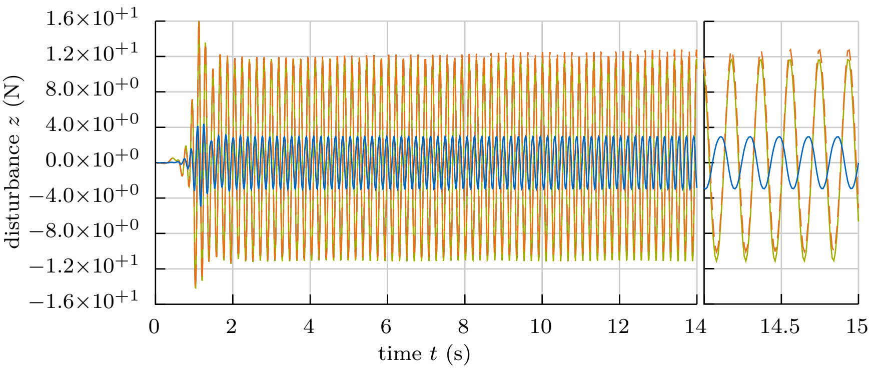

(c) Disturbance (zoomed view).

FSI **FSCI:** LQR LQI LQS

(d) Legend.

Figure 9.18 Measured outputs and disturbances in FSCI's with low-fidelity structural (CSM) subsystem scaled by $q = 10^{-1}$.

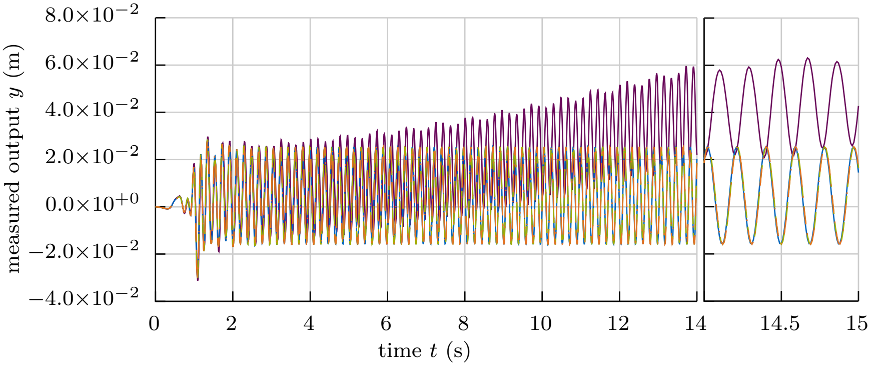

(a) Measured output.

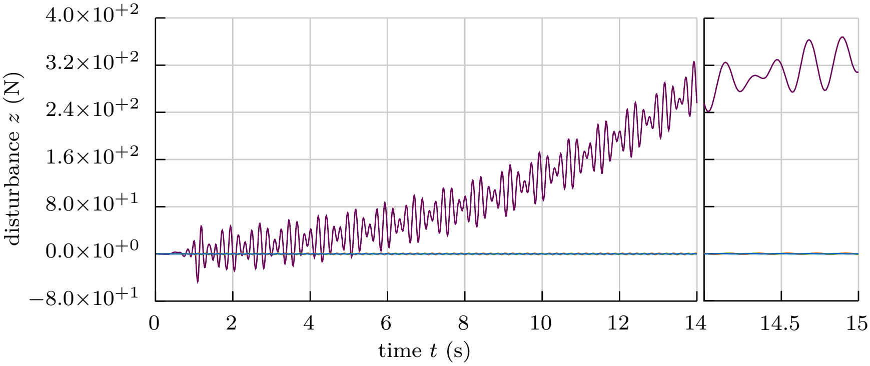

(b) Disturbance.

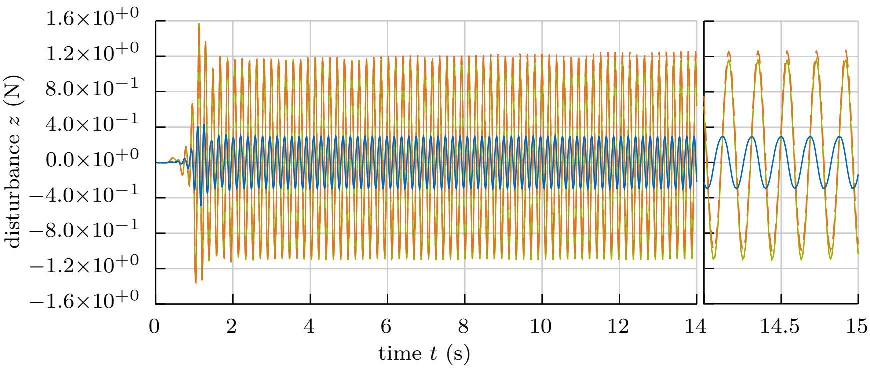

(c) Disturbance (zoomed view).

FSI **FSCI:** LQR LQI LQS

(d) Legend.

Figure 9.19 Measured outputs and disturbances in FSCI's with low-fidelity structural (CSM) subsystem scaled by $q = 10^{-2}$.

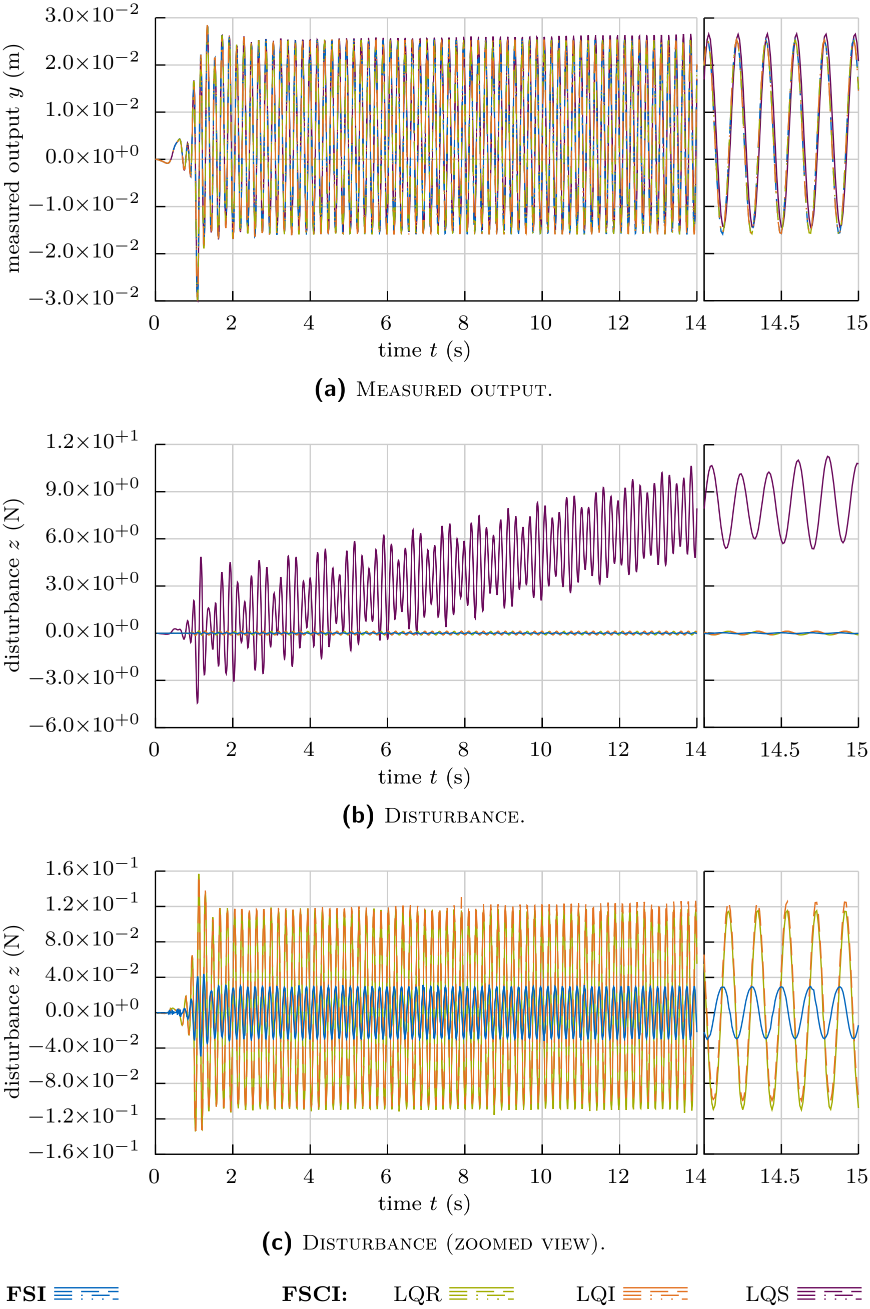

(a) MEASURED OUTPUT.

(b) DISTURBANCE.

(c) DISTURBANCE (ZOOMED VIEW).

(d) LEGEND.

Figure 9.20 MEASURED OUTPUTS AND DISTURBANCES IN FSCI'S WITH LOW-FIDELITY STRUCTURAL (CSM) SUBSYSTEM SCALED BY $q = 10^{-3}$.

9.3 Assessment of Partitioned Schemes

The previous sections of this chapter already proposed partitioned schemes for FSCI and applied them in the FSCI parameter scaling tests. The intention behind this very last section is now the assessment of those schemes. Conclusions concerning their stability and convergence behavior have already been drawn with the help of a simple single-degree of freedom (SDoF) model problem in Chapter 3 Model Problem (pp. 32 ff.). Those should now also be verified for the multi-degree of freedom (MDoF) case. Furthermore, the numerical effort related with each proposed scheme will be analyzed allowing for comparisons and ranking. The procedure is exemplarily presented on the FSCI co-simulations with the low-fidelity strurctural (CSM) and the LQI controller (CLC) subsystem.

In order to be able to evaluate the numerical effort of each scheme, a weighting of the individual numerical effort of the subsystems has to be provided: Within this work the fluid (CFD) subsystem states the most expensive one. Its numerical effort is estimated to approximately 90 % of the total amount while structural (CSM) or controller (CLC) subsystem and coupling logic each demand around 3 %. These numbers are rough, subjective estimations and therefore do not represent objective studies.

Appropriate time responses which are reflecting the numerical effort of each scheme in dependency on the parameter scaling factor are shown in Figures 9.21 (p. 151) for $q = 1^6$ to 9.30 (p. 160) for $q = 1^{-3}$. Illustrated are the number of total iterations

$$N_{\text{total}} = \begin{cases} k_{\text{end}} & \text{for} \quad \text{FSCI} \\ \sum_{k=1}^{k_{\text{end}}} m_{\text{end}} & \text{for} \quad \text{[FS]CI} \\ \sum_{k=1}^{k_{\text{end}}} m_{\text{end}} & \text{for} \quad \text{F[SC]I,} \end{cases} \tag{9.6a}$$

the number of fluid solver runs

$$N_{\text{F}} = \begin{cases} k_{\text{end}} & \text{for} \quad \text{FSCI} \\ \sum_{k=1}^{k_{\text{end}}} m_{\text{end}} & \text{for} \quad \text{[FS]CI} \\ k_{\text{end}} & \text{for} \quad \text{F[SC]I,} \end{cases} \tag{9.6b}$$

the number of structural solver runs

$$N_{\text{S}} = \begin{cases} k_{\text{end}} & \text{for} \quad \text{FSCI} \\ \sum_{k=1}^{k_{\text{end}}} m_{\text{end}} & \text{for} \quad \text{[FS]CI} \\ \sum_{k=1}^{k_{\text{end}}} m_{\text{end}} & \text{for} \quad \text{F[SC]I,} \end{cases} \tag{9.6c}$$

and the number controller solver runs

$$N_{\text{C}} = \begin{cases} k_{\text{end}} & \text{for} \quad \text{FSCI} \\ k_{\text{end}} & \text{for} \quad \text{[FS]CI} \\ \sum_{k=1}^{k_{\text{end}}} m_{\text{end}} & \text{for} \quad \text{F[SC]I.} \end{cases} \tag{9.6d}$$

The number of total iterations is decisive in case of similar subsystem weightings, while the number of certain subsystem solver runs becomes meaningful in case of significantly differing weightings. Thus, the number fluid solver runs determines this work's numerical effort. Additionally, the number of total iterations is considered another criterion, however, with less impact.

All performed FSCI simulations including those with LQR and LQS control laws confirm the conclusion of unconditional stability (convergence) for all schemes as predicted with the simple model problem. If certain simulations fail then this is the result of instable dynamics of the underlying physical problem. Schemes which are nesting sub-problems show clearly higher numerical efforts. Only equal stability properties but at the same time higher numerical efforts render nesting redundant. The single-looped FSCI scheme works best for all parameter scaling factors as well as all control laws even if not specifically demonstrated here.

Down to a parameter scaling factor of $q = 10^{-1}$ the number of fluid solver runs in the FSI, FSCI and F[SC]I schemes is nearly identical. Thus, FSCI co-simulations with the FSCI scheme do not possess a significantly higher numerical effort than pure FSI. Due to the nesting the F[SC]I scheme however requires a higher number of total iterations. Moreover, it is drastically increasing with decreasing q. The [FS]CI and FSCI schemes do not indicate such convergence problems for lower q-values. But again the nesting of the FSI sub-problem reflects in a higher amount of total iterations. Therefore, the single-looped FSCI scheme missing any nesting of sub-problems is the best choice for all q-values and control laws in case of *force* control.

First tests of FSCI with displacement control ($f_u > 0$) have been performed unsuccessfully. Conclusions regarding failure reasons (instable numerics or instable system dynamics) can not be drawn up to that point. During FSCI with force control it is observed that the controller in the outer loop of the [FS]CI scheme seems to improve (stabilize) convergence of the inner loop. The controller in the inner loop of the F[SC]I scheme on the other hand seems to harm (destabilize) convergence of the outer loop. One conjecture is therefore, that this stabilizing nature of the [FS]CI scheme could also improve the numerics in FSCI with displacement control. Nevertheless, numerical instabilities need to be proven, or disproven first. Further testing by adding an additional scaling with the u-output factor f_u to the FSCI parameter scalings tests (e.g. $f_u = 10^{-15}, 10^{-12}, \ldots, 10^{0}, 10^{3}$) is suggested. Thus, a f_u-failure bound can be exploited for each scheme in terms of q. This possibly provides further hints.

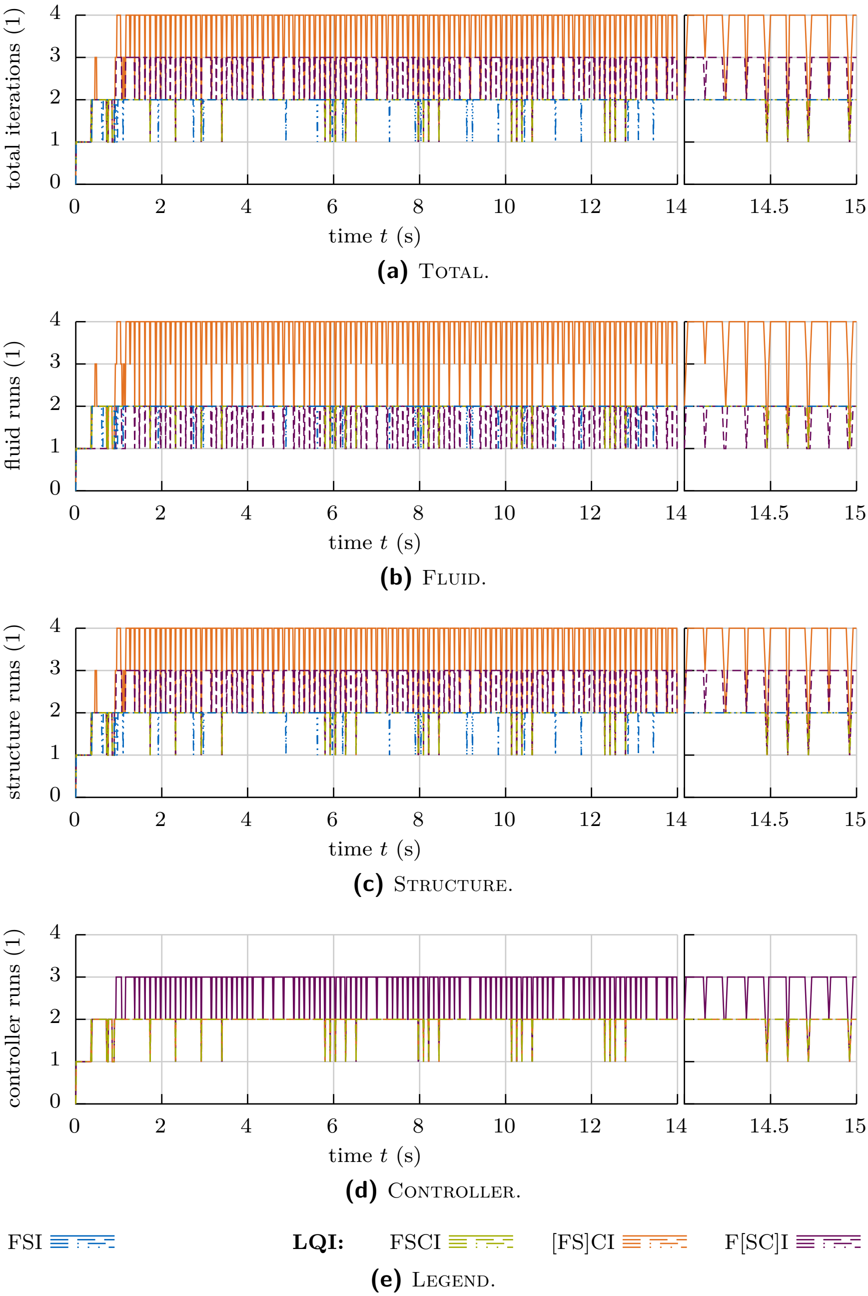

Figure 9.21 Numerical effort in FSCI with LQI controller (CLC) subsystem and low-fidelity structural (CSM) subsystem scaled by $q = 10^6$.

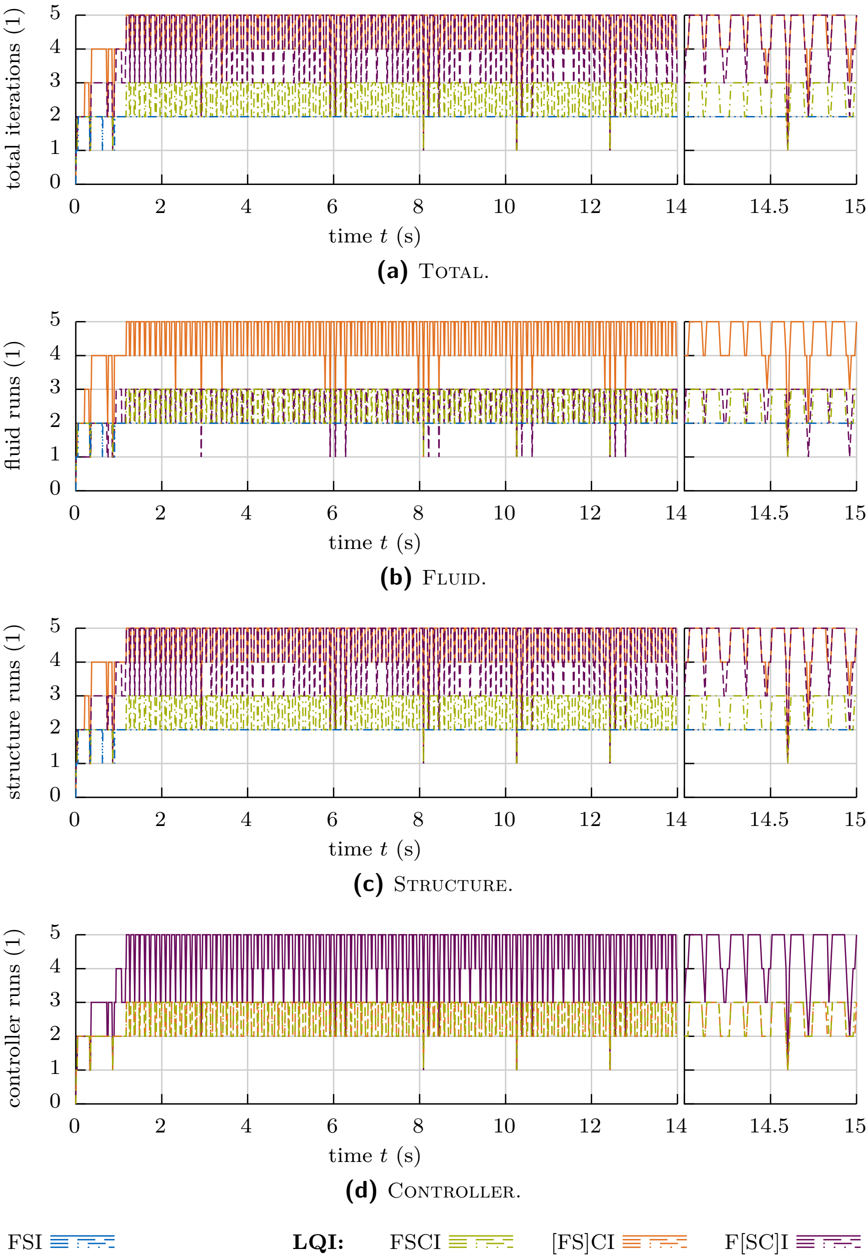

(a) Total.

(b) Fluid.

(c) Structure.

(d) Controller.

(e) Legend.

Figure 9.22 Numerical effort in FSCI with LQI controller (CLC) subsystem and low-fidelity structural (CSM) subsystem scaled by $q = 10^5$.

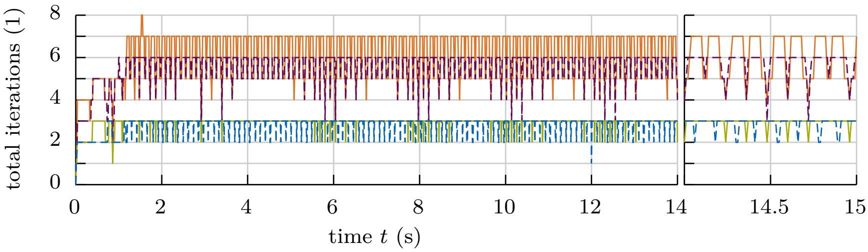

(a) TOTAL.

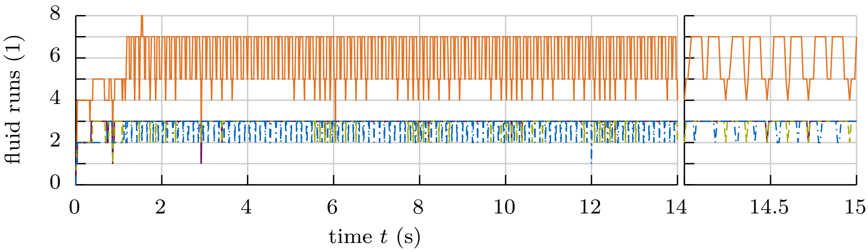

(b) FLUID.

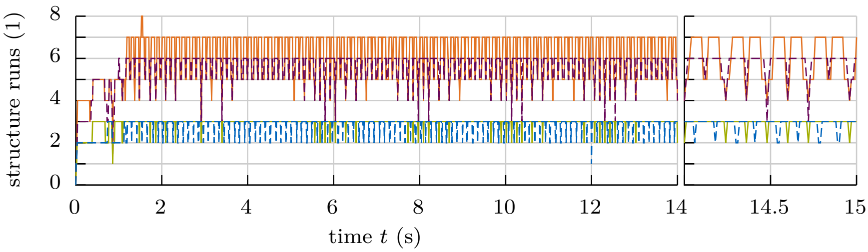

(c) STRUCTURE.

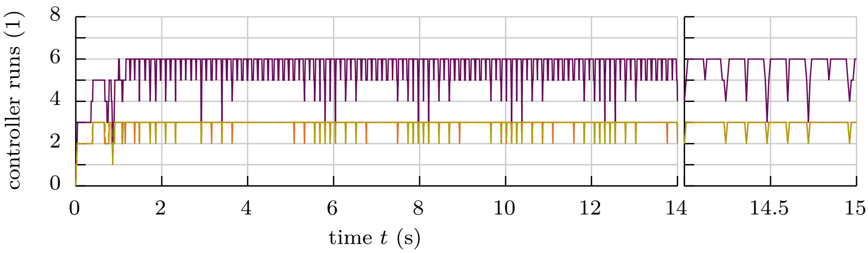

(d) CONTROLLER.

FSI **LQI:** FSCI [FS]CI F[SC]I

(e) LEGEND.

Figure 9.23 NUMERICAL EFFORT IN FSCI WITH LQI CONTROLLER (CLC) SUBSYSTEM AND LOW-FIDELITY STRUCTURAL (CSM) SUBSYSTEM SCALED BY $q = 10^4$.

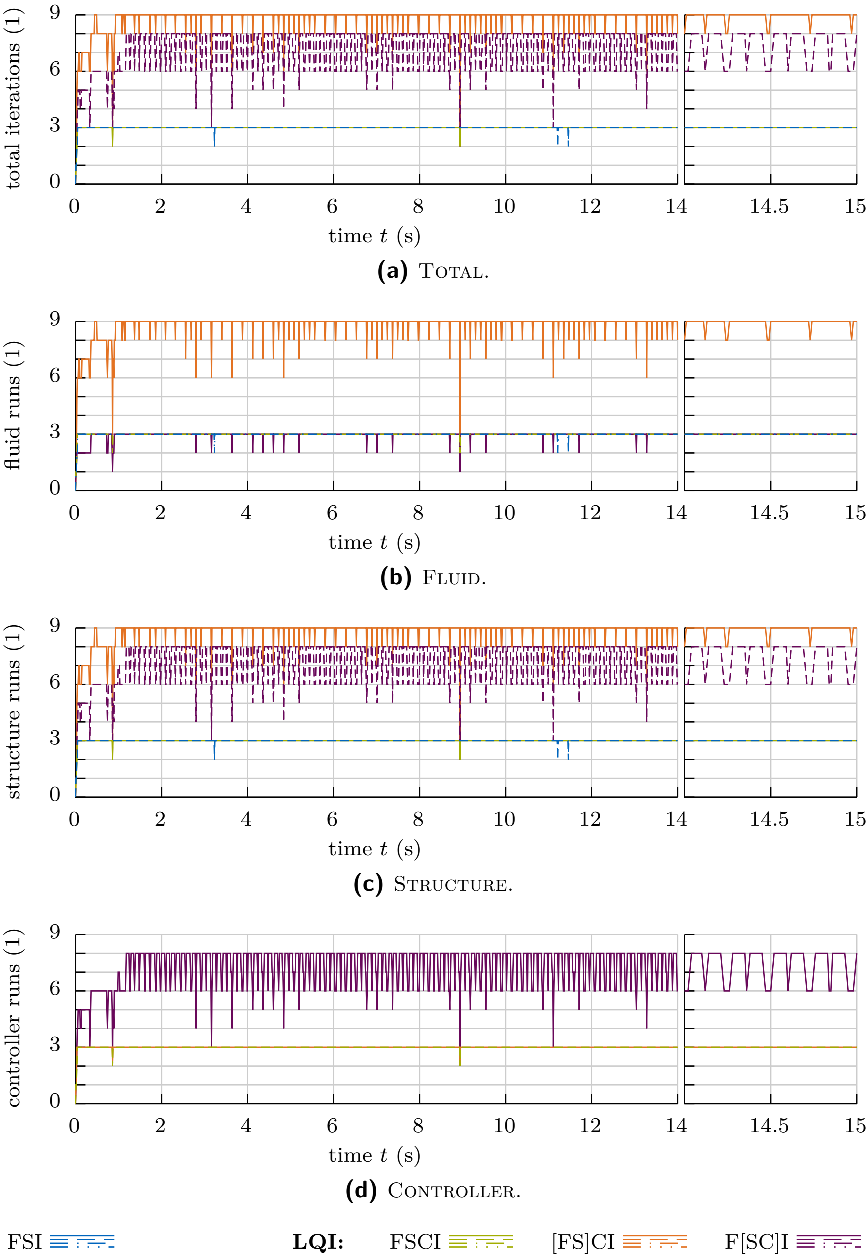

(a) TOTAL.

(b) FLUID.

(c) STRUCTURE.

(d) CONTROLLER.

(e) LEGEND.

Figure 9.24 NUMERICAL EFFORT IN FSCI WITH LQI CONTROLLER (CLC) SUBSYSTEM AND LOW-FIDELITY STRUCTURAL (CSM) SUBSYSTEM SCALED BY $q = 10^3$.

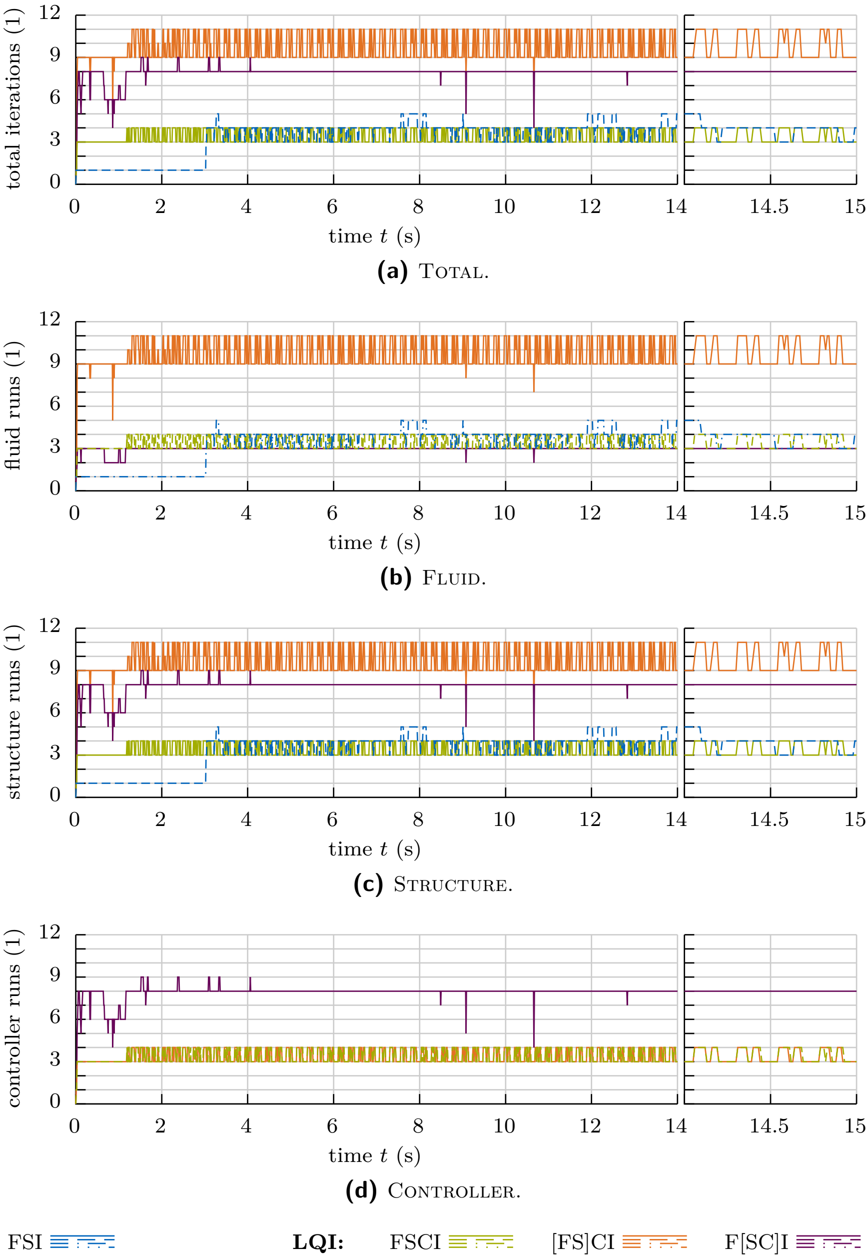

(a) Total.

(b) Fluid.

(c) Structure.

(d) Controller.

(e) Legend.

Figure 9.25 Numerical effort in FSCI with LQI controller (CLC) subsystem and low-fidelity structural (CSM) subsystem scaled by $q = 10^2$.

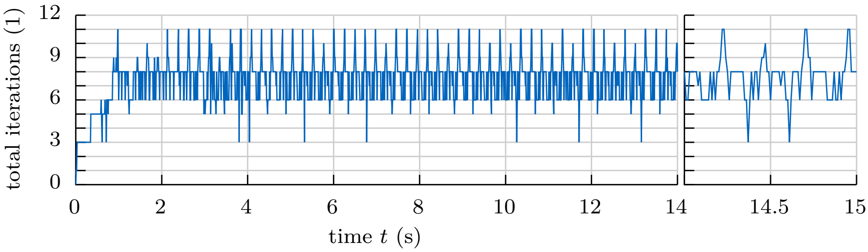

(a) TOTAL.

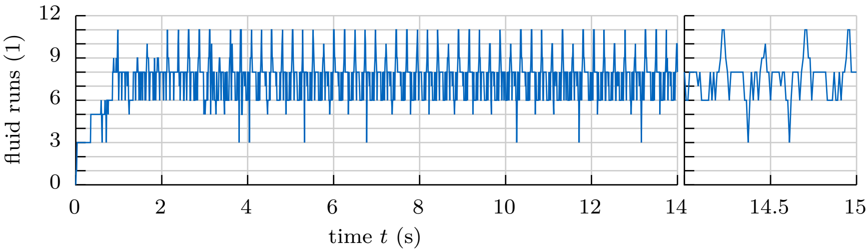

(b) FLUID.

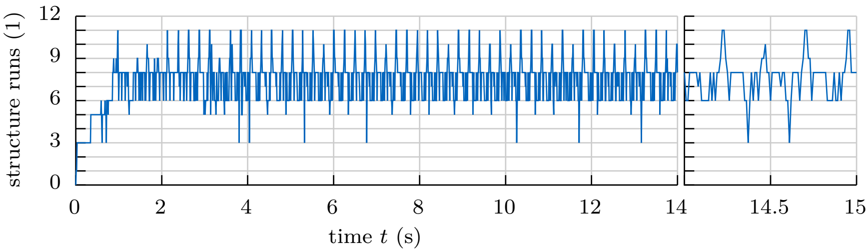

(c) STRUCTURE.

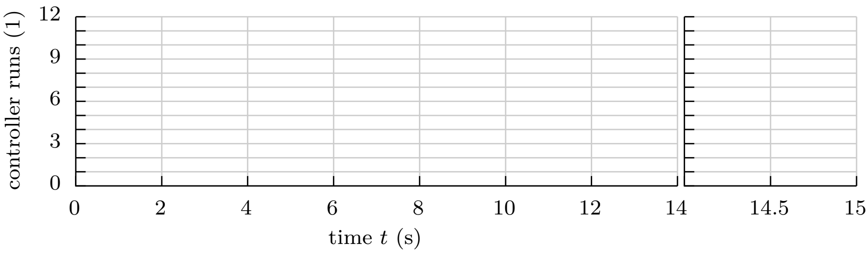

(d) CONTROLLER.

(e) LEGEND.

Figure 9.26 NUMERICAL EFFORT IN FSCI WITH LQI CONTROLLER (CLC) SUBSYSTEM AND LOW-FIDELITY STRUCTURAL (CSM) SUBSYSTEM SCALED BY $q = 10^1$.

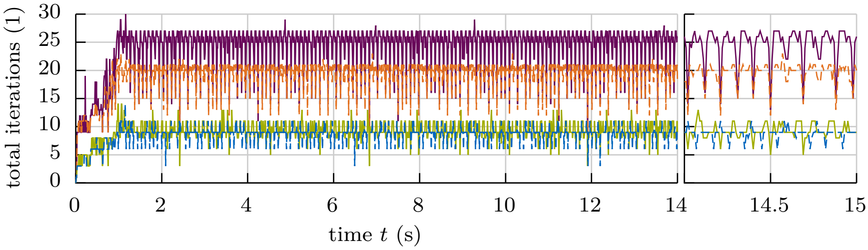

(a) Total.

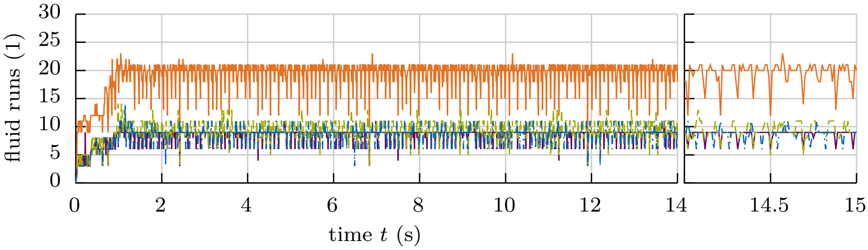

(b) Fluid.

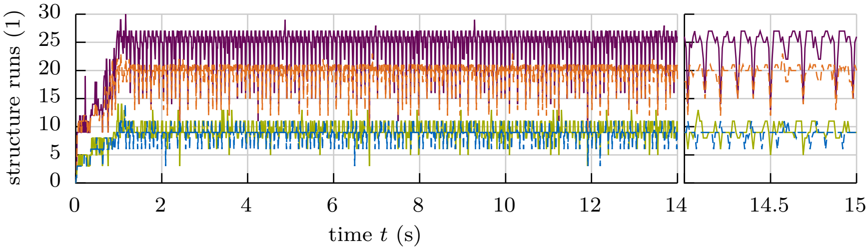

(c) Structure.

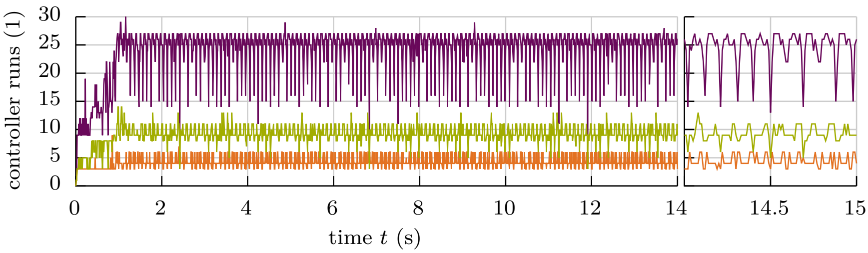

(d) Controller.

(e) Legend.

Figure 9.27 Numerical effort in FSCI with LQI controller (CLC) subsystem and low-fidelity structural (CSM) subsystem scaled by $q = 10^0$.

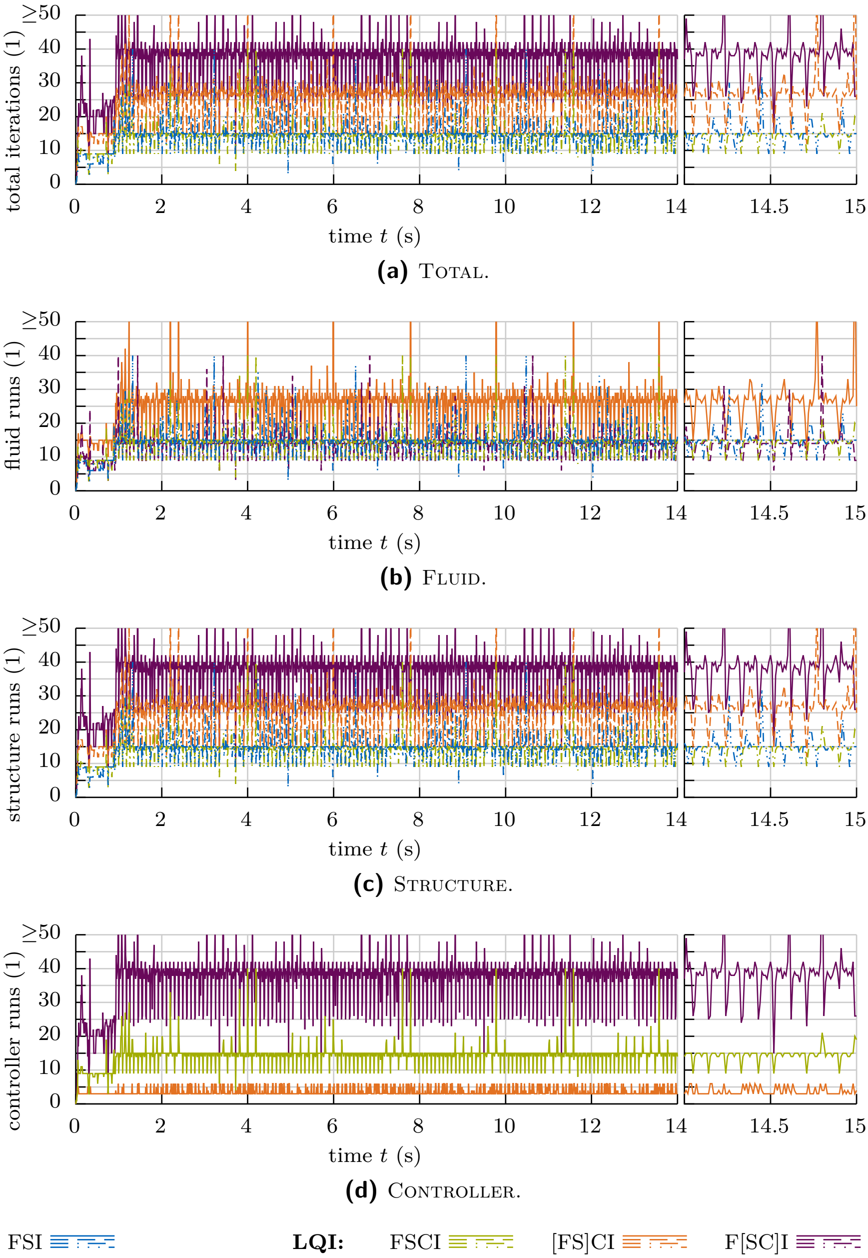

(a) TOTAL.

(b) FLUID.

(c) STRUCTURE.

(d) CONTROLLER.

(e) LEGEND.

Figure 9.28 NUMERICAL EFFORT IN FSCI WITH LQI CONTROLLER (CLC) SUBSYSTEM AND LOW-FIDELITY STRUCTURAL (CSM) SUBSYSTEM SCALED BY $q = 10^{-1}$.

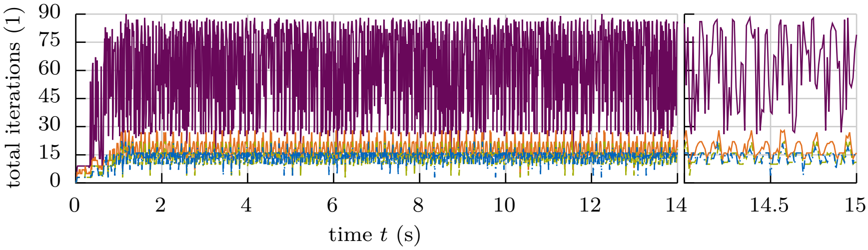

(a) Total.

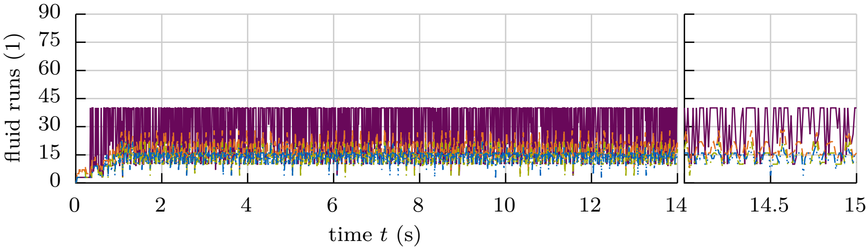

(b) Fluid.

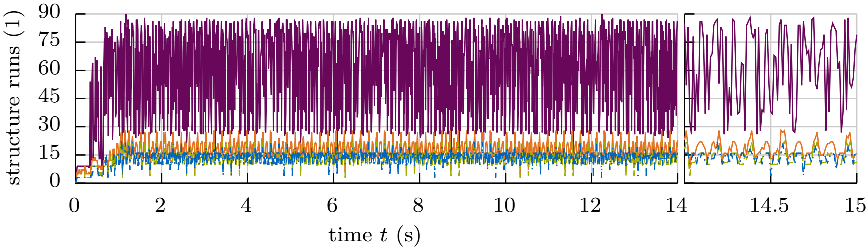

(c) Structure.

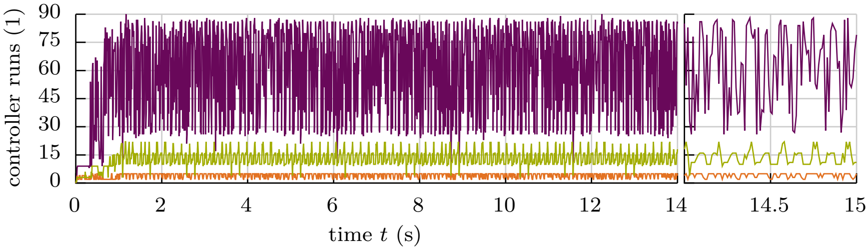

(d) Controller.

FSI **LQI:** FSCI [FS]CI F[SC]I

(e) Legend.

Figure 9.29 Numerical effort in FSCI with LQI controller (CLC) subsystem and low-fidelity structural (CSM) subsystem scaled by $q = 10^{-2}$.

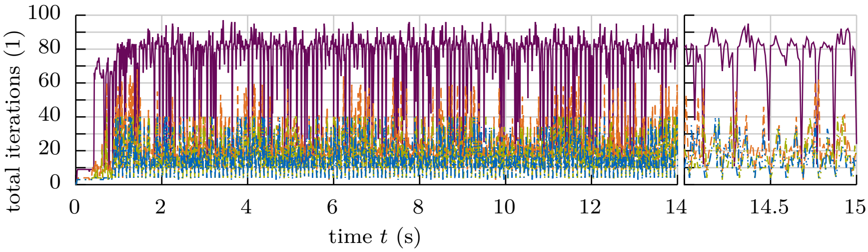

(a) Total.

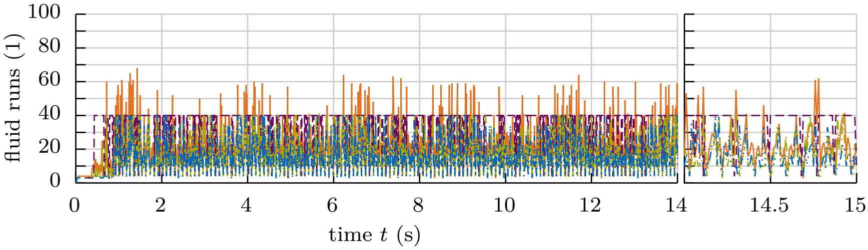

(b) Fluid.

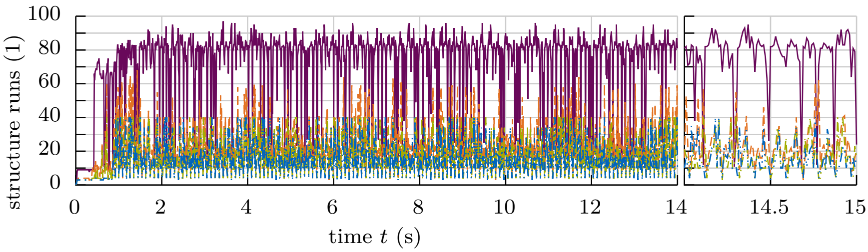

(c) Structure.

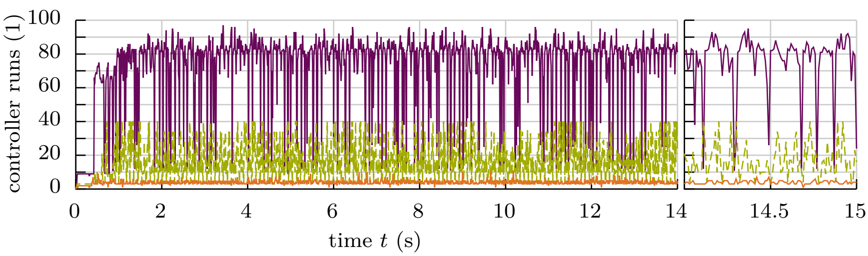

(d) Controller.

(e) Legend.

Figure 9.30 Numerical effort in FSCI with LQI controller (CLC) subsystem and low-fidelity structural (CSM) subsystem scaled by $q = 10^{-3}$.

Part III

Conclusion and Outlook

Computational fluid-structure-control interaction (FSCI) is realized. So far, this covers closed-loop control of the structural part in a fluid-structure interaction system via Neumann boundary conditions stated by the controller, briefly force control. It is implemented in a single degree of freedom (SDoF) model problem as well as in full multi-degree of freedom (MDoF) simulations of an elastic flag attached to a rigid square cylinder in channel flow. The latter involves computational fluid dynamics, computational solid mechanics, closed-loop control laws and a coupling logic.

In this regard three solution procedures are proposed: FSCI, [FS]CI and F[SC]I. They identify partitioned schemes with iterative coupling based on fixed-point formulations for the displacements and a Gauß-Seidel communication pattern. Aitken Acceleration is included. Scheme FSCI employs a single interface iteration loop while [FS]CI and F[SC]I use inner and outer loops for nesting respective sub-problems FSI and SCI. With the SDoF model problem unconditional stability (convergence) is predicted for all schemes. This also proves true for all performed MDoF simulations. The single-looped FSCI scheme convinces with the least numerical effort.

The full framework for FSCI with displacement control is also provided. Displacement control identifies here closed-loop structural control via Dirichlet boundary conditions for the root-point of the elastic flag. The efforts cover especially the modeling and implementation of the root-point excitation. Schemes FSCI, [FS]CI and F[SC]I can be applied. Up to now, only scheme FSCI has been tested without results. Failure reasons (e.g. instable numerics or instable physics) have not been investigated so far. Furthermore, the SDoF model problem is not capable of reproducing essential effects. Consequently, it can not be representative for displacement control. A new model problem must be formulated as already mentioned by Section 3.5 Résumé (p. 51) of Chapter 3 Model Problem. With that, two further ways are feasible: assessment of stability and accuracy properties for fixed control law or assessment of requirements on the control law for specified stability and accuracy properties. Subsequently, the results have to be verified in full MDoF simulations.

Observations made during the numerical experiments recommend modifications on the experimental setup: The narrow channel, i.e. the poor width of the fluid domain causes more demanding numerics, pressure shocks and a limitation of the maximum structural deflections. The latter refers to failure of the mesh updating scheme. Thus, the fluid domain should be widened and boundary conditions of top and bottom wall adjusted to slip or periodic. Additionally, the mesh quality may be improved to cover further details. Absolute convergence criteria employed so far should be replaced by relative ones for better comparison. Furthermore, necessary maximum values should be investigated. Disturbance responses tend to show wrinkles in regions of metastable dynamics for residuals left too high. The partitioned schemes prove sufficiently successful in case of force control.

Nevertheless, with regard to displacement control other more advanced schemes should be considered. This is in particular the interface Jacobian-based co-simulation algorithm (IJCSA) (Sicklinger, Belsky, Engelmann, Elmqvist, Olsson, Wüchner, and Bletzinger 2014; Sicklinger 2014).

So far, the FSCI investigations primarily focus on numerical aspects. Only three basic control laws are implemented: LQR, LQI and LQS. They prove to be successful for force control in their intended parameter ranges. Further assessment in case of displacement control should be done. In the following proposals/ideas concerning future research with focus on advanced control are given: The LQS controller could be improved further by making it, in particular the frequencies in its disturbance model, adaptive. Actual distributed-parameter systems can be accessed by classical control theory via appropriate lumped-parameter models stemming from measurements during simulations or model order reduction (see e.g. Kotyczka and Wolf 2014). Finally real distributed-parameter control can be realized by using a one-dimensional cantilever beam model for the elastic flag (compare e.g. Krstic and Smyshlyaev 2008). One last note: In contrast to Bazilevs, Hsu, and Bement (2013) the framework and control laws applied in this work are also feasible in real live applications.

Appendices

Notation

Symbols

${}_{\square}A$	(non-) relaxed iteration factor, for fixed-point iterations, in model problem
$\boldsymbol{A}_{\mathrm{d}}$	discrete amplification matrix, in time integration schemes
$\boldsymbol{A}$	left hand side matrix, in linear equation system
α	angle, in rad
α_f	coefficient, in time integration scheme generalized–α
$\widehat{\alpha}_{n\pm\square}$	modified coefficients, in time integration scheme BDFN
α	mass ratio, in 1, in model problem
α_m	coefficient, in time integration scheme generalized–α
$\alpha_{n\pm\square}$	coefficients, in time integration scheme BDFN
$\boldsymbol{A}$	state/dynamic/system matrix, Ger. *Zustands-/Dynamik-/Systemmatrix*, in state-space differential equation/linear first order IVP
$\lvert\square\rvert$	absolute value of quantity $\square$
$\square\rvert_{\square}$	evaluation of quantity $\square$ at $\square$
$\square\rvert_{\square}^{\square}$	evaluation of quantity $\square$ from $\square$ to $\square$

$\boldsymbol{b}_\mathrm{d}$	discrete right-hand side, in time integration schemes
β	coefficient, in time integration scheme generalized–α
β_{n+1}	coefficient, in time integration scheme BDFN
β	relaxation (or Aitken) factor, in 1
$\boldsymbol{B}$	input matrix, Ger. *Eingangsmatrix*, for control input, in state-space differential equation/for linear first order IVP
$b_\square$	lumped input coefficients for control input
${}^\square b^n$	constant part, for fixed-point iterations, in model problem
$\boldsymbol{b}$	right-hand side vector, in linear equation system
$\mathbb{C}$	complex numbers
$\boldsymbol{C}$	damping matrix, Ger. *Dämpfungsmatrix*, in linear second-order IVP
✗	failure, unsuccessful simulation
✓	success, successful simulation
c	lumped damping coefficient, in ${}^{\mathrm{Ns}}/_{\mathrm{m}}$
$\boldsymbol{C}$	output matrix, Ger. *Ausgangsmatrix*, in state-space output equation
$\square'$	first spatial derivative of quantity $\square$, $\square' = {}^{\mathrm{d}\square}/_{\mathrm{d}x}$
d	cylinder diameter, in m
δt	time step size, in s
$\delta\square$	variation of quantity $\square$
$\ddot{\square}$	second temporal derivative of quantity $\square$, $\ddot{\square} = {}^{\mathrm{d}^2\square}/_{\mathrm{d}t^2}$
$\dot{\square}$	first temporal derivative of quantity $\square$, $\dot{\square} = {}^{\mathrm{d}\square}/_{\mathrm{d}t}$
$\mathrm{e}^\square$	exponential function
$\boldsymbol{E}$	input matrix, Ger. *Eingangsmatrix*, for disturbance, in state-space differential equation
e	lumped input coefficient for disturbance, in 1
η	Cartesian coordinate, in m, $\boldsymbol{\xi} = [\xi\ \eta\ \zeta]^\mathrm{T}$
$\square_\eta$	component of quantity $\square$ in coordinate direction η
$\square!$	factorial of quantity $\square$
$\overset{!}{\square}$	has to be $\square$
E	Young's modulus, in ${}^{\mathrm{N}}/_{\mathrm{m}^2}$

$\mathcal{F}\{\square\}$	Fourier transform of quantity $\square$, in $^{\text{rad}}/_{\text{s}}$
f	frequency, in $^{1}/_{\text{s}}$
$\boldsymbol{M}_{\square}$	prefilter matrix, Ger. *Vorfilter (-matrix)*, in control law/controller
$\mathcal{F}(\square)$	system state differential operator, Ger. *Systemzustandsdifferentialoperator*
f_u	u-output scaling factor, in 1, for force control $f_u = 0$ or scaled displacement control $f_u > 0$
Γ	boundary
γ	coefficient, in time integration scheme generalized–α
g	gravity, in $^{\text{m}}/_{\text{s}^2}$
$\mathcal{G}(\square)$	system output operator, Ger. *Systemausgangsoperator*
$\mathcal{G}^{[\square]}(\square)$	system transfer operator, Ger. *Systemübertragungsoperator*, integrated system state differential and transfer operator, input-output relation
$\widehat{\square}$	combined quantity $\square$, in control law/controller LQS
$\widehat{\widehat{\square}}$	combined quantity $\square$, in control law/controller LQS
H	channel height, in m
h	flag height, in m
$\mathbf{I}$	identity matrix
$\mathcal{I}(\square)$	interface constraints operator, Ger. *Interfacezwangsbedingungsoperator*
$\mathrm{Im}\{\square\}$	imaginary part of quantity $\square \in \mathbb{C}$
$\int_{\square}^{\square} \square \, \mathrm{d}\square$	integral
i	running index
I_ξ	area moment of inertia with respect to coordinate direction ξ, in m^4
j	imaginary unit, $\mathrm{j}^2 = -1$
j	running index

κ	distributed sectional stiffness, in Nm
$k_{\mathrm{B}\square}$	output-feedback coefficient(s) in state (and disturbance) observer
$\boldsymbol{K}_{\square}$	feedback matrix, Ger. *Rückführmatrix*, in control law/controller
k_{I}	integral output-feedback coefficient in control law/controller, in $^1/_\mathrm{s}$
k	lumped (spring) stiffness, in $^\mathrm{N}/_\mathrm{m}$
$k_{\mathrm{R}\square}$	state-feedback coefficients in control law/controller
k	simple/inner interface iteration count
$\boldsymbol{K}$	stiffness matrix, Ger. *Steifigkeitsmatrix*, in linear second-order IVP
λ	eigenvalue, in $^\mathrm{rad}/_\mathrm{s}$, $\lambda = \sigma + \mathrm{j}\omega$
L	channel length, in m
l	flag length, in m
$[LHS]$	left-hand side, in implementation
$\lim\limits_{\square}\{\square\}$	limit value/limes of quantity $\square$ for $\square$
$\ln\{\square\}$	natural logarithm function
l	running index, in BDFN
$\max\limits_{\square}\{\square\}$	maximum value of quantity $\square$ for $\square$
$\boldsymbol{M}$	feedforward gains/matrices, Ger. *Matrizen für Vorsteuerung*, in control law/controller
$\square^{-1}$	inverse of quantity $\square$
m	lumped mass, in kg
$\boldsymbol{M}$	mass matrix, Ger. *Massenmatrix*, in linear second-order IVP
m	outer interface iteration count
μ	distributed sectional mass, in $^\mathrm{kg}/_\mathrm{m}$, $\mu = \rho w h$
$\boldsymbol{N}_{\square}$	disturbance-feedforward gains/matrices, Ger. *Matrizen für Störgrößenaufschaltung*, in control law/controller
N	number of solver runs, in numerical effort
N	number of subsystems/single-physics, in N-code coupling/multi-physical problem
N	order of/number of steps, in BDFN

n	time step count
ν	kinematic viscosity, in $\mathrm{m^2/s}$
ν	Poisson ratio, in 1
Ω	domain
ω	imaginary part of eigenvalue, in $\mathrm{rad/s}$, $\lambda = \sigma + \mathrm{j}\omega$
$\overline{\square}$	combined quantity $\square$, in control law/controller LQI
$p(\square)$	characteristic polynomial in $\square$
$\boldsymbol{\Phi}$	general time-discrete quantity, Ger. *allgemeine zeitdiskrete Größe*, in time integration schemes
$\boldsymbol{\phi}$	general time-continuous quantity, Ger. *allgemeine zeitkontinuierliche Größe*, in time integration schemes
π	pi, Ger. *Kreiszahl*, mathematical constant, $\pi = 3.141'592'653'589'793'238'462'643'383'279'502'884'197'169\ldots$
p	pressure
$\boldsymbol{p}$	pressures/pressure DoF's
$\boldsymbol{\Psi}$	general time-discrete input, Ger. *allgemeine zeitdiskrete Eingangsgröße*, in time integration schemes
$\boldsymbol{\psi}$	general time-continuous input, Ger. *allgemeine zeitkontinuierliche Eingangsgröße*, in time integration schemes
q	parameter scaling factor, in 1, in parameter scaling tests
$\boldsymbol{Q}$	weight for states, in LQR approach
$\mathrm{Re}\{\square\}$	real part of quantity $\square \in \mathbb{C}$
Re	Reynolds number, in 1
ρ	density, in $\mathrm{kg/m^3}$
ρ_∞	coefficient, in time integration scheme generalized–α
$[RHS]$	right-hand side, in implementation
$\mathbb{R}$	real numbers
r	weight for control input, in LQR approach
σ	real part of eigenvalue, in $\mathrm{rad/s}$, $\lambda = \sigma + \mathrm{j}\omega$
$\sqrt{\square}$	square root function

Sr	Strouhal number, in 1
$\square^*$	optimal value of quantity $\square$
s	time-continuous frequency/Laplace domain, in $^{\mathrm{rad}}/_{\mathrm{s}}$
τ	integration variable for time
$\widetilde{\square}$	estimation of quantity $\square$, in control law/controller
t	time variable, in s
$\square^\mathrm{T}$	transposed of quantity $\square$
u	control input, Ger. *Stellgröße*, signal, force/load (force control) or root-point displacement/excitation (displacement control)
$\boldsymbol{U}$	general (system) input, Ger. *allgemeine (System-) Eingangsgröße*, field and/or signal
$\underline{\square}$	intermediate stage to quantity $\square$
$\boldsymbol{v}$	velocities/velocity DoF's
v	velocity
W	channel width, in m
$\boldsymbol{W}$	disturbance state/dynamic/system matrix, Ger. *Zustands-/Dynamik-/Systemmatrix im Störmodell*, in disturbance state-space differential equation
$\boldsymbol{w}$	disturbance states, Ger. *Zustandsgrößen im Störmodell*, signal
w	flag width, in m
$\boldsymbol{X}$	general (system) state, Ger. *allgemeine (System-) Zustandsgröße*, field and/or signal
ξ	Cartesian coordinate, in m, $\boldsymbol{\xi} = [\xi\ \eta\ \zeta]^\mathrm{T}$
$\boldsymbol{\xi}$	Cartesian coordinates, in m, $\boldsymbol{\xi} = [\xi\ \eta\ \zeta]^\mathrm{T}$
$\square_\xi$	component of quantity $\square$ in coordinate direction ξ
x	state, Ger. *Zustandsgröße*, signal
$\boldsymbol{x}$	states, Ger. *Zustandsgrößen*, field or signal
y_d	desired output, Ger. *Führungsgröße*, signal, desired end-point displacement

$\boldsymbol{Y}$	general (system) output, Ger. *allgemeine (System-) Ausgangsgröße*, field and/or signal
$\boldsymbol{y}$	interface displacements, Ger. *Interfaceverschiebungen*, field
y	measured output, Ger. *Ausgangsgröße*, signal, end-point displacement
z	disturbance, Ger. *Störgröße*, signal, force/load, concentrated equivalent of distributed interface disturbances
$\boldsymbol{Z}$	disturbance output matrix, Ger. *Ausgangsmatrix im Störmodell*, in disturbance state-space output equation
$\square_0$	initial value of quantity $\square$
$\mathbf{0}$	zero matrix
ζ	Cartesian coordinate, in m, $\boldsymbol{\xi} = [\xi\ \eta\ \zeta]^{\mathrm{T}}$
$\square_\zeta$	component of quantity $\square$ in coordinate direction ζ
$\boldsymbol{z}$	interface disturbances, Ger. *Interfacestörgrößen*, field, forces/loads
z	time-discrete frequency/Laplace domain, in $^{\mathrm{rad}}/_{\mathrm{s}}$

Indices and Acronyms

2D	two-dimensional
ALE	arbitrary Eulerian-Lagrangian
B	observer, Ger. *Beobachter*
BC	boundary condition
BDF	backward differentiation formula
BDFN	backward differentiation formula of order N
bot	bottom wall
BVP	boundary value problem
C	center point of cylinder
CFD	computational fluid dynamics
CI	control input domain
CIMNE	Centre Internacional de Mètodes Numèrics a l'Enginyeria (International Center for Numerical Methods in Engineering), UPC

CLC	closed-loop control, Ger. *Regelung*
C	open- and/or closed-loop controller
crit	critical value
CSM	computational solid mechanics
cyl	cylinder wall

DoF	degree of freedom

E	end-point of elastic flag
EMPIRE	enhanced multi-physics interface research engine
end	ending value

f.	and the following page
FE	finite element
ff.	and the following pages
f	fictive
F	fluid
FSCI	fluid-structure-control interaction
FSCI	partitioned scheme without nesting
[FS]CI	partitioned scheme with nesting of FSI
F[SC]I	partitioned scheme with nesting of SCI
FSI	fluid-structure interaction, sub-problem of FSCI
FSI	FSI boundary
FV	finite volume

GS	Gauß-Seidel communication pattern

HHT	Hilber–Hughes–Taylor

IBVP	initial boundary value problem
IC	initial condition
IJCSA	interface Jacobian-based co-simulation algorithm
in	inlet boundary
init	initial value

I	integral output-feedback
I	interface
IVP	initial value problem
JC	Jacobi communication pattern
LQI	state- and integral output-feedback control law/controller
LQR	state-feedback control law/controller
LQS	state- and integral output-feedback and disturbance-feedforward control law/controller
max	maximum value
MDoF	multi degree of freedom
MO	measured output boundary
ODE	ordinary differential equation
OLC	open-loop control, Ger. *Steuerung*
out	outlet boundary
p.	page
PDE	partial differential equation
pp.	pages
PvW	principle of virtual work
R	root-point of elastic flag
R	(state-) feedback, Ger. *(Zustands-) Rückführung*
S	structure/solid
SCI	structure-control interaction, sub-problem of FSCI
SDoF	single degree of freedom
start	starting value
top	top wall
TUM	Technische Universität München (Technical University of Munich), Munich, Germany

UPC	Universitat Politècnica de Catalunya (Technical University of Catalonia), Barcelona, Spain
VMS	variational multi-scale
WBZ	Wood–Bossak–Zienkiewicz

Lists

Figures

Tables

Algorithms

Bibliography

(unknown) (1998). *GiD. Pre and Post Processor.* Centre Internacional de Mètodes Numèrics a l'Enginyeria, Universitat Politècnica de Catalunya, Barcelona, Spain. URL: `http://www.gidhome.com/` (visited on 02/21/2016).

— (2008). *Carat++. Wiki.* Chair of Structural Analysis, Prof. Dr.-Ing. K.-U. Bletzinger, Technische Universität München, München. URL: `http://carat.st.bv.tum.de/` (visited on 02/24/2016).

Bazilevs, Y., M.-C. Hsu, and M.T. Bement (2013). "Adjoint-Based Control of Fluid-Structure Interaction for Computational Steering Applications." In: *Procedia Computer Science* 18, pp. 1989–1998. DOI: `10.1016/j.procs.2013.05.368`.

Blevins, R.D. (1990). *Flow-Induced Vibration.* 2nd ed. New York, NY, USA: Van Nostrand Reinhold. ISBN: 978-0-442-20651-2.

Brüls, O. and M. Arnold (2008). "The Generalized-α Scheme as a Linear Multistep Integrator: Toward a General Mechatronic Simulator." In: *Journal of Computational and Nonlinear Dynamics* 3.4, pp. 041007-1–10. DOI: `10.1115/1.2960475`.

Brummelen, E.H. van (2009). "Added Mass Effects of Compressible and Incompressible Flows in Fluid-Structure Interaction." In: *Journal of Applied Mechanics* 76.2, pp. 021206-1–7. DOI: `10.1115/1.3059565`.

Causin, P., J.-F. Gerbeau, and F. Nobile (2005). "Added-Mass Effect in the Design of Partitioned Algorithms for Fluid-Structure Problems." In: *Computer Methods in Applied Mechanics and Engineering* 194.42, pp. 4506–4527. DOI: `10.1016/j.cma.2004.12.005`.

Chawner, J.R. and J.P. Steinbrenner (1984). *Pointwise. CFD Mesh Generation.* Pointwise, Inc., Fort Worth, Texas, USA. URL: `http://www.pointwise.com/` (visited on 02/21/2016).

Chung, J. and G.M. Hulbert (1993). "A Time Integration Algorithm for Structural Dynamics With Improved Numerical Dissipation: The Generalized-α Method." In: *Journal of Applied Mechanics* 60.2, pp. 371–375. DOI: 10.1115/1.2900803.

Dadvand, P. and R. Rossi (2007a). *Kratos Multi-Physics.* Centre Internacional de Mètodes Numèrics a l'Enginyeria, Universitat Politècnica de Catalunya, Barcelona, Spain. URL: http://www.cimne.com/kratos (visited on 07/18/2015).

— (2007b). *Kratos Multi-Physics. Wiki.* Centre Internacional de Mètodes Numèrics a l'Enginyeria, Universitat Politècnica de Catalunya, Barcelona, Spain. URL: http://kratos-wiki.cimne.upc.edu (visited on 07/18/2015).

Dalmau, J.C. (2016). "Applications of Turbulence Modeling in Civil Engineering." Doctoral Thesis. Barcelona: Universitat Politècnica de Catalunya.

Dettmer, W.G. (2004). "Finite Element Modelling of Fluid Flow with Moving Free Surfaces and Interfaces Including Fluid-Solid Interaction." PhD Thesis. Swansea, Wales, United Kingdom: University of Wales Swansea. URL: http://engweb.swan.ac.uk/~cgdettmer/papers/phd.pdf.

— (2015). "On Partitioned Solution Strategies for Computational Fluid-Structure Interaction. C. Kadapa, D. Perić, R. Liang, M.M. Joosten, Swansea University, College of Engineering, Swansea, Wales, United Kingdom." Seminar, November 2015, Technische Universität München. München.

Dettmer, W.G. and D. Perić (2013). "A New Staggered Scheme for Fluid-Structure Interaction." In: *International Journal for Numerical Methods in Engineering* 93.1, pp. 1–22. DOI: 10.1002/nme.4370.

Deutscher, J. (2012). *Zustandsregelung verteilt-parametrischer Systeme.* Berlin, Heidelberg: Springer-Verlag. ISBN: 978-3-642-19558-7. DOI: 10.1007/978-3-642-19559-4.

Felippa, C.A., K.C. Park, and C. Farhat (2001). "Partitioned Analysis of Coupled Mechanical Systems." In: *Computer Methods in Applied Mechanics and Engineering* 190.24–25, pp. 3247–3270. DOI: 10.1016/S0045-7825(00)00391-1.

Franke, D. (1987). *Systeme mit örtlich verteilten Parametern. Eine Einführung in die Modellbildung, Analyse und Regelung.* 1st ed. Hochschultext. Berlin, Heidelberg: Springer-Verlag. ISBN: 978-3-540-17333-5. DOI: 10.1007/978-3-662-13070-4.

Gear, C.W. (1971). *Numerical Initial Value Problems in Ordinary Differential Equations.* Prentice-Hall Series in Automatic Computation. Englewood Cliffs, NJ, USA: Prentice Hall, Inc. ISBN: 978-0-136-26606-8.

— (2007). "Backward Differentiation Formulas." In: *Scholarpedia* 2.8. revision #91024, p. 3162. DOI: 10.4249/scholarpedia.3162. URL: http://www.scholarpedia.org/article/Backward_differentiation_formulas (visited on 07/30/2015).

Gross, D., W. Hauger, J. Schröder, and W.A. Wall (2014). *Technische Mechanik 2. Elastostatik.* 12th ed. Springer-Lehrbuch. Berlin, Heidelberg: Springer-Verlag. ISBN: 978-3-642-40965-3. DOI: 10.1007/978-3-642-40966-0.

Gross, D., W. Hauger, and P. Wriggers (2011). *Technische Mechanik 4. Hydromechanik, Elemente der Höheren Mechanik, Numerische Methoden.* 8th ed. Springer-Lehrbuch. Berlin, Heidelberg: Springer-Verlag. ISBN: 978-3-642-16827-7. DOI: 10.1007/978-3-642-16828-4.

Han, S.M., H. Benaroya, and T. Wei (1999). "Dynamics of transversely vibrating beams using four engineering theories." In: *Journal of Sound and Vibration* 225.5, pp. 935–988. DOI: 10.1006/jsvi.1999.2257.

Hilber, H.M., T.J.R. Hughes, and R.L. Taylor (1977). "Improved Numerical Dissipation for Time Integration Algorithms in Structural Dynamics." In: *Earthquake Engineering & Structural Dynamics* 5.3, pp. 283–292. DOI: 10.1002/eqe.4290050306.

Iserles, A. (2009). *A First Course in the Numerical Analysis of Differential Equations.* 2nd ed. Cambridge Texts in Applied Mathematics. Cambridge, United Kingdom: Cambridge University Press. ISBN: 978-0-521-73490-5.

Jansen, K.E., C.H. Whiting, and G.M. Hulbert (2000). "A Generalized-α Method for Integrating the Filtered Navier-Stokes Equations with a Stabilized Finite Element Method." In: *Computer Methods in Applied Mechanics and Engineering* 190.3, pp. 305–319. DOI: 10.1016/S0045-7825(00)00203-6.

Jay, L.O. and D. Negrut (2009). "A Second Order Extension of the Generalized-α Method for Constrained Systems in Mechanics." In: *Multibody Dynamics. Computational Methods and Applications.* Ed. by C.L. Bottasso. Vol. 12. Computational Methods in Applied Sciences. Netherlands: Springer, pp. 143–158. ISBN: 978-1-402-08828-5. DOI: 10.1007/978-1-4020-8829-2_8. URL: http://homepage.math.uiowa.edu/~ljay/publications.dir/GenerAlphaDAEs.pdf.

Joosten, M.M., W.G. Dettmer, and D. Perić (2009). "Analysis of the Block Gauss-Seidel Solution Procedure for a Strongly Coupled Model Problem with Reference to Fluid-Structure Interaction." In: *International Journal for Numerical Methods in Engineering* 78.7, pp. 757–778. DOI: 10.1002/nme.2503.

— (2010). "On the Temporal Stability and Accuracy of Coupled Problems with Reference to Fluid-Structure Interaction." In: *International Journal for Numerical Methods in Fluids* 64.10-12, pp. 1363–1378. DOI: 10.1002/fld.2333.

King, R. (2007). "Regelungstechnik I." Lecture Notes, Technische Universität Berlin, Institut für Prozess- und Verfahrenstechnik, Fachgebiet Mess- und Regelungstechnik, Prof. Dr.-Ing. habil. Rudibert King. Berlin.

— (2008). "Regelungstechnik II." Lecture Notes, Winter Term 2008/2009, Technische Universität Berlin, Institut für Prozess- und Verfahrenstechnik, Fachgebiet Mess- und Regelungstechnik, Prof. Dr.-Ing. habil. Rudibert King. Berlin.

Kotyczka, P. (2013). "Abtastregelung und Computeralgebra." Lecture, Summer Term 2013, Technische Universität München, Lehrstuhl für Regelungstechnik, Prof. Dr.-Ing. habil. Boris Lohmann. München. URL: https://www.rt.mw.tum.de/studium-lehre/vorlesungen/abtastregelung-und-computeralgebra/.

Kotyczka, P. and N. Gehring (2015). "Advanced Control." Lecture, Winter Term 2015/2016, Technische Universität München, Lehrstuhl für Regelungstechnik, Prof. Dr.-Ing. habil. Boris Lohmann. München. URL: http://www.rt.mw.tum.de/studium-lehre/vorlesungen/advanced-control/.

Kotyczka, P. and T. Wolf (2014). "Moderne Methoden der Regelungstechnik 3. Ljapunowmethoden, energiebasierte Modellbildung und passivitätsbassierte Regelung (Teil A). Einführung in die Modellordnungsreduktion (Teil B)." Lecture, Summer Term 2014, Technische Universität München, Lehrstuhl für Regelungstechnik, Prof. Dr.-Ing. habil. Boris Lohmann. München. URL: http://www.rt.mw.tum.de/studium-lehre/vorlesungen/moderne-methoden-3/.

Krstic, M. and A. Smyshlyaev (2008). *Boundary Control of PDEs. A Course on Backstepping Designs*. Vol. 16. Advances in Design and Control. Philadelphia, Pennsylvania, USA: Society for Industrial and Applied Mathematics (SIAM). ISBN: 978-0-898-71650-4. URL: http://zenodo.org/record/12814/files/Miroslav_Krstic_Andrey_Smyshlyaev_Boundary_contBookos.org.pdf.

Küttler, U. (2009). "Effiziente Lösungsverfahren für Fluid-Struktur-Interaktions-Probleme." Dissertation. München: Technische Universität München. URL: http://mediatum.ub.tum.de/?id=820910.

Küttler, U. and W.A. Wall (2008). "Fixed-Point Fluid-Structure Interaction Solvers with Dynamic Relaxation." In: *Computational Mechanics* 43.1, pp. 61–72. DOI: 10.1007/s00466-008-0255-5.

Lafortune, P., R. Arís, M. Vázquez, and G. Houzeaux (2012). "Coupled Electromechanical Model of the Heart: Parallel Finite Element Formulation." In: *International Journal for Numerical Methods in Biomedical Engineering* 28.1, pp. 72–86. DOI: 10.1002/cnm.1494.

Lienhard, J.H. (1966). *Synopsis of Lift, Drag, and Vortex Frequency Data for Rigid Circular Cylinders*. Bulletin 300. Pullman, Washington, USA: College of Engineering, Research Division, Washington State University. URL: http://uh.edu/admin/engines/vortexcylinders.pdf.

Link, G., M. Kaltenbacher, M. Breuer, and M. Döllinger (2009). "A 2D Finite-Element Scheme for Fluid-Solid-Acoustic Interactions and its Application to Human Phonation." In: *Computer Methods in Applied Mechanics and Engineering* 198.41–44, pp. 3321–3334. DOI: 10.1016/j.cma.2009.06.009.

Little, J. and C. Moler (1984a). *MATLAB and Simulink.* The MathWorks, Inc., Natick, Massachusetts, USA. URL: http://www.mathworks.com (visited on 07/19/2015).

— (1984b). *MATLAB and Simulink. Documentation.* The MathWorks, Inc., Natick, Massachusetts, USA. URL: http://www.mathworks.com/help/ (visited on 07/19/2015).

Lohmann, B. (1997). *Zur Störgrößenaufschaltung im Zustandsraum. On Disturbance Feedforward Control by State Space Methods.* Technical Report. Bremen: Universität Bremen, Institut für Automatisierungstechnik. URL: https://www.rt.mw.tum.de/fileadmin/w00bhf/www/publikationen/forschungsberichte/FB_1998_Lohmann_feedf_dist.pdf.

— (2015a). “Moderne Methoden der Regelungstechnik 1/Modern Control 1.” Lecture, Summer Term 2015, Technische Universität München, Lehrstuhl für Regelungstechnik, Prof. Dr.-Ing. habil. Boris Lohmann. München. URL: http://www.rt.mw.tum.de/studium-lehre/vorlesungen/moderne-methoden-1.

— (2015b). “Moderne Methoden der Regelungstechnik 2/Modern Control 2.” Lecture, Winter Term 2015/2016, Technische Universität München, Lehrstuhl für Regelungstechnik, Prof. Dr.-Ing. habil. Boris Lohmann. München. URL: http://www.rt.mw.tum.de/studium-lehre/vorlesungen/moderne-methoden-2.

— (2015c). “Regelungstechnik/Automatic Control.” Lecture, Summer Term 2015, Technische Universität München, Lehrstuhl für Regelungstechnik, Prof. Dr.-Ing. habil. Boris Lohmann. München. URL: http://www.rt.mw.tum.de/studium-lehre/vorlesungen/regelungstechnik.

— (2015d). “Systemtheorie in der Mechatronik/Systems Theory in Mechatronics.” Lecture, Winter Term 2015/2016, Technische Universität München, Lehrstuhl für Regelungstechnik, Prof. Dr.-Ing. habil. Boris Lohmann. München. URL: http://www.rt.mw.tum.de/studium-lehre/vorlesungen/systemtheorie-in-der-mechatronik.

Lunze, J. (2014a). *Regelungstechnik 1. Systemtheoretische Grundlagen, Analyse und Entwurf einschleifiger Regelungen.* 10th ed. Springer-Lehrbuch. Berlin, Heidelberg: Springer-Verlag. ISBN: 978-3-642-53908-4. DOI: 10.1007/978-3-642-53909-1.

— (2014b). *Regelungstechnik 2. Mehrgrößensysteme, Digitale Regelung.* 8th ed. Springer-Lehrbuch. Berlin, Heidelberg: Springer-Verlag. ISBN: 978-3-642-53943-5. DOI: 10.1007/978-3-642-53944-2.

Mini, A. (2014). “Implementation and Evaluation of Mesh-Updating Strategies for Computational Fluid-Structure Interaction.” Master’s Thesis. München: Technische Universität München.

Newmark, N.M. (1959). “A Method of Computation for Structural Dynamics.” In: *Journal of the Engineering Mechanics Division* 85.3, pp. 67–94.

Okajima, A. (1982). "Strouhal Numbers of Rectangular Cylinders." In: *Journal of Fluid Mechanics* 123, pp. 379–398. DOI: 10.1017/S0022112082003115.

Rao, S.S. (2011). *Mechanical Vibrations.* Vol. 5. Upper Saddle River, NJ, USA: Pearson Education, Inc. as Prentice Hall. ISBN: 978-0-13-212819-3.

Rossi, R. and P. Dadvand (2015). "The Finite Element Method for Fluid-Structure Interaction with Open Source Software. Kratos Team. Centre Internacional de Mètodes Numèrics en Enginyeria (CIMNE)." AMADEO Training Workshop FSI 2nd–6th February 2015, Technische Universität München. München.

Shearer, C.M. and C.E.S. Cesnik (2006). "Modified Generalized-α Method for Integrating Governing Equations of Very Flexible Aircraft." In: *47th AIAA/ASME/ASCE/AHS/ASC Structures, Structural Dynamics, and Materials Conference.* Newport, Rhode Island, USA: American Institute of Aeronautics and Astronautics, pp. 1–21. DOI: 10.2514/6.2006-1747. URL: http://deepblue.lib.umich.edu/bitstream/handle/2027.42/76125/AIAA-2006-1747-309.pdf?sequence=1&isAllowed=y.

Sicklinger, S.A. (2014). "Stabilized Co-Simulation of Coupled Problems Including Fields and Signals." Dissertation. München: Technische Universität München. ISBN: 978-3-943-68328-8. URL: https://mediatum.ub.tum.de/node?id=1223319.

Sicklinger, S.A., V. Belsky, B. Engelmann, H. Elmqvist, H. Olsson, R. Wüchner, and K.-U. Bletzinger (2014). "Interface Jacobian-based Co-Simulation." In: *International Journal for Numerical Methods in Engineering* 98.6, pp. 418–444. DOI: 10.1002/nme.4637.

Sicklinger, S.A., C. Lerch, R. Wüchner, and K.-U. Bletzinger (2015). "Fully Coupled Co-Simulation of a Wind Turbine Emergency Brake Maneuver." In: *Journal of Wind Engineering and Industrial Aerodynamics* 144, pp. 134–145. DOI: 10.1016/j.jweia.2015.03.021.

Sicklinger, S.A. and T. Wang (2013). *EMPIRE. Enhanced Multi Physics Interface Research Engine.* Chair of Structural Analysis, Prof. Dr.-Ing. K.-U. Bletzinger, Technische Universität München, München. URL: http://empire.st.bv.tum.de (visited on 07/18/2015).

Stein, W. (2005). *SageMath.* University of Washington, Seattle, Washington, USA. URL: http://www.sagemath.org/ (visited on 03/02/2016).

Süli, E. and D. Mayers (2003). *An Introduction to Numerical Analysis.* Cambridge, United Kingdom: Cambridge University Press. ISBN: 978-0-521-00794-8.

Turek, S. and J. Hron (2006). "Proposal for Numerical Benchmarking of Fluid-Structure Interaction Between an Elastic Object and Laminar Incompressible Flow." In: *Fluid-Structure Interaction. Modelling, Simulation, Optimisation.* Ed. by H.-J. Bungartz and M. Schäfer. Vol. 53. Lecture Notes in Computational Science and Engineering. Berlin, Heidelberg: Springer-Verlag, pp. 371–385. ISBN: 978-3-540-34595-4. DOI: 10.1007/3-540-34596-5_15.

Uekermann, B., B. Gatzhammer, and M. Mehl (2014). "Coupling Algorithms for Partitioned Multi-Physics Simulations." In: *44. Jahrestagung der Gesellschaft für Informatik. INFORMATIK 2014*. Ed. by E. Plödereder, L. Grunske, E. Schneider, and D. Ull. Stuttgart, Deutschland, pp. 113–124.

Unbehauen, H. (2007). *Regelungstechnik II. Zustandsregelungen, digitale und nichtlineare Regelsysteme.* 9th ed. Studium Technik. Wiesbaden: Vieweg+Teubner Verlag. ISBN: 978-3-528-83348-0. DOI: 10.1007/978-3-8348-9139-6.

— (2008). *Regelungstechnik I. Klassische Verfahren zur Analyse und Synthese linearer kontinuierlicher Regelsysteme, Fuzzy-Regelsysteme.* 15th ed. Studium Technik. Wiesbaden: Vieweg+Teubner Verlag. ISBN: 978-3-834-80497-6. DOI: 10.1007/978-3-8348-9491-5.

Wall, W.A. (1999). "Fluid-Struktur-Interaktion mit stabilisierten Finiten Elementen." Dissertation. Stuttgart: Universität Stuttgart. URL: http://elib.uni-stuttgart.de/opus/volltexte/2000/623.

Wall, W.A. and E. Ramm (1998). "Fluid-Structure Interaction Based Upon a Stabilized (ALE) Finite Element Method." In: *4th World Congress on Computational Mechanics: New Trends and Applications, CIMNE.* Ed. by S.R. Idelsohn, E. Oñate, and E.N. Dvorkin. Barcelona, Spain, pp. 1–20.

Wang, T. (2016). "Development of Co-Simulation Environment and Mapping Algorithms." Dissertation. München: Technische Universität München. ISBN: (unknown). URL: http://mediatum.ub.tum.de/?id=1281102.

Wang, T., S.A. Sicklinger, R. Wüchner, and K.-U. Bletzinger (2016). "Assessment and Improvement of Mapping Algorithms for Non-Matching Meshes and Geometries in Computational FSI." In: *Computational Mechanics* 1, pp. 1–24. DOI: 10.1007/s00466-016-1262-6.

Weller, H. (2004). *OpenFOAM. Open source Field Operation And Manipulation.* Developed by OpenCFD Ltd (ESI Group) and distributed by The OpenFOAM Foundation. URL: http://www.openfoam.com (visited on 07/18/2015).

Wood, W.L., M. Bossak, and O.C. Zienkiewicz (1980). "An Alpha Modification of Newmark's Method." In: *International Journal for Numerical Methods in Engineering* 15.10, pp. 1562–1566. DOI: 10.1002/nme.1620151011.